PSL★
UNIVERSITÉ PARIS

THÈSE DE DOCTORAT
DE L'UNIVERSITÉ PSL

Préparée à MINES Paristech

Towards the full field modeling and simulation of annealing twins using a Finite Element Level Set method.

Soutenue par
Julien Fausty
Le 23 janvier, 2020

École doctorale n°364
ED SFA

Spécialité
Mécanique numérique et Matériaux

Composition du jury :

Julien BRUCHON
Professeur, École Nationale Supérieure
des Mines de Saint-Étienne   *Président*

Carl KRILL
Professeur, Ulm University   *Rapporteur*

Lukasz MADEJ
Professeur, AGH University of Science
and Technology   *Rapporteur*

Daniel PINO MUÑOZ
Maître de Conférence, MINES Paristech   *Examinateur*

Jean-Michel FRANCHET
Chef de Projet, SAFRAN Tech   *Membre invité*

Nathalie BOZZOLO
Professeur, MINES Paristech   *Directrice de thèse*

Marc BERNACKI
Professeur, MINES Paristech   *Directeur de thèse*

MINES
ParisTech ★ | PSL★

Aknowledgements

I would like to start by thanking all the people I'm likely to forget in the following text. There are many more people to whom I owe my success up until now than I can give credit to in one page. I would also like to thank the group SAFRAN, and more specifically Jean-Michel Franchet and Mikaël Peillard, for financing this project and giving me the opportunity to complete this thesis. A special thanks also goes to Sélim Kraria, Carole Torrin and the whole IT department of the CEMEF without whom this work would be impossible. Also, special thanks to Marie-Françoise Guenegan for being such an administrative genius.

Next I would like to thank Nathalie Bozzolo, my doctoral co-supervisor, for building this research proposal from scratch and trusting me to complete it. Without her tenacity many of the things I took for granted in this investigation would likely have been much more difficult. Marc Bernacki, my other co-supervisor, is one of the most hard-working, accessible and generous people I know. I would like to thank him, first, for putting up with my stubbornness and, second, for believing that good ideas can come from Phd students. Without his regular check-ups and demands for more precise formulations and more numerous simulations this manuscript would very likely be of much lesser quality.

I would like to thank all the friends I made here in the lab for their support, the laughs, the coffees and the pints. Ludovic Maire introduced me to life at the CEMEF and helped me find my bearings in the beginning. He was always there if I needed him for something inside or outside of the lab. Suzanne Vernier, thank you for being there at the CEMEF and always being the voice of reason and a great friend. I would like to thank Malik Durand, Brayan Murgas, Baptiste Flipon, Inès Sahli, Anthony Seret, Diego Uribe, Juhi Sharma, Jules Baton, Carlos Mensah, Corentin Perderiset, David Ruiz Sarrazola, Vincent Maguin, Ghalia Guiza, Pierrick Rambaud, Romain Fleurisson, Danaï Polychronopoulou and Gerry Agboda for their "water-cooler" discussions and general joviality. A big thanks goes out to my Columbian dynamic duo Sebastian Florez and Karen Alvarado. I probably would have gone crazy if you guys weren't here to set me back straight. Thanks for the great discussions, your boundless patience and empathy and drive to always do the right thing for your friends and family.

Lulu and Sandro I want to thank for their great hospitality. I don't know how I would have been able to get my head out of the thesis without the weekends in Toulon. The uno

games, the laughs, the apéros and the shared joys have been instrumental in keeping my spirits high. You guys are great and I'm happy I get to keep it going forever.

Léa and Alexis, I'll try to find the words to describe how lucky I am to have found you two but I don't think I'll succeed. Alexis, I'm so grateful that I got put into you're office at the get go because I don't think I could have picked a better person to spend 3 years with. From my perspective our relationship evolved very quickly from colleague towards friend. I can't say how happy I am to have met someone so thoughtful and who shares the same love of beer as me. Léa, when I first met you, you were my colleague's girlfriend. Now, I do believe that I can truly call you friend. Thank you for all the good times we had together smoking cigarettes, eating Indian food and talking metaphysics. You are a beautiful person with so much to offer the world and I know you know it and I think that that's great. Both of you are friends that I don't want to lose. My single biggest regret in leaving the CEMEF is not being able to see you two on a daily basis.

I would also like to thank my Mom. Mom, you know I would never have been able to do this without you. I want to thank you for the drive you taught me to have and the creativity you've instilled in me all these years. It hasn't always been easy to be your son, but the things you've taught me over the years are largely what got me through this thesis work and I can't thank you enough. I also want to thank you for you're unrelenting pride in my work and career path and for caring enough to try to understand what the work is about. You're an amazing person and I'm very lucky to have you.

Romane, my love. You know that this thesis would never have happened the way it did if it wasn't for you. Thank you for always being there, always contributing, always taking up my problems as "our" problems and not making any distinctions between your well being and mine. Thank you for sharing your life with me, the laughs and the tears, the joy and the anger, the good and the bad and everything in between. You are really the only one who knew how difficult these three years have been and you are also the one who has always thought about my well being throughout. It's a good thing you were here to tell me when to stop working and have fun because if not I fear I would have never made it. I'm so grateful to have such a special person in my life and I wouldn't have it any other way.

Introduction

Since the advent of high performance computing, or HPC for short, our computing capabilities have been growing exponentially over time. The HPC market has followed this trend, going from a 5 billion dollar industry in the year 2000 to a 21 billion dollar market in 2015 [1]. The applications in the R&D space are multifold, going from the most precise simulations of the human brain (Human Brain Project) to the understanding of graphene's properties and potential (Graphene Flagship). This growth is an indicator not only of the improvements in the technology underlying the computing infrastructure (both hardware and software), but also of the democratization of its use. Computer models have become integral actors in the design, validation and manufacturing of products ranging from automobiles to detergents. The industrial leaders in almost every sector are now using HPC technologies to improve their products as well as their processes.

Perhaps no industry is more in need of advanced computer models than the aerospace sector. Indeed, airplane manufacturers face multi-physics problems that combine elements of fluid-mechanics, thermal efficiency, energy conversion, acoustics, structural mechanics, metallurgy and many more. Engineers are faced with all the constraints that the physical laws impose naturally on flight along with the safety regulations and international norms necessary to set a standard for passenger transport when improving the performance of aircraft. The parameter space to be explored while designing an airplane is also enormous, every piece of the machine encompasses many variables. As such, the number of possible design iterations, which is on par with the number of points in the parameter space, is extensive. Moreover, the strict minimum number of validating tests, of the order of the number of regulatory and physical constraints, that must be run on each design is also substantial. If physical experiments had to be run on each prototype in order to evaluate its relevance, new technologies would be far and few in between and the costs would be monumental. Therefore, models are of immense importance in the design process.

The possibilities afforded to industry, and particularly the aerospace sector, by HPC technologies are the abilities to create more complex models that can be solved in shorter times. Indeed, companies are integrating powerful computer modeling approaches not only into product design, but also into process design. Massive gains in both time and energy can be obtained with an optimized manufacturing process. However, also as a consequence of the growing requirements on optimized components from more complicated design loops,

the requirements on the manufacturing processes are becoming more stringent. As the specifications list for individual pieces of complex machinery become longer, the margin of error in the manufacturing process is becoming thinner.

Typically, the nickel based superalloy disks in aircraft motors are forged components that follow complex processing routes in order to meet both mechanical strength and thermal resistance requirements at the hearts of turbines. The dimensions of the disks must be controlled throughout the process of heating, deforming and cooling the material potentially in multiple combinations of these three steps. However, as the prescriptions on the properties of the disks multiply in order to meet the demands of the next generations of aircraft motors, the parameter space of the forging process has remained largely untouched as being multiple combinations of heat and force. As such, disk manufacturers are looking to fine-tune their processes in order to produce components with better properties. However, the link between the processing of a forged metallic component and its final properties is known to be controlled for a large part by its microstructure. This is the general goal of the OPALE industrial chair co-financed by the French National Research Agency (ANR) and the SAFRAN group. In order to systematically optimize the manufacturing process of nickel based superalloys numerical methods and experimental studies must work hand in hand. This work is part of the numerical aspect of the OPALE project.

The evolution of a metallic material's microstructure along its manufacture influences almost all of its final properties (yield strength, conductivity, elastic limit, corrosion resistance, etc.). However, both the exact property/microstructure and microstructure/process relationships are, in themselves, active fields of research with few definite answers and many unanswered questions. For example, while it is known that materials with finer microstructures tend to last longer under fatigue loading, the exact role of secondary phases in both crack initiation and propagation is still the subject of many studies [2]. Here, computer models of crystal plasticity are already contributing elements to try and answer these questions in real-world applications [3–5]. The total effects of deformation and heating on metallic microstructures remain also relatively unknown even though certain results are reproducible. Here too, HPC technologies can have a great impact on the prediction of microstructures and subsequent parametrization of manufacturing chains or in testing working hypotheses of the mechanisms at play [6–10]. However, even if one chooses to use the tools of HPC in order to improve design cycles and gain both time and energy, a numerical framework is only as good as the predictive power of the physical laws it is based on.

This is the spirit and motivation for the work accomplished during this study and of which we can decompose the title in order to understand more deeply the elements and different components :

Towards the full field modeling and simulation of annealing twins using a Finite Element Level Set method.

4

where the words are color coded into three distinct categories: modeling, computing and physical metallurgy. As such, this thesis is truly at the crossroads in between three domains, all equally important, that will interplay with each other in order to form a coherent view of the goal of this project.

First, one may understand annealing twin boundaries as special crystalline defects in polycrystals which are found in great number in nickel based superalloys. While certain studies present these defects as strengthening elements of the microstructure [11–14], others present these defects as preferential sites of crack nucleation and general degradation of the material [15–17]. In any case, their presence in material microstructures plays a definite role in the final properties of machine components and thus are of general interest to the engineering community. However, physical models for their appearance and evolution during material processing have long remained elusive despite a plethora of phenomenological data [18–31]. As such, this work is focused on applying specific mathematical modeling tools along with fundamental physical principles and powerful numerical methods in order to contribute to the understanding of the evolution of these defects with respect to given process parameters. Also, the computer models created using this approach can serve as a testing ground for a number of hypotheses related to the nucleation of annealing twins as well as their particular morphologies and advance the fundamental understanding of their role in material processing.

From this initial analysis, the work program of this study can be deciphered:

- construct predictive mathematical models, starting from physical principles and results in the domain of physical metallurgy, capable of describing the behavior of the annealing twin during material processing,

- implement these models in a Finite Element Level Set framework such that their relevance and validity may be tested and compared to the current state of the art,

- and use these computer models, in a preliminary approach, to glean insights into the role that annealing twins may play during the processing of nickel based superalloys.

Of course, this program is rather ambitious, and by no means does this work aspire to explain everything there is to explain about annealing twins. The focus here is rather to build a sound physical and mathematical modeling approach capable of considering the particularity of the twin boundary and proposing certain application cases that act as proofs of concept moving forward. Indeed, this is also the structure given to this document.

The choice made here to concentrate on the annealing aspect of the processing path, independently of the deformation aspect, is one of necessity. The physical mechanisms that are attributed to the deformation of crystalline materials are numerous and usually considered separately from those that take place during heating or cooling even if they may couple during the deformation of hot matter [32]. Indeed, the coupled mechanisms

are of such complexity that the choice is made to concentrate on a subset of the phenomena, considered independently, occurring during the forming of a component in order to make progress in studying the whole. The hope is that when the physical models created separately from each other for all the phenomena are then combined coherently, this will constitute an accurate enough representative of reality. The first chapter reflects this choice and acts as a repository of information regarding the physical processes that take place during the annealing of polycrystalline media, the proper definition of the annealing twin and its particularities and the tools commonly used to model these processes.

The second chapter serves to give both the mathematical concepts and physical foundation used to create a model for the polycrystal as well as derive the proposed equations that guide the behavior of grain boundaries in crystalline media. Therefore, the second chapter contains perhaps the most important contribution of this study including the inception of the proposed mathematical model from which the subsequent chapters are inspired. Although the explanation of the mathematics used to generate this model is an attempt to be thorough, given the constraints of writing a coherent manuscript, for a full understanding of both the terms and symbols used in this chapter the reader is referred to the numerous monographs on differential geometry of which a few are listed here [33, 34].

The third and fourth chapters are direct applications of the theory developed in the second. They constitute numerical implementations of the mathematical model in specific cases. As such, these chapters are also where the mathematical model finds validation in the form of computer models that give predictions that are coherent with physical observations and analytical expansions generally regarded as true in the literature. An important aspect of these computer models is their "full field" nature often opposed to "mean field" models. As such, the approach taken here is to attempt an idealization of the microstructural scale in a continuum mechanics style and to actually simulate the dynamics of the created idealized objects individually and throughout space-time. In contrast, mean field models usually also idealize the microstructure but then proceed to simulate evolutions of statistical variables such as average quantities or the distributions of certain variables. Therefore, full field models are usually more predictive but also much more costly in terms of computational resources. In these two chapters the differentiation between "heterogeneous" and "anisotropic" models of polycrystals will also be important. Heterogeneous polycrystals will cover microstructures where the properties of each grain boundary are homogenized even if these properties may vary when comparing interface between each other. Anisotropic boundaries, however, allow for the variation of these properties along interfaces as well as in between them leading to a more general class of objects.

The fifth and final chapter serves to act as a primer for the predictive qualities of these computer models when applied to more "real-world" situations. Both the limits and the capacities of the developed tools are discussed with regards to the type of information one wishes to quantitatively predict about a microstructural evolution during annealing. Of course, one very real limitation in the predictions given by these models is not intrinsic to

the method at all but comes from the extrinsic data used to parametrize them. Indeed, the exact properties of all grain boundaries, including the twin boundary, is a subject of much discussion in the current literature [35–43]. As such, the data used to parameterize microstructural evolution models, especially models that attribute anisotropic or heterogeneous properties to boundaries, are often generated from some sort of combination of experimental data, simulated data and "best guesses" of the parties doing the parametrizations. Even so, it is shown that certain qualitative aspects of microstructural evolution, hypothesized from experimental observations, can be reproduced in certain conditions. This shows rather clearly that these physical computer models can also be used as research tools to both verify and disprove certain hypotheses of cause and effect.

Introduction en Français

Les disques de turbine des parties chaudes d'un moteur d'avion sont souvent fait en superalliage base nickel. L'optimisation des propriétés physiques de ces disques est un processus contraignant qui passe par le choix adéquat du chemin de mise en forme du composant. Ce chemin thermomécanique est, en grande partie, responsable de la microstructure de la matère forgée et donc des performances en service des pièces. Par contre, le lien procédé/microstructure est une relation complexe et couplée. La chaire industrielle OPALE, dont ce projet fait partie, a été menée conjointement avec le groupe SAFRAN, fabriquant de moteurs d'avion, pour proposer des gammes de forgeage optimisées pour les superalliages base nickel en partant de la connaissance actuelle des phénomènes métallurgiques mis en jeu pendant les étapes de mise en forme.

Dans cette optique, les modèles numériques capables de simuler les évolutions de microstructures pendant les traitements thermomécaniques sont des outils essentiels pour les ingénieurs de procédés métallurgiques. En effet, tout un ensemble de modèles, en champ complet et en champ moyen, ont été développés par la communauté pour répondre à ce besoin. Cependant, la grande majorité de ces outils font l'hypothèse d'une énergie de joints de grains homogène dans la microstructure même si la cristallographie de la matière impose le contraire. Sans prendre en compte les variations des propriétés de ces joints, il est impossible pour ces modèles de simuler correctement certains phénomènes se produisant localement dans la microstructure. Le joint de macle, omniprésent dans la plupart des microstructures forgées de superalliage base nickel, constitue un exemple parfait des limitations des modèles homogènes à l'heure actuelle.

Pour reproduire les particularités du joint de macle dans les modèles numériques il faut donc lever l'hypothèse d'homogénéité du joint de grains. Ce travail est donc dédié à l'enrichissement du modèle level set éléments finis appliqué aux évolutions de microstructures. En effet, prendre en compte l'anisotropie de la densité énergétique des joints de grains demande d'abord d'introduire les éléments de cristallographie nécéssaires dans le champ complet. Aussi, il est possible que des forces supplémentaires agissant sur les joints de grains se manifestent à cause de cette anisotropie. Ce travail consiste donc, dans un premier temps, à revisiter les premiers principes liés aux évolutions microstructurales et de les appliquer dans le cas anisotrope. Une fois le modèle complété, il doit être testé sur des cas analytiques afin de vérifier la justesse de l'approche et en sonder les limites. Enfin, certains cas applicatifs sont étudiés afin de souligner les capacités de la méthode dans des cas plus réalistes.

Oral and written communications

This investigation has lead or contributed to the following written and oral communications.

Articles

- Ludovic Maire, Julien Fausty, Marc Bernacki, Nathalie Bozzolo, Pascal de Micheli, et al.. A new topological approach for the mean field modeling of dynamic recrystallization. Materials and Design, Elsevier, 2018, 146, pp.194-207. 10.1016/j.matdes.2018.03.011.

- Julien Fausty, Nathalie Bozzolo, Daniel Pino Muñoz, Marc Bernacki. A novel Level-Set Finite Element formulation for grain growth with heterogeneous grain boundary energies. Materials and Design, Elsevier, 2018, 160, pp.578-590. 10.1016/j.matdes.2018.09.050

- Julien Fausty, Nathalie Bozzolo, Marc Bernacki. A 2D Level Set Finite Element Grain Coarsening Study with Heterogeneous Grain Boundary Energies. Applied Mathematical Modelling, 2019, https://doi.org/10.1016 /j.apm.2019.10.008.

- Jean Furstoss, Marc Bernacki, Carole Petit, Julien Fausty, Daniel Pino Muñoz, Clément Ganino. Full field and mean field modeling of grain growth in a multiphase material under dry conditions : application to peridotites. Journal of Geophysical Research: Solid Earth, 2019. Under review.

- Julien Fausty, Brayan Murgas, Sebastien Florez, Nathalie Bozzolo, Marc Bernacki. A new level set finite element formulation for anisotropic grain boundary migration. Under review.

Proceedings

- Julien Fausty, Nathalie Bozzolo, Marc Bernacki. A Level Set Finite Element Anisotropic Grain Growth Study . EUROMAT 2017, Sep 2017, Thessaloniki, Greece.

- Julien Fausty, Nathalie Bozzolo, Yuan Jin, Marc Bernacki. Simulation élément finis de la croissance de grains anisotrope dans les métaux. Journées annuelles SF2M, SF2M (Société Française de Métallurgie et des Matériaux), Oct 2017, Lyon, France.

- Ludovic Maire, Julien Fausty, Marc Bernacki, Nathalie Bozzolo, Pierre de Micheli, et al.. A new topological model for the prediction of dynamic recrystallization . ECCM - ECFD 2018, Jun 2018, Glasgow, United Kingdom.

- Julien Fausty, Marc Bernacki, Daniel Pino Muñoz, Nathalie Bozzolo. A new level set finite element formulation for anisotropic grain growth . ECCM - ECFD 2018, Jun 2018, Glasgow, United Kingdom.

- Marc Bernacki, Ludovic Maire, Julien Fausty, Nathalie Bozzolo, Daniel Pino Muñoz, et al.. A 3D numerical framework for the full field modeling of recrystallization. THERMEC2018, Jul 2018, Paris, France.

- Julien Fausty, Marc Bernacki, Nathalie Bozzolo. Thermal twinning in nickel based superalloys - a review. EuroSuperalloys 2018, Sep 2018, Oxford, United Kingdom.

- Daniel Pino Muñoz, Julien Fausty, Nathalie Bozzolo, Marc Bernacki. Recent advances in the Full-Field modeling of microstructural evolutions using a finite-element level set integrated framework. 9th International Conference on Multiscale Materials Modeling, Oct 2018, Osaka, Japan.

- Marc Bernacki, Ludovic Maire, Julien Fausty, Nathalie Bozzolo, Charbel Moussa, et al.. Towards the full modeling of microstructure evolutions during metal forming industrial processes. Matériaux 2018, Nov 2018, Strasbourg, France.

- Julien Fausty, Nathalie Bozzolo, Daniel Pino Muñoz, Jean-Michel Franchet, Marc Bernacki. A new level set - finite element formulation for anisotropic grain growth. Matériaux 2018, Nov 2018, Strasbourg, France.

- Marc Bernacki, Nathalie Bozzolo, Charbel Moussa, Daniel Pino Muñoz, Pascal de Micheli, et al.. Towards the full field modeling of microstructure evolutions during metal forming industrial processes. 7th International Conference on Recrystallization and Grain Growth - ReX GG 2019, Aug 2019, Ghent, Belgium.

- Julien Fausty, Nathalie Bozzolo, Marc Bernacki. Anisotropic grain boundary energies and their effects on simulations of grain growth in polycrystals. JA SF2M 2019, Paris, France.

Posters

- Julien Fausty, Nathalie Bozzolo, Marc Bernacki. A Level Set Finite Element Anisotropic Grain Growth Study . EUROMAT 2017, Sep 2017, Thessaloniki, Greece.

- Julien Fausty, Nathalie Bozzolo, Yuan Jin, Marc Bernacki. Simulation élément finis de la croissance de grains anisotrope dans les métaux. Journées annuelles SF2M, SF2M (Société Française de Métallurgie et des Matériaux), Oct 2017, Lyon, France.

- Julien Fausty, Marc Bernacki, Nathalie Bozzolo. Thermal twinning in nickel based superalloys - a review. EuroSuperalloys 2018, Sep 2018, Oxford, United Kingdom.

Presentations

- Julien Fausty, Marc Bernacki, Daniel Pino Muñoz, Nathalie Bozzolo. A new level set finite element formulation for anisotropic grain growth . ECCM - ECFD 2018, Jun 2018, Glasgow, United Kingdom.

- Julien Fausty, Nathalie Bozzolo, Daniel Pino Muoz, Jean-Michel Franchet, Marc Bernacki. A new level set - finite element formulation for anisotropic grain growth. Matériaux 2018, Nov 2018, Strasbourg, France.

- Julien Fausty, Nathalie Bozzolo, Marc Bernacki. Anisotropic grain boundary energies and their effects on simulations of grain growth in polycrystals. JA SF2M 2019, Paris, France.

Contents

Chapter 1

Context

In order to begin modeling physical phenomena, the underlying experimental observations and the state of the art of the domain must first be understood. The following sections are devoted to not only describing the natural processes of interest in this work but also defining the terminology that is given to these mechanisms so that readers may become aware of the current state of knowledge of the field if they are not already. However, the domain of "physical metallurgy", which studies the physical properties of metals and their alloys, is vast. The goal of these sections is not to give a comprehensive view of this subject, but rather to introduce the natural systems at work during the heating and cooling of a certain class of metals and alloys. The class of alloys that are of interest here, at least in an initial approach, is that of "monophase" polycrystals as opposed to "multiphase" polycrystals or single crystals in general. Monophase systems describe often idealized versions of reality. Even so, under certain conditions of temperature, composition and thermo-mechanical history, a significant number of metallic materials are in a monophase state. Thus, monophase materials are chosen as the main topic of this work. Once the physical aspects of annealing have been outlined, a certain number of models for reproducing these mechanisms that have been developed in the literature will be described and analyzed.

1.1 The microstructures of monophase metallic materials.

Although the etymology of the term "crystal" can be traced back to the ancient Greeks, the first indirect measurements of the atomic structure of a crystal can be placed in 1912 in the work by Friedrich, Knipping and Laue who made the first observations of the interaction between X-rays and structured matter [44]. Their findings, on the diffraction of X-rays through certain materials, gave birth to the field of crystallography and thus our modern notion of what is a crystal [45].

Definition 1. *A crystal structure is a state of matter characterized by the regular arrangement of a unit motif over relatively large atomic distances.*

In order to clarify this definition, some of the terminology must first be detailed. First, the "unit motif" referred to can be any structuration of the atomic scale. As such, this unit structure can be itself an atom, a molecule, a group of atoms, a protein, the motif of a polymer, etc. The notion of "regular arrangement" holds within it the notion of a symmetry of the whole structure. This symmetry can be described as translational, where the unit motif may repeat itself periodically in given directions, or rotational, where the crystal may look exactly the same in certain directions, or even mirror, where the structure might be indistinguishable from the mirror image of itself. "Large" atomic distances are distances that are orders of magnitude larger than the characteristic size of the unit structure. This means that the crystallinity of the matter is not just a local characteristic but a global one. Figure 1.1 is a diagram of a 2D crystal lattice where the unit structure is the circle and the various symmetries are portrayed as operations on the lattice that leave the entire structure unchanged. These symmetries are in reality what differentiates crystal structures from each other.
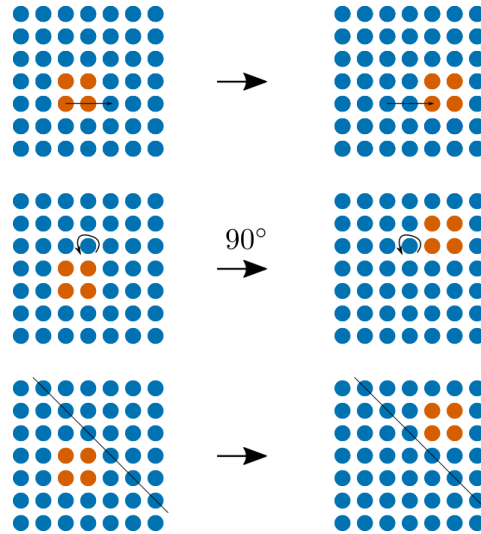

Figure 1.1: 2D crystal lattice diagram of translational, rotational and mirror symmetries.

Almost the entirety of stable metallic matter comes in a crystal state. This means that the "natural", at least for the conditions of pressure and temperature found commonly on earth, solid state of a metallic material is structured periodically. However, this symmetric ordering at the atomic/"super-atomic" scale does not necessarily extend all the way to the macroscopic scale except in so-called single crystal materials. There is notably one intermediate scale of great interest for the material properties of metals and alloys which is called the *microstructure* of the material [46]. This scale of the material, ranging

potentially from a few nanometres to the millimeter, can be seen as a composition of different crystallites or grains, regions of space with the structural periodicity characteristic of a crystal, stuck together to form the bulk of the material called a *polycrystal*. Figure 1.2 illustrates this concept by considering different regions of space made out of the same crystal structures oriented in different manners.
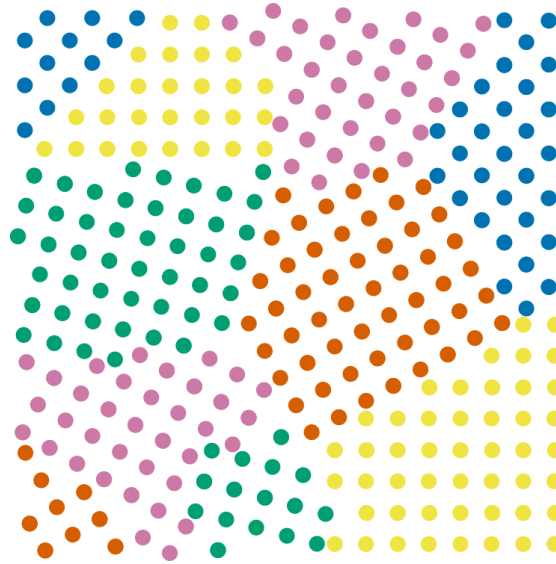

Figure 1.2: A 2D monophase microstructure diagram where the grains with the same orientation are colored the same way (the spatial scale is not representative).

Indeed, the Figure 1.2 does not quite do justice to the richness of the most complex real microstructures which might be composed of different phases, regions where the chemical composition and crystal structure might change. However, considering "monophase" systems allow us to consider materials made up of one phase, and therefore one crystal structure, and as such operate in this simplistic view of the polycrystal microstructure. Even so, certain metallic alloys, such as Inconel® 718, a nickel based superalloy, can be found in this monophase form as shown in Figure 1.3 under certain conditions. Sometimes, nickel based superalloys are actually processed in such a monophase state during the forging process.

However, even as simple as one might want to consider monophase polycrystals, they come with their own complex features. These objects can be classified as crystallographic defects and constitute deviations from the perfectly periodic crystal structure. These distortions come in three large geometric classes:

Point Defects associated to missing or extraneous atoms in the lattice arrangement generating a local disordering of the atomic structure.
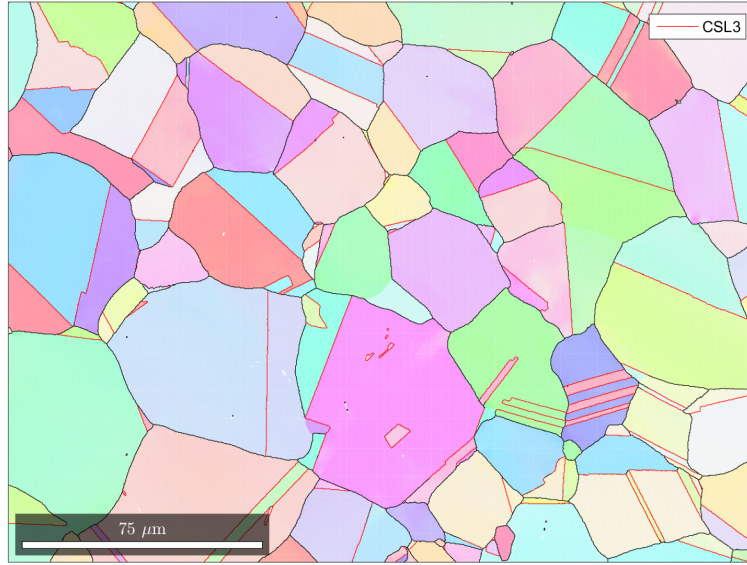
17

Figure 1.3: Electron Backscattered Diffraction (EBSD) map of a monophase Inconel® 718 sample, provided by Alexis Nicolaÿ [47], in which the twin boundaries are shown in red, the general grain boundaries are in black and the crystallites are colored according to their crystallographic orientations.

Line Defects of which the largest group are called dislocations, which are locally structured distorsions in the crystal structure that generate elastic stress fields in the nearby lattice.

Surface Defects the most prominent example being grain boundaries, structures created when two crystallites with different crystallographic orientations meet.

Of course, the examples given are the most commonly discussed objects in the literature and do not constitute an exhaustive list. For example, one could classify a triple line, the meeting of three grain boundaries in three dimensions, as a line defect that does not adhere to a dislocation type structure. Figure 1.4 illustrates examples of these of defects projected into 2D planes of a crystal.

These defects and their distributions play a large role in the final properties of metallic materials. Their concentration is the metric by which a polycrystal's deviation from a perfect crystal structure is quantified both globally and locally. For example, dislocation densities in polycrystals are directly related to work hardening, the phenomenon by which a metallic material becomes harder as it is deformed [46]. Grain boundaries implicitly define the size of the grains in a material, the distribution of which can be related to the yield strength of polycrystalline matter by the Hall-Petch effect [48]. As such, a monophase material's microstructure can truly be characterized by the spatial distribution of crystallographic defects.
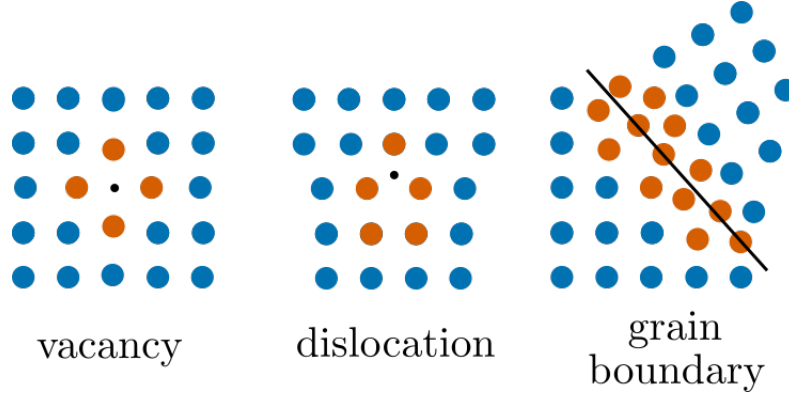
vacancy   dislocation   grain boundary

Figure 1.4: Diagram of a vacancy, a dislocation and a grain boundary in two dimensions where the neighboring units are in orange and the matrix is in blue while the geometric aspect of the defect is in black.

Taking a more quantitative view of the microstructure, we can attempt to define the energy of a defect as follows

Definition 2. *The energy of a crystallographic defect is the work one must furnish in order to insert this defect into an initially defect-free crystal structure.*

Therefore, defining the ground state energy of a certain mass of perfect crystal G_0 and potentially calculating the energy of the same mass of crystal containing one defect G_d, one may calculate the energy of the given defect $\aleph_d$ as

$$\aleph_d = G_d - G_0 \tag{1.1}$$

While this definition is perfectly usable for point defects, the notion of an energy density must be used for higher dimensional geometric defects. Indeed, line and surface defects are ill-quantifiable in terms of number because they span certain regions of physical space. As such, we may define more precisely the energy density ρ_d of a line or surface defect as

$$\rho_d = \lim_{\mu \to 0} \frac{G_d - G_0}{\mu} \tag{1.2}$$

where μ is the spatial *measure* of the defect (length if it spans a line and area if it spans a surface). As such, one has the necessary notions to define the total energy of a monophase polycrystal microstructure G as

$$G = G_0 + \sum_{p \in P} \aleph_p + \sum_{l \in L} \int_l \rho_l d\mu_l + \sum_{s \in S} \int_s \rho_s d\mu_s \tag{1.3}$$

where P is the set of all point defects, L is the set of all line defects and S is the set of all surface defects. Now even though most of the symbols in equation (1.3), have not yet been properly defined, it serves the symbolic purpose to define the total energy of the microstructure in terms of a sum of energies of individual defects.

However, there is a zoology of sub-classifications of all kinds of defects. These classes may or may not follow the geometric categorization given here and can be broken down into more and more specific sub-groups. For example, point defects can be decomposed into vacancies, substitutional defects and interstitial defects. The interstitial group may be sub-divided into interstitials that are made of different types of atoms present in the nominal composition of the material or impurities that can be found in small quantities. Dislocations can, schematically, be found in two extreme flavours, edge and screw. Each of these groups can be hierarchically divided into multitudes of subgroups and so on. Ultimately, the granularity with which one describes these defects is not so much a physical choice but a modeling one. The sub-classification of these defects that one might use is thus a reflection of both the model's scale and its complexity.

For example, if one considers a model that represents all grain boundaries as equivalent objects with the same properties, then this model would be incapable of differentiating between the behaviors of physically different interfaces. Yet, in the most general cases and close to the atomic scale, grain boundaries can be parameterized by *thirteen* independent structural parameters [49]. In this work the goal is to generate a model capable of simulating annealing twin boundaries as distinct objects from other types of grain boundaries. As such, the first question to ask in this situation is what level of detail does our model need in the description of the twin boundary? A reformulation of the question is what is the minimum set of structural parameters of the grain boundary such that the annealing twins can be successfully differentiated, at the scale of the polycrystal, from other grain boundaries?

Taking into account the fact that target model is a microstructural model, and not atomic or macroscopic, and that the properties of the grain boundaries must be measurable using conventional experimental microscopy techniques, the *five* parameter description of the grain boundary [49] is chosen.

Definition 3. *The grain boundary space $\mathcal{B}$ can be parameterized by five independent parameters:*

- *three related to the **misorientation** of the grains on either side of the boundary,*

- *and two related to the **inclination** of the boundary plane.*

Figure 1.5 illustrates the concept behind the five parameter description of the grain boundary in 3D. Indeed, the misorientation of the boundary is defined by both the orientation relationship of both neighboring grains and the symmetries of the base crystal. The inclination of the boundary is then defined more locally by following the geometry of the
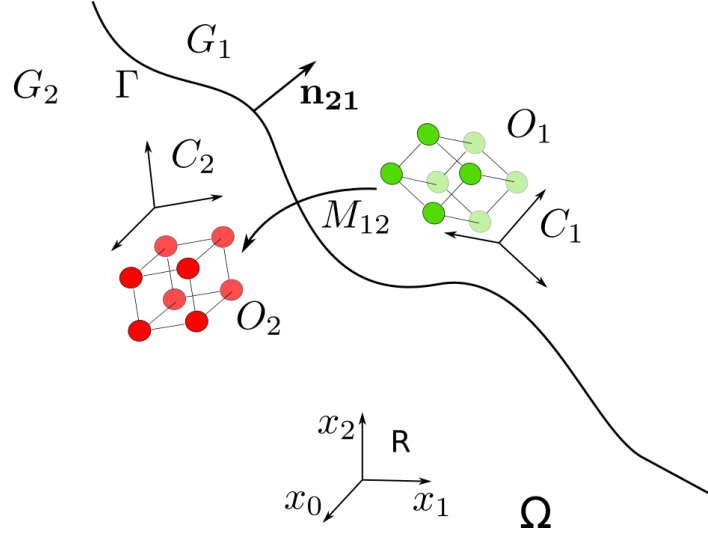
Figure 1.5: 3D diagram of the five parameter description of the grain boundary Γ between grains G_1 and G_2 with respective crystal orientations O_1 and O_2 with crystal frames C_1 and C_2 generating a misorientation M_{12} and an inclination vector n_{21} in the Ω space equipped with a reference frame R.

interface with respect to the neighboring crystal structures. However, in order to introduce these notions properly, their mathematical representations must be first understood [49].

Let $\Omega \subset \mathbb{R}^3$ be the domain of the microstructure equipped with a reference frame $R \in \mathcal{R}$, with $\mathcal{R}$ the set of all possible frames of $\mathbb{R}^3$

$$\mathcal{R} = \{\{x_0, x_1, x_2\} \in (\mathbb{R}^3)^3 | \{x_0, x_1, x_2\} \text{ is an orthonormal basis of } \mathbb{R}^3\} \qquad (1.4)$$

$(\mathcal{SO}(3), \cdot)$ is the special orthogonal group equipped with its classical group operation. The elements of this group can be represented by rotations in $\mathbb{R}^3$. Given an element $M \in \mathcal{SO}(3)$, its action on any set of vectors $\{x_{i=1,...,n}\} \in (\mathbb{R}^3)^n$ conserves both lengths, angles and orientations between these vectors. As such, the action of M on any frame in $\mathcal{R}$ is also a frame and thus $\mathcal{R}$ is closed under the action of any element of $\mathcal{SO}(3)$

$$M \in \mathcal{SO}(3) \implies M : \mathcal{R} \to \mathcal{R}$$

Any crystal structure can be attributed a crystal frame C that serves to parametrize the lattice positions of its unit motifs. However, in a polycrystal, the crystal frames of each crystallite are all potentially oriented differently from each other in space. As such, given the reference frame R and the crystal frame of any grain $C_n \in \mathcal{R}$ one can define the orientation of the grain as follows

Definition 4. *An orientation O_n of a grain with a crystal frame $C_n \in \mathcal{R}$ is an element*

of $\mathcal{SO}(3)$ such that

$$C_n = O_n(R) \tag{1.5}$$

with R the reference frame.

However, this definition does not ensure the uniqueness of the description of the orientation of a grain because of the symmetries of the crystal structure. These symmetries naturally define a crystallographic equivalence relation $\equiv_{cry}$ between frames in $\mathcal{R}$. Let S be the rotational symmetry group of the crystal defined as

$$S = \{s \in \mathcal{SO}(3)|s(C) \equiv_{cry} C, \ \forall C \in \mathcal{R}\}$$

As such, the crystallographic equivalence set $[C]$ of a frame $C \in \mathcal{R}$ is the set of frames defined as

$$[C] = \{s(C), \ s \in S\}$$

Analogously, using the group operation $\cdot$ on $\mathcal{SO}(3)$, the equivalence set $[O]$ of a given grain orientation $O \in \mathcal{SO}(3)$ can be defined as

$$[O] = \{(s \cdot O), \ s \in S\} \tag{1.6}$$

This means that each crystallographic orientation has as many representations as there are rotational symmetries in the symmetry group of the crystal. This fact is important because if we would like to define the orientation relationship D_{nm} between two grains accepting orientations O_n and O_m as

$$D_{nm} = O_n \cdot O_m^{-1} \tag{1.7}$$

we come to the conclusion that this object is not unique and admits its own crystallographic equivalence set $[D_{nm}]$ as

$$[D_{nm}] = \{(s \cdot O_n) \cdot (s' \cdot O_m)^{-1}, \ (s, s') \in S\} \tag{1.8}$$

whose size is actually the number of rotational symmetries squared. From a computational point of view, this set is rather cumbersome to deal with in that it contains, by definition, the same information many times over. One would much rather deal with one representative object of the set than all of them. However, any choice of an individual orientation relationship from the equivalence set must be made in a systematic manner such that the same representative is chosen each time the same set is considered.

Definition 5. *A fundamentalization operation Y is a function that takes a set of objects A and returns one representative of the set a such that each time the same set is given, the same representative is chosen*

$$Y : \mathcal{P}(V) \to V$$
$$A \to a \in A \tag{1.9}$$

where $\mathcal{P}(V)$ is the power set of a set V.

As such, for a given choice of fundamentalization operation Y on the base set $\mathcal{SO}(3)$ we can define the misorientation as

Definition 6. *The misorientation M_{nm} between two grains accepting orientations O_n and O_m respectively is an element of $\mathcal{SO}(3)$ such that*

$$M_{nm} = Y([D_{nm}]) \tag{1.10}$$

Corollary 1. *The misorientation of a grain boundary is the misorientation between its neighboring grains.*

Therefore, the misorientation of a grain boundary contains the information regarding the *bicrystallography* of its constitutive grains. It does so in a unique and systematic way. Also, being elements of $\mathcal{SO}(3)$ the misorientations can be parameterized by three independent parameters, three Euler angles for instance.

In practice, the orientation relationships D_{nm} in an equivalence class $[D_{nm}]$ can be represented by angle-axis pairs $[(\theta_{nm}, a_{nm})]$ where the θ_{nm} parameter is the rotation angle and the unitary vector a_{nm} is the axis around which one rotates. This description is not very useful from a computational point of view where one might need to combine different rotations together. For this purpose, unit quaternions

$$q_{nm} = (\cos(\theta_{nm}), \sin(\theta_{nm})a_1, \sin(\theta_{nm})a_2, \sin(\theta_{nm})a_3)$$

are actually easier to use. The quaternions have a natural Hamiltonian algebra which make the computation of subsequent rotation much more efficient than other representations. Also, the fundamentalization operation for the quaternion representation of the misorientation m_{nm} can be expressed as the unique quaternion

$$m_{nm} \in \{q \in [q_{nm}] \,|\, \forall u \in [q_{nm}], \, q^0 \geq u^0\} \cap \{q \in [q_{nm}] \,|\, q^0 > q^1 > q^2 > q^3\}$$

which is relatively efficiently computed in a numerical setting.

At the mesoscopic scale, the information regarding the inclination of the grain boundary is contained in the normal vector n to the interface at each point of the interface.

However, the normal vector represented in the reference frame R gives no information about the crystal planes of the grain boundary. The normal vector only describes the atomic planes when it is expressed in the crystal reference frames of the neighboring grains

$$(n_n, n_m) = (O_n^{-1}n, O_m^{-1}n), \tag{1.11}$$

which holds redundant information when considered with the misorientation M_{nm}

$$(n_n, n_m) = (O_n^{-1}n, M_{nm}^{-1}O_n^{-1}n) = (n_n, M_{nm}^{-1}n_n), \tag{1.12}$$

where the orientations act on vectors with the classic operation of $\mathcal{SO}(3)$. Therefore the inclination of the grain boundary, when put into relation with the misorientation, is fully characterized by the inclination of the boundary plane in the reference grain, n_n in this case. Normalizing this vector, it becomes unique and can thus be parameterized by $3 - 1 = 2$ parameters, two angles in spherical coordinates for example.

As such, a grain boundary B_{nm} can be characterized by a tuple

$$B_{nm} = (M_{nm}, n_n) \tag{1.13}$$

containing the misorientation and the inclination.

As such, when dealing with the parameterization of grain boundaries, extreme care must be given to respecting this equivalence relation $\equiv_{cry}$. In this sense, the choice of equivalent orientation for both grains must not influence any physical property one might wish to calculate.

In fact, in this work, there are only two physical quantities of interest for the dynamics of grain boundaries during annealing which are the energy density γ and the mobility μ both maps from $\mathcal{B}$ to $\mathbb{R}^+$ [32].

However, the measurement of the actual maps γ and μ are still open lines of inquiry that are studied by both experimental investigations [37–39] and numerical calculations [40,42, 50,51]. What is striking in the results of these studies is the dependence of both the energy density and the mobility of a grain boundary on its five parameter characterization B_{nm}. Indeed, these quantities vary by *orders of magnitude*, in the same material, at different points of the five parameter grain boundary space [51]. It is hypothesized that these two properties of grain boundaries might control both the dynamics and statics of grain boundaries at the scale of the microstructure. For example, in [52] the faceting behavior of boundaries are related to the evolution of γ function as the temperature changes. However, all analytical approaches to define a function of the entire grain boundary space that could describe the energy density, for example, have been either inconclusive or very new and untested [50, 51]. The most successful, and perhaps simplest, such analytical function is perhaps the Read-Shockley model for grain boundary energies [36] based on a dislocation type reduction of the grain boundary. This model does not cover the entire space of grain boundaries but only those with the "smallest" relative misorientations, i.e. the "low angle"

grain boundary subspace. This model is not of particular use in what concerns the twin boundary which can be classified as a "high angle" grain boundary.

Definition 7. *A* twin orientation relationship *between two crystal orientations is one which creates an additional bicrystal mirror symmetry.*

Given that the most common Nickel based superalloys have face centered cubic (FCC) crystal structures, the twin boundary in this context can also be more specifically described.

Corollary 2. *In a FCC crystallographic structure, twin boundary is a grain boundary that accepts an orientation relationship between its neighboring grains described as a* $60°$ *rotation around a* $\langle 111 \rangle$ *axis common to both grains.*

The particular bicrystallography of the twin orientation relationship accepts many crystallographically equivalent representations. Another noteworthy one is

Corollary 3. *Two FCC crystallites in a twin orientation relationship can have their orientations transformed one into the other after applying a mirror symmetry with respect to their common* (111) *plane.*

Therefore, an annealing twin is classified as such only with respect to its misorientation. One may also further subdivide the annealing twin class of boundaries into two groups that depend only on the inclination of the boundary

Corollary 4. *A* coherent *twin boundary is a twin boundary whose boundary plane is the* (111) *plane that both grains share while an* incoherent *twin boundary is any other twin boundary.*

As such, the twin boundaries are actually just a subspace $\mathcal{B}_T$ of the total boundary space $\mathcal{B}$. The coherent twin boundary is one point in $t_{coh} \in \mathcal{B}_T$ while the space of incoherent twin boundaries is the complement of t_{coh} with respect to $\mathcal{B}_T$. Figure 1.6 depicts 2D representations of both types of twins in FCC lattices. Even though these singular boundaries generate more bicrystallographic symmetries than a more general grain boundary, this is not what generates the interest surrounding them. Their preponderance in processed microstructures of certain metallic materials (low to medium stacking fault energy materials to be precise) has long remained a mystery in the physical metallurgy community [32, 49].

The working hypothesis for the disproportionate amount of annealing twin boundaries in material microstructures is related to their relatively low energy density [32]. Indeed, in all atomistic calculations of the energy density of grain boundaries in low stacking fault energy materials, the coherent twin boundary is often computed to have an order of magnitude lower energy density than other more general boundaries [40]. The idea is that, statistically, since the energy of the coherent twin boundary is so low, the coherent

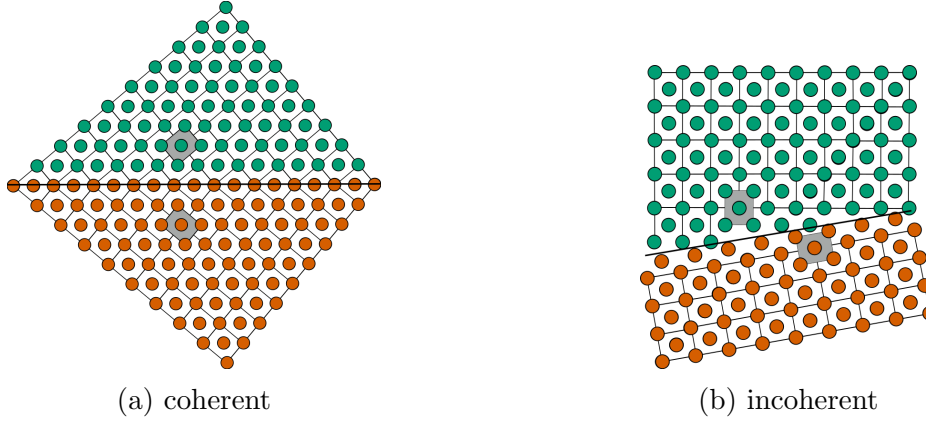(a) coherent   (b) incoherent

Figure 1.6: Diagrams of 2D projections of twin grain boundaries for an FCC structure viewed along $\langle 110 \rangle$ in the coherent (1.6a) and incoherent (1.6b) cases.

twin boundary is thus favoured over other grain boundaries as the microstructure evolves during processing. Nickel is a low to medium stacking fault energy material and thus most nickel based superalloys are as well. Indeed, as is shown in Figure 1.3, a great number of nickel based superalloys are subject to larger amounts of twin boundaries as compared to other types of grain boundaries. Even so, the distinction between coherent and incoherent twin boundaries is an important one. The same atomistic simulation investigations that show the coherent twin boundary as having very low energy density in pure nickel for example [40] also show that incoherent twin boundaries may have energy densities of the same order as other more general boundaries. Thus, the energetic singularity of the coherent twin boundary does not necessarily extend to the entire twin boundary space $\mathcal{B}_T$. Thus a model capable of predicting the behavior of twin boundaries must not only be able to differentiate boundaries with respect to their misorientations but also with respect to their inclinations.

1.2 The phenomenology of annealing processes

Now that the general structures present at the microstructural level in monophase polycrystal materials have been enumerated, one may consider the more dynamic aspects of the microstructure during annealing. For the monophase polycrystal, there are three main processes at work during the annealing of these types of materials after deformation: recovery, recrystallization and grain growth [32]. A brief overview of each before looking at how the twin boundaries evolve during these processes will be given here.

Definition 8. *Recovery is a process by which, at high enough temperatures, both point defects and line defects become more dynamic in the microstructure, interact with each other and anihilate or evolve to create more structured configurations of lower energy.*

As such, recovery is often associated with the evolution of dislocations since these are the easiest line defects to observe experimentally. Indeed, in a metallic microstructure where dislocations and point defect have been inserted, either by cold work, hot deformation, irradiation or some other energy injective approach, these defects become mobile enough to start making lower energy configurations at high enough temperatures. The most relevant example of recovery is the process by which tangles of dislocations, created often during cold working, reconfigure into what are called "subgrain" boundary structures. Seemingly initially randomly dispersed dislocations in a grain may, under the effect of temperature, evolve into a regular cellular structure within the grain. These "subgrains" are often devoid of dislocations in their interior with very high concentrations in their boundaries. Of course, the temperatures at which recovery starts to become visible and the extent to which a microstructure may recover depend heavily on the aptitude of the defects to move as well as their density. Once again, the parameter of primary importance has been shown to be the stacking fault energy of the material, where low stacking fault energy metallic materials generate very little recovery while high stacking fault energy materials tend to use recovery as the primary mechanism for stabilizing their microstructures [32]. In this work, concentrating on low to medium stacking fault energy materials such as nickel based superalloys, recovery is not the primary mechanism of interest.

Definition 9. *Recrystallization is the mechanism by which defect-heavy microstructures create new grains that are almost completely defect free and subsequently evolve, favouring the new crystallites.*

The primary mechanism of stabilizing the microstructure in low stacking fault energy materials is mostly reported to be *discontinuous recrystallization*. This phenomenon is often divided into two phases: nucleation and growth, as schematically represented in Figure 1.7. In very defect heavy microstructures, nucleation is the process by which a reconfiguration at the atomic level gives rise to a new crystallite with its own crystal orientation. This new grain has a rather "perfect" crystal structure and its bulk is thus favoured over its defect heavy surroundings. As such, the new grain grows into the surrounding matrix reconfiguring the largely distorted crystal structure into a much more regular atomic arrangement. The reason for which the microstructure must be concentrated in defects is that the appearance of a new grain costs a considerable amount of energy due to the new interface that is created. This energy must be over-balanced by the amount of defects destroyed during the process for the nucleation step to be energetically favourable and thus drive the microstructure to a more stable state. There exists thus a competition between the energy contained in the defects per volume area of the old microstructure as compared with the interface energy created when creating new grain boundaries analogous to phase transformations. However, the growth that can be observed during recrystallization is differentiated from the so-called process called grain growth.
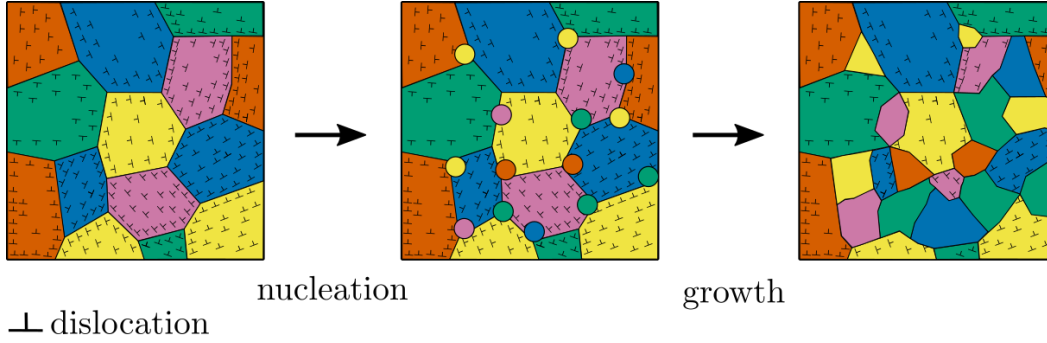
Figure 1.7: Diagram of nucleation and growth during the discontinuous recrystallization process where only the dislocations and grain boundaries are drawn. The colors help visualize the different grains.

Definition 10. *Grain growth is the process by which a microstructure, relatively free of point and line defects, becomes more stable by having the grains grow.*

Indeed, a microstructure that has very few point and line defects but potentially many grain boundaries has only one avenue of stabilization which is to reduce the energetic contribution of its interfaces. The grains thus grow, not under the influence of reorganizing a defect heavy crystallite, but in order to reduce the quantity and energy density of interfaces in the material. In order to do so, the grain boundaries tend to exhibit properties of *curvature flow*, by which the polycrystal interfaces evolve in the opposite direction to their maximal curvatures. As such, the curvature of the grain boundaries is directly related to the driving forces of their dynamics. Grain growth is a process that may follow recrystallization once the most defect heavy grains have disappeared. Possibly the most reliable way to differentiate in between these two growth mechanisms is the characteristic driving force magnitude and time scales that one may attribute to each. While recrystallization processes can be very "fast", lasting only of the order of a hundred seconds in some cases, in comparison, grain growth is considered to be very "slow", lasting orders of hours in order to observe comparable increases in grain size in the microstructure , in metallic materials [32]. However, what the grain growth mechanism lacks in effectiveness it makes up for in ubiquity. Any polycrystal, submitted to sufficient temperature conditions, will undergo a grain growth mechanism. Often this growth is detrimental to target macroscopic mechanical properties in industrial processes however can be beneficial for materials that require large grains such as materials with specific electromagnetic properties.

These three microstructural evolution mechanisms find their origin in the same place. Indeed, recovery, recrystallization and grain growth are processes that reorganize atomic arrangements in order to bring the material closer to its ground state, the monocrystal. The emergence of these phenomena at the microstructural level thus depend on the defect structure of the material itself. Even so, the temperature of the material plays a non-trivial role. In order to operate these processes at the atomic level, certain energetic barriers to

the movement of units in the lattice must be surmounted [53]. Increase in temperature serves to increase the vibrational energy of the crystal lattice and thus enables these barriers to be negotiated. Exactly which temperatures must be provided depend on the energetic barriers to each process which in turn depend on the metallic materials structural properties (composition, crystallographic structure, etc.). Thus, these annealing processes fall under the more general class of *thermally activated* phenomena.

Given that the defect distribution in a polycrystal is heavily affected by these phenomena, as a subset, the twin boundary distribution also evolves considerably during annealing. So much so that a another subclass of twin had to be defined.

Definition 11. *An annealing twin, and associated boundary, is a twin that has appeared during the annealing process.*

Annealing twins are distinct from deformation twins which appear during the deformation process [46]. In this work, deformation twins will be set aside and only annealing twins and their boundaries will be considered.

Given the definition of an annealing twin boundary, they must appear and evolve during the annealing process thus subsequently during either the recrystallization or grain growth steps. Exactly how they behave during these processes has been the subject of many experimental investigations, [18–25, 54–57] to only cite a few, conducted since their first observation in [58]. Indeed, the mechanism by which these boundaries appear during annealing is the subject of much contention in the literature [26–30]. Globally, three principle mechanisms have been proposed which are illustrated in Figure 1.8.

The most common mechanism cited in the literature is the "Grain Growth Accident" mechanism by which a stacking fault is created at a moving (111) boundary of a growing grain [30]. During recrystallization or grain growth, atoms move across grain boundaries effectively switching from one grain to another. There can be mistakes in the placement of these new atoms in a growing grain. This mistake or accident in the configuration of incoming atoms can lead to the beginning of a stacking fault which propagates itself using the incoming atoms, arranging them in a twin configuration. In low stacking fault energy materials, the new boundary is relatively stable due to the fact that it is a coherent twin boundary and thus of low energy. As such, a new twin oriented crystallite is nucleated at a moving grain boundary and continues to grow where its "parent" would have grown before.

Another mechanism called "Grain Boundary Dissociation" [28] or "Pop-Out" [27] described in different papers at different times but ultimately remaining the same mechanism is a close contender. In this case, a wave of partial dislocations (i.e. an incoherent twin boundary) nucleates at a grain boundary for a given reason (lower energy resulting boundaries, encounter of special dislocation structure, etc...) and propagates itself within the grain, reorienting a space within the crystallite into a twin configuration. This is considered energetically favorable since most of the boundary length created is coherent. The twin can grow as well if the boundaries with which it is in contact are moving. At first

(a) Grain growth accident [30]

(b) Pop-Out [27, 28]
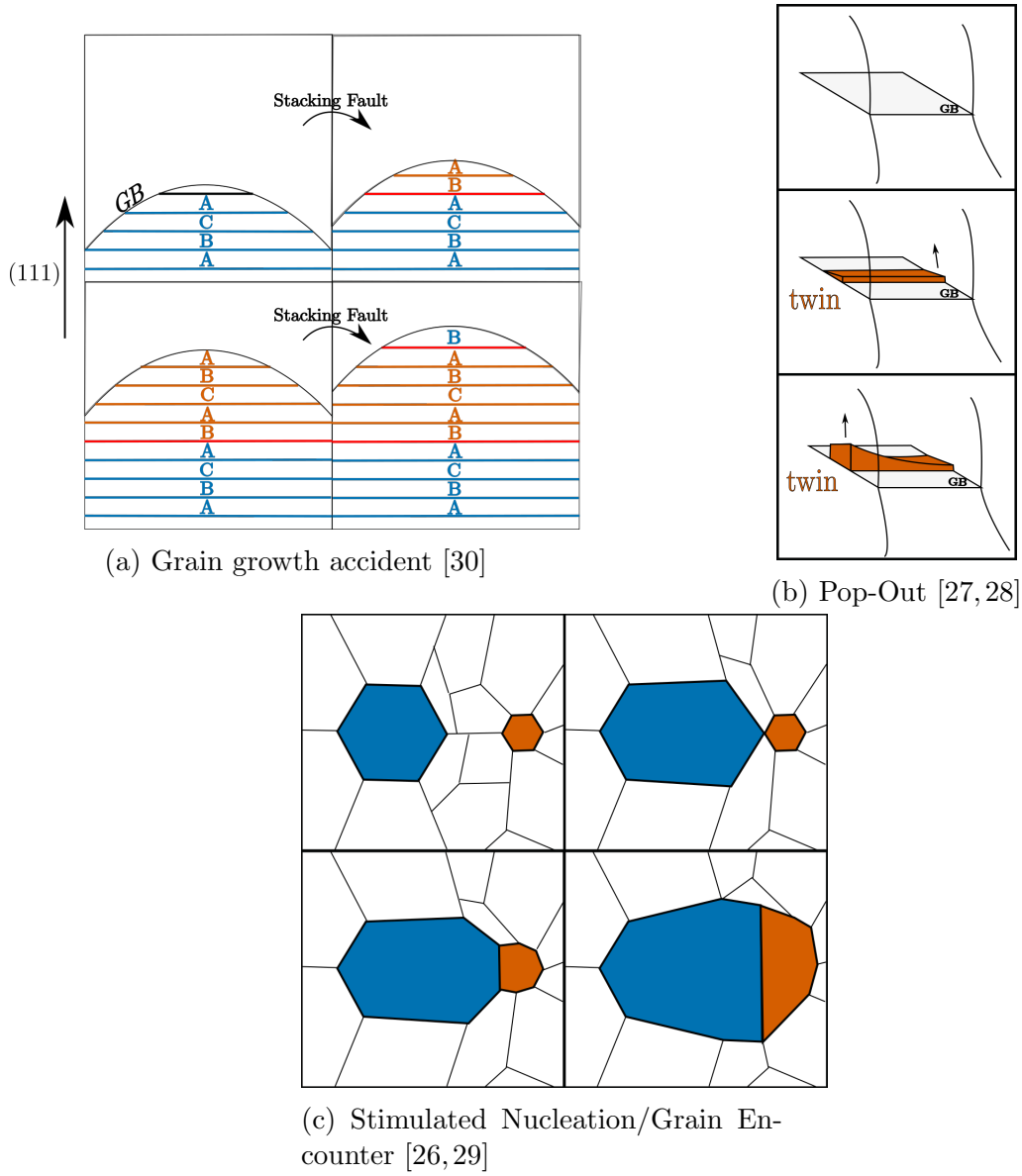
(c) Stimulated Nucleation/Grain Encounter [26, 29]

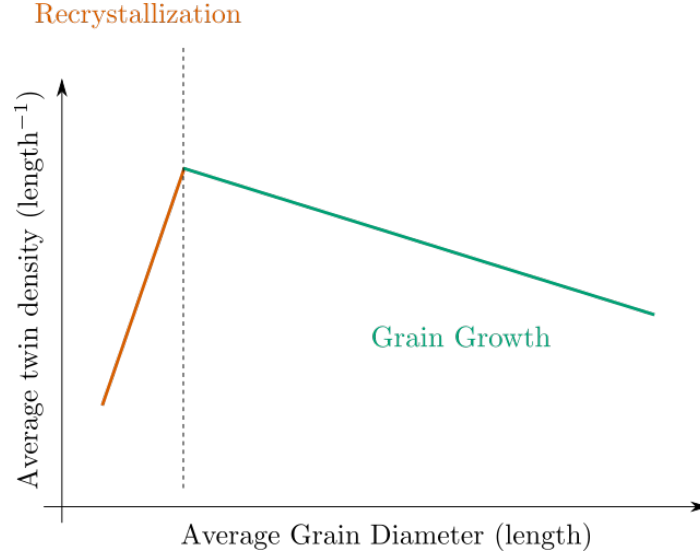Figure 1.8: Diagrams of the three main proposed mechanisms for annealing twinning.

Figure 1.9: Diagram of the phenomenological evolution of annealing twin boundary densities during recrystallization and subsequent grain growth adapted from [60]

glance, it seems like a peculiar way for a new orientation to appear. The twin orientation actually propagates into a grain relatively devoid of defects in order to create a sort of lamellar structure. However, experimentally observed morphologies tend to corroborate this type of anatomy of a twinned grain.

The final identified mechanism is a "Stimulated" twinning/Grain Encounter [26, 29] in which a growing grain encounters its twin orientation in the surrounding polycrystal matrix. Upon meeting this twin "nucleus", the original grain's growth is hampered by a sort of orientation pinning while the twin grain's growth is stimulated. The twin then grows out from the original grain's boundary much as a new nucleated grain. However, not much interest is afforded to this explanation. The probability of a given grain encountering another grain with a twin orientation cannot account for the abundance of twin boundaries observed in experimental microstructures [59].

Putting aside the mechanisms of formation of twin boundaries, much can be said about the statistical evolution of twin boundaries in polycrystal microstructures. Indeed, there is an abundance of investigations into the evolution of twin densities during annealing processes [21, 54–57, 59, 60]. Even so, given the diversity of thermomechanical conditions and materials for which these studies are conducted, general conclusions are difficult to extract from all the data. Of particular interest here is the work of [60] in pure nickel and nickel based superalloys.

The work in [60] can be partially summarized in the diagram shown in Figure 1.9. The figure schematically represents the evolution of twin boundary density, the length of the twin boundaries per unit area in a micrograph, in the microstructure during recrystallization and subsequent grain growth. The density is shown to increase quickly during

recrystallization where it is hypothesized most of the twins are nucleated. During grain growth, the twin density decreases at a much slower rate. It is shown that many of the grains nucleated during the recrystallization process already contain a multitude of twin boundaries. As such, during the growth of these grains, the twin boundaries follow the fate of their "parent" grains so to speak. If a new grain containing twin boundaries grows, the twin boundary grows as well and if the grain shrinks, so too does its twin boundary. As such, since globally the amount of boundary decreases during grain growth, so too does the twin density. However, given the large proportion of twinned grains, it seems that annealing processes would favour the persistence of twin boundaries in the microstructure unless new twins are nucleated during the grain growth process. In [21] the authors show that even during grain growth it was possible to nucleate twins, even if it was very rare. This nucleation during grain growth only occurred at multiple junctions. However, this twin boundary nucleation during grain growth is much too sporadic to account for the orders of magnitude of twin densities observed experimentally.

In any case, these observations are in accordance with the abnormally twinned microstructures one obtains in "multi-pass" forging operations [31]. In these processes one might deform the material at ambient temperature than anneal it for a very short time and then repeat the process multiple times. The microstructures of these materials are often the fruit of recrystallization processes where grains grow under the influence of strain induced grain boundary migration (SIBM). SIBM is a phenomenon where boundaries already present in the microstructure (i.e. no nucleation step) migrate in order to minimize the stored energy due to dislocations. As such, the heterogeneity of dislocation distribution in the polycrystal is the main driving force for the grain boundary migration.

Even if this sort of mean value accounting of twin density and its evolution is vital to the understanding of the evolution of twins, it does not illustrate the singular morphology of the twin boundary. Indeed, twins are often separated by a combination of coherent and incoherent boundaries with the same configurations being oddly widespread in real microstructures. Figure 1.10 illustrates many of the twin configurations one may find in 2D micrographs schematically. This illustration is directly confirmed by many of the twin boundaries that can be observed in Figure 1.3 and Figure 1.11.

These morphologies become more convoluted however when looking at 3D microstructures. Figure 1.12 shows the 3D reconstruction of a twinned grain taken from [59]. This Figure demonstrates that the 3D morphologies of annealing twins may be more complicated than what the 2D sections may suggest at first sight. These considerations become even more important when one studies twin related domains (TRDs) in engineered microstructures [61, 62] where large portions of the microstructure can be considered to be one twinned grain. In any case, the straight coherent twin boundary seems to be disproportionally present in real microstructures which tends to support its supposed low energy density.

From a modeling perspective, what is clear from the above bibliography and Figure 1.11 is that one of the main aspects in explaining the behavior of these annealing twins, once
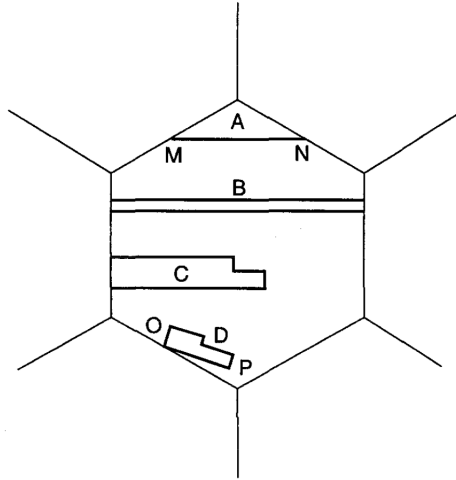
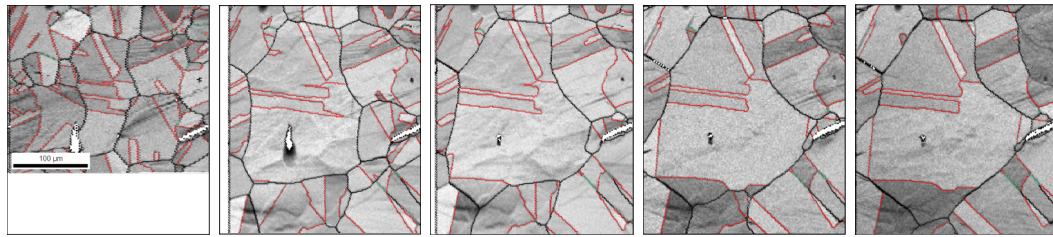Figure 1.10: Diagram of 2D observed twin morphologies reproduced from [30]

Figure 1.11: Unpublished results of twin boundary evolution during an in-situ annealing series of a 304L steel. Twin boundaries are in red and more general boundaries are black.
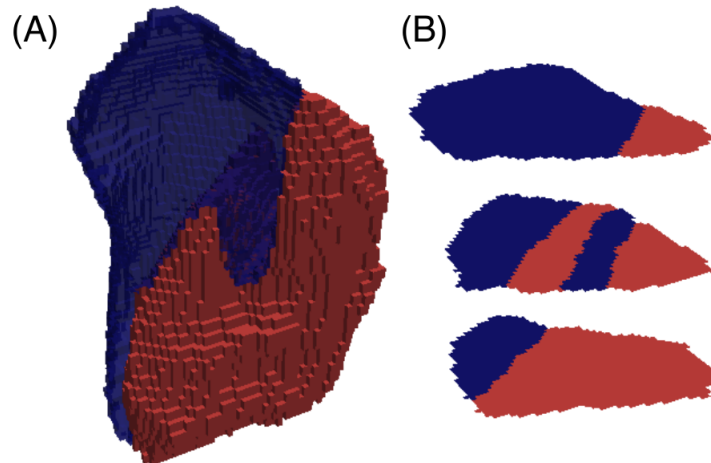

Figure 1.12: 3D reconstruction of a twinned grain in a pure nickel microstructure using High Energy X-ray Diffraction Microscopy (HEDM) reproduced from [59]

they've appeared, is related to their special energy densities, specifically concerning the coherent twin boundary. Indeed, the *hypothesis made in this work is that the energy density of the twin boundary is the first order property in explaining the behavior of this grain boundary during annealing.* In summary, a physically based model capable of taking into account a twin boundary is a model that can account for a grain boundary energy density function $\gamma(M, n)$, where (M, n) is the five parameter description of the grain boundary. Once this model is developed the boundary energy density should have characteristics that reproduce the behavior and morphologies of the twin boundaries.

1.3 Full field modeling approaches

The word *model* has been used thoroughly in this document. Even though most readers will have an intuitive understanding of the meaning, it may be helpful to give a simple definition.

Definition 12. *A model is a simplified description, especially a mathematical one, of a system or process, to assist calculations and predictions (Oxford Dictionary).*

As such, in the case of physical models, a model does not faithfully represent reality. Indeed, it is an approximation of reality that can be made richer by integrating more aspects of reality into it. In this sense, the quality of a model is based only on the predictions it is capable of making. Any mathematical model that is supposed to describe natural processes must be faithful to a certain number of observed phenomena in order to be useful. The best models are capable of predicting phenomena that have not yet been observed.

This definition gives rise to a spectrum of types of models ranging from very simple to deeply complex. The simple models are often easy to comprehend but have limited predictive power. The more complex models tend to cover a much larger range of observable phenomena with more precision. Thus the process of enriching a model is that which takes a given representation for a given process and extends the applicability of it to a more diverse set of mechanisms. However, increasing the complexity of a system comes with a cost. The more complex a scheme the more difficult it is to extract a prediction from it. If the model is too complex to solve or to parameterize, it is of no practical use since no predictions can be made from it. As such, the enriching of any structure is a balancing act between incorporating the relevant aspects of reality while keeping the system tractable.

This line of thought has given rise to many different types of models with differing complexities and goals. Some terminology of particular interest is the distinction between *mean field* models and *full field* models.

Definition 13. *Mean field models describe the behavior of statistical quantities of a system.*

Definition 14. *Full field models describe the behavior of local quantities of a system.*

Given these definitions, it is clear that full field models are generally richer than their mean field counterparts from a physical point of view. Statistical properties can always be computed from local properties, provided a large enough volume element, while the converse is not true. However, mean field models provide efficient methods to bridge scales. For example, a mean field model of the atomic scale can become a full field model of the microstructural scale when computed everywhere locally. As such, this distinction is less about comparing the complexity of the relevant models and more about the nature of the relevant input and output data being either valued locally in a given domain or globally over the entire space.

Many mean field models have been studied for predicting the effects of annealing on microstructures [63]. In this work, our concern will be about full field models at the microstructural level in polycrystalline metallic materials. The choice of constructing a full field system instead of using a mean field approach was made because the twin boundary is a local aspect of the microstructure. Indeed, both the geometry and character of the grain boundary is important in describing the twin boundary. As such, the complete modeling of the twin boundary and its morphologies can only be undertaken in a full field model. In the literature, many different approaches are taken to construct full field models of annealing processes. While specific codes and algorithms such as the vertex [64] and surface evolver [65] can be used to model grain growth effectively, they tend to be implementation dependent with each using its own rules. Of the more systematic modeling approaches, four large families of can be discerned: Monte-Carlo models [66–69], Cellular Automata algorithms [70–73], Phase-Field systems [74–80] and Level-Set methods [81–95].

The Monte-Carlo method for modeling recrystallization and grain growth is perhaps the most used approach due to its ease of implementation [66–69]. It is also a relatively good example of a mean field model used at a higher scale than its domain. The idea in the Monte-Carlo approach is to describe the microstructure Ω at each spatial point by a set of intrinsic structural variables (crystal orientation, dislocation density, etc.) and have these variables evolve using stochastic laws. Indeed, for example, the crystal orientation at a point x has, at any time t, a given probability P to transform into a neighboring orientation or not. This probability is calculated by first calculating the energy difference ΔG of the entire microstructure before $G(\Omega_i)$ and after the transformation $G(\Omega_f)$

$$\Delta G = G(\Omega_f) - G(\Omega_i) \tag{1.14}$$

Then, the probability for the event to occur is given depending on this energy difference by a function $P(\Delta G)$. For example, in [66]

$$P(\Delta G) = \left\{ \begin{array}{ll} \mu e^{-\frac{\Delta G}{k_B T}} & \Delta G > 0 \\ \mu & \Delta G \leq 0 \end{array} \right\} \tag{1.15}$$

where μ is a mobility parameter, k_B is the Boltzmann constant and T is the absolute temperature. The model is capable of taking into account both the thermodynamical aspects of the process, through the calculation of its $G(\Omega)$ function, and certain kinetic aspects, through the probability transition function. However, each transformation operation is discrete and thus takes a pseudo-time step. This pseudo-time step does not have much to do with the physical time of the mechanism since the transformations are sequential in the model while in reality multiple points may change orientations at the same time. Indeed, the absence of a notion of physical time is most likely the largest limiting factor of the classical Monte-Carlo method.

In contrast, the Cellular Automata method can have a physical representation of time [70–73]. The idea behind the Cellular Automata method, in recrystallization and grain growth, is to divide the microstructure into a certain number of units or "cells" that all have intrinsic states. These cells then evolve using the information from the neighboring cells and simple rules/laws. In [73], for example, the microstructure is divided into square cells and the laws that govern each cell are as follows

(a) *If three cells among four surrounding cells a, b, d, e have the same state as the cell c, the state of the cell c will definitely keep its original state at the next time step.*

(b) *A cell must overcome the energy barrier to reach its new state.*

(c) *A cell can have states from 1 to Q (Q ≫ 1) instead of 0 and 1. Each state represents the orientation of grain in a simulated microstructure.*

(d) *Grain boundary energy is homogeneously distributed.*

These laws, with the correctly chosen energy barrier, simulate grain growth in a given microstructure. The major caveat with this type of approach is the regularity of the grid that one must chose in order to constitute the unit structures. For complex microstructures with complex surfaces, this type of cell description is generally difficult to make precise. For example, in order to compute the curvature of the grain boundaries often higher order definitions of neighborhoods must be taken into account which make the computation both more costly and more difficult. The curvature being such a difficult quantity to evaluate, any supplemental models that might use the local curvature as an input are also relatively difficult to implement in these settings.

The third type of method used widely throughout the literature is the phase-field approach [74–80]. This method has a long history in the phase transformation modeling field and has been adapted to be able to simulate recrystallization and grain growth. The so-called multi phase field method uses a number of fields defined everywhere on the microstructure called order parameters or phase-fields η_i. These fields take values in $[0; 1]$. They are used to describe the spatial distribution of different states of matter. During the annealing of monophase polycrystals they can describe a crystallographic orientation

for example. One may compute the free energy $F[\eta_0, \ldots, \eta_i, \ldots]$ of a microstructure by summing over the individual contributions of the phase-fields as well as their interactions. Looking to minimize this free energy, a set of partial differential equations can be developed using the concepts of gradient descent

$$\frac{\partial \eta_i}{\partial t} + L\frac{\delta F}{\delta \eta_i} = 0, \tag{1.16}$$

where L is a kinetic parameter related to the dissipation of energy of the system. In order to avoid creations of vacuums in between phases, the order parameters must form a partition of unity of the microstructure

$$\sum_i \eta_i(x, t) = 1 \quad \forall(x, t), \tag{1.17}$$

a condition which, in most cases, must be imposed on the system. However, while the approach is firmly based in thermodynamics, there exists a certain arbitrariness to the choice of free energy functional F in the case of grain growth. In the general case [80] the functional for grain growth can be expressed as

$$F = \int_M \left[f(\eta_0, \ldots, \eta_i, \ldots) + \sum_i \langle \nabla \eta_i, \nabla \eta_i \rangle_F \right] dM \tag{1.18}$$

where f is a potential energy density function and $\langle \cdot, \cdot \rangle_F$ is a certain inner product capable of evaluating pairwise interaction energies between order parameters. The choices for these objects are not unique. While the choice for the inner product is essentially just a parameterization of the model, the choices for f rely on both physical parameters and the form of the function one wishes to use. As such, different equally plausible formulations for the functional are capable of giving different results for microstructural evolution. Also, given the often highly non-linear nature of f, the implementation of the model in numerical codes is relatively demanding and costly.

The last method described in this section is the Level-Set (LS) method [81–95]. In the LS approach a family of level-set functions $\Phi = \{\phi_i, i = 0, \ldots, N\}$ are defined over the microstructure. These fields are used to model interfaces using their iso-zero values as shown in Figure 1.13. Immediately from Figure 1.13 it can be surmised that the level-set function is capable of representing very simple but also very complex surfaces in an implicit manner.

The order parameter of the phase-field method is in fact a level-set field. Indeed, the interface of the grain boundaries in a polycrystal are described by the level-set values of the phase-field itself. However, the two models remain quite different. While the phase-field order parameters describe grain boundaries as diffuse objects that occupy a certain
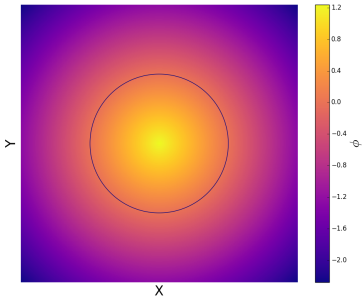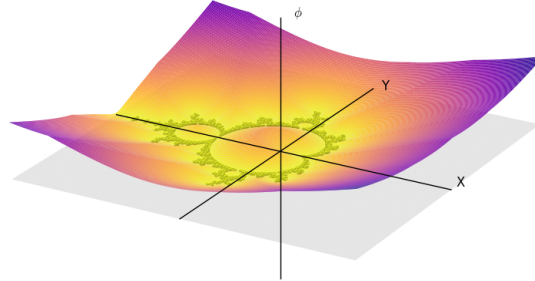
(a) Heatmap view with zero iso-contour of a circle level-set
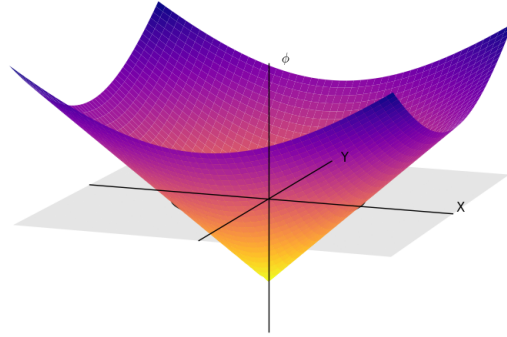
(b) 3D view of a circle level-set
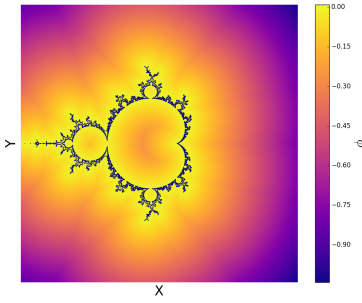
(c) Heatmap view with zero iso-contour of an enclosing Mandelbrot set level-set

(d) 3D view of an enclosing Mandelbrot set level-set

Figure 1.13: Different views of level-set fields ϕ that enclose a circle (a,b) and the Mandelbrot set (c,d)

volume of space, the level-set method uses level-set functions to localise the interfaces at the zero-iso values. Indeed, the level-set model is what is often referred to as a "sharp interface" approach as opposed to the diffuse view espoused by the phase-field methods.

While it might be clear that the level-set approach is capable of describing interfaces in a static sense, the capabilities of this model to interpret the dynamics of objects is not yet apparent. Indeed, a supplemental concept is needed to make have these fields simulate grain boundary movement: the transport equation.

$$\frac{\partial \phi}{\partial t} + v \cdot \nabla \phi = 0 \tag{1.19}$$

where ϕ is a level set field and v is the velocity field defined on the interface and extended everywhere in the domain. Contrary to the phase-field formulations, the thermodynamics of the problem are not inherent to the method. As such, the level-set method is much more flexible in terms of defining the velocity field v. Indeed, the physics of the problem at hand is completely encapsulated in this vector field. The flexibility comes with a cost. Given that there are very few constraints on v, it is very easy to construct velocity fields that do not minimize the free energy functional of the microstructure and thus potentially go against fundamental principles. As such, the utmost care in the modeling process must be given to the construction of these velocity fields so that the predictions offered by the method are correct. One may go even further to say that the *entire* modeling process, in the case of the level-set approach, can be boiled down to the construction of this velocity field. The following section is entirely devoted to finding candidates for this velocity field in the case of annealing in polycrystal materials. Even so, certain formulations of this velocity do exist in the literature, for example, for the case of grain growth with a homogeneous grain boundary energy density function $\gamma(\cancel{M}, \cancel{n})$ [90]

$$v = -\mu \gamma \kappa n \tag{1.20}$$

where μ is the grain boundary mobility, κ is the local mean curvature of the boundary (simply curvature in 2D and trace of the curvature tensor in 3D) and n is the outward unit normal to the boundary. When modeling recrystallization phenomena [90], a supplemental term must be added to the velocity, often written as

$$v = \mu(\nabla \rho \cdot n - \gamma \kappa)n \tag{1.21}$$

where ρ is considered to be a scalar dislocation energy density per unit volume defined throughout the microstructure and ∇ is a spatial differential operator.

In this work the Level-Set method was chosen to construct a full field model, in part, because of its flexibility. The extension of a Level-Set model to other phenomena is rather

simple since the only modification is in the construction of the velocity field. This gives the LS methodology a modular structure where one can chose to model certain phenomena and neglect others. Also, the numerical implementation of the model in well established methods such as Finite Element, Finite Difference or Fast Fourier Transform is relatively straightforward since the linearization of the transport equation is often simple. The Finite Element method will be chosen in this work because an unstructured mesh can be used and remeshed for optimal numerical efficiency. The numerical efficiency of the algorithm is an important aspect of the approach since the Level Set method, like the phase field method, is known to be costly in computer resources. Also, the use of an unstructured mesh allows for a simpler integration of the method into existing tools for simulating large deformations such as in forging processes. One must also remain acutely aware of the pitfalls of the method which has no firm basis in physical laws or phenomena. As such, the majority of this work, outside of the development of the mathematical model, is devoted to testing in specific analytical cases to ensure that the thus constructed velocity field has some physical relevance.

Résumé en Français du Chapitre 1

Ce chapitre est dédié à l'introduction des concepts de métallurgie physique nécessaires pour la bonne compréhension de la suite du manuscrit. En partant de la définition du cristal, le texte décrit la structuration de la microstructure des polycrystaux monophasés et les défauts cristallins que l'on peut y trouver. Ensuite, les mécanismes agissant sur la dynamique de ces polycrystaux sont passés en revue avec la description successive de la restauration, la recristallisation et enfin la croissance de grains. Une reflexion particulière est menée sur les macles et le maclage thermique en termes de structure, de mécanismes d'apparition et de morphologie. Notamment, l'énergie très faible des joints de macles cohérentes a été proposée comme la propriété déterminante pour expliquer les comportements spécifiques de ces joints. Les modèles physiques de polycristaux qui ont pour but d'inclure les macles thermiques doivent donc assimiler l'énergie de joints de grains comme une quantité qui varie au sein de la microstructure. Les méthodes existantes pour la modélisation et simulation des phénomènes d'évolutions microstructurales sont présentés en dernier lieu pour servir de socle pour les développements menés dans le reste du travail.

Chapter 2

Theoretical Considerations

The model developed here for the grain boundary network is heavily seated in differential geometry. While a rough introduction to the notions is provided in what follows, the curious reader might want to first want to look into [33,34]. The first concept broached in this chapter is that of a differentiable manifold which, to understand in its entirety, one must have some prerequisite knowledge of both set theory [96] and topology (more specifically topological manifolds) [97]. The reasoning in using such advanced mathematics is more motivated by necessity than by choice. Without the definitions provided by differential geometry, it is very difficult to recognize the objects manipulated in complex models for surfaces. Indeed, while previous attempts at integrating arbitrary grain boundary energy densities into models for grain boundary dynamics [98–100] have been fruitful, there has remained some ambiguity as to how to use some of the objects defined in these works correctly and extend them to numerical schemes for solving these anisotropic problems. As such, the goal of this chapter is to develop the adequate framework for describing surfaces in a holistic manner and deriving their dynamics from first principles.

2.1 Notions of Differential Geometry

Definition 15. *A smooth n-manifold $\mathcal{M} = (M, \mathcal{O}, \mathcal{A})$ is a triple comprised of*

- *an underlying set M.*

- *a topology $\mathcal{O}$ for M such that $(M, \mathcal{O})$ is a topological n-manifold (locally Euclidean of dimension n and Hausdorff).*

- *a smooth atlas $\mathcal{A}$ comprised of charts (U, x), where $U \subseteq M$ and x is a bijective map from U to a subset of $\mathbb{R}^n$, which are all smoothly compatible and cover $M = \cup_{U \in \mathcal{A}} U$.*

The exact definition of a topological manifold can be found in [97]. However, one may intuitively think of a topological n-manifold as a space which can locally look like $\mathbb{R}^n$ but globally may be very different.

The smooth compatibility condition for the charts is rather simple. If one takes two charts $(U, x) \in \mathcal{A}$ and $(V, y) \in \mathcal{A}$ such that $U \cap V \neq \emptyset$ than the chart transition map

$$x \circ y^{-1} : U \subseteq \mathbb{R}^n \to V \subseteq \mathbb{R}^n$$

must be smooth for the atlas to be smoothly compatible.

Smooth manifolds are useful because they are spaces endowed with the minimal amount of structure for which derivatives start making sense. Indeed, any differential equation must be written with respect to some differential manifold in order to have meaning. Therefore, looking for a model whose dynamics might be written as a collection of differential equations, the underlying smooth manifolds are relevant objects.

Notation. $C^\infty(\mathcal{M})$ is the set of all smooth functions that can be defined on the smooth manifold $\mathcal{M}$.

Definition 16. *Let $\mathcal{M}$ be a smooth n-manifold. The tangent space $T_p\mathcal{M}$ at the point $p \in \mathcal{M}$ is the vector space comprised of elements X such that there exists C a smooth curve of $\mathcal{M}$*

$$\begin{aligned} C : \quad &\mathbb{R} \to M \\ &t \mapsto C(t) \end{aligned}$$

with $C(0) = p$ and

$$\begin{aligned} X : \quad &C^\infty(\mathcal{M}) \to \mathbb{R} \\ &f \mapsto Xf := \frac{d}{dt}(f \circ C)(0) \end{aligned}$$

Corollary 5. *There exists an equivalence class between all the smooth curves that pass through the point p and the elements of the tangent space.*

The elements of the tangent space to a point $p \in M$ are also often called *tangent vectors.* Indeed, there is a rather intuitive relationship between the elements of the tangent space to a point of a manifold and the classical notion of a vector in space. Figure 2.1 is an attempt to illustrate that relationship geometrically. In a very rough sense, the tangent vector to each smooth curve passing through a point has a unique representative in the tangent space to the point.

Making the intuition more formal, if one chooses a chart $(U, x) \in \mathcal{A}$ such that $p \in U$ and a function $f \in C^\infty(\mathcal{M})$ then and element $X \in T_p\mathcal{M}$ acts on f through its equivalent curve C

$$\begin{aligned} Xf \quad &= \frac{d}{dt}(f \circ C) \\ &= \frac{d}{dt}(f \circ x^{-1} \circ x \circ C) \end{aligned}$$

$\mathcal{M}$
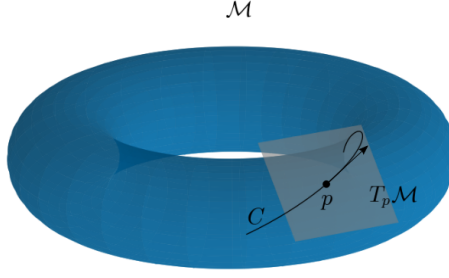
Figure 2.1: Illustration of the geometrical relationship between the tangent space to a point of a smooth manifold and the curves passing through that point.

which, using the multidimensional chain rule brings one too

$$Xf = \frac{d}{dt}(x^i \circ C)\partial_i(f \circ x^{-1})$$

where x^i is the ith component function of the chart x, ∂_i is the derivative operator of a multidimensional function with respect to its ith component and the *Einstein summation convention* is in effect, which will be implied from here on unless stated otherwise.

Constructing a basis for $T_p\mathcal{M}$ with the vectors $\{\frac{\partial}{\partial x^i}, i = 1, \ldots, n\}$ defined as

$$\frac{\partial}{\partial x^i}f := \partial_i(f \circ x^{-1}) \tag{2.1}$$

the component functions can act as sort of curves on the manifold. One may express the components of X in this basis $\{X^i, i = 1, \ldots, n\}$

$$X^i = \frac{d}{dt}(x^i \circ C)(0) \tag{2.2}$$

In this vector basis X is often decomposed as

$$X = X^i \frac{\partial}{\partial x^i} \tag{2.3}$$

Also, seeing as $T_p\mathcal{M}$ is a vector space, it admits a dual space.

Definition 17. *The dual vector space $T_p^*\mathcal{M}$ or co-tangent space to the tangent space $T_p\mathcal{M}$ is the space of* linear *maps ω such that*

$$\omega : \begin{aligned} T_p\mathcal{M} &\to \mathbb{R} \\ X &\mapsto \omega(X) \end{aligned}$$

45

More generally, the local tensor spaces can be constructed.

Definition 18. *The space of (q,s)-tensors, $(q,s) \in \mathbb{N}^2$, at $p \in \mathcal{M}$ is defined as*

$$T^q_{p,s}\mathcal{M} := \underbrace{T^*_p\mathcal{M} \otimes \cdots \otimes T^*_p\mathcal{M}}_{s} \otimes \underbrace{T_p\mathcal{M} \otimes \cdots \otimes T_p\mathcal{M}}_{q}$$

As such, from the tangent spaces at each point of $\mathcal{M}$ the tangent bundle can be constructed.

Definition 19. *Let $T\mathcal{M}$ be defined as*

$$T\mathcal{M} = \bigcup_{p \in \mathcal{M}} (p, T_p\mathcal{M})$$

such that the tangent bundle $(T\mathcal{M}, \mathcal{M}, \pi)$ is defined as

$$T\mathcal{M} \xrightarrow{\pi} \mathcal{M}$$

where π is a continuous surjective map.

Analogously, the (q,s)-tensor bundles $(T^q_s\mathcal{M}, \mathcal{M}, \pi_{s,q})$ are defined in the same manner.

Definition 20. *A section of a bundle (E, B, π) is a continuous map σ such that*

$$\sigma : \begin{aligned} B &\to E \\ \pi(\sigma(p)) &= p \end{aligned}$$

Colloquially, the sections of the tangent bundle are called *vector fields* and in the same manner sections of the tangent bundles are called *tensor fields*.

Notation. $\Gamma(T^q_s\mathcal{M})$ is the space of all smooth sections of the bundle $(T^q_s\mathcal{M}, \mathcal{M}, \pi_{s,q})$.

Definition 21. *A Riemannian n-manifold $(\mathcal{M}, g)$ is a smooth n-manifold $\mathcal{M}$ equipped with a symmetric $(0,2)$-tensor field $g \in \Gamma(T^0_2\mathcal{M})$, called a metric, such that $\forall p \in M$ $g(p)$ is a positive-definite tensor.*

The positive definiteness of g means that for any $X \in T_p\mathcal{M}, X \neq 0$

$$g(p)(X, X) > 0$$

$\forall p \in M$.

Riemannian manifolds are of general interest since the metric structure defines inner products on the tangent spaces. As such, in order to define lengths of curves, and more general measures of volume, one needs a Riemannian manifold. Indeed, this metric structure is what allows one to define the Riemannian integral on the manifold.

Definition 22. *A differential q-form ω on a smooth manifold is a completely anti-symmetric $(0,q)$-tensor field.*

Corollary 6. *The volume form dM of an oriented Riemmannian n-manifold $(\mathcal{M}, g)$ is the differential q-form such that for a given a chart $(U, x) \in \mathcal{A}$ the volume form may be expressed as*

$$dM = \sqrt{\det(g)}dx^1 \wedge \cdots \wedge dx^n$$

where $\det(g)$ is the determinant of the matrix composed by the components of g in the chart (U, x), $\{dx^i, i = 0, \dots, n\}$ is the dual basis of the co-vector space and $\wedge$ is the exterior product of differential forms.

Using this machinery, any function can be integrated over the manifold.

Definition 23. *Let $\{\rho_i \in C^\infty(\mathcal{M})\}$ be a partition of unity of $\mathcal{M}$ and let $\{(U_i, x_{(i)}) \in \mathcal{A}\}$ be a set of charts covering the entire Riemannian n-manifold $(\mathcal{M}, g)$ such that the overlaps between the charts are the overlaps between the partitions. The integral of a function $f \in C^\infty(M)$ over $\mathcal{M}$ is defined as*

$$\int_M f dM = \sum_i \int_{x_{(i)}(U_i)} (\rho_i \circ x^{-1})(f \circ x^{-1})\sqrt{\det(g)}dx^1_{(i)} \cdots dx^n_{(i)}$$

where the right hand side is to be understood in the classical sense of the integral.

Given the heaviness of the notation, the taking of charts as well as the partition of unity will be implicit in the notation from here on.

Also, working with a Riemannian manifold, one is able to define a relatively straightforward connection on the space called the *Levi-Civita* connection.

Definition 24. *A connection ∇ over a bundle (E, B, π) is a set of linear maps*

$$\nabla : \Gamma(T^q_s B) \to \Gamma(T^q_s B \otimes T^* B)$$

that respect the Leibniz rule, $f \in C^\infty(B), \sigma \in \Gamma(T^q_s B), \tau \in \Gamma(T^j_i B)$

$$\nabla(f\sigma) = \sigma \otimes df + f\nabla\sigma \qquad (2.4)$$
$$\nabla(\tau \otimes \sigma) = \nabla\tau \otimes \sigma + \tau \otimes \nabla\sigma \qquad (2.5)$$

where df is the classic differential of a smooth function $df = \frac{\partial f}{\partial x^i}dx^i$.

Remark. From a given connection ∇, one may construct rather simply a covariant derivative

$$\nabla_\cdot : \Gamma(TB) \times \Gamma(T^q_s B) \to \Gamma(T^q_q B)$$
$$\nabla_\cdot(X, \sigma) = \nabla_X \sigma = (\nabla\sigma)(X)$$

where, when working in a chart, one may use

$$(\nabla_X \sigma)^{k\dots}_{j\dots} = (\nabla\sigma)^{k\dots}_{j\dots i}X^i = \nabla_i \sigma^{k\dots}_{j\dots}X^i$$
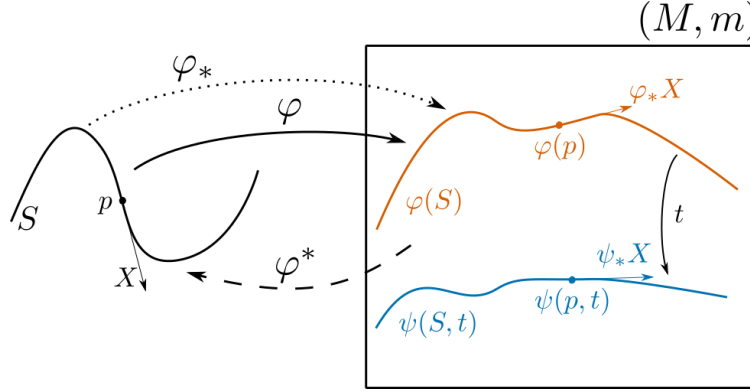
Figure 2.2: Diagram of the embedding φ.

Definition 25. *The Levi-Civita connection ∇ on a Riemannian manifold $(\mathcal{M}, g)$ is the unique connection on the tensor bundles which satisfies*

$$\nabla g = 0$$

and has no torsion.

2.2 A smooth manifold model for interfaces

Let $\mathcal{M} = (M, \mathcal{O}_M, \mathcal{A}_M)$ be a Riemmanian n-manifold with metric m and $\mathcal{S} = (S, \mathcal{O}_S, \mathcal{A}_S)$ be a smooth s-manifold with $n \geq s$. Let φ be a smooth embedding from $\mathcal{S}$ to $\mathcal{M}$

$$\begin{aligned}
\varphi: \quad & S \to M \\
& S \equiv_{homeo} \varphi(S)
\end{aligned} \tag{2.6}$$

where $\equiv_{homeo}$ describes a homeomorphism equivalence and Figure 2.2 provides an illustration. Indeed, a smooth interface is nothing other than an embedding of a smooth manifold in the special case where $n = s + 1$.

The embedding also quite naturally provides a map from the tangent bundle of $\mathcal{S}$ to the tangent bundle of $\mathcal{M}$.

Definition 26. *The pushforward φ_* of a map φ from $\mathcal{S}$ to $\mathcal{M}$, two smooth manifolds, is the linear map such that*

$$\begin{aligned}
\varphi_*: \quad & T\mathcal{S} \to T\mathcal{M} \\
& (p, X) \mapsto (\varphi(p), \varphi_* X) \\
& (\varphi_* X)f := X(f \circ \varphi)
\end{aligned}$$

for $f \in C^\infty(\mathcal{M})$

Much in the same manner, the embedding gives rise to a map from the co-tangent bundles $T_q^0\mathcal{M}$, at least the restriction to $\varphi(S)$, to $T_q^0\mathcal{S}$.

Definition 27. *The pullback φ^* of a map φ from $\mathcal{S}$ to $\mathcal{M}$, two smooth manifolds, is the linear map such that*

$$\varphi^* : T_q^0\mathcal{M}|_{\varphi(S)} \to T_q^0\mathcal{S}$$
$$(\varphi(p), \sigma) \mapsto (p, \varphi^*\sigma)$$
$$(\varphi^*\sigma)(X^{(1)}, \dots, X^{(q)}) = \sigma(\varphi_* X^{(1)}, \dots, \varphi_* X^{(q)})$$

These two maps are very useful in that they allow one to relate objects of each space concretely. Indeed, using the charts $(U, x) \in \mathcal{A}_S$ and $(V, Z) \in \mathcal{A}_M$ and using the convention by which objects in $\mathcal{M}$ are indexed by Greek letters and objects in $\mathcal{S}$ are indexed by Latin numbers one can express the components of the pushforward of a vector $X \in T_p\mathcal{S}$ with its action on a function $f \in C^\infty(\mathcal{M})$

$$\begin{aligned}
(\varphi_* X)f &= (\varphi_* X)^\alpha \frac{\partial f}{\partial Z^\alpha} \\
&= X(f \circ \varphi) \\
&= X^i \frac{\partial(f \circ \varphi)}{\partial x^i} \\
&= X^i \frac{\partial(f \circ Z^{-1} \circ Z \circ \varphi)}{\partial x^i} \\
&= X^i \frac{\partial(Z^\alpha \circ \varphi)}{\partial x^i} \partial_\alpha(f \circ Z^{-1}) \\
&= X^i \frac{\partial(Z^\alpha \circ \varphi)}{\partial x^i} \frac{\partial f}{\partial Z^\alpha}
\end{aligned}$$

Which, defining

$$\varphi^\alpha : S \to \mathbb{R}$$
$$p \to Z^\alpha(\varphi(p))$$

leads to, through identification,

$$(\varphi_* X)^\alpha = X^i \frac{\partial \varphi^\alpha}{\partial x^i} \tag{2.7}$$

Using the pullforward one may induce a metric g on $\mathcal{S}$ and therefore turn $\mathcal{S}$ into a Riemannian manifold $(\mathcal{S}, g)$ by the following construction

$$g(p) = (\varphi^* m)(\varphi(p)) \tag{2.8}$$

which, using the charts and two vectors $(X, Y) \in T_{p \in S} \mathcal{S}$

$$
\begin{aligned}
g(X, Y) &= (\varphi^* m)(X, Y) \\
g_{ij} X^i Y^j &= m(\varphi_* X, \varphi_* Y) \\
&= m_{\alpha\beta}(\varphi_* X)^\alpha (\varphi_* Y)^\beta \\
&= m_{\alpha\beta} \frac{\partial \varphi^\alpha}{\partial x^i} \frac{\partial \varphi^\beta}{\partial x^j} X^i Y^j
\end{aligned}
$$

and, by identification, gives the components of the induced metric

$$g_{ij} = m_{\alpha\beta} \frac{\partial \varphi^\alpha}{\partial x^i} \frac{\partial \varphi^\beta}{\partial x^j} \tag{2.9}$$

Considering $\mathcal{B}$ a property space (for example the five parameter grain boundary space described in Section 1.1). Let

$$S\mathcal{B} = \bigcup_{p \in S} (p, \mathcal{B}) = S \times \mathcal{B} \tag{2.10}$$

and define the property bundle $(S\mathcal{B}, \mathcal{S}, \pi_B)$

$$S\mathcal{B} \xrightarrow{\pi_B} S \tag{2.11}$$

such that a section $b \in \Gamma(S\mathcal{B})$ of the property bundle describes exactly the properties of the s-manifold at each point. If one was to define an energy density map

$$\gamma : \mathcal{B} \to \mathbb{R}^+$$

then one could calculate the energy density at any point $p \in S$ through the property field as $\gamma(b(p))$ creating a scalar field. Given that $(\mathcal{S}, g)$ is now a Riemannian manifold, this energy density can be integrated in order to give the total interface energy I of the embedding as

$$I = \int_S (\gamma \circ b) dS$$

The model developed here for the interface is thus a triple $(\mathcal{S}, \varphi, b)$ from which, with an energy density map γ, the total energy of the interface may be expressed. By design, this model puts no lower bound on s. Therefore, this structural model is readily generalized to objects that are not strictly interfaces but can be of lower dimension, such as lines if $n \geq 3$. This is an important aspect of this model, even if it might be out of the scope of this thesis, if ever one was to attempt to attribute properties and therefore energies to other defects in the polycrystal microstructure such as triple lines or dislocations.

2.3 Interface dynamics

Considering now a closed thermodynamic system made up of a Riemannian n-manifold $(\mathcal{M}, m)$ of volume V with an embedded interface $(\mathcal{S}, \varphi, b)$, a boundary energy density map γ, a temperature T, an entropy η and a homogeneous pressure field p. In this idealized case, one may conduct a thought experiment of the free evolution of the system for a normalized time $t \in [0; 1]$ at a constant temperature T and pressure p (those conditions that would be in effect during an isothermal heat treatment). The evolution of the internal energy can be expressed as

$$\frac{dU}{dt} = \frac{dI}{dt} + T\frac{d\eta}{dt} - p\frac{dV}{dt} \tag{2.12}$$

In the model developed here, the interface $(\mathcal{S}, \varphi, b)$ is sharp. Thus, the interface evolution cannot modify the volume of the system and $\frac{dV}{dt} = 0$. However, if one considers an evolving grain boundary and the subsequent reshuffling of atoms with its passage, it is very likely that the process is not isenthalpic $\frac{d\eta}{dt} \neq 0$.

Reformulating the conservation equation (2.12) in terms of the Gibbs free energy G one may show

$$\begin{aligned}
\frac{dG}{dt} &= \frac{dU}{dt} - \frac{d(T\eta)}{dt} + \frac{d(pV)}{dt} \\
&= \frac{dI}{dt} - \eta\frac{dT}{dt} + V\frac{dp}{dt}
\end{aligned}$$

which, given that the heat treatment is isothermal and isobaric,

$$\frac{dG}{dt} = \frac{dI}{dt} \tag{2.13}$$

The second principle of thermodynamics gives that

$$\frac{dG}{dt} \leq 0$$

and, therefore,

$$\frac{dI}{dt} \leq 0 \qquad (2.14)$$

Using the principle of least action one may suitably affirm that the energy dissipation must be maximal and thus $\frac{dI}{dt}$ must be minimal $\forall t \in [0; 1]$.

The flow ψ of the interface in is defined as

$$\psi : S \times [0; 1] \to M$$
$$(p, t) \mapsto \psi(p, t)$$
$$\psi(p, 0) = \varphi(p)$$

and thus describes an embedding of $\mathcal{S}$ at each time t.

The only properties of the interface that might evolve during its flow are geometric ones. For example, a grain boundary should not see its misorientation change while moving, only its inclination parameters can vary. As such, the property field b should be completely parameterized by the embedding during the flow of the interface. Indeed, if one considers the misorientation/inclination parameterization of a grain boundary $b = (M, n) \in \mathcal{B}$, symbolically

$$\frac{dM}{dt} = 0 \qquad (2.15)$$

in any representation space of the misorientation value. However, the inclination n of the boundary does change. Indeed, the n field depends heavily on the embedding, and the two are related by the fact that n must be orthogonal to any tangent vector to the interface. As such, for any $X \in T_p\mathcal{S}$ at any time t the value of $n(\psi(p, t))$ is in part determined by

$$m(n, \psi_* X) = 0$$
$$m_{\alpha\beta} n^\alpha \frac{\partial \psi^\beta}{\partial x^i} X^i = 0$$

Since this must be true for any vector X,

$$m_{\alpha\beta}n^\alpha \frac{\partial \psi^\beta}{\partial x^i} = 0, \quad \forall i = 1, \ldots, s \tag{2.16}$$

the remaining condition on n is the unitary condition which is simply that

$$m(n, n) = 1 \tag{2.17}$$

Therefore,

$$\gamma\left(M, n\left(\ldots, \frac{\partial \psi^\alpha}{\partial x^i}, \ldots\right)\right) = \gamma\left(\ldots, \frac{\partial \psi^\alpha}{\partial x^i}, \ldots\right) \tag{2.18}$$

for the sake of the derivations that follow. The following will also make extensive use of the Levi-Civita connection ∇ on $(\mathcal{S}, g)$ with the knowledge that $\frac{\partial \psi^\alpha}{\partial x^i} = \nabla_i \psi^\alpha$.

The velocity field $v \in \Gamma(T\mathcal{M})$ of the interface flow can thus be defined for $q = \psi(p, t)$ as, with $f \in C^\infty(\mathcal{M})$

$$\begin{aligned} (vf)(q) &= \frac{d}{dt}(f \circ \psi(p, \cdot))(t) \\ &= \frac{d\psi^\alpha}{dt}(p, t)\frac{\partial f}{\partial Z^\alpha}(q) \\ &= v^\alpha \frac{\partial f}{\partial Z^\alpha} \end{aligned}$$

such that, by identification

$$v^\alpha(\psi(p, t)) = \frac{d\psi^\alpha}{dt}(p, t) \tag{2.19}$$

Using these objects

$$\begin{aligned} \frac{dI}{dt} &= \int_S \frac{d}{dt}\left(\gamma dS\right) \\ &= \int_S \frac{d}{dt}\left(\gamma\sqrt{\det(g)}\right) dx^1 \wedge \cdots \wedge dx^s \\ &= \int_S \frac{\partial}{\partial \nabla_i \psi^\alpha}\left(\gamma\sqrt{\det(g)}\right)\frac{d\nabla_i \psi^\alpha}{dt} dx^1 \wedge \cdots \wedge dx^s \\ &= \int_S \frac{1}{\sqrt{\det(g)}}\frac{\partial \gamma\sqrt{\det(g)}}{\partial \nabla_i \psi^\alpha}\nabla_i\frac{d\psi^\alpha}{dt}\sqrt{\det(g)}dx^1 \wedge \cdots \wedge dx^s \\ &= \int_S \frac{1}{\sqrt{\det(g)}}\frac{\partial(\gamma\sqrt{\det(g)})}{\partial \nabla_i \psi^\alpha}\nabla_i v^\alpha dS \end{aligned}$$

53

and expressing separately

$$\frac{\partial(\gamma\sqrt{\det(g)})}{\partial\nabla_i\psi^\alpha} = \sqrt{\det(g)}\frac{\partial\gamma}{\partial\nabla_i\psi^\alpha} + \gamma\frac{\partial\sqrt{\det(g)}}{\partial\nabla_i\psi^\alpha}$$

such that, using the Kronecker delta symbol

$$\delta_i^j = \begin{cases} 1 & i = j \\ 0 & i \neq j \end{cases},$$

the Jacobi formula, if A is an invertible matrix and depends on a parameter χ,

$$\frac{d\det(A)}{d\chi} = \det(A)(A^{-1})_i^j\frac{dA_j^i}{d\chi},$$

and the convention that one may simply identify the components of an inverse metric tensor as $(g^{-1})^{ij} = g^{ij}$, thus letting the position of the indices inform the reader whether the metric tensor or inverse metric tensor is in play, one may write

$$\begin{aligned}
\frac{\partial\sqrt{\det(g)}}{\partial\nabla_i\psi^\alpha} &= \frac{1}{2\sqrt{\det(g)}}\frac{\partial\det(g)}{\partial\nabla_i\psi^\alpha} \\
&= \frac{\det(g)}{2\sqrt{\det(g)}}g^{sq}\frac{\partial g_{qs}}{\partial\nabla_i\psi^\alpha} \\
&= \frac{1}{2}\sqrt{\det(g)}g^{sq}\frac{\partial m_{\sigma\varsigma}\nabla_q\psi^\sigma\nabla_s\psi^\varsigma}{\partial\nabla_i\psi^\alpha} \\
&= \frac{1}{2}\sqrt{\det(g)}g^{sq}m_{\sigma\varsigma}(\delta_q^i\delta_\alpha^\sigma\nabla_s\psi^\varsigma + \nabla_q\psi^\sigma\delta_s^i\delta_\alpha^\varsigma)
\end{aligned}$$

Because of the symmetry of both m and g^{-1}, one may simplify the equation

$$\frac{\partial\sqrt{\det(g)}}{\partial\nabla_i\psi^\alpha} = \sqrt{\det(g)}(g^{-1})^{iq}m_{\sigma\alpha}\nabla_q\psi^\sigma \tag{2.20}$$

Then

$$\frac{\partial(\gamma\sqrt{\det(g)})}{\partial\nabla_i\psi^\alpha} = \sqrt{\det(g)}\left(\frac{\partial\gamma}{\partial\nabla_i\psi^\alpha} + \gamma g^{iq}m_{\sigma\alpha}\nabla_q\psi^\sigma\right) \tag{2.21}$$

and

$$\frac{dI}{dt} = \int_S \left(\frac{\partial \gamma}{\partial \nabla_i \psi^\alpha} + \gamma g^{iq} m_{\sigma \alpha} \nabla_q \psi^\sigma \right) \nabla_i v^\alpha dS \qquad (2.22)$$

Using Stokes' theorem and defining the boundary (if there is one) of $\mathcal{S}$ as $\partial \mathcal{S}$

$$\frac{dI}{dt} = \int_{\partial S} g_{ik} \tau^k \left(\frac{\partial \gamma}{\partial \nabla_i \psi^\alpha} + \gamma g^{iq} m_{\sigma \alpha} \nabla_q \psi^\sigma \right) v^\alpha d\partial S$$
$$- \int_S \nabla_i \left(\frac{\partial \gamma}{\partial \nabla_i \psi^\alpha} + \gamma g^{iq} m_{\sigma \alpha} \nabla_q \psi^\sigma \right) v^\alpha dS$$

where τ is the outside pointing unitary normal field to the boundary of $\mathcal{S}$.

In order to encapsulate the quantities of interest, we define to restricted vector fields, $B \in \Gamma(T\mathcal{M}|_{\varphi(\partial S)})$

$$B^\alpha = m^{\alpha \beta} g_{ik} \tau^k \left(\frac{\partial \gamma}{\partial \nabla_i \psi^\beta} + \gamma g^{iq} m_{\sigma \beta} \nabla_q \psi^\sigma \right) \qquad (2.23)$$

and $A \in \Gamma(T\mathcal{M}|_{\varphi(S)})$

$$A^\alpha = m^{\alpha \beta} \nabla_i \left(\frac{\partial \gamma}{\partial \nabla_i \psi^\beta} + \gamma g^{iq} m_{\sigma \beta} \nabla_q \psi^\sigma \right) \qquad (2.24)$$

such that

$$\frac{dI}{dt}(t) = \int_{\partial S} m(B, v))|_{\psi(p,t)} d\partial S - \int_S m(A, v)|_{\psi(p,t)} dS \qquad (2.25)$$

Now, one could continue in the general case where $\partial S \neq \emptyset$ such that v could remain smooth on $\mathcal{S}$ and minimize $\frac{dI}{dt}$. However, for the model being developed in this work this seems slightly overzealous. The Level-Set method, in this work, will only be applied to compact interfaces in order to describe the grains in polycrystals. For this reason, a restriction of the theory to the case $\partial S = \emptyset$ is not a limiting one given that any boundary of the interface will be subject to special boundary conditions anyway. This is thus the case to be considered from here on out and

$$\frac{dI}{dt} = - \int_S m(A, v) dS \qquad (2.26)$$

Given the metric properties of m one may define the inner product

$$\langle \cdot, \cdot \rangle : \Gamma(TM|_{\psi(S)}) \times \Gamma(TM|_{\psi(S)}) \to \mathbb{R}$$

$$\langle u, w \rangle = \int_S m(u, w) dS$$

such that $(\Gamma(TM_{\psi(S)}), \langle \cdot, \cdot \rangle)$ becomes a Hilbert space with a norm, $u \in \Gamma(TM|_{\psi(S)})$

$$||u|| = \sqrt{\langle u, u \rangle}$$

Now using the Cauchy-Schwarz inequality

$$\frac{dI}{dt} = -\langle A, v \rangle \geq ||v|| ||A||$$

$$\frac{\langle A, v \rangle}{||v||} \leq ||A||$$

Since we would like to minimize $\frac{dI}{dt}$ we would like to maximize $\langle A, v \rangle$. Thus

$$\langle A, \frac{v}{||v||} \rangle = ||A||$$

$$\langle \frac{A}{||A||}, \frac{v}{||v||} \rangle = 1$$

Which, since both $\frac{A}{||A||}$ and $\frac{v}{||v||}$ are unitary elements of the Hilbert space, they must be equal

$$\frac{v}{||v||} = \frac{A}{||A||}$$

$$v = \frac{||v||}{||A||} A$$

Thus, $\mu \in \mathbb{R}$

$$v = \mu A \tag{2.27}$$

where μ is often called the mobility of the boundary. Far from being undetermined, physical meaning can be given to the mobility by returning to the energy dissipation equation (2.13)

$$\frac{dI}{dt} = \frac{dG}{dt}$$

$$-\mu\langle A, A \rangle = \frac{dG}{dt}$$

such that,

$$\mu = -\frac{1}{\langle A, A \rangle}\frac{dG}{dt} \tag{2.28}$$

Therefore, the mobility of the interface is determined by a normalized rate of dissipation of energy over time. For example, if one cosiders that the interfacial energy is entirely dissipated in terms of heat exhaust, then

$$\mu = \frac{T}{\langle A, A \rangle}\frac{d\eta_{ext}}{dt}$$

where η_{ext} is the entropy of the environement outside of the closed system.

2.4 The Level-Set setting for interface dynamics

Definition 28. *A level-set map or function ϕ is a smooth scalar field over the smooth manifold $\mathcal{M}$ such that, given an embedding $\varphi : S \to M$*

$$\phi(\varphi(p)) = 0 \tag{2.29}$$

$\forall p \in S.$

Now, most often, one defines the level-set function as a signed distance function to the interface such that with

$$d : M \times M \to \mathbb{R}^+$$

$$(p, q) \mapsto \min_{C(p,q)} \int_{C(p,q)} dC$$

where $C(p, q)$ is any curve from p to q, one may then fix

$$\phi(q) = \pm d(q, \varphi(S)) := \pm\min_{p \in S} d(q, \varphi(p))$$

where one makes a choice of sign over the domains that the interface separates. By defining the level-set field in this manner, it is relatively straightforward that, using $\tilde{\nabla}$ the Levi-Civita connection on $(\mathcal{M}, m)$,

$$\tilde{\nabla}\phi(n) = \pm m(n, n) = \pm 1$$
$$\tilde{\nabla}\phi(\varphi_* X) = 0 \quad \forall X \in \Gamma(T\mathcal{S})$$

given that $\tilde{\nabla}\phi \in \Gamma(T^*\mathcal{M})$. Pushing the equations in charts

$$\tilde{\nabla}_\alpha \phi = \pm m_{\alpha\beta} n^\beta \tag{2.30}$$
$$\tilde{\nabla}_\alpha \phi \nabla_i \varphi^\alpha = 0 \quad \forall i = 1, \ldots, s \tag{2.31}$$

which, by applying the covariant derivative ∇_j on $\mathcal{S}$ to the equation (2.31)

$$\nabla_j(\nabla_i \varphi^\alpha \tilde{\nabla}_\alpha \phi) = 0$$
$$\nabla_j \nabla_i \varphi^\alpha \tilde{\nabla}_\alpha \phi + \nabla_i \varphi^\alpha \nabla_j \tilde{\nabla}_\alpha \phi = 0$$

and, using the following chain rule,

$$\nabla_i = \nabla_i \varphi^\alpha \tilde{\nabla}_\alpha \tag{2.32}$$

one arrives at the following geometric equality

$$\nabla_j \nabla_i \varphi^\alpha \tilde{\nabla}_\alpha \phi = -\nabla_i \varphi^\alpha \nabla_j \varphi^\beta \tilde{\nabla}_\beta \tilde{\nabla}_\alpha \phi \tag{2.33}$$

thus linking the derivatives of the level-set ϕ with the derivatives of the embedding components φ^α.

As such, given an interface $(\mathcal{S}, \varphi, b)$ embedded in a smooth Riemannian n-manifold $(\mathcal{M}, m)$, the level-set function ϕ can be constructed with an arbitrary choice of sign. The dynamics of this interface can then be modeled by the transport equation (1.19) by replacing the velocity with the expression (2.27) derived in the previous section. For $p \in S$ one has

$$\frac{\partial \phi}{\partial t} + \mu A^\alpha \tilde{\nabla}_\alpha \phi = 0 \tag{2.34}$$

Expanding A

$$A^\alpha \tilde{\nabla}_\alpha \phi = m^{\alpha\beta} \nabla_i \left(\frac{\partial \gamma}{\partial \nabla_i \varphi^\beta} + \gamma g^{iq} m_{\sigma\beta} \nabla_q \varphi^\sigma \right) \tilde{\nabla}_\alpha \phi$$

$$= m^{\alpha\beta} \left(\frac{\partial^2 \gamma}{\partial \nabla_j \varphi^\zeta \partial \nabla_i \varphi^\beta} \nabla_i \nabla_j \varphi^\zeta + \nabla_i (\gamma g^{iq} m_{\sigma\beta} \nabla_q \varphi^\sigma) \right) \tilde{\nabla}_\alpha \phi$$

such that, using

$$g^{ij} g_{ji} = s$$
$$\nabla_k (g^{ij} g_{ji}) = \nabla_k(s)$$
$$(\nabla_k g^{ij}) g_{ji} + g^{ij} \nabla_k g_{ij} = 0$$
$$(\nabla_k g^{ij}) g_{ji} = 0$$
$$\nabla_k g^{ij} = 0$$

and

$$\nabla_i m_{\alpha\beta} = \nabla_i \varphi^\sigma \tilde{\nabla}_\sigma m_{\alpha\beta} = 0$$

we obtain

$$A^\alpha \tilde{\nabla}_\alpha \phi = m^{\alpha\beta} \left(\frac{\partial^2 \gamma}{\partial \nabla_j \varphi^\zeta \partial \nabla_i \varphi^\beta} \nabla_i \nabla_j \varphi^\zeta + (\nabla_i \gamma) g^{iq} m_{\sigma\beta} \nabla_q \varphi^\sigma + \gamma g^{iq} m_{\sigma\beta} \nabla_i \nabla_q \varphi^\sigma \right) \tilde{\nabla}_\alpha \phi$$

$$= m^{\alpha\beta} \frac{\partial^2 \gamma}{\partial \nabla_j \varphi^\zeta \partial \nabla_i \varphi^\beta} \nabla_i \nabla_j \varphi^\zeta \tilde{\nabla}_\alpha \phi + g^{iq} (\nabla_i \gamma) \nabla_q \varphi^\alpha \tilde{\nabla}_\alpha \phi + \gamma g^{iq} \nabla_i \nabla_q \varphi^\alpha \tilde{\nabla}_\alpha \phi$$

so that using equation (2.33)

$$A^\alpha \tilde{\nabla}_\alpha \phi = m^{\alpha\beta} \frac{\partial^2 \gamma}{\partial \nabla_j \varphi^\zeta \partial \nabla_i \varphi^\beta} \nabla_i \nabla_j \varphi^\zeta \tilde{\nabla}_\alpha \phi + g^{iq} \nabla_i \gamma \nabla_q \varphi^\alpha \tilde{\nabla}_\alpha \phi - \gamma g^{iq} \nabla_i \varphi^\alpha \nabla_q \varphi^\beta \tilde{\nabla}_\beta \tilde{\nabla}_\alpha \phi$$

Defining a tangential projection tensor field $P \in \Gamma(T_0^2 \mathcal{M}|_{\varphi(S)})$

$$P^{\alpha\beta} = g^{ij} \nabla_j \varphi^\alpha \nabla_i \varphi^\beta = m^{\alpha\beta} - n^\alpha n^\beta \tag{2.35}$$

we obtain

$$A^\alpha \tilde{\nabla}_\alpha \phi = m^{\alpha\beta} \frac{\partial^2 \gamma}{\partial \nabla_j \varphi^\zeta \partial \nabla_i \varphi^\beta} \nabla_i \nabla_j \varphi^\zeta \tilde{\nabla}_\alpha \phi + g^{iq} \nabla_i \gamma \nabla_q \varphi^\alpha \tilde{\nabla}_\alpha \phi - \gamma P^{\alpha\beta} \tilde{\nabla}_\beta \tilde{\nabla}_\alpha \phi$$

in order to reduce the expression, one may write,

$$g^{iq}\nabla_i\gamma\nabla_q\varphi^\alpha\tilde{\nabla}_\alpha\phi = g^{iq}\nabla_i\varphi^\beta\tilde{\nabla}_\beta\gamma\nabla_q\varphi^\alpha\tilde{\nabla}_\alpha\phi = P^{\alpha\beta}\tilde{\nabla}_\beta\gamma\tilde{\nabla}_\alpha\phi \qquad (2.36)$$

so that

$$A^\alpha\tilde{\nabla}_\alpha\phi = \frac{\partial^2\gamma}{\partial\nabla_j\varphi^\zeta\partial\nabla_i\varphi^\beta}\nabla_i\nabla_j\varphi^\zeta m^{\alpha\beta}\tilde{\nabla}_\alpha\phi + P^{\alpha\beta}\tilde{\nabla}_\beta\gamma\tilde{\nabla}_\alpha\phi - \gamma P^{\alpha\beta}\tilde{\nabla}_\beta\tilde{\nabla}_\alpha\phi \qquad (2.37)$$

Using equations (2.30) and (2.33)

$$\delta^\sigma_\alpha = n^\sigma\tilde{\nabla}_\alpha\phi + m_{\alpha\beta}P^{\beta\sigma}$$
$$\nabla_i\nabla_j\varphi^\alpha\delta^\sigma_\alpha = \nabla_i\nabla_j\varphi^\alpha(n^\sigma\tilde{\nabla}_\alpha\phi + m_{\alpha\beta}P^{\beta\sigma})$$
$$\nabla_i\nabla_j\varphi^\sigma = \nabla_i\nabla_j\varphi^\alpha\tilde{\nabla}_\alpha\phi n^\sigma + \nabla_i\nabla_j\varphi^\alpha m_{\alpha\beta}P^{\beta\sigma}$$
$$\nabla_i\nabla_j\varphi^\sigma = -\nabla_i\varphi^\delta\nabla_j\varphi^\zeta\tilde{\nabla}_\delta\tilde{\nabla}_\zeta\phi n^\sigma + \nabla_i\nabla_j\varphi^\alpha m_{\alpha\beta}g^{sq}\nabla_s\varphi^\beta\nabla_q\varphi^\sigma$$

for which, given

$$\nabla_k(g_{ij}) = 0$$
$$m_{\alpha\beta}\nabla_k(\nabla_i\varphi^\alpha\nabla_j\varphi^\beta) = 0$$
$$2m_{\alpha\beta}\nabla_k\nabla_i\varphi^\alpha\nabla_j\varphi^\beta = 0$$
$$m_{\alpha\beta}\nabla_i\nabla_j\varphi^\alpha\nabla_s\varphi^\beta = 0$$

we have that

$$\nabla_i\nabla_j\varphi^\sigma = -\nabla_i\varphi^\delta\nabla_j\varphi^\zeta\tilde{\nabla}_\delta\tilde{\nabla}_\zeta\phi n^\sigma \qquad (2.38)$$

Also,

$$\frac{\partial^2\gamma}{\partial\nabla_j\varphi^\zeta\partial\nabla_i\varphi^\beta} = \frac{\partial^2\gamma}{\partial\tilde{\nabla}_\delta\phi\partial\tilde{\nabla}_\alpha\phi}\frac{\partial\tilde{\nabla}_\alpha\phi}{\partial\nabla_i\varphi^\beta}\frac{\partial\tilde{\nabla}_\delta\phi}{\partial\nabla_j\varphi^\zeta} + \frac{\partial\gamma}{\partial\tilde{\nabla}_\alpha\phi}\frac{\partial^2\tilde{\nabla}_\alpha\phi}{\partial\nabla_j\varphi^\zeta\partial\nabla_i\varphi^\beta}$$

where, once again using the orthogonal condition (2.30),

$$\frac{\partial}{\partial \nabla_i \varphi^\beta}(\tilde{\nabla}_\alpha \phi \nabla_k \varphi^\alpha) = 0$$

$$\frac{\partial \tilde{\nabla}_\alpha \phi}{\partial \nabla_i \varphi^\beta} \nabla_k \varphi^\alpha + \tilde{\nabla}_\alpha \phi \delta_\beta^\alpha \delta_k^i = 0$$

$$\frac{\partial \tilde{\nabla}_\alpha \phi}{\partial \nabla_i \varphi^\beta} \nabla_k \varphi^\alpha = -\tilde{\nabla}_\beta \phi \delta_k^i$$

$$\frac{\partial \tilde{\nabla}_\alpha \phi}{\partial \nabla_i \varphi^\beta} \nabla_k \varphi^\alpha = -\tilde{\nabla}_\beta \phi g^{is} m_{\sigma\alpha} \nabla_s \varphi^\sigma \nabla_k \varphi^\alpha$$

to which, applying a second derivative,

$$\frac{\partial^2 \tilde{\nabla}_\alpha \phi}{\partial \nabla_j \varphi^\zeta \partial \nabla_i \varphi^\beta} \nabla_k \varphi^\alpha = -\frac{\partial \tilde{\nabla}_\zeta \phi}{\partial \nabla_i \varphi^\beta} \delta_k^j - \frac{\partial \tilde{\nabla}_\beta \phi}{\partial \nabla_j \varphi^\zeta} \delta_k^i$$

$$= -\frac{\partial \tilde{\nabla}_\zeta \phi}{\partial \nabla_i \varphi^\beta} g^{jq} m_{\delta\alpha} \nabla_q \varphi^\delta \nabla_k \varphi^\alpha - \frac{\partial \tilde{\nabla}_\beta \phi}{\partial \nabla_j \varphi^\zeta} g^{iq} m_{\delta\alpha} \nabla_q \varphi^\delta \nabla_k \varphi^\alpha$$

$$= -\left(\frac{\partial \tilde{\nabla}_\zeta \phi}{\partial \nabla_i \varphi^\beta} g^{jq} + \frac{\partial \tilde{\nabla}_\beta \phi}{\partial \nabla_j \varphi^\zeta} g^{iq} \right) m_{\delta\alpha} \nabla_q \varphi^\delta \nabla_k \varphi^\alpha$$

such that, by identification

$$\frac{\partial \tilde{\nabla}_\alpha \phi}{\partial \nabla_i \varphi^\beta} = -\tilde{\nabla}_\beta \phi g^{is} m_{\sigma\alpha} \nabla_s \varphi^\sigma \tag{2.39}$$

$$\frac{\partial^2 \tilde{\nabla}_\alpha \phi}{\partial \nabla_j \varphi^\zeta \partial \nabla_i \varphi^\beta} = -\left(\frac{\partial \tilde{\nabla}_\zeta \phi}{\partial \nabla_i \varphi^\beta} g^{jq} + \frac{\partial \tilde{\nabla}_\beta \phi}{\partial \nabla_j \varphi^\zeta} g^{iq} \right) m_{\delta\alpha} \nabla_q \varphi^\delta \tag{2.40}$$

and, with (2.38),

61

$$\frac{\partial^2 \tilde{\nabla}_\alpha \phi}{\partial \nabla_j \varphi^\zeta \partial \nabla_i \varphi^\beta} \nabla_i \nabla_j \varphi^\zeta = \left(\frac{\partial \tilde{\nabla}_\zeta \phi}{\partial \nabla_i \varphi^\beta} g^{jq} + \frac{\partial \tilde{\nabla}_\beta \phi}{\partial \nabla_j \varphi^\zeta} g^{iq} \right) m_{\delta\alpha} \nabla_q \varphi^\delta \nabla_i \varphi^\sigma \nabla_j \varphi^\xi \tilde{\nabla}_\sigma \tilde{\nabla}_\xi \phi n^\zeta$$

$$= \left(\frac{\partial \tilde{\nabla}_\zeta \phi}{\partial \nabla_i \varphi^\beta} P^{\delta\xi} \nabla_i \varphi^\sigma + \frac{\partial \tilde{\nabla}_\beta \phi}{\partial \nabla_j \varphi^\zeta} P^{\delta\sigma} \nabla_j \varphi^\xi \right) m_{\delta\alpha} \tilde{\nabla}_\sigma \tilde{\nabla}_\xi \phi n^\zeta$$

$$= \left(-\tilde{\nabla}_\beta \phi g^{is} m_{\gamma\zeta} \nabla_s \varphi^\gamma P^{\delta\xi} \nabla_i \varphi^\sigma + \frac{\partial \tilde{\nabla}_\beta \phi}{\partial \nabla_j \varphi^\zeta} P^{\delta\sigma} \nabla_j \varphi^\xi \right) m_{\delta\alpha} \tilde{\nabla}_\sigma \tilde{\nabla}_\xi \phi n^\zeta$$

$$= - \left(\tilde{\nabla}_\beta \phi m_{\gamma\zeta} P^{\gamma\sigma} P^{\delta\xi} + \tilde{\nabla}_\zeta \phi m_{\gamma\beta} P^{\gamma\xi} P^{\delta\sigma} \right) m_{\delta\alpha} \tilde{\nabla}_\sigma \tilde{\nabla}_\xi \phi n^\zeta$$

$$= - \left(\tilde{\nabla}_\beta \phi m_{\gamma\zeta} n^\zeta P^{\gamma\sigma} P^{\delta\xi} + \tilde{\nabla}_\zeta \phi n^\zeta m_{\gamma\beta} P^{\gamma\xi} P^{\delta\sigma} \right) m_{\delta\alpha} \tilde{\nabla}_\sigma \tilde{\nabla}_\xi \phi$$

$$= -m_{\delta\alpha} m_{\gamma\beta} P^{\gamma\xi} P^{\delta\sigma} \tilde{\nabla}_\sigma \tilde{\nabla}_\xi \phi$$

with also

$$\frac{\partial \tilde{\nabla}_\alpha \phi}{\partial \nabla_i \varphi^\beta} \frac{\partial \tilde{\nabla}_\delta \phi}{\partial \nabla_j \varphi^\zeta} \nabla_i \nabla_j \varphi^\zeta = -\tilde{\nabla}_\beta \phi g^{is} m_{\sigma\alpha} \nabla_s \varphi^\sigma \tilde{\nabla}_\zeta \phi g^{jq} m_{\xi\delta} \nabla_q \varphi^\xi \nabla_i \varphi^\gamma \nabla_j \varphi^\epsilon \tilde{\nabla}_\gamma \tilde{\nabla}_\epsilon \phi n^\zeta$$

$$= -\tilde{\nabla}_\beta \phi m_{\gamma\alpha} m_{\epsilon\delta} P^{\xi\epsilon} P^{\gamma\sigma} \tilde{\nabla}_\sigma \tilde{\nabla}_\xi \phi$$

so that finally

$$\frac{\partial^2 \gamma}{\partial \nabla_j \varphi^\zeta \partial \nabla_i \varphi^\beta} \nabla_i \nabla_j \varphi^\zeta m^{\alpha\beta} \tilde{\nabla}_\alpha \phi$$

$$= \left(\frac{\partial^2 \gamma}{\partial \tilde{\nabla}_\delta \phi \partial \tilde{\nabla}_\alpha \phi} \frac{\partial \tilde{\nabla}_\alpha \phi}{\partial \nabla_i \varphi^\beta} \frac{\partial \tilde{\nabla}_\delta \phi}{\partial \nabla_j \varphi^\zeta} + \frac{\partial \gamma}{\partial \tilde{\nabla}_\alpha \phi} \frac{\partial^2 \tilde{\nabla}_\alpha \phi}{\partial \nabla_j \varphi^\zeta \partial \nabla_i \varphi^\beta} \right) \nabla_i \nabla_j \varphi^\zeta m^{\kappa\beta} \tilde{\nabla}_\kappa \phi$$

$$= - \left(\frac{\partial^2 \gamma}{\partial \tilde{\nabla}_\delta \phi \partial \tilde{\nabla}_\alpha \phi} \tilde{\nabla}_\beta \phi m_{\gamma\alpha} m_{\epsilon\delta} P^{\xi\epsilon} P^{\gamma\sigma} \tilde{\nabla}_\sigma \tilde{\nabla}_\xi \phi + \frac{\partial \gamma}{\partial \tilde{\nabla}_\alpha \phi} m_{\delta\alpha} m_{\gamma\beta} P^{\gamma\xi} P^{\delta\sigma} \tilde{\nabla}_\sigma \tilde{\nabla}_\xi \phi \right) m^{\kappa\beta} \tilde{\nabla}_\kappa \phi$$

$$= - \left(\frac{\partial^2 \gamma}{\partial \tilde{\nabla}_\delta \phi \partial \tilde{\nabla}_\alpha \phi} m_{\gamma\alpha} m_{\epsilon\delta} P^{\xi\epsilon} P^{\gamma\sigma} \tilde{\nabla}_\sigma \tilde{\nabla}_\xi \phi + \frac{\partial \gamma}{\partial \tilde{\nabla}_\alpha \phi} m_{\delta\alpha} m_{\gamma\beta} P^{\gamma\xi} P^{\delta\sigma} m^{\kappa\beta} \tilde{\nabla}_\kappa \phi \tilde{\nabla}_\sigma \tilde{\nabla}_\xi \phi \right)$$

using $P_\alpha^\beta = m_{\alpha\sigma} P^{\sigma\beta}$

$$\frac{\partial^2 \gamma}{\partial \nabla_j \varphi^\zeta \partial \nabla_i \varphi^\beta} \nabla_i \nabla_j \varphi^\zeta m^{\alpha\beta} \tilde{\nabla}_\alpha \phi = - \left(\frac{\partial^2 \gamma}{\partial \tilde{\nabla}_\beta \phi \partial \tilde{\nabla}_\alpha \phi} + \frac{\partial \gamma}{\partial \tilde{\nabla}_\alpha \phi} m^{\kappa\beta} \tilde{\nabla}_\kappa \phi \right) P_\beta^\xi P_\alpha^\sigma \tilde{\nabla}_\sigma \tilde{\nabla}_\xi \phi$$

$$\tag{2.41}$$

Thus leading to the transport equation

$$\frac{\partial \phi}{\partial t} + \mu \left(- \left(\frac{\partial^2 \gamma}{\partial \tilde{\nabla}_\beta \phi \partial \tilde{\nabla}_\alpha \phi} + \frac{\partial \gamma}{\partial \tilde{\nabla}_\alpha \phi} m^{\kappa\beta} \tilde{\nabla}_\kappa \phi \right) P_\beta^\xi P_\alpha^\sigma \tilde{\nabla}_\sigma \tilde{\nabla}_\xi \phi + P^{\alpha\beta} \tilde{\nabla}_\beta \gamma \tilde{\nabla}_\alpha \phi - \gamma P^{\alpha\beta} \tilde{\nabla}_\alpha \tilde{\nabla}_\beta \phi \right) = 0$$

Considering now that

$$\tilde{\nabla}_\alpha \phi n^\alpha = 1$$
$$\tilde{\nabla}_\beta \tilde{\nabla}_\alpha \phi n^\alpha + \tilde{\nabla}_\alpha \phi \tilde{\nabla}_\beta n^\alpha = 0$$
$$\tilde{\nabla}_\beta \tilde{\nabla}_\alpha \phi n^\alpha + n^\delta \tilde{\nabla}_\beta \tilde{\nabla}_\delta \phi = 0$$

which, because $\tilde{\nabla}_\alpha \tilde{\nabla}_\beta = \tilde{\nabla}_\beta \tilde{\nabla}_\alpha$

$$n^\alpha \tilde{\nabla}_\alpha \tilde{\nabla}_\beta \phi = 0 \tag{2.42}$$

and, as such,

$$P_\alpha^\sigma \tilde{\nabla}_\sigma \tilde{\nabla}_\xi \phi = (\delta_\alpha^\sigma - n^\sigma \nabla_\alpha \phi) \tilde{\nabla}_\sigma \tilde{\nabla}_\xi \phi$$
$$= \tilde{\nabla}_\alpha \tilde{\nabla}_\xi \phi$$

and

$$P^{\alpha\beta} \tilde{\nabla}_\alpha \tilde{\nabla}_\beta \phi = m^{\alpha\beta} \tilde{\nabla}_\alpha \tilde{\nabla}_\beta \phi$$
$$= \Delta \phi$$

where Δ is the classic Laplacian operator in $\mathcal{M}$.
Using equation (2.42),

$$\frac{\partial \phi}{\partial t} + \mu \left(- \frac{\partial^2 \gamma}{\partial \tilde{\nabla}_\beta \phi \partial \tilde{\nabla}_\alpha \phi} \tilde{\nabla}_\alpha \tilde{\nabla}_\beta \phi + P^{\alpha\beta} \tilde{\nabla}_\beta \gamma \tilde{\nabla}_\alpha \phi - \gamma \Delta \phi \right) = 0$$

and, rewriting the equation,

$$\frac{\partial \phi}{\partial t} + \mu \left(- \left(\gamma m^{\alpha\beta} + \frac{\partial^2 \gamma}{\partial \tilde{\nabla}_\beta \phi \partial \tilde{\nabla}_\alpha \phi} \right) \tilde{\nabla}_\alpha \tilde{\nabla}_\beta \phi + P^{\alpha\beta} \tilde{\nabla}_\beta \gamma \tilde{\nabla}_\alpha \phi \right) = 0 \tag{2.43}$$

one may identify two distinct terms:

A curvature contribution, which can be tied to the terms developped in [100],

$$-\mu\left(\gamma m^{\alpha\beta} + \frac{\partial^2\gamma}{\partial\tilde{\nabla}_\beta\phi\partial\tilde{\nabla}_\alpha\phi}\right)\tilde{\nabla}_\alpha\tilde{\nabla}_\beta\phi, \qquad (2.44)$$

and a "stabilization" term

$$\mu P^{\alpha\beta}\tilde{\nabla}_\beta\gamma\tilde{\nabla}_\alpha\phi \qquad (2.45)$$

which should be null using equation (2.31). The extension of the differential equation from $\varphi(S)$ to all of M can render this stabilization term possibly non-null. Indeed, although the transport equation is valid for all $\varphi(S)$, the level set is defined over $\mathcal{M}$. As such, the resolution of the equations must be undertaken over the entire domain. One must, therefore, devise an extension procedure such that the relevant fields can be extended everywhere in $\mathcal{M}$ and still produce the correct dynamics of the iso-zero value of the level set field.

The two fields that must be extended everywhere are

$$\gamma(p \in S), \ \frac{\partial^2\gamma}{\partial\tilde{\nabla}_\beta\phi\partial\tilde{\nabla}_\alpha\phi}(p \in S)$$

Any extension operation that fixes the values of these two fields such that, $\forall p \in S$,

$$\gamma(p) = \gamma(\varphi(p))$$
$$\frac{\partial^2\gamma}{\partial\tilde{\nabla}_\beta\phi\partial\tilde{\nabla}_\alpha\phi}(p) = \frac{\partial^2\gamma}{\partial\tilde{\nabla}_\beta\phi\partial\tilde{\nabla}_\alpha\phi}(\varphi(p))$$

and the fields remain regular throughout the domain $\mathcal{M}$, should produce the correct solution for the dynamics of the interface.

The above developments have generated a prospective velocity field v and the transport equation necessary to solve for simulating the dynamics of a level set field ϕ. Quite naturally, the model proposes a global definition for the mobility μ of the boundaries in this system. What remains is to test this mathematical formulation in some relevant cases so as to confirm its value. Remaining lines of inquiry include the well-posedness of the equations with adequate boundary conditions which will be touched upon in the following chapter. Also, the role of the metric m of the base manifold $\mathcal{M}$ in the cases where the manifold is not "flat" has interesting applications for a theory with a local tensorial value for the mobility. Perhaps the most daunting aspect in the resolution of these equations is the high non-linearity. Indeed, given that $\gamma(\tilde{\nabla}\phi)$, every term of the transport equation is non-linear except for the time derivative.

Résumé en Français du Chapitre 2

Ce chapitre est une application directe des outils de la géométrie différentielle à la minimisation de l'énergie d'un système par le déplacement des interfaces internes qui y sont présentes. En effet, après avoir défini tous les termes mathématiques utiles, le problème consistant à exhiber le champ de vitesse optimal pour la minimisation de l'énergie liée à une variété imbriquée dans une autre variété de plus haute dimension est introduit. En utilisant des principes variationnels, le champ de vitesse "minimal" est exprimé en fonction des degrés de liberté naturels. Ensuite, ce formalisme est traduit en termes de méthodologie level set en spécifiant que l'espace imbriqué est une hypersurface de la variété de base. Par la même occasion, une nouvelle équation de transport du champ level set est définie dans ce cas plus général. Une définition globale de la mobilité d'une interface est proposée assez naturellement comme étant un taux de production d'entropie par unité de temps. Une nouvelle vitesse d'interface dans le cas d'une énergie de joints de grains anisotrope est donc prête à être testée dans des situations adaptées.

Chapter 3

Dynamics of the Anisotropic Grain Boundary

The best way to test a numerical algorithm for solving a physical problem is by using an analytical test case. When doing so, one may look at the absolute precision of the numerical solution as a function of the parameterization of the procedure (mesh sizes, time steps, domain sizes, etc.). One may then evaluate the performance of the solver in a controlled environment. In the case of isotropic grain growth, two well-known benchmarks exist for evaluating numerical codes: the shrinking sphere and the so-called "Grim Reaper" form [101]. Considering truly anisotropic grain growth, no such analytical benchmark is known to the community. In this chapter, the first section will present the numerical algorithm used to compute solutions to anisotropic grain growth in the absence of multiple junctions. The second section is dedicated to developing an analytical solution to the anisotropic grain growth problem in the specific case of a shrinking ellipse. The third section will present the results of the proposed algorithm using the ellipse shrinkage case. The final section will use related test cases to compare the effects of velocity fields with and without anisotropic torque terms.

3.1   The numerical formulation

In order to solve the minimizing energy flow for the level set function using the Finite Element (FE) method, the problem must first expressed in a weak form, then it can be discretized in both time and space.

Consider the transport equation (2.43), reproduced here for convenience,

$$\frac{\partial \phi}{\partial t} + \mu \left(- \left(\gamma m^{\alpha\beta} + \frac{\partial^2 \gamma}{\partial \tilde{\nabla}_\beta \phi \partial \tilde{\nabla}_\alpha \phi} \right) \tilde{\nabla}_\alpha \tilde{\nabla}_\beta \phi + P^{\alpha\beta} \tilde{\nabla}_\beta \gamma \tilde{\nabla}_\alpha \phi \right) = 0$$

where the relevant fields have already been extended from the smooth manifold $\mathcal{S}$ to the enclosing manifold $\mathcal{M}$ and μ is known. With any test function $\omega \in H^1(\mathcal{M})$ and

$$D^{\alpha\beta} = \gamma m^{\alpha\beta} + \frac{\partial^2 \gamma}{\partial \tilde{\nabla}_\beta \phi \partial \tilde{\nabla}_\alpha \phi}$$

a weak form of the equation can be derived as

$$\frac{\partial \phi}{\partial t}\omega - \mu D^{\alpha\beta}\tilde{\nabla}_\alpha\tilde{\nabla}_\beta\phi\omega + \mu P^{\alpha\beta}\tilde{\nabla}_\beta\gamma\tilde{\nabla}_\alpha\phi\omega = 0$$

$$\int_\mathcal{M} \frac{\partial \phi}{\partial t}\omega dM - \int_\mathcal{M} \mu D^{\alpha\beta}\tilde{\nabla}_\alpha\tilde{\nabla}_\beta\phi\omega dM + \int_\mathcal{M} \mu P^{\alpha\beta}\tilde{\nabla}_\beta\gamma\tilde{\nabla}_\alpha\phi\omega dM = 0$$

$$\int_\mathcal{M} \frac{\partial \phi}{\partial t}\omega dM + \int_\mathcal{M} \tilde{\nabla}_\alpha(\mu D^{\alpha\beta}\omega)\tilde{\nabla}_\beta\phi dM - \int_{\partial\mathcal{M}} \tilde{\nabla}_\alpha(\mu D^{\alpha\beta}\omega\tilde{\nabla}_\beta\phi)d\partial M$$

$$+ \int_\mathcal{M} \mu P^{\alpha\beta}\tilde{\nabla}_\beta\gamma\tilde{\nabla}_\alpha\phi\omega dM = 0$$

$$\int_\mathcal{M} \frac{\partial \phi}{\partial t}\omega dM + \int_\mathcal{M} \mu D^{\alpha\beta}\tilde{\nabla}_\alpha\omega\tilde{\nabla}_\beta\phi dM + \int_\mathcal{M} \mu(\tilde{\nabla}_\alpha D^{\alpha\beta})\omega\tilde{\nabla}_\beta\phi)dM - 0$$

$$+ \int_\mathcal{M} \mu P^{\alpha\beta}\tilde{\nabla}_\beta\gamma\tilde{\nabla}_\alpha\phi\omega dM = 0$$

such that

$$\int_\mathcal{M} \frac{\partial \phi}{\partial t}\omega dM + \int_\mathcal{M} \mu D^{\alpha\beta}\tilde{\nabla}_\alpha\omega\tilde{\nabla}_\beta\phi dM + \int_\mathcal{M} \mu(P^{\alpha\beta}\tilde{\nabla}_\beta\gamma + \tilde{\nabla}_\beta D^{\beta\alpha})\omega\tilde{\nabla}_\alpha\phi dM = 0 \quad (3.1)$$

With respectively three distinct terms: the time derivative, a diffusive term and a convective contribution.

In this numerical framework, the Riemannian manifold $\mathcal{M}$ is meshed using an unstructured simplicial grid. If the manifold is two dimensional the cells are triangles, if it is three dimensional the cells are tetrahedra, etc. The mesh $\bar{\mathcal{M}}$ is composed of two sets $\bar{\mathcal{M}} = (\mathcal{P}, \mathcal{E})$ respectively the nodes of the mesh $\mathcal{P}$ and the cells/connectivity of the mesh $\mathcal{E}$. Thus, the smooth Riemannian manifold $\mathcal{M}$ is approximated by a C^1 by parts manifold $\bar{\mathcal{M}}$ and thus any initially smooth field is approximated by a field whose component functions are in H^1 (i.e. a P1 field). The nodes enclosed in the embedding are referred to as $N \subset \mathcal{P}$. In order to get a numerical representative of the level set field $\bar{\phi}$ Algorithm 1 is used.

As such, the level set field is approximated by a linear by parts (inside each cell of $\mathcal{E}$) field $\bar{\phi}$. The details of the algorithm used to compute the distance function can be found in [102]. The brute force algorithm used for the calculation of the distance function also gives access to an inward pointing P1 unit normal field n. This normal field can be used

Algorithm 1 LS field computation

---

    for $q \in \mathcal{P}$ **do**
        $\bar{\phi}(q) = d(q, \varphi(S))$
        if $q \notin N$ **then**
            $\bar{\phi}(q) = -\bar{\phi}(q)$
        end if
    end for

---

to compute a P1 representation of the covariant derivative of ϕ as $n^\beta = \overline{m^{\alpha\beta} \nabla_\alpha \phi}$. This representation is more accurate than the numerical covariant derivative of the level set $\bar{\nabla} \bar{\phi}$ that would be a P0 field (piecewise constant in each of the cells). This normal field is also used to compute the surface projector field $P = m^{-1} - n \otimes n$.

> **Simplification**   *Flat metric, Cartesian chart*
>
> In the context of a flat metric m for $\mathcal{M}$ and in a Cartesian chart in the base space, the components of m resemble the identity such that
>
> $$m^{\alpha\beta} = \delta^{\alpha\beta}$$
>
> where $\delta^{\alpha\beta}$ is a Kronecker delta symbol. This means that, in simple cases, the components of the P tensor will be
>
> $$P^{\alpha\beta} = \delta^{\alpha\beta} - n^\alpha n^\beta.$$
>
> This will be the case in what follows.

Thus, given a boundary energy map $\gamma : \mathcal{B} \to \mathbb{R}^+$, with $\mathcal{B}$ the boundary property space, the C^1 geometry dependence of γ can easily be evaluated at each node of the mesh $\bar{\mathcal{M}}$. Considering that $\mathcal{B}$ is only parameterized by the normal to the boundary n for a given boundary, both values for γ and $\frac{\partial^2 \gamma}{\partial \nabla \phi^2}$ can be evaluated everywhere on the mesh. As such, the level set field induces a natural discretized extension of both γ and $\frac{\partial^2 \gamma}{\partial \nabla \phi^2}$ from $\varphi(S)$ to the entire discretized space $\bar{\mathcal{M}}$. Outside the interface the γ field has no physical meaning. However, this extension is necessary for solving the problem in a FE setting. The interpolated values of the fields at the interface $\varphi(S)$ are also guaranteed to be the correct values given the linear by parts interpolation of $\bar{\phi}$. Figure 3.1 illustrates the construction for a circle and a particular choice of $\gamma(n)$.

The $\tilde{\nabla}\gamma$ and $\tilde{\nabla} \cdot D$ are computed numerically on the mesh using a Superconvergent Patch Recovery method inspired from [103] such as to obtain P1 fields. As such, both the diffusive tensor D and the convective velocity are introduced explicitly into the formulation so as to create linearized approximations of the equation (3.1). Thus, solving the problem is completely linear without need for non-linear solvers or algorithms.
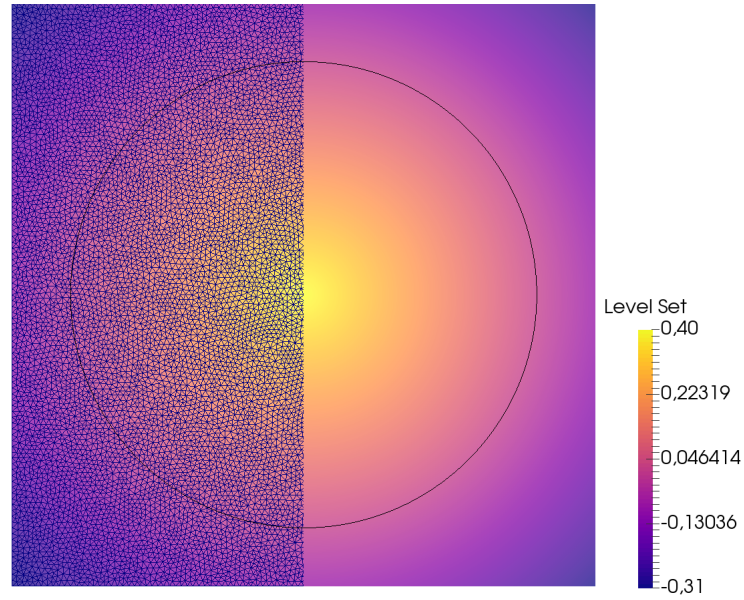
(a) The level set field ϕ
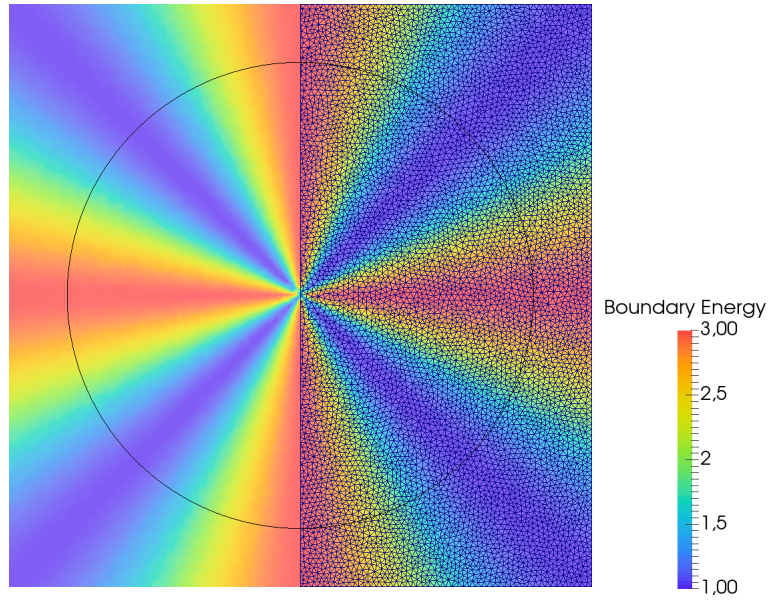
(b) The boundary energy field γ

Figure 3.1: Image of the ϕ and γ fields defined on an unstructured mesh. The iso-zero value of the level set is represented in black and $\gamma = 2 + \cos(4\arccos(X \cdot \nabla\phi))$ where X is the unit vector field in the direction of the x axis.

In this work a Generalized Minimal Residual (GMRES) type solver along with an Incomplete LU (ILU) type preconditionner, both linked from the PetsC open source libraries, are used unless specified otherwise. The system is assembled using typical P1 FE elements with a Streamline Upwind Petrov-Galerkin (SUPG) stabilization for the convective term [104]. The boundary conditions used are classical von Neumann conditions $\tilde{\nabla}\phi \cdot n_{\partial M} = 0$ which guarantees the orthogonality of the level sets to the boundary of the domain, $n_{\partial M}$ being an outgoing unit normal vector field to $\partial\mathcal{M}$. The discretization of time is obtained using a fully implicit backward Euler method with time step Δt. Using classical linear hat functions $\omega_k, k = 1, \dots, \mathcal{P}$ as the basis functions for the solution, the weak form (3.1) projections are expressed as follows

$$\sum_{c \in \mathcal{E}} \int_c \frac{\partial \bar{\phi}}{\partial t} \omega_k dM + \int_c \mu D^{\alpha\beta} \tilde{\nabla}_\alpha \omega_k \tilde{\nabla}_\beta \bar{\phi} dM$$

$$+ \int_c \mu (P^{\alpha\beta} \tilde{\nabla}_\beta \gamma + \tilde{\nabla}_\beta D^{\beta\alpha}) \omega_k \tilde{\nabla}_\alpha \bar{\phi} dM = R_k(\bar{\phi}, \tilde{\nabla}\bar{\phi})$$

where $R_k(\bar{\phi}, \tilde{\nabla}\bar{\phi})$ is the residual error with respect to the ω_k test function. Using the Galerkin method where, $\forall q \in M$ and ϕ^i the value of $\bar{\phi}$ at the ith node of $\mathcal{P}$,

$$\bar{\phi}(q) = \sum_{p_i \in \mathcal{P}} \omega_i \phi^i$$

one obtains, using the Einstein sum convention when applicable,

$$\sum_{c \in \mathcal{E}} \int_c \frac{\partial \phi^i}{\partial t} \omega_i \omega_k dM + \int_c \mu D^{\alpha\beta} \tilde{\nabla}_\alpha \omega_k \tilde{\nabla}_\beta \omega_i \phi^i dM$$

$$+ \int_c \mu (P^{\alpha\beta} \tilde{\nabla}_\beta \gamma + \tilde{\nabla}_\beta D^{\beta\alpha}) \omega_k \tilde{\nabla}_\alpha \omega_i \phi^i dM = R_k(\bar{\phi}, \tilde{\nabla}\bar{\phi})$$

where, introducing the time discretization $t_{n+1} = t_n + \Delta t$ and the notation $\phi_n^i = \phi^i(t_n)$,

$$\sum_{c \in \mathcal{E}} \int_c \frac{\phi_{n+1}^i - \phi_n^i}{\Delta t} \omega_i \omega_k dM + \int_c \mu D^{\alpha\beta} \tilde{\nabla}_\alpha \omega_k \tilde{\nabla}_\beta \omega_i \phi_{n+1}^i dM$$

$$+ \int_c \mu (P^{\alpha\beta} \tilde{\nabla}_\beta \gamma + \tilde{\nabla}_\beta D^{\beta\alpha}) \omega_k \tilde{\nabla}_\alpha \omega_i \phi_{n+1}^i dM = R_k(\bar{\phi}(t_{n+1}), \tilde{\nabla}\bar{\phi}(t_{n+1}))$$

and, rearranging,

$$\phi_{n+1}^i \sum_{c \in \mathcal{E}} \int_c (\omega_i \omega_k + \Delta t \mu (D^{\alpha\beta} \tilde{\nabla}_\alpha \omega_k \tilde{\nabla}_\beta \omega_i + (P^{\alpha\beta} \tilde{\nabla}_\beta \gamma + \tilde{\nabla}_\beta D^{\beta\alpha}) \omega_k \tilde{\nabla}_\alpha \omega_i)) dM$$

$$= \Delta t R_k(\bar{\phi}(t_{n+1}), \tilde{\nabla}\bar{\phi}(t_{n+1})) + \phi_n^i \sum_{c \in \mathcal{E}} \int_c \omega_i \omega_k dM$$

so that, reintroducing the residual error into the formulation using the SUPG method [104] as modifications to the test functions $\omega_k \to \tilde{\omega}_k$ and defining

$$\mathbb{M}_{ik} = \sum_{c \in \mathcal{E}} \int_c (\omega_i \tilde{\omega}_k + \Delta t \mu (D^{\alpha\beta} \tilde{\nabla}_\alpha \omega_k \tilde{\nabla}_\beta \omega_i + (P^{\alpha\beta} \tilde{\nabla}_\beta \gamma + \tilde{\nabla}_\beta D^{\beta\alpha}) \tilde{\omega}_k \tilde{\nabla}_\alpha \omega_i)) dM$$

$$\mathbb{B}_k = \phi_n^i \sum_{c \in \mathcal{E}} \int_c \omega_i \omega_k dM$$

the resolution of the discretized problem becomes a linear algebra system

$$\mathbb{M}u = \mathbb{B} \tag{3.2}$$

where $u = [\phi_{n+1}^i]$ is a vector where the ith component is the value of the level set function at the ith node $p_i \in \mathcal{P}$ and the next time step $u^i = \phi_{n+1}^i = \bar{\phi}(p_i, t_{n+1})$.

The convention for the level-set fields used here on out will be positive inside closed objects and negative outside of them. Because the resolution of the transport equation does not conserve the distance property of the level set field, the solution is reinitialized using the algorithm developed in [102]. Also, since the geometry of the interface evolves after each time increment, all the other fields must also be recomputed from the reinitialized level set at each step of the simulation. The complete procedure for the minimizing interface energy flow simulation is reported in Algorithm 2.

3.2   An analytical solution for the ellipse

Consider a circle $\mathcal{C} = ([0; 2\pi], \mathcal{O}_C, \mathcal{A}_C)$ as a smooth manifold with the circle topology and smooth structure and the Riemannian manifold $\mathcal{M} = (\mathbb{R}^2, \mathcal{O}_{std}, \mathcal{A}_{std}, m)$ equipped with the standard topology and differentiable structures and the flat metric m. Using the chart $([0; 2\pi], \theta) \in \mathcal{A}_C$ and the Cartesian chart $(\mathbb{R}^2, (x, y)) \in \mathcal{A}_{std}$ one may construct the following embedding

$$\varphi : [0; 2\pi] \longrightarrow \mathbb{R}^2$$
$$\theta \mapsto (a \cos \theta, b \sin \theta)$$

Algorithm 2 Minimizing Interface Energy Flow

Data: Initial Embedding, $\bar{\mathcal{M}}$, Δt, t_{end}
Compute the initial Level Set and unit normal fields
Calculate the P field
Calculate γ and D fields and their derivatives
$t = 0$
while $t < t_{end}$ **do**
    Assemble $\mathbb{M}, \mathbb{B}$
    Solve $\mathbb{M}u = \mathbb{B}$
    $t = t + \Delta t$
    Reinitialize the Level Set and unit normal fields
    Update the P field
    Update the γ and D fields and their derivatives
end while
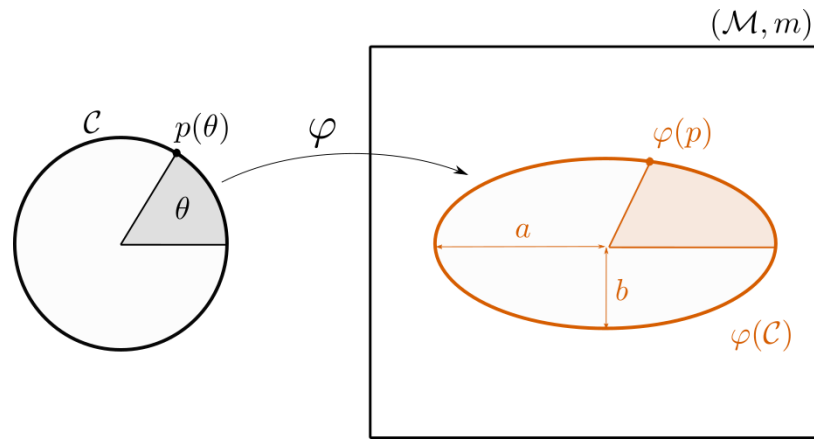
Figure 3.2: Ellipse embedding of the circle $\mathcal{C}$ into $\mathcal{M}$

where $(a, b) \in \mathbb{R}^2$ and Figure 3.2 illustrates this embedding.

Simplification   *One dimensional object*

Given that the $\mathcal{C}$ is a one dimensional object, any (p, q)-tensor field σ defined on the space will only ever have one component

$$\sigma^{i_1 \cdots i_p}_{j_1 \cdots j_q} = \sigma^{\theta \cdots \theta}_{\theta \cdots \theta}$$

where every index refers to the unique dimension of $\mathcal{C}$. However, even if this is the case, these tensor fields cannot be considered as scalar fields directly due to their transformation behavior under chart transitions.

All of the relevant geometrical information may thus be extracted from the embedding. A basis of the tangent space at each point

$$\frac{\partial \varphi^x}{\partial \theta} = -a \sin \theta \tag{3.3}$$

$$\frac{\partial \varphi^y}{\partial \theta} = b \cos \theta \tag{3.4}$$

and the induced metric tensor

$$g_{ij} = m_{\alpha\beta} \nabla_i \varphi^\alpha \nabla_j \varphi^\beta$$

Simplification   *Flat metric, Cartesian chart, One dimensional object*

$$g_{\theta\theta} = \delta_{\alpha\beta} \nabla_\theta \varphi^\alpha \nabla_\theta \varphi^\beta$$
$$= (\nabla_\theta \varphi^x)^2 + (\nabla_\theta \varphi^y)^2$$

such that

$$g_{\theta\theta} = a^2 \sin^2 \theta + b^2 \cos^2 \theta \tag{3.5}$$

The Levi-Civita connection ∇ is thus defined by

$$\nabla_\theta g_{\theta\theta} = 0$$

$$\frac{\partial g_{\theta\theta}}{\partial\theta} - 2\Gamma^\theta_{\theta\theta} g_{\theta\theta} = 0$$

$$\Gamma^\theta_{\theta\theta} = \frac{1}{2g_{\theta\theta}} \frac{\partial g_{\theta\theta}}{\partial\theta}$$

where Γ^k_{ij} are Christoffel symbols. Therefore,

$$\Gamma^\theta_{\theta\theta} = \frac{(a^2 - b^2)\cos\theta\sin\theta}{a^2\sin^2\theta + b^2\cos^2\theta} \tag{3.6}$$

Now consider the boundary energy

$$\gamma(\theta) = G^{\theta\theta} g_{\theta\theta} \tag{3.7}$$

where $G^{\theta\theta}$ is a $(2,0)$-tensor field of $\mathcal{C}$ whose component is actually a constant in this chart. As such, using equations (2.27) and (2.24) the velocity field of the minimizing energy flow is

$$v^\alpha = \mu m^{\alpha\beta} \nabla_i \left(\frac{\partial\gamma}{\partial\nabla_i\psi^\beta} + \gamma g^{iq} m_{\sigma\beta} \nabla_q \varphi^\sigma \right)$$

where, replacing with the expression for γ in equation (3.7) and letting $\mu \in \mathbb{R}$, one has

$$v^\alpha = \mu m^{\alpha\beta} \nabla_i \left(\frac{\partial G^{sk} g_{ks}}{\partial\nabla_i\psi^\beta} + G^{sk} g_{ks} g^{iq} m_{\sigma\beta} \nabla_q \varphi^\sigma \right)$$

$$= \mu m^{\alpha\beta} \nabla_i \left(2G^{si} m_{\beta\zeta} \nabla_s \varphi^\zeta + G^{sk} g_{ks} g^{iq} m_{\sigma\beta} \nabla_q \varphi^\sigma \right)$$

<div style="background:#fbe9de">

Simplification   *One dimensional object, Constant $G^{\theta\theta}$*

$$v^\alpha = \mu m^{\alpha\beta} \nabla_\theta \left(2G^{\theta\theta} m_{\beta\zeta} \nabla_\theta \varphi^\zeta + G^{\theta\theta} g_{\theta\theta} g^{\theta\theta} m_{\sigma\beta} \nabla_\theta \varphi^\sigma \right)$$

$$= 3\mu G^{\theta\theta} \nabla_\theta \nabla_\theta \varphi^\alpha$$

</div>

using

$$\nabla_\theta \nabla_\theta \varphi^\alpha = \frac{\partial^2\varphi^\alpha}{\partial\theta^2} - \Gamma^\theta_{\theta\theta} \frac{\partial\varphi^\alpha}{\partial\theta}$$

one arrives at

$$
\begin{pmatrix} v^x \\ v^y \end{pmatrix} = -3\mu G^{\theta\theta} \begin{pmatrix} a\cos\theta \\ b\sin\theta \end{pmatrix} - \frac{(a^2-b^2)\cos\theta\sin\theta}{a^2\sin^2\theta + b^2\cos^2\theta} \begin{pmatrix} -a\sin\theta \\ b\cos\theta \end{pmatrix}
$$

However, any tangential terms in the velocity, such as the second term in the above equation, have no influence on the flow of the interface such that the flow generated by the velocity field above is equivalent to the flow generated by

$$
\begin{pmatrix} v^x \\ v^y \end{pmatrix} = -3\mu G^{\theta\theta} \begin{pmatrix} a\cos\theta \\ b\sin\theta \end{pmatrix} \tag{3.8}
$$

Thus, turning φ into a flow $\varphi : [0; 2\pi[\times[0; 1] \to \mathbb{R}^2$, one has

$$
\frac{d\varphi^\alpha}{dt}(\theta, t) = -3\mu G^{\theta\theta}\varphi^\alpha(\theta, t)
$$

for which there is only one solution

$$
\varphi^\alpha(\theta, t) = \varphi^\alpha(\theta, 0)e^{-3\mu G^{\theta\theta}t}
$$

leading to

$$
\begin{pmatrix} \varphi^x(\theta, t) \\ \varphi^y(\theta, t) \end{pmatrix} = e^{-3\mu G^{\theta\theta}t} \begin{pmatrix} a\cos\theta \\ b\sin\theta \end{pmatrix}
$$

Now given that the minimizing energy flow of the embedding is just the original embedding multiplied by a time dependent function, the flow is actually simply shrinking the ellipse in a homothetic manner to the center $(0, 0)$ point of $\mathcal{M}$. Thus, assuming $a > b$, the eccentricity e is a constant of the flow

$$
e = \sqrt{1 - \left(\frac{\varphi^y(\frac{\pi}{2}, t)}{\varphi^x(0, t)}\right)^2} = \sqrt{1 - \left(\frac{e^{-3\mu G^{\theta\theta}t}b}{e^{-3\mu G^{\theta\theta}t}a}\right)^2} = \sqrt{1 - \left(\frac{b}{a}\right)^2} \tag{3.9}
$$

and the scalar velocity of any point of the ellipse is

$$
v(\theta, t) = \sqrt{(v^x)^2 + (v^y)^2} = 3\mu G^{\theta\theta}e^{-3\mu G^{\theta\theta}t}\sqrt{a^2\cos^2\theta + b^2\sin^2\theta} \tag{3.10}
$$

with, in particular,

$$
v(0, t) = 3\mu G^{\theta\theta}e^{-3\mu G^{\theta\theta}t}a \tag{3.11}
$$

$$
v(\frac{\pi}{2}, t) = 3\mu G^{\theta\theta}e^{-3\mu G^{\theta\theta}t}b \tag{3.12}
$$

3.3   Test cases

The two previous sections have served to explain the numerical formulation and develop an analytical benchmark. One now has an embedding and a way to represent it as a level set field ϕ on an unstructured mesh. One also has the FE formulation needed to simulate the dynamics of the minimizing energy flow of the interface. However, the boundary energy $\gamma = G^{\theta\theta}g_{\theta\theta}$ is not readily computable on the finite element mesh since it does not explicitly depend on the normal to the interface. Using

$$
\begin{pmatrix} n^x \\ n^y \end{pmatrix} = -\frac{1}{\sqrt{g_{\theta\theta}}} \begin{pmatrix} b\cos\theta \\ a\sin\theta \end{pmatrix}
$$

and the embedding functions φ^x and φ^y, one may express,

$$
g_{\theta\theta} = \frac{\varphi^x \varphi^y}{n^x n^y}
$$

However, this definition is ill-defined given that in certain areas the components of n as well as the embedding functions may take null values. Numerically, this leads to very large calculation errors on the values of γ when dividing by very small values. As such, a much simpler method is to consider equation (3.5) such that

$$
\begin{aligned}
g_{\theta\theta} &= (b^2 \frac{a^2}{b^2} \sin^2\theta + b^2 \cos^2\theta) \\
&= b^2 (\frac{a^2}{b^2} \sin^2\theta + \cos^2\theta)
\end{aligned}
$$

which, if one considers $r = \dfrac{a}{b}$ which should remain constant throughout the simulation, then γ can easily be extended throughout the mesh using

$$
\frac{n^y}{n^x} = r\tan\theta
$$
$$
\theta = \arctan\left(\frac{1}{r}\frac{n^y}{n^x}\right)
$$

with

$$
\gamma(\theta) = b^2(r^2 \sin^2\theta + \cos^2\theta) \tag{3.13}
$$

Given the definition of the level set field, ϕ takes maximal values at the points within the ellipse furthest away from the interface, i.e. the center of the ellipse. Seeing as b is the smallest of both ellipse axes and the level set is minimal distance valued, the value of the level set at the center of the ellipsis should be the value of the small axis. Therefore

$$b = \max_{q \in M} \phi(q) \tag{3.14}$$

Also, implicit in the calculations in the previous section is the fact that

$$\frac{\partial^2 \gamma}{\partial \tilde{\nabla}_\alpha \phi \partial \tilde{\nabla}_\beta \phi} = 2\gamma m^{\alpha\beta} \tag{3.15}$$

so that knowing the extension of the boundary energy γ is sufficient for calculating $D^{\alpha\beta} = 3\gamma m^{\alpha\beta}$.

Simplification	Flat metric, Cartesian chart

$$D^{\alpha\beta} = 3\gamma \delta^{\alpha\beta}$$

Thus the boundary energy field γ can be computed at each iteration of the simulation. Using $\mu G^{\theta\theta} = 1$, the simulation can be run on any arbitrary mesh with arbitrary mesh size h using any time step Δt. All meshes used in this section were generated using Gmsh software [105].

Figure 3.3 illustrates the time evolution of the level set field for an isotropic unstructured 1×1 mesh with $h = 3e - 3$, $\Delta t = 5e - 4$, $a(t = 0) = 0.2$ and $r = 2$. A sensitivity analysis has been conducted with respect to the isotropic mesh size h and time step Δt whose results are reported in Figures 3.4, 3.5, 3.6 and 3.7. The data is evaluated by looking at the time evolution of both b and a as well as their time derivatives $V_b = \frac{db}{dt}$ and $V_a = \frac{da}{dt}$. The b value is evaluated using equation (3.14) while the a parameter is evaluated at each time step by

$$a = a(t = 0) + \phi(x = a(t = 0), y = 0) \tag{3.16}$$

The values are compared with their analytical analogs in order to compute errors. The convention in the legend is that bared quantities are measured while non-bared quantities are the analytical counterparts.

Each simulation can be given a scalar error value by computing the L^2 error between the analytical evolution of b and the measured values
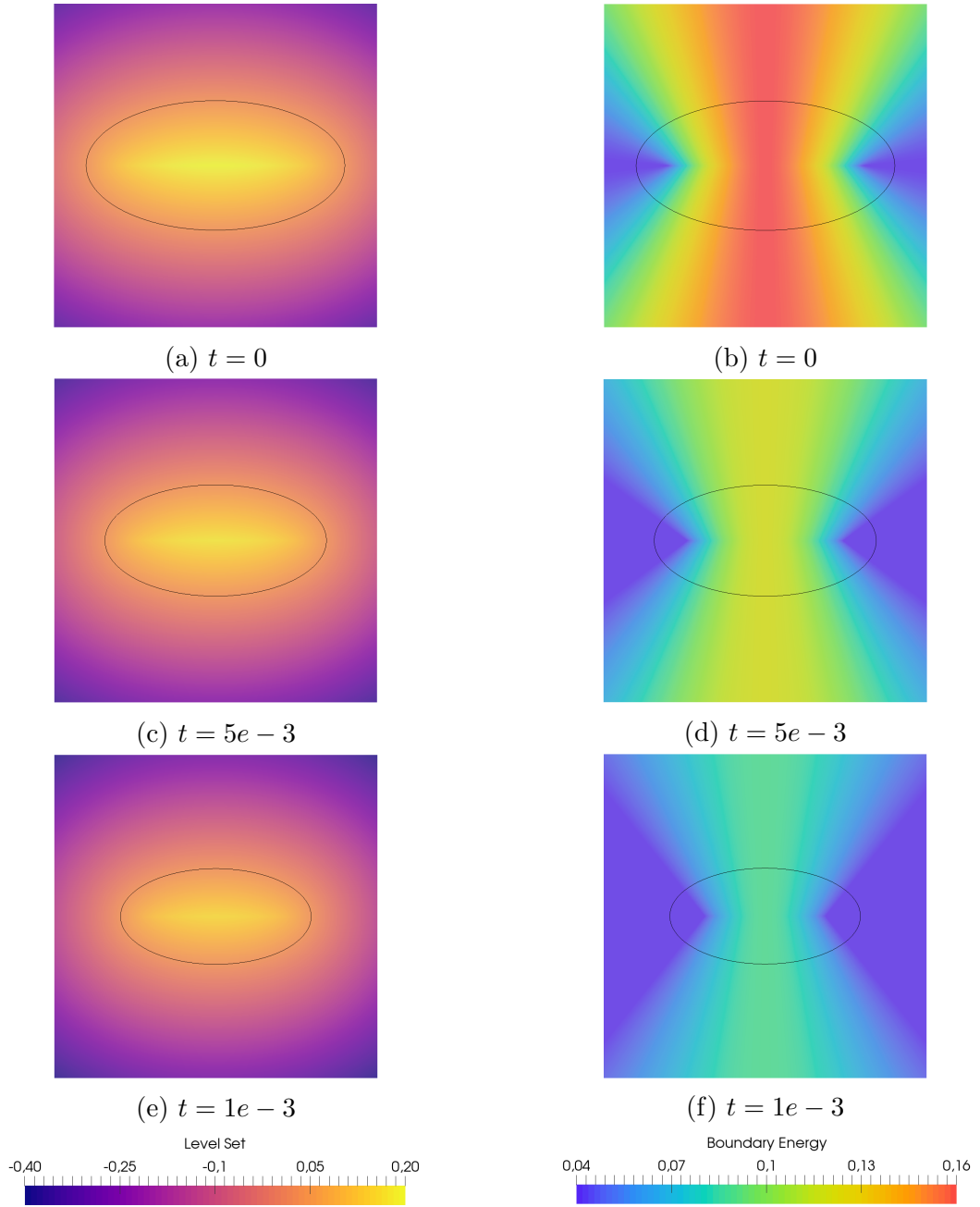
Figure 3.3: Time evolution of the level set ϕ and boundary energy γ fields for the ellipse shrinkage test case. The iso-zero value of the level-set field is in black. The mesh size is $h = 3e - 3$ and the time step is $\Delta t = 5e - 4$ and the ellipse axes ratio is $r = 2$.
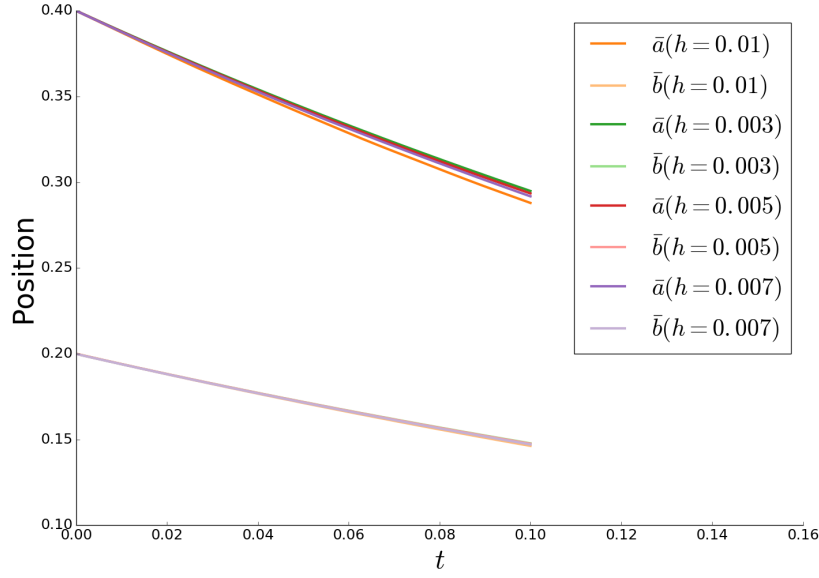
(a) Both a and b as a function of simulated time t
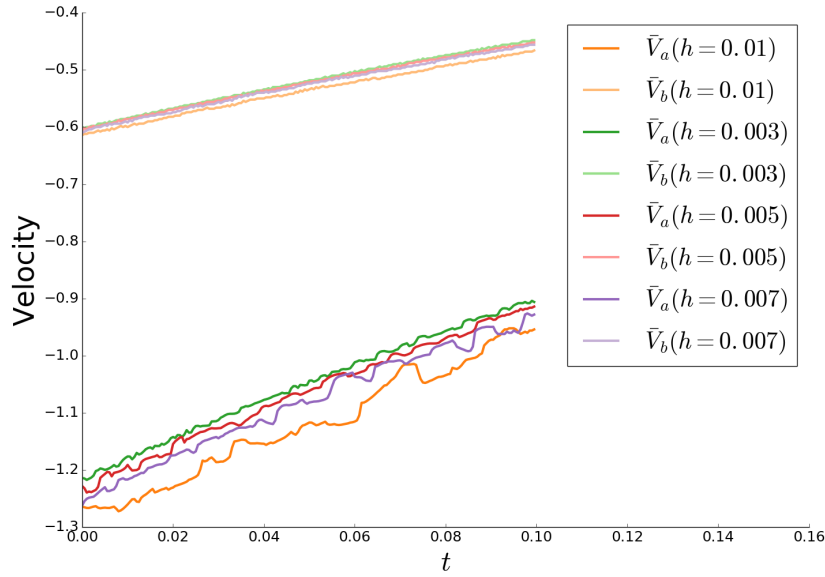
(b) Both V_a and V_b as a function of simulated time t

Figure 3.4: Sensitivity of the trajectory and velocity to the mesh size h parameter study with $\Delta t = 5e - 4$, $r = 2$ and $a(t = 0) = 0.4$ on a 1×1 size mesh.
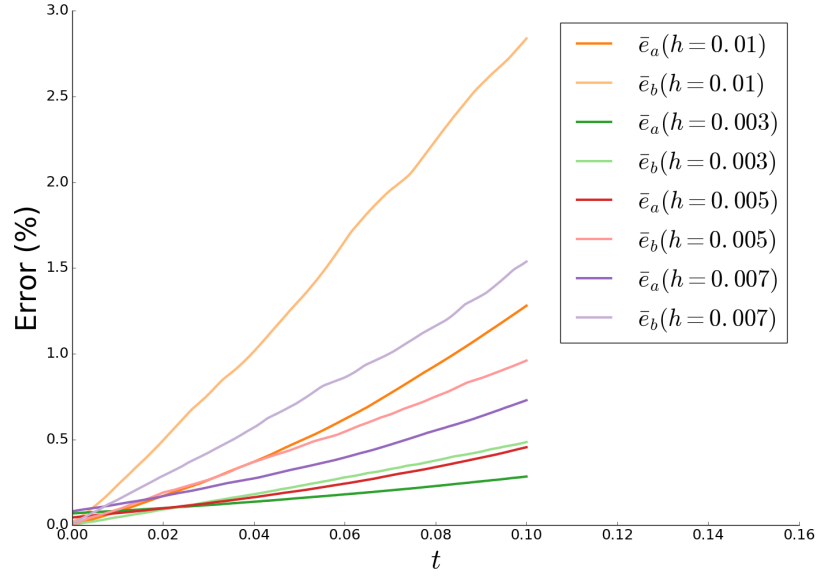
(a) Both e_a and e_b errors committed on the positions as a function of simulated time t
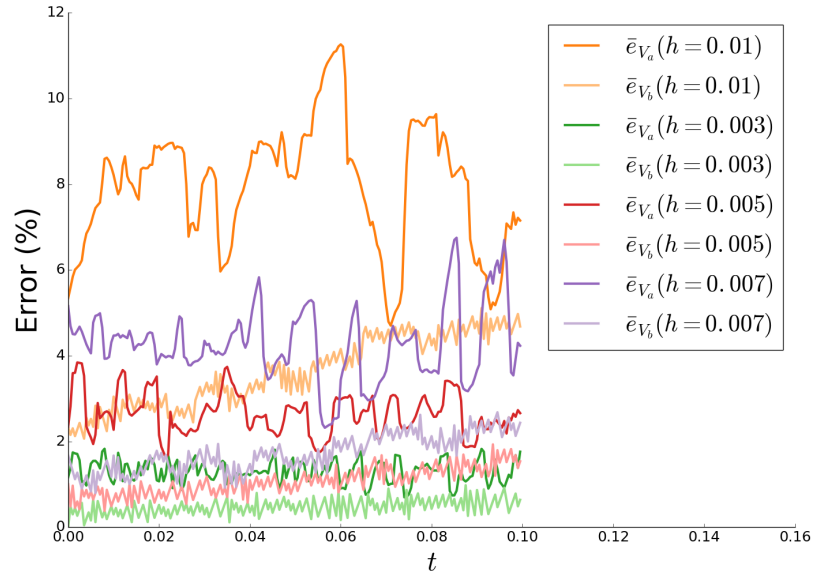
(b) Both e_{V_a} and e_{V_b} errors committed on the velocities as a function of simulated time t

Figure 3.5: Sensitivity of the errors to the mesh size h parameter study with $\Delta t = 5e - 4$, $r = 2$ and $a(t = 0) = 0.4$ on a 1×1 size mesh.
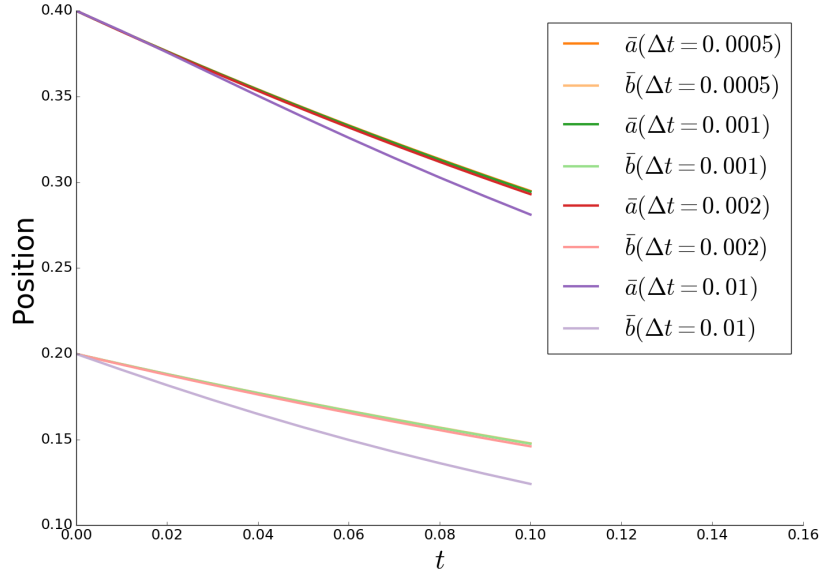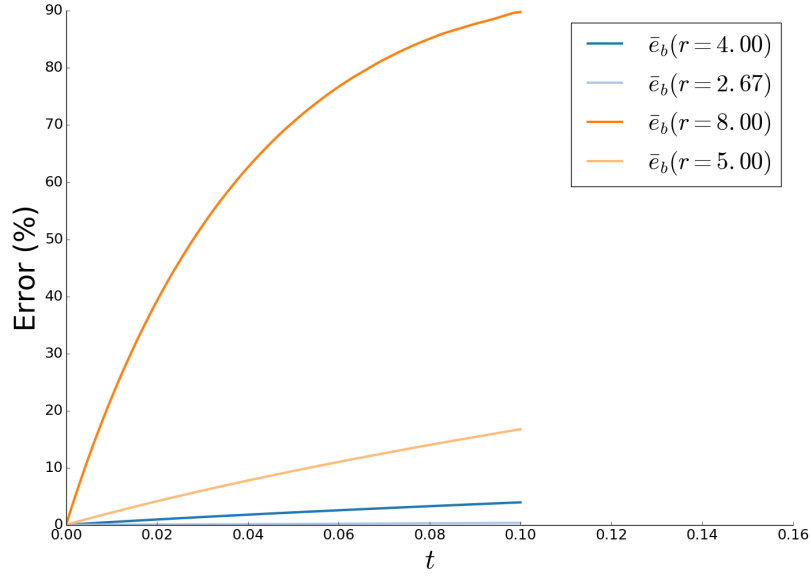
(a) Both a and b as a function of simulated time t
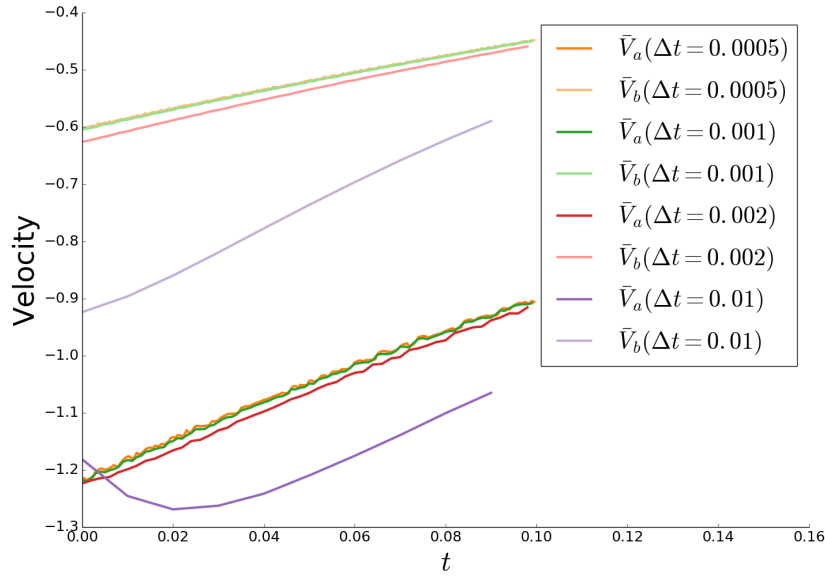
(b) Both V_a and V_b as a function of simulated time t

Figure 3.6: Sensitivity of the trajectory and velocity to the time step Δt parameter study with $h = 3e - 3$, $r = 2$ and $a(t = 0) = 0.4$ on a 1×1 size mesh.
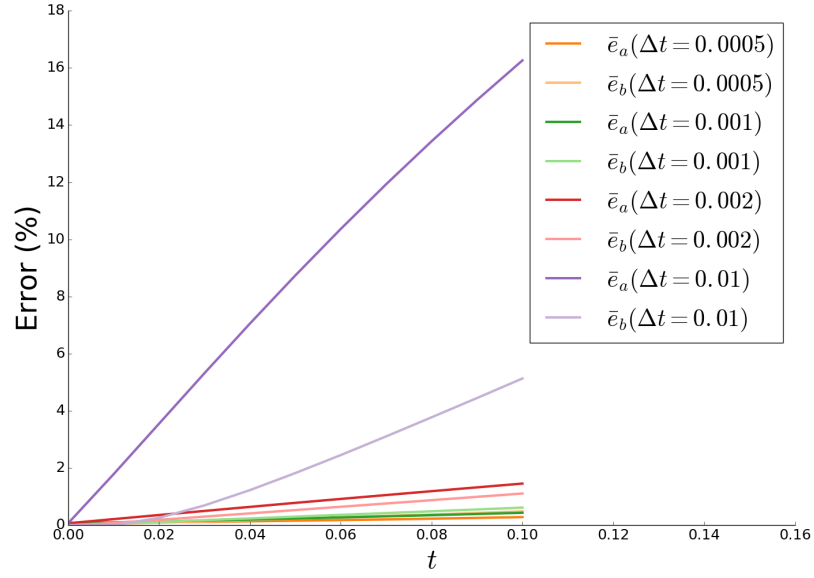
(a) Both e_a and e_b errors committed on the positions as a function of simulated time t
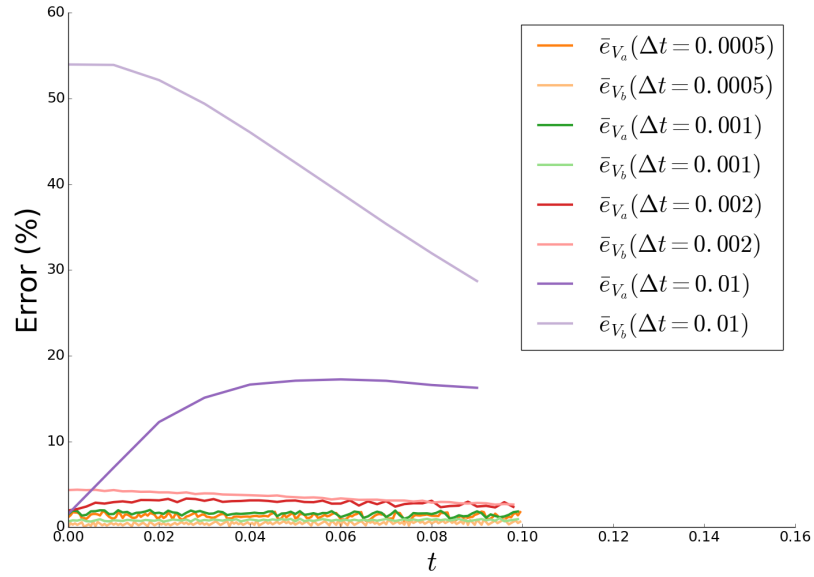
(b) Both e_{V_a} and e_{V_b} errors committed on the velocities as a function of simulated time t

Figure 3.7: Sensitivity of the errors to the time step Δt parameter study with $h = 3e - 3$, $r = 2$ and $a(t = 0) = 0.4$ on a 1×1 size mesh.

$$e_{L^2} = \int_0^{t_{end}} (b - \bar{b})^2 dt \qquad (3.17)$$

which can be approximated using a trapezoidal rule. Figure 3.8 depicts the evolution of the logarithm of this L^2 error with respect to both h and Δt.

Figures 3.4, 3.5, 3.6, 3.7 and 3.8 clearly establish convergence of the method towards the analytical solution as both the time step Δt and mesh size h become smaller. While it may seem that the simulation is actually less accurate in predicting the larger axis a, this can actually be attributed to the method of calculating $\bar{a}$ described in equation (3.16) which is much less precise than the measure of b.

For ellipses with ratio $r = 2$ one may expect the numerical formulation to give adequate approximations of the minimizing energy flow with a convergence rate of approximately 3 in space and 1.5 in time. However, one may remain dubious in terms of ellipses with even stronger axis ratios $r > 2$. Figures 3.9, 3.10 and 3.11 report some results that have been obtained for $r = \{\frac{8}{3}, 4, 5, 8\}$ using $h = 3e - 3$, $\Delta t = 5e - 4$, $a(t = 0) = 0.4$ and a 1×1 domain.

While, in a qualitative sense, in Figure 3.9 the simulations give sensible results. For the ratios tested here, the level set fields remain elliptical while shrinking. However, in a quantitative sense, in Figures 3.10 and 3.11 one may observe that the errors committed during the simulation increase with increasing ellipse ratio r. Indeed, the mesh size used for these simulation is not sufficient to accurately describe the curvatures of the ellipses in the highest ratio cases. These simulations prove that in order to describe strong geometrical features and their evolution accurately, the mesh size must be sufficiently refined. The results could be greatly improved by using adaptive remeshing algorithms throughout the simulations to capture the strongest features of the geometry. In any case, the numerical parameters $(h, \Delta t)$ must be adapted to the geometry of the problem in order to obtain sensible results.

Overall, the numerical formulation is adept at simulating the shrinking ellipse test case and converging towards the analytical solution when refining the discretization.

3.4 Comparison between the anisotropic and isotropic velocities

While no doubt relevant to the evaluation of the numerical formulation for the minimizing energy flow, the ellipse shrinkage case cannot truly distinguish between a velocity that does not include the anisotropic terms

$$D_{iso}^{\alpha\beta} = \gamma m^{\alpha\beta}$$
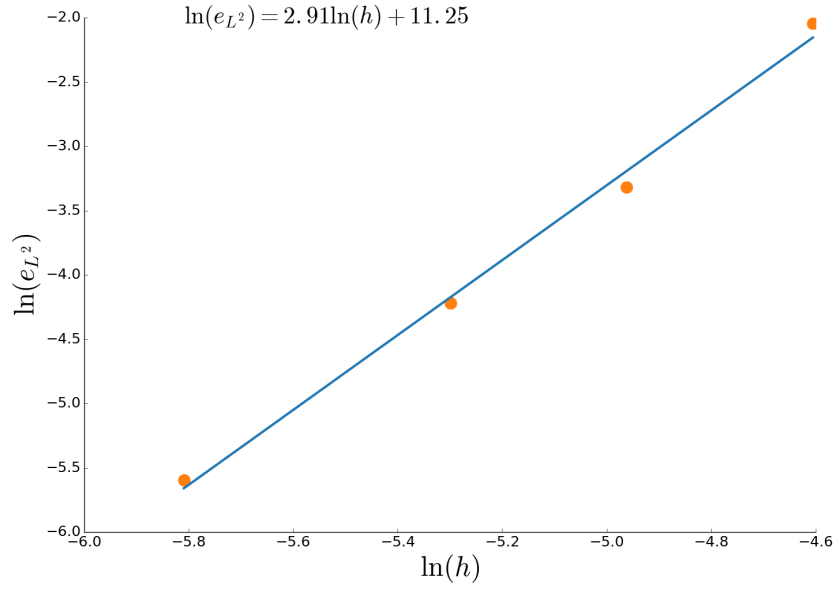
(a) $\ln(e_{L^2}) = f(\ln(h))$
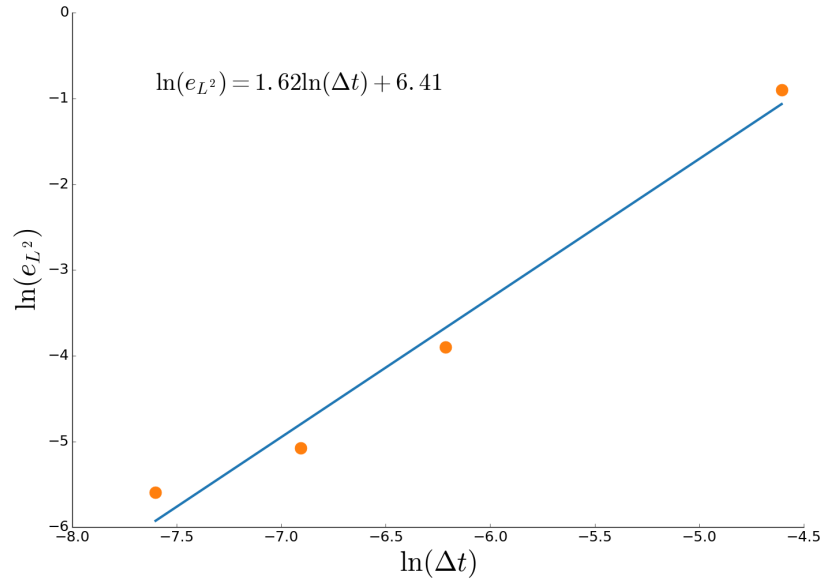
(b) $\ln(e_{L^2}) = f(\ln(\Delta t))$

Figure 3.8: Evolution of the $\ln(e_{L^2})$ as a function of h (for $\Delta t = 5e-4$) and Δt (for $h = 3e-3$) with $r = 2$, $a(t=0) = 0.4$ in a 1×1 domain.
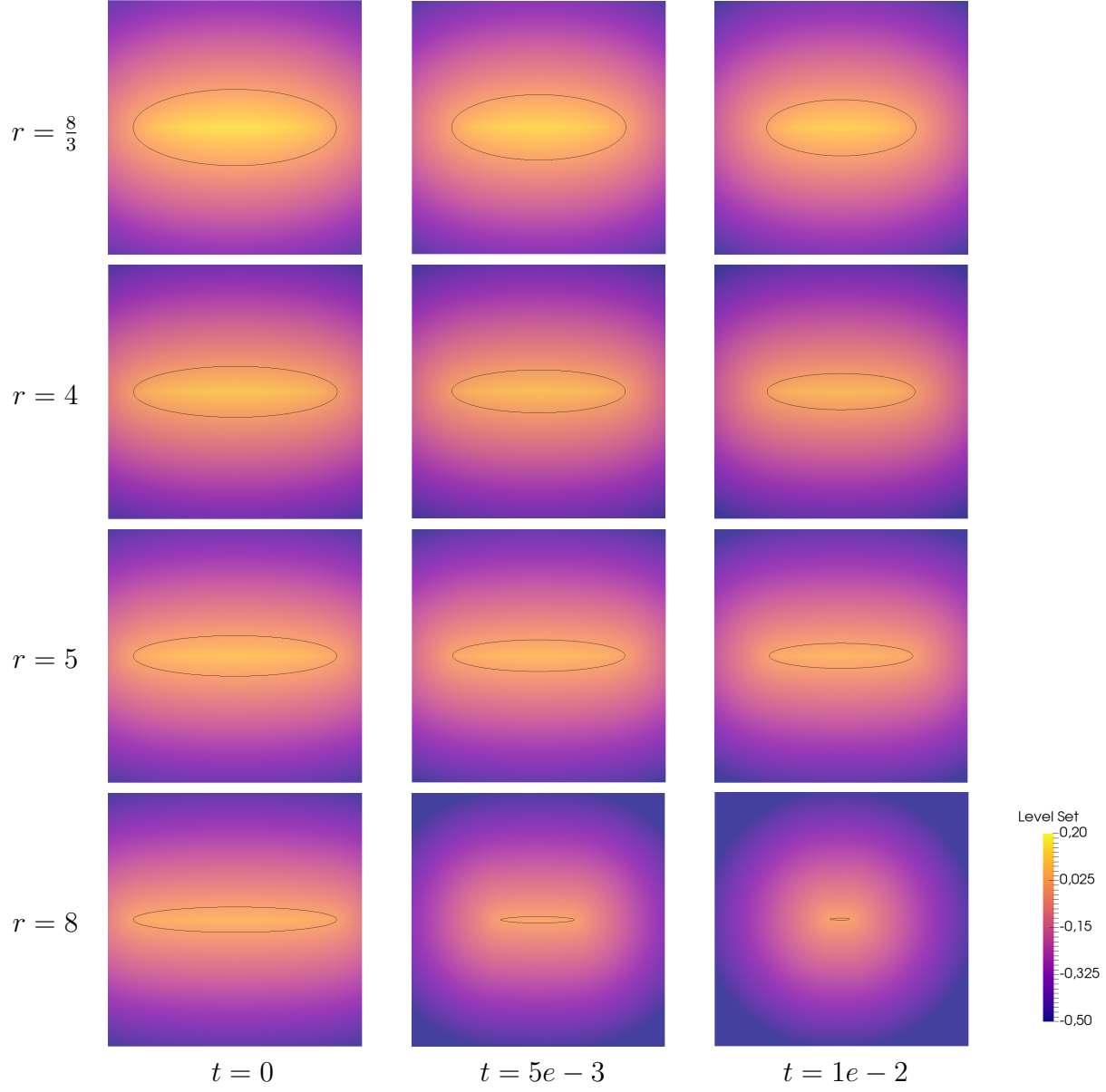
Figure 3.9: Time evolution of the level set ϕ for the ellipse shrinkage test case for different ellipse ratios. The iso-zero value of the level-set field is in black. The mesh size is $h = 3e-3$ and the time step is $\Delta t = 5e-4$.
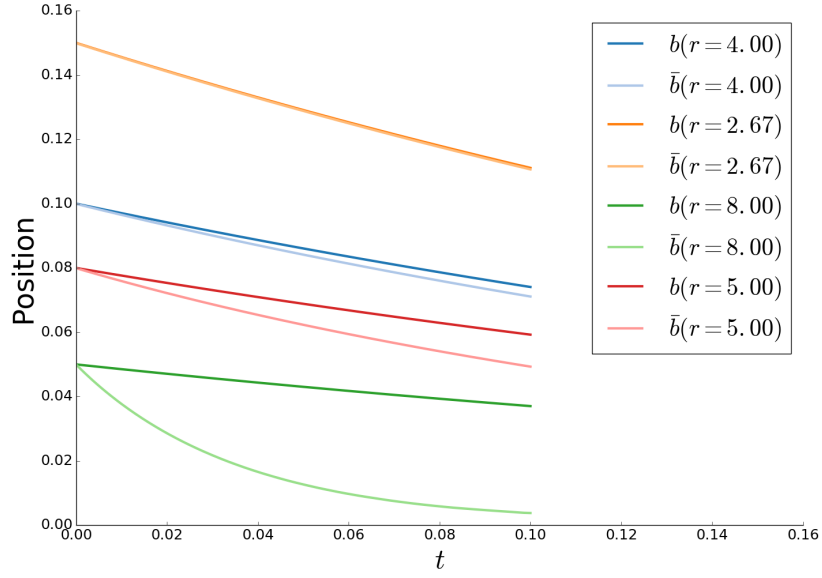
(a) b as a function of simulated time t
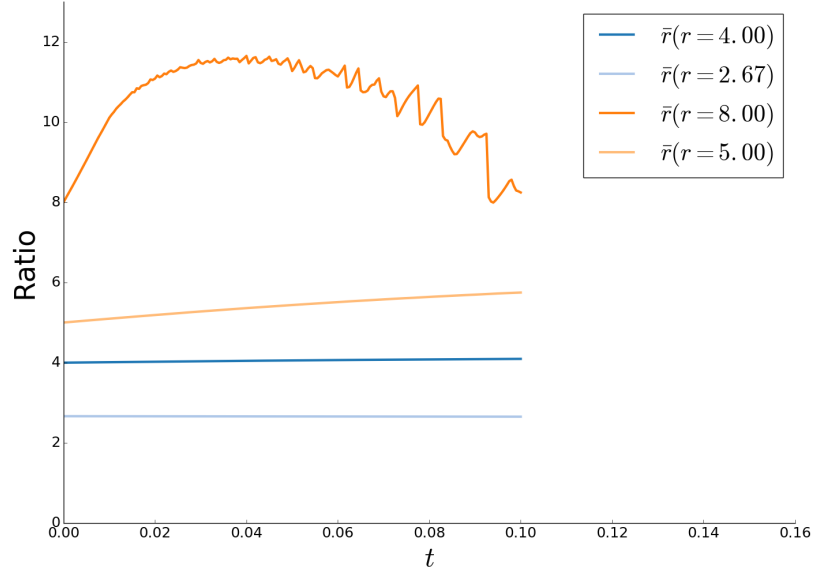
(b) r as a function of simulated time t

Figure 3.10: Sensitivity of the trajectory and measured ratio $\bar{r}$ to the initial ratio r parameter study with $h = 3e - 3$, $\Delta t = 5e - 4$, and $a(t = 0) = 0.4$ on a 1×1 size mesh.

(a) e_b errors committed on the positions as a function of simulated time t
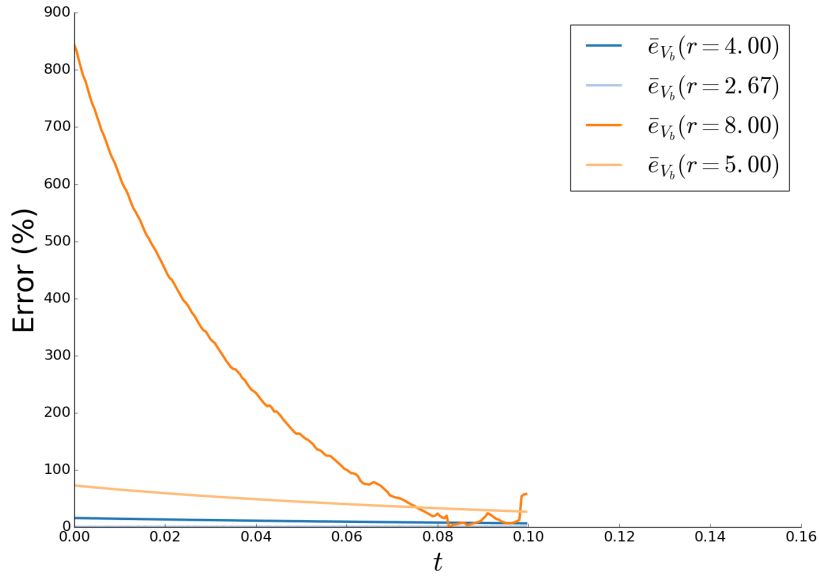
(b) e_{V_b} the errors committed on the velocities as a function of simulated time t

Figure 3.11: Sensitivity of the errors to the ellipse ratio r parameter study with $h = 3e-3$, $\Delta t = 5e-4$ and $a(t=0) = 0.4$ on a 1×1 size mesh.

and one that does

$$D_{aniso}^{\alpha\beta} = \gamma m^{\alpha\beta} + \frac{\partial^2 \gamma}{\partial \tilde{\nabla}_\alpha \phi \partial \tilde{\nabla}_\beta \phi}$$

even if one does compute a boundary energy density field that depends on the geometry $\gamma(\tilde{\nabla}\phi)$. This is because of equation (3.15) where, for the boundary energy used in the ellipse shrinkage, case $D_{aniso} = 3 D_{iso}$ which can be rectified in practice by a scaling of the mobility or of the time parameter. So, while the ellipse shrinkage case would differ by a factor of 3 in comparing the cases, the geometry of the interface flow would be the same.

As such, in order to observe the added benefits of including the anisotropic term to the formulation, one may study a test case where the analytical solution is unknown but the anisotropic term modifies the velocity differently then the isotropic term. One may then compare simulations where the D_{iso} is used to results where the D_{aniso} is employed for the same boundary energy density functions γ and the same initial geometries.

The most important aspect in the choice of the boundary energy density γ is the continued positive definiteness of the D_{aniso} tensor such that the problem is well posed. Indeed, D_{aniso}, as a sort of diffusion tensor, must be positive definite

$$D_{aniso}(\omega, \omega) > 0, \quad \forall \omega \in \Gamma(T^*\mathcal{M})|\omega \neq 0$$

Simplification	*One dimensional object*

Using the change of parameter $\cos \lambda = \tilde{\nabla}_x \phi$ one may express the derivatives

$$\frac{\partial \gamma}{\partial \tilde{\nabla}_\beta \phi} = \frac{\partial \gamma}{\partial \lambda} \frac{\partial \lambda}{\partial \tilde{\nabla}_\beta \phi}$$

$$\frac{\partial^2 \gamma}{\partial \tilde{\nabla}_\alpha \phi \partial \tilde{\nabla}_\beta \phi} = \frac{\partial^2 \gamma}{\partial \lambda^2} \frac{\partial \lambda}{\partial \tilde{\nabla}_\alpha \phi} \frac{\partial \lambda}{\partial \tilde{\nabla}_\beta \phi} + \frac{\partial \gamma}{\partial \lambda} \frac{\partial^2 \lambda}{\partial \tilde{\nabla}_\alpha \phi \partial \tilde{\nabla}_\beta \phi} \tag{3.18}$$

Such that

$$\left[\frac{\partial \lambda}{\partial \tilde{\nabla}_\alpha \phi}\right] = \begin{bmatrix} \dfrac{-1}{\sin \lambda} \\ \dfrac{1}{\cos \lambda} \end{bmatrix}$$

$$\left[\frac{\partial^2 \lambda}{\partial \tilde{\nabla}_\alpha \phi \partial \tilde{\nabla}_\beta \phi}\right] = \begin{bmatrix} \dfrac{-\cos \lambda}{\sin^3 \lambda} & \dfrac{1}{\sin^2 \lambda} \\ \dfrac{-1}{\cos^2 \lambda} & \dfrac{\sin \lambda}{\cos^3 \lambda} \end{bmatrix}$$

in 2D. Given that $D^{\alpha\beta}$ is always contracted on symmetric tensors, it too may be symmetrized such that one may write

$$\frac{1}{2}\left[\frac{\partial^2 \lambda}{\partial \tilde{\nabla}_\alpha \phi \partial \tilde{\nabla}_\beta \phi} + \frac{\partial^2 \lambda}{\partial \tilde{\nabla}_\beta \phi \partial \tilde{\nabla}_\alpha \phi}\right] = \begin{bmatrix} \dfrac{-\cos \lambda}{\sin^3 \lambda} & \dfrac{1}{2\sin^2 \lambda} - \dfrac{1}{2\cos^2 \lambda} \\ \dfrac{1}{2\sin^2 \lambda} - \dfrac{1}{2\cos^2 \lambda} & \dfrac{\sin \lambda}{\cos^3 \lambda} \end{bmatrix}$$

and the other component

$$\left[\frac{\partial \lambda}{\partial \tilde{\nabla}_\alpha \phi}\frac{\partial \lambda}{\partial \tilde{\nabla}_\beta \phi}\right] = \begin{bmatrix} \dfrac{1}{\sin^2 \lambda} & \dfrac{-1}{\sin \lambda \cos \lambda} \\ \dfrac{-1}{\sin \lambda \cos \lambda} & \dfrac{1}{\cos^2 \lambda} \end{bmatrix}$$

so that

$$[D^{\alpha\beta}_{aniso}] = \gamma \begin{bmatrix} 1 & 0 \\ 0 & 1 \end{bmatrix} + \frac{\partial^2 \gamma}{\partial \lambda^2} \begin{bmatrix} \dfrac{1}{\sin^2 \lambda} & \dfrac{-1}{\sin \lambda \cos \lambda} \\ \dfrac{-1}{\sin \lambda \cos \lambda} & \dfrac{1}{\cos^2 \lambda} \end{bmatrix} \tag{3.19}$$
$$+ \frac{\partial \gamma}{\partial \lambda} \begin{bmatrix} \dfrac{-\cos \lambda}{\sin^3 \lambda} & \dfrac{1}{2\sin^2 \lambda} - \dfrac{1}{2\cos^2 \lambda} \\ \dfrac{1}{2\sin^2 \lambda} - \dfrac{1}{2\cos^2 \lambda} & \dfrac{\sin \lambda}{\cos^3 \lambda} \end{bmatrix}$$

Acceptable grain boundary energy density functions respect the positive definiteness of D_{aniso}. For any $\omega \in \Gamma(T^*\mathcal{M})$,

$$D_{aniso}(\omega, \omega) = \gamma(\omega_x^2 + \omega_y^2) + \frac{\partial^2 \gamma}{\partial \lambda^2}\left(\frac{\omega_x^2}{\sin^2 \lambda} - 2\frac{\omega_x \omega_y}{\sin \lambda \cos \lambda} + \frac{\omega_y^2}{\cos^2 \lambda}\right)$$

$$+ \frac{\partial \gamma}{\partial \lambda}\left(\frac{\omega_y^2 \sin \lambda}{\cos^3 \lambda} - \frac{\omega_x^2 \cos \lambda}{\sin^3 \lambda} + \omega_x \omega_y \left(\frac{1}{\sin^2 \lambda} - \frac{1}{\cos^2 \lambda}\right)\right) > 0$$

$$\omega_x^2\left(\gamma - \frac{\cos \lambda}{\sin^3 \lambda}\frac{\partial \gamma}{\partial \lambda} + \frac{1}{\sin^2 \lambda}\frac{\partial^2 \gamma}{\partial \lambda^2}\right) + \omega_y^2\left(\gamma + \frac{\sin \lambda}{\cos^3 \lambda}\frac{\partial \gamma}{\partial \lambda} + \frac{1}{\cos^2 \lambda}\frac{\partial^2 \gamma}{\partial \lambda^2}\right)$$

$$+ \omega_x \omega_y \left(\left(\frac{1}{\sin^2 \lambda} - \frac{1}{\cos^2 \lambda}\right)\frac{\partial \gamma}{\partial \lambda} - \frac{2}{\sin \lambda \cos \lambda}\frac{\partial^2 \gamma}{\partial \lambda^2}\right) > 0$$

which, given the arbitrariness of ω

$$D_{aniso}^{xx} = \gamma - \frac{1}{\sin^2 \lambda \tan \lambda}\frac{\partial \gamma}{\partial \lambda} + \frac{1}{\sin^2 \lambda}\frac{\partial^2 \gamma}{\partial \lambda^2} > 0 \qquad (3.20)$$

$$D_{aniso}^{yy} = \gamma + \frac{\tan \lambda}{\cos^2 \lambda}\frac{\partial \gamma}{\partial \lambda} + \frac{1}{\cos^2 \lambda}\frac{\partial^2 \gamma}{\partial \lambda^2} > 0 \qquad (3.21)$$

and using

$$2D_{aniso}^{xy} = \left(\frac{1}{\sin^2 \lambda} - \frac{1}{\cos^2 \lambda}\right)\frac{\partial \gamma}{\partial \lambda} - \frac{2}{\sin \lambda \cos \lambda}\frac{\partial^2 \gamma}{\partial \lambda^2}$$

one may show

$$2|D_{aniso}^{xy}| < \min_{(\omega_x, \omega_y)}\left|\frac{D_{aniso}^{xx}\omega_x^2 + D_{aniso}^{yy}\omega_y^2}{\omega_x \omega_y}\right|$$

which admits a unique minimum

$$|D_{aniso}^{xy}| < \sqrt{D_{aniso}^{xx} D_{aniso}^{yy}} \qquad (3.22)$$

Thus, any boundary energy density function γ must satisfy the conditions (3.20), (3.21) and (3.22). If it does not, the problem becomes ill-posed and the solutions are not unique. However, these conditions do not amount to a prescription for the choosing of the grain boundary energy density. A host functions are viable candidates. While delimiting the space of possible functions is a worthwhile endeavor, it is not the goal of this work in particular. As such, in what follows, one particular density that respects these conditions will be constructed and its effect on the direct embedding of the circle will be studied.

Considering

$$\gamma(\lambda) = 1 + \varepsilon(\cos(6\lambda) - 9\cos(2\lambda)) \tag{3.23}$$

where $\varepsilon \in \mathbb{R}^+$. The derivatives can then be expressed

$$\frac{\partial \gamma}{\partial \lambda} = 192\varepsilon \sin^3 \lambda \cos^3 \lambda \tag{3.24}$$

$$\frac{\partial^2 \gamma}{\partial \lambda^2} = 576\varepsilon \sin^2 \lambda \cos^2 \lambda(\cos^2 \lambda - \sin^2 \lambda) \tag{3.25}$$

thus generating

$$\begin{aligned}
D^{xx}_{aniso} &= 1 + \varepsilon(\cos(6\lambda) - 9\cos(2\lambda)) + 192\varepsilon \cos^4 \lambda + 576\varepsilon \cos^2 \lambda(\cos^2 \lambda - \sin^2 \lambda) \\
&= 1 + \varepsilon(375\cos(2\lambda) + 168\cos(4\lambda) + \cos(6\lambda) + 216) \\
D^{yy}_{aniso} &= 1 + \varepsilon(\cos(6\lambda) - 9\cos(2\lambda)) + 192\varepsilon \sin^4 \lambda + 576\varepsilon \sin^2 \lambda(\cos^2 \lambda - \sin^2 \lambda) \\
&= 1 + \varepsilon(183\cos(2\lambda) - 120\cos(4\lambda) + \cos(6\lambda) - 72) \\
D^{xy}_{aniso} &= 96\varepsilon(\sin \lambda \cos^3 \lambda - \sin^3 \lambda \cos \lambda) - 576\varepsilon \sin \lambda \cos \lambda(\cos^2 \lambda - \sin^2 \lambda) \\
&= -120\varepsilon \sin(4\lambda)
\end{aligned}$$

so that

$$[D^{\alpha\beta}_{aniso}] = \begin{bmatrix} 1 & 0 \\ 0 & 1 \end{bmatrix} + \varepsilon \begin{bmatrix} \begin{array}{c} 375\cos(2\lambda) + 168\cos(4\lambda) \\ + \cos(6\lambda) + 216 \end{array} & -120\sin(4\lambda) \\ -120\sin(4\lambda) & \begin{array}{c} 183\cos(2\lambda) - 120\cos(4\lambda) \\ + \cos(6\lambda) - 72 \end{array} \end{bmatrix} \tag{3.26}$$

Now, in order to fulfill the conditions in equations (3.20), (3.21) and (3.22) as well as the positivity $\gamma > 0$, one may express these conditions as acting on ε. Using that $\forall x \in \mathbb{R}$ both $\cos(x)$ and $\sin(x)$ are bounded by -1 and 1

$$D^{xx}_{aniso} > 1 + \varepsilon(-375 - 168 - 1 + 216) > 0$$
$$\varepsilon < \frac{1}{328}$$
$$D^{yy}_{aniso} > 1 + \varepsilon(-183 - 120 - 1 - 72) > 0$$
$$\varepsilon < \frac{1}{376}$$
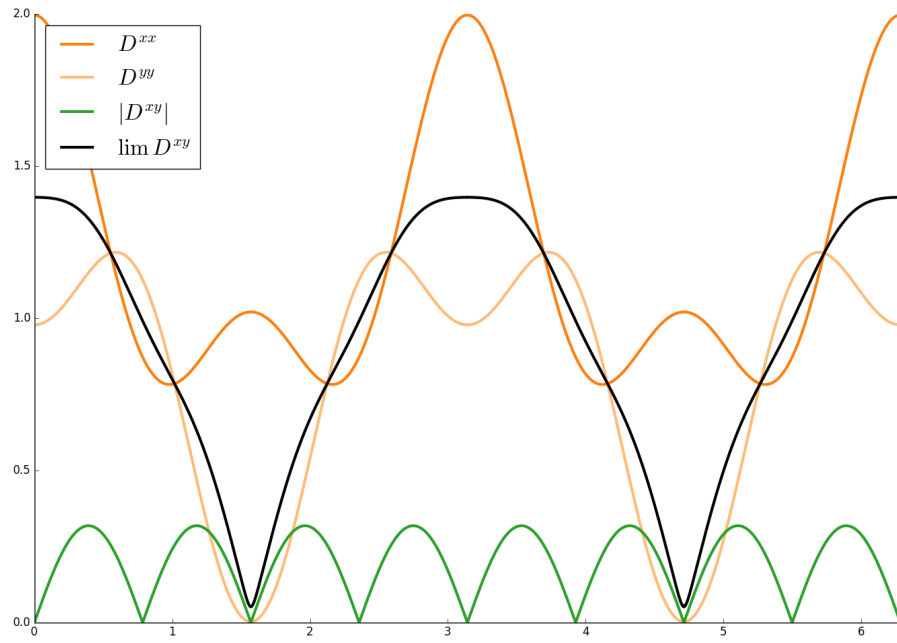
Figure 3.12: Components D_{aniso}^{xx}, D_{aniso}^{yy} and D_{aniso}^{xy} as a function of $\lambda \in [0, 2\pi]$. The limit expressed in the inequality (3.22) is also shown for comparison as $\lim D^{xy}$.
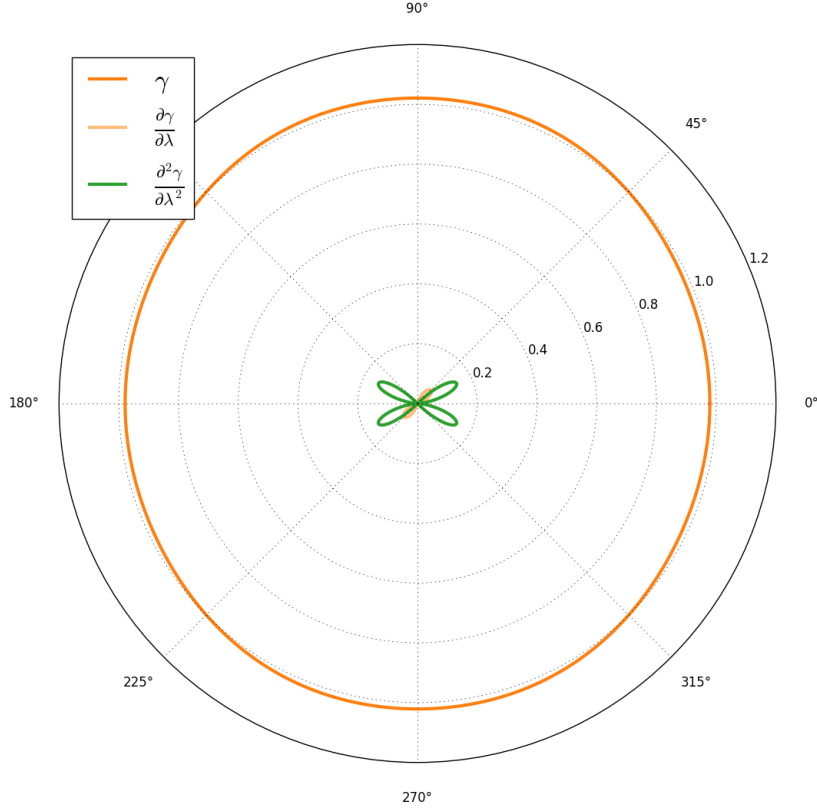
Figure 3.13: Wulff plot, $(r, \theta) = (\gamma, \lambda)$, for the grain boundary energy density γ and its derivatives.

which is actually the best possible majoration of ε since for $\lambda = \frac{\pi}{2}$ one has that $\cos(2\lambda) = \cos(6\lambda) = -\cos(4\lambda) = -1$ which is the actual minimum of D_{aniso}^{yy}.

Choosing $\varepsilon = \frac{1}{377}$, Figure 3.12 illustrates the components of the D_{aniso} tensor as a function of λ. Graphically, D_{aniso}^{xy} is strictly inferior to the required limit.

Figure 3.13 shows a polar plot of the boundary energy density $\gamma(\lambda)$ as well as its derivatives. Indeed, in this case, the variations of the boundary energy density are constrained to be rather small. However, even these relatively small variations can induce relatively large second derivative terms. The proposed γ function meets all the criteria for the positive definiteness of D_{aniso}.

Having the grain boundary energy function γ and thus being able to calculate D_{aniso}, we will consider once again the circle $\mathcal{C} = ([0; 2\pi], \mathcal{O}_C, \mathcal{A}_C)$ and the Riemannian manifold $\mathcal{M} = (\mathbb{R}^2, \mathcal{O}_{std}, \mathcal{A}_{std}, m)$. However, the initial embedding φ is more direct

$$\varphi : [0; 2\pi] \longrightarrow \mathbb{R}^2$$
$$\theta \mapsto (R\cos\theta, R\sin\theta)$$

where $R \in \mathbb{R}^+/\{0\}$ is the radius of the embedded circle. The initial conditions for both the level set field and the grain boundary energy field as well as its derivatives are represented in Figure 3.14 for $R = 0.4$.

The test case was run for both D_{iso} and D_{aniso} on a 1×1 size isotropic mesh with $h = 3e - 3$ and $\Delta t = 5e - 4$. The results of the form evolution of the circle as well as the evolution of the grain boundary energy field are presented in Figure 3.15. The D_{iso} and D_{aniso} tensors generate very different boundary flows. While the D_{iso} case tends to remain circular until disappearing, the D_{aniso} case takes on a very distinctive form. The persistence of circularity of the D_{iso} case is most likely due to the very small variations in the boundary energy of the order of only 3%.

However, the most efficient of the two simulations in terms of energy dissipation is thus the closer to reality since the principle of minimal action is in effect. Thus, the parameter of most relevance to comparing the two simulations is the energy efficiency of the geometry obtained in each step of the simulation, defined here as

$$\Lambda = \left(\frac{\int_C \gamma dC}{\int_C dC} \right)^{-1}. \tag{3.27}$$

with respect to the smooth manifold $\mathcal{C}$.

Figure 3.16 shows the evolution of the computed energy efficiency Λ for both simulations. Clearly, the energy efficiency of the form developed by the D_{aniso} flow is better than that of the D_{iso} flow from the start of the simulation to the disappearance of the boundary. While not being a direct proof of the validity of the D_{aniso} formulation, these test cases show that the full D_{aniso} formulation is definitely more adept then the D_{iso} formulation for the minimizing energy flow problem.

In conclusion, two test cases have been studied in this chapter. The ellipse shrinkage study shows that the formulation is capable of accurately converging towards the minimal boundary energy flow. The more arbitrary boundary energy density shows that the additional torque term can have a large impact on the dynamics of the interface even when the anisotropy is relatively small. The constraints on the γ function for the well-posedness of the problem were derived in a practical setting. No other benchmarks, to the author's knowledge, exist in the state of the art to test minimal energy interfacial flows in an anisotropic setting.

(a) γ

(b) D_{aniso}^{xx}

(c) $\frac{\partial \gamma}{\partial \lambda}$

(d) D_{aniso}^{yy}

(e) $\frac{\partial^2 \gamma}{\partial \lambda^2}$

(f) D_{aniso}^{xy}

(g) ϕ
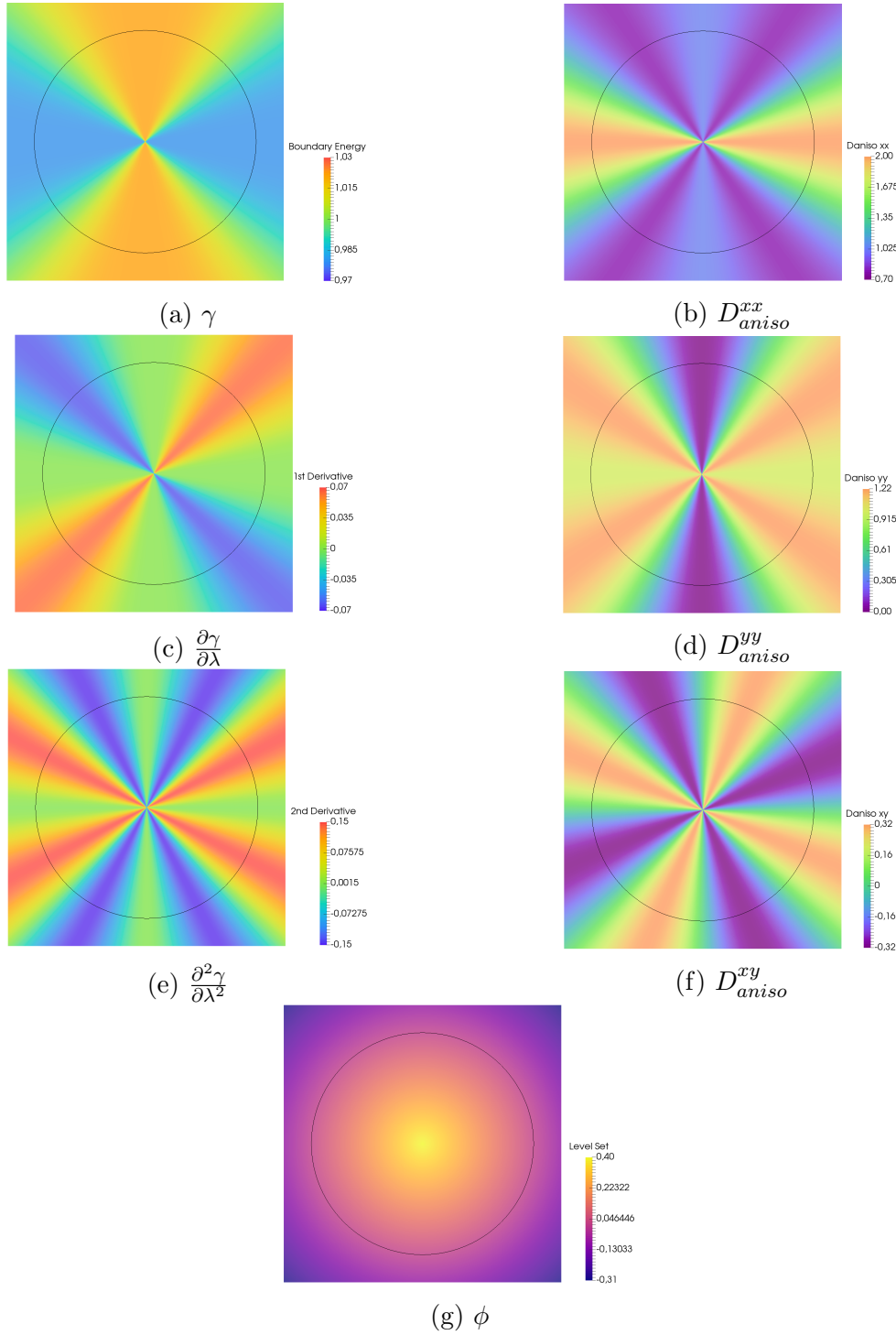
Figure 3.14: Initial values of the level set field ϕ, boundary energy field γ, its derivatives and the components of D_{aniso}. The iso-zero value of the level set is in black.
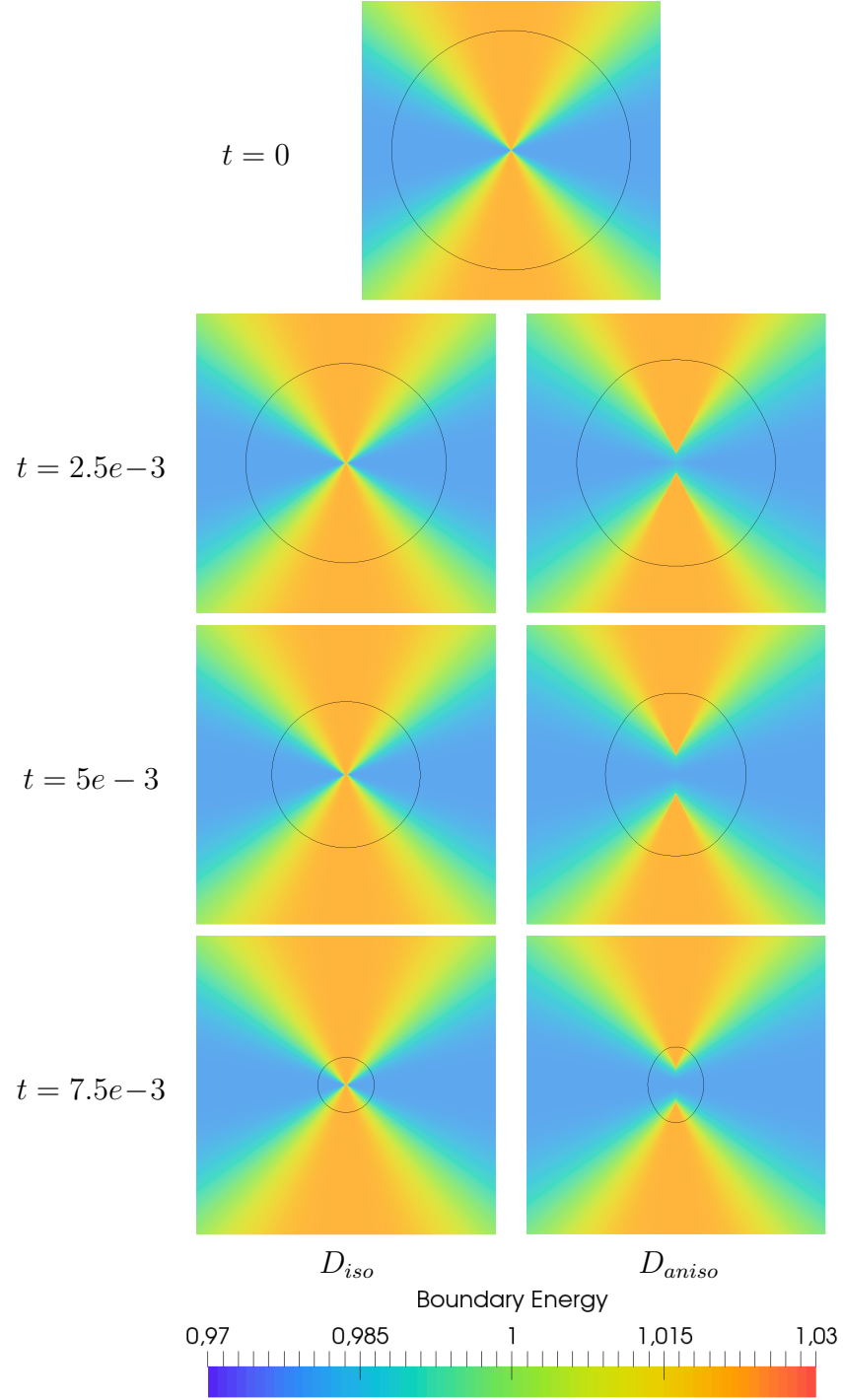
Figure 3.15: Time evolution of the grain boundary energy field γ and the iso-zero value of the level set for the circle shrinkage test case run with D_{iso} and D_{aniso}. The iso-zero value of the level-set field is in black. The mesh size is $h = 3e - 3$ and the time step is $\Delta t = 5e - 4$.
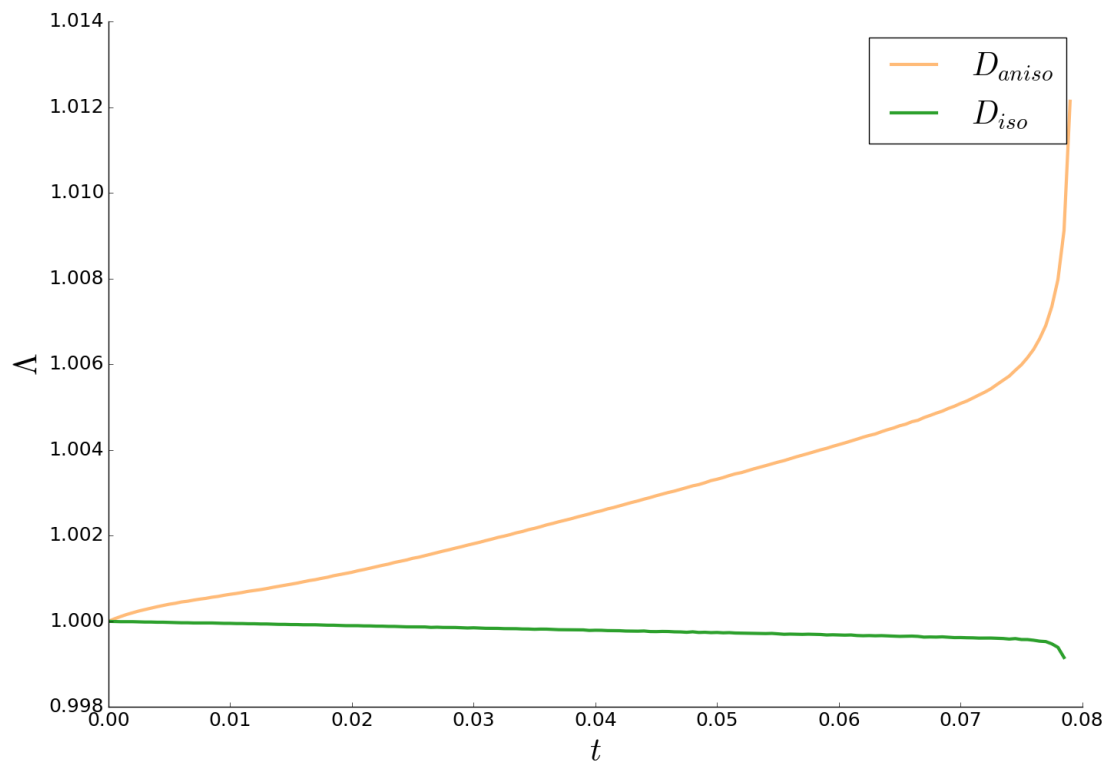
Figure 3.16: Computed energy efficiency Λ as a function of time t for circle shrinkage test cases run with D_{iso} and D_{aniso}.

Résumé en Français du Chapitre 3

Ce chapitre a pour but de tester les équations développées dans le chapitre précédent en utilisant des cas idéalisés. Dans un premier temps, l'implémentation numérique de type éléments finis pour le transport des champ level set est décrite. Puis, un nouveau cas analytique anisotrope, concernant le rétrécissement d'une ellipse, est explicité. La convergence numérique de l'algorithme est démontrée à travers une campagne de simulations faisant varier la discrétisation spatiale et temporelle aussi bien que quelques paramètres géométriques du système. Enfin, le formalisme est testé sur un cas non-analytique où la comparaison des résultats issus de simulations utilisant le champ de vitesse dit "classique" et le nouveau illustre clairement la supériorité de ce dernier. On considerera comme résultat phare de ce chapitre les équations (3.20), (3.21) et (3.22) qui imposent des conditions claires et calculables sur l'anisotropie acceptable de l'énergie de joints de grains.

Chapter 4

Multiple Junctions

The previous chapters have been devoted to developing the mathematical and numerical framework needed to model a single interface. The monophase metallic material's microstructure is composed of a great number of interfaces, or grain boundaries, that are connected between each other. In the following, this gap we attempt to be bridged using level set techniques. The main difficulty confronted in this work is attempting to model the grain boundary network as a sum of grain boundaries. Indeed, the junctions at which these boundaries meet in the polycrystal break the classic topology of the interfaces and therefore the differential structure. Techniques to circumvent this issue are developed and tested. Also, the crystallography of the material, through the orientations of the grains, is introduced. This enrichment of the description of the polycrystal comes with the development of supplemental numerical choices as well as procedures for evaluating the dynamics of the grains.

4.1 Statics of the polycrystal

Let Ω be a Riemannian d-manifold with metric ω and the entire polycrystal domain. This enclosing manifold can be partitioned into N mutually disjoint sub-manifolds $\{G_i, i \in \{1, \ldots, N\}\}$ called grains

$$\Omega = \bigcup_i G_i \tag{4.1}$$

$$G_i \cap G_j = \emptyset, \quad i \neq j \tag{4.2}$$

where the underlying sets of each G_i are open in Ω. Thus, using the topological closure of the grains $\bar{G}_i$ one can give a precise definition of the grain boundary network Γ as a topological space

$$\Gamma = \bigcap_i \bar{G}_i \tag{4.3}$$

However, Γ is not a topological manifold since the multiple junctions where more than three grains meet can not be given a locally Euclidean topology. Failing to be a topological manifold, there is no way to define a differentiable structure and thus make it into a smooth manifold. As such, in order to continue to use level set models for the interfaces, each interface

$$S_i = \bar{G}_i / G_i, \tag{4.4}$$

which inherits its topology from Ω, must be modeled individually. However, in order to attribute a differentiable structure to the interfaces in a strong sense, the "corners" of the interface generated by the multiple junctions must be smoothed. Defining any one parameter smoothing operation η_ε, $\varepsilon \in \mathbb{R}^+$ such that

$$\lim_{\varepsilon \to 0} \eta_\varepsilon(S_i) = S_i$$

one may define the level set field ϕ_i describing the grain G_i as

$$\phi_i(X \in \Omega) = \pm d(X, \eta_\varepsilon(S_i)) \tag{4.5}$$

with the sign convention that $\phi_i(X) > 0$ when $X \in G_i$. In practice, the smoothing operation η_ϵ is implicitly performed when defining the level set field on the FE mesh where the smoothing parameter ε is related to the mesh size. Figure 4.1 summarizes the description and subsequent approximations of the polycrystal.

However, if one was to implement this description directly on microstructures with a large number of grains, there would be N level set fields. This is highly inefficient when considering that the dynamics of each level set field are solved separately. As such, using coloring techniques from graph theory, multiple non-neighboring grains G_j are heaped into one level set field ϕ_i using the developments described in [7, 106] such that

$$\phi_i : \Omega \longrightarrow \mathbb{R}$$
$$\phi_i(X) = \pm \min_{j \in \mathcal{G}_i} d(X, G_j)$$

where $\mathcal{G}_i$ is a set containing the indexes of the grains modeled by the ith level set field. One may define $\Phi = \{\phi_i, i = 0, \dots, M\}$, where M is the number of level set fields, as the set containing all the level sets.
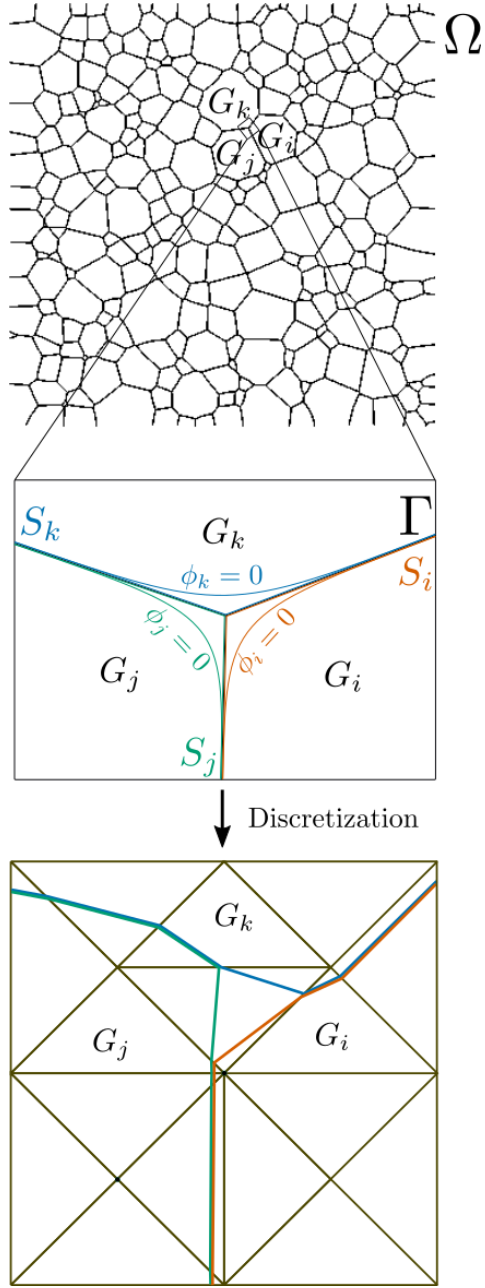
Figure 4.1: Illustration of the mathematical description of the polycrystal, the approximations applied to generate a smooth level set description and the numerical adaptation on a FE mesh.

The crystallographic orientations $\{O_i\}$ of the grains $\{G_i\}$ are then modeled by a unit quaternion field $q(X)$ such that, using the characteristic functions of the grains χ_i

$$\chi_i(X) = \begin{cases} 1 & X \in G_i \\ 0 & X \notin G_i \end{cases}$$

one may define,

$$q(X) = \sum_{i=1,\dots,N} W(O_i)\chi_i(X) \tag{4.6}$$

where W takes crystallographic orientations to their unit quaternion representatives. On a finite element mesh, the quaternion field is defined on the nodes of the mesh. As such, the misorientation between two grains G_i and G_j with unit quaternion orientations q_i and q_j respectively may be simply expressed as the unit quaternion m_{ij}

$$m_{ij} = \underset{\substack{\min \\ s,q}}{(s_s q_i)^{-1} q_j s_q}{}_{\theta(s_s q_i, s_j q_j)} \tag{4.7}$$

where the s_k are the unit quaternion representatives of the symmetry group of the crystal, $\theta(\cdot, \cdot)$ is a function that calculates the disorientation angle between two quaternions and the classical Hamiltonian quaternion algebra $\mathbb{H}$ is used. However, in order to define a misorientation field on the discretized finite element mesh one must use the misorientation equation locally at each cell. As such, we define the misorientation field m_e as a P0 (constant per element/cell) field as

$$m_e = \underset{\substack{\max \\ i,j}}{\underset{\substack{\min \\ s,q}}{(s_s q(X_i))^{-1} q(X_j) s_q}}{}_{\theta(s_s q(X_i), s_j q(X_j))} \tag{4.8}$$

where X_k are the nodes that constitute the element e. Figure 4.2 illustrates the configuration on a FE mesh.

With this definition of misorientation, an element traversed by two iso-zero level sets will have a non-null misorientation which will be the value of the misorientation in between the neighboring grains. However, in elements traversed by three or more iso-zero level set values, the misorientation is ill-defined. As such, the discrete equation (4.8) calculates all the possible misorientations between neighboring grains and attributes the one with the highest disorientation value to the element. Thus, all elements traversed by grain boundaries have non-null misorientations, while the elements completely enclosed in the grains have null misorientations.
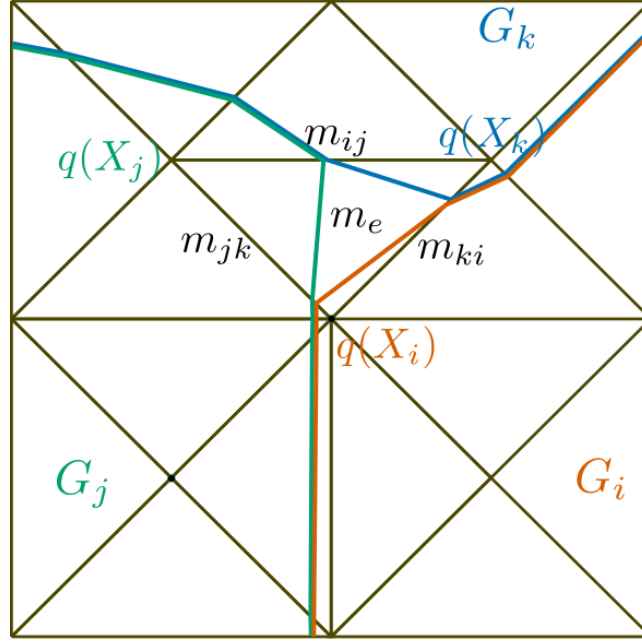
Figure 4.2: Illustration of the misorientation m_e and orientation fields q on a finite element mesh.

A P0 unitary normal vector field to the boundary is quite readily available from the gradient of the level set fields $n^\alpha = \sum_i \chi_i \omega^{\alpha\beta} \tilde{\nabla}_\beta \phi_i$ which can then be expressed in any crystallographic frame. Thus, the grain boundary character $b(X) = (m(X), n(X))$ can be computed in any element traversed by a grain boundary. As such, a grain boundary energy density $\gamma(b(X))$ can also be calculated for any cell crossed by a boundary and thus generate a grain boundary energy field $\gamma(X)$. However, this grain boundary energy field is highly discontinuous seeing that it is a field that is constant per element and only takes non-null values at elements traversed by boundaries. This field must be extended to the entire manifold Ω for the finite element calculation.

The proposed extension algorithm is reported in Algorithm 3 and [94]. The algorithm iterates over the nodes of the mesh attributing maximal values of the energy to nodes that neighbor grain boundaries. The result is a P1 γ field with adequate values of grain boundary energy interpolated at the boundaries and mostly null elsewhere. By solving a Laplace equation for the new boundary energy field γ, conserving the calculated values at the boundaries, one extends the field to all of Ω without modifying the values at the boundaries. As such, the new $\gamma(X)$ field is a P1 field with non-null values everywhere with adequate regularity properties.

Figure 4.3 illustrates the entire process from orientation field to extended grain boundary energy visually.

As such, the polycrystal in Ω is characterized by a tuple (Φ, q) representing the geom-
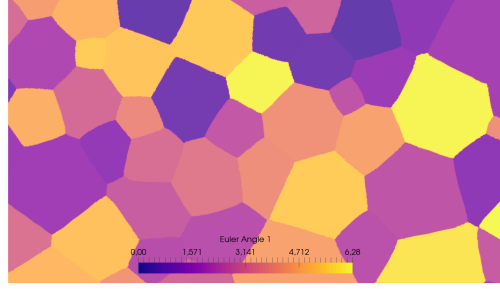
$$q \to (m, n)$$
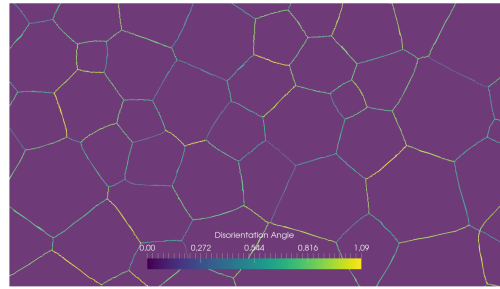
$$(m, n) \to \gamma_{P0}$$
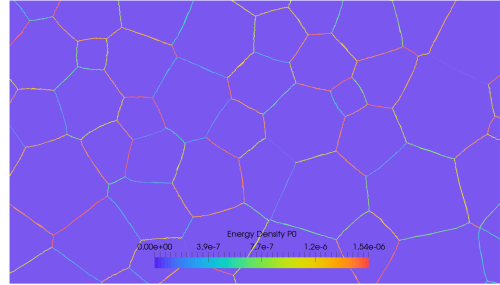
$$\gamma_{P0} \to \gamma_{P1}$$
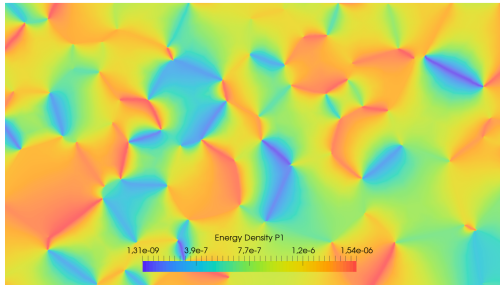
Figure 4.3: Visual illustration of the process from $q(X) \to \gamma(X)$ for a close-up of a polycrystal

Algorithm 3 γ extension

$\mathcal{N}_\Gamma = \{\}$
for node X in mesh **do**
    $\gamma_{BC}(X) = 0$
    for element e connected with X **do**
        $\gamma_{BC}(X) = \max(\gamma(e), \gamma_{BC}(X))$
    end for
    if $\gamma_{BC}(X) \neq 0$ **then**
        put X in $\mathcal{N}_\Gamma$
    end if
end for
solve $\Delta\gamma(X \in \Omega) = 0$ **for boundary conditions** $\gamma(X \in \mathcal{N}_\Gamma) = \gamma_{BC}(X)$

etry of the grain boundary network and the crystallography of the microstructure from which all the relevant fields may be computed.

4.2 Dynamics of the polycrystal

Now that the static description of the polycrystal is complete, the dynamics of the grain boundary network can be modeled. All the level set fields $\phi_i \in \Phi$ are subject to the interface migration equation (2.43) individually

$$\frac{\partial \phi_i}{\partial t} + \mu \left(-\left(\gamma m^{\alpha\beta} + \frac{\partial^2 \gamma}{\partial \tilde{\nabla}_\beta \phi \partial \tilde{\nabla}_\alpha \phi} \right) \tilde{\nabla}_\alpha \tilde{\nabla}_\beta \phi_i + P^{\alpha\beta} \tilde{\nabla}_\beta \gamma \tilde{\nabla}_\alpha \phi_i \right) = 0 \qquad (4.9)$$

such that there are as many equations as there are level set fields. However, after a resolution increment of the FE problem there are a number of regularization procedures one must perform on the fields describing the polycrystal.

Firstly, seeing as the transport equation is solved individually for each of the level sets, it does not conserve the configuration described in Figure 4.1. Due to the very intense hessian values of the level set fields $\tilde{\nabla}\tilde{\nabla}\phi_i$ at the multiple junctions, the geometric voids created by the level set description tend to grow. For this reason authors in [82] proposed a regularization procedure after each resolution increment that reduces these voids and also cancels potential overlaps. For $\phi_i \in \Phi$

$$\phi_i(X) = \frac{1}{2} \left(\phi_i(X) - \max_{\phi_j \in \Phi, j \neq i} \phi_j(X) \right) \qquad (4.10)$$

This is the procedure used in this numerical model to deal with the extraneous voids generated by the FE resolution. A more general variational approach to the voids and overlaps is proposed in [107]. This method was not used here for simplicity. The algorithms in [106] allow for the redistribution of the grains in the different level set fields (i.e. the reconfiguration of the sets $\mathcal{G}_i$) so as to avoid coalescence of grains, described by the same level set, that might come into contact. However, due to both these regularizations and the solution of the FE problem, the level set field loses its distance property. Given the development in Chapter 2, the level set must be a distance function for the migration equation to be valid. As such, as in the previous chapter, the direct reinitialization method developed in [102] is used to recompute the level set fields as distance functions to the grain boundaries.

As the level set fields evolve and the grains in the polycrystal reconfigure themselves with respect to one another the crystallographic orientation field q must also be updated to track the new contours of the crystallites. In practice, this operation is achieved by attributing the value of the orientation found at the intersection of the old and new description of the grains. Such that, considering χ_i as the characteristic field of the updated grain $\tilde{G}_i$ and G_i the old description of the same grain,

$$q = \sum_i q(\tilde{G}_i \cap G_i)\chi_i \tag{4.11}$$

with the insight that the orientation field in the overlap between the new and old grains $q(\tilde{G}_i \cap G_i)$ is a constant.

Once the orientation field has been updated, one may once again compute the grain boundary character field $b = (m, n)$ and the initial P0 grain boundary energy field γ. Using the extension operation in Algorithm 3, the P1 γ field may be calculated. Of course, the extension algorithm remains general enough to also extend the tensor quantity $\frac{\partial^2 \gamma}{\partial \tilde{\nabla}\phi \partial \tilde{\nabla}\phi}$. As in the previous chapter, the covariant derivatives of γ and the associated fields are computed using higher order interpolations [103].

The above described procedure for the fully anisotropic pure grain growth of a polycrystal is summarized in Algorithm 4.

4.3 The Grim Reaper test case

In [101] the most well known analytical test case for the heterogeneous triple junction is described. Using the so-called "Grim Reaper" profile solution of the isotropic grain growth, the authors develop a stationary solution for the evolution of a symmetric triple junction. Figure 4.4 illustrates the configuration for this benchmark.

Indeed, a stable triple junction should respect Herring's equilibrium at the junction itself

108

Algorithm 4 Anisotropic Grain Growth
___
Data: Initial Polycrystal: Ω, $\{G_i\}$, $\{O_i\}$ Δt, t_{end}
Compute the initial $\Phi(\{G_i\})$ and $q(\{O_i\})$
$t = 0$
while $t < t_{end}$ **do**
    Calculate $b = (m(q), n(q, \Phi))$
    Calculate $\gamma(b)$ and $\frac{\partial^2 \gamma}{\partial \bar{\nabla}\phi \partial \bar{\nabla}\phi}(b)$
    Extend both γ and $\frac{\partial^2 \gamma}{\partial \tilde{\nabla}\phi \partial \tilde{\nabla}\phi}$
    Compute covariant derivatives for the convective term
    Solve the FE element problems for all $\phi_i \in \Phi$
    $t = t + \Delta t$
    Regularize the multiple junction voids
    Redistribute the grains among the level sets
    Reinitialize the Level Set fields
    Update the q field
end while
___

$$\sum_{i=1,2,3} \gamma_i \tau_i + \frac{\partial \gamma_i}{\partial \tau_i} = 0 \tag{4.12}$$

where the γ_i are the boundary energy densities of the three boundaries and the τ_i are the inward pointing tangent vectors to each of the interfaces at the junction. In conditions where the boundary energy functions $\gamma(M, n)$ are independent of the inclination of the boundary $\gamma(M)$, the values of the energy density are constants per interface and the equations become those of a Young equilibrium

$$\sum_{i=1,2,3} \gamma_i \tau_i = 0 \tag{4.13}$$

This equation admits a solution of the form

$$\frac{\sin \xi_1}{\gamma_1} = \frac{\sin \xi_2}{\gamma_2} = \frac{\sin \xi_3}{\gamma_3} \tag{4.14}$$

where the ξ_i are the angles made by the boundaries opposite to the ith boundary in the steady state. In cases where $\gamma_1 = \gamma_2 = \gamma_{top}$ and $\gamma_3 = \gamma_{bot}$ then using the ratio $r = \frac{\gamma_{top}}{\gamma_{bot}}$ one may directly express
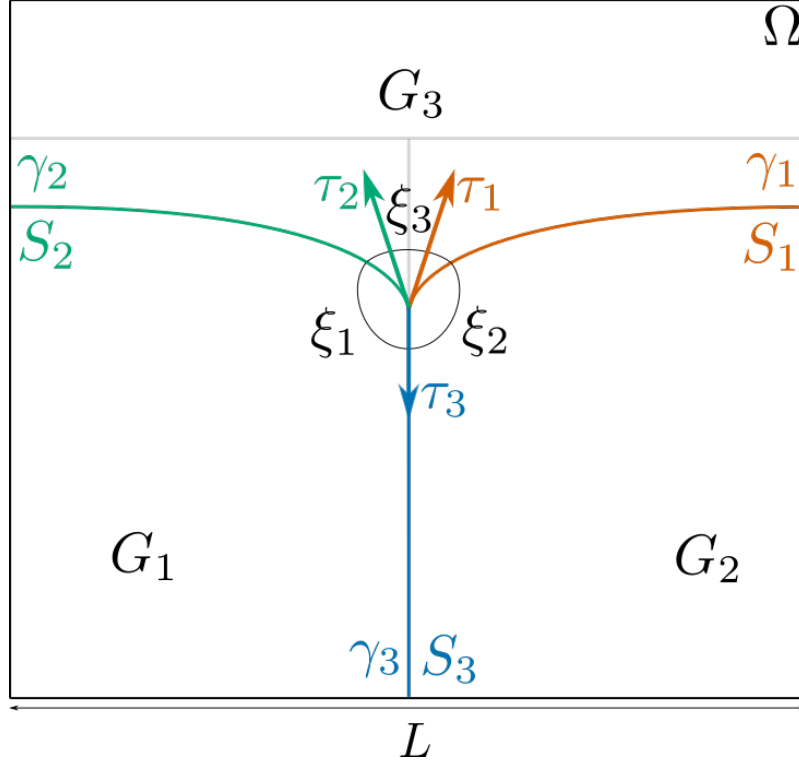
Figure 4.4: Diagram of the "Grim Reaper" test case for the triple junction. The initial state of the case is in gray.

$$\xi_3 = 2\arccos\left(\frac{1}{2r}\right) \tag{4.15}$$

where the two other angles are given, using symmetry and geometry, by $\xi_1 = \xi_2 = \pi - \frac{\xi_3}{2}$. The authors of [101] were able to construct boundary conditions for the S_1 boundary (and by symmetry the S_2 boundary as well) using these angles and orthogonal settings for the boundaries at their intersection with the boarder of the domain. This system admits a constant velocity solution $y(x,t)$ with a stationary geometry of the boundaries given by the "Grim Reaper" profile

$$\begin{cases} y(x,t) = g(x) + ct \\ g(x) = -\dfrac{\mu\gamma_{top}}{c}\ln\cos\left(\dfrac{c}{\mu\gamma_{top}}x\right) + y_0 \end{cases} \tag{4.16}$$

where c is the magnitude of the constant velocity, μ is the mobility of the boundaries, y_0 is a shift and (x,y) is a Cartesian chart for the domain. The c parameter is related to the size of the simulated domain

$$c = -\frac{2\mu\gamma_{top}}{L}\left(\frac{\pi}{2} - \frac{\xi_3}{2}\right) \tag{4.17}$$

As such, the simulations of this benchmark can be evaluated on three interconnected criteria

- the respect of the analytical profile $g(x)$ of the boundary,

- the obtention of the ξ_3 angle

- and the adherence to the stationary velocity c.

Also, starting from an initial "T" junction (represented in gray in Figure 4.4) the simulation should have a transition period towards the stationary solution depending on the imposed energy density ratio r and the length of the simulation domain L.

From the atomistic calculations in [40] the energy density ratio between the coherent twin boundary and a more general boundary can be roughly estimated at $r = 10$. As such, this will be the test ratio used for the convergence analysis of the formulation in this benchmark. Also, for convenience $L = 1$.

This analytical case is also the perfect setting to investigate the effects of the convective term in the formulation. As such, three different formulations will be studied:

Classic

$$\frac{\partial\phi_i}{\partial t} - \mu\gamma m^{\alpha\beta}\tilde{\nabla}_\alpha\tilde{\nabla}_\beta\phi_i = 0$$

Projected

$$\frac{\partial\phi_i}{\partial t} + \mu\left(-\gamma m^{\alpha\beta}\tilde{\nabla}_\alpha\tilde{\nabla}_\beta\phi_i + P^{\alpha\beta}\tilde{\nabla}_\beta\gamma\tilde{\nabla}_\alpha\phi_i\right) = 0$$

Full

$$\frac{\partial\phi_i}{\partial t} + \mu\left(-\gamma m^{\alpha\beta}\tilde{\nabla}_\alpha\tilde{\nabla}_\beta\phi_i + m^{\alpha\beta}\tilde{\nabla}_\beta\gamma\tilde{\nabla}_\alpha\phi_i\right) = 0$$

Defining both the gradient and the laplacian generally as

$$m^{\alpha\beta}\tilde{\nabla}_\beta \cdot = grad(\cdot)^\alpha$$

and

$$m^{\alpha\beta}\tilde{\nabla}_\alpha\tilde{\nabla}_\beta \cdot = \Delta\cdot$$

and applying the flat metric and cartesian chart hypotheses, the formulations can be written in more conventional terms

Classic

$$\frac{\partial\phi_i}{\partial t} - \mu\gamma\Delta\phi_i = 0$$

Projected

$$\frac{\partial\phi_i}{\partial t} - \mu\gamma\Delta\phi_i + \mu(\delta^{\alpha\beta} - n^\alpha n^\beta)\tilde{\nabla}_\beta\gamma\tilde{\nabla}_\alpha\phi_i = 0$$

Full

$$\frac{\partial\phi_i}{\partial t} - \mu\gamma\Delta\phi_i + \mu grad(\gamma)^\alpha\tilde{\nabla}_\alpha\phi_i = 0$$

where the goal is to compare the effects of the inclusion of the additional term in the covariant derivative of γ (the second derivative term $\frac{\partial^2\gamma}{\partial\tilde{\nabla}\phi^2}$ is implicitly null because the energy density does not depend upon the inclination of the boundary). In the strictly formal sense of the one interface model described in the two previous chapters this additional term should be null due to the orthogonality of $\tilde{\nabla}\gamma$ and $\tilde{\nabla}\phi$ and the three formulations should yield the same results. However, the various regularizations and treatments of both the level set fields and the energy density field around the triple junction actually render this term non-negligible. The genesis of the "Full" formulation might seem completely arbitrary at first sight as compared to the two other expressions. In the chronology of this investigation, the "Full" formulation was actually found to be a candidate before the "Projected" one. As such, in order to be coherent with currently published works such as [94], this supplemental equation is included here. Figure 4.5 reports on the vector fields $m^{-1} \cdot \tilde{\nabla}\gamma$ and $P \cdot \tilde{\nabla}\gamma$.

As is customary when testing a new numerical model, a convergence analysis has been conducted for the $(r = 10, L = 1)$ case for the three formulations. Figure 4.6 reports on the time evolution of all three formulations in the most precise case. While both the Classic

(a) $grad(\gamma)$ (b) $P \cdot \tilde{\nabla}\gamma$
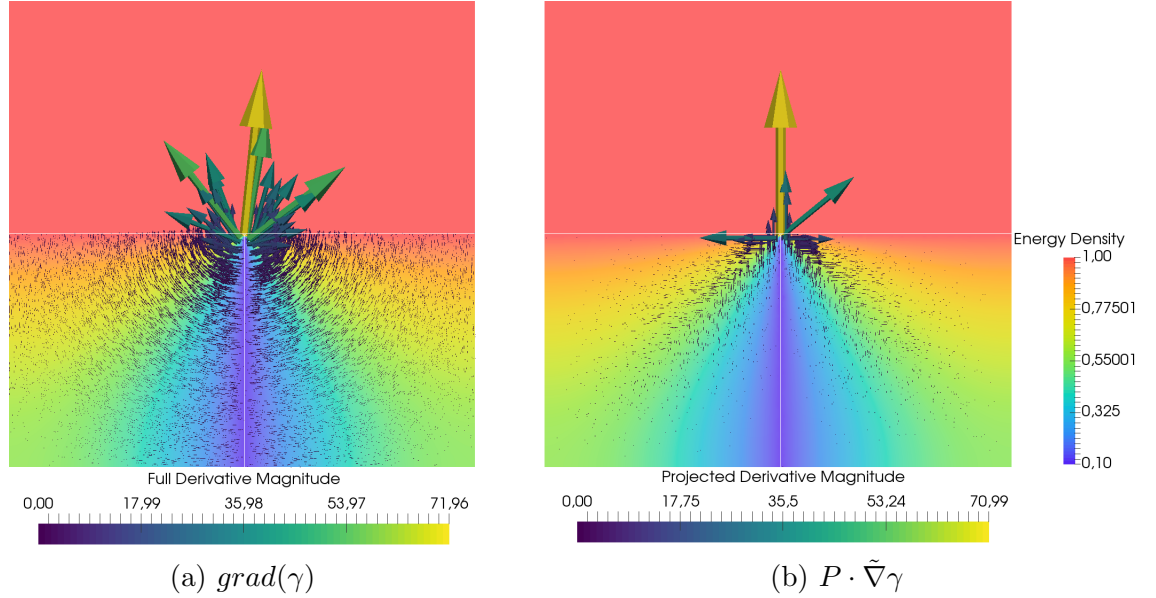
Figure 4.5: Glyph views of the $grad(\gamma)$ and $P \cdot \tilde{\nabla}\gamma$ vector fields close to the T junction for $r = 10$. Boundaries are in white.

and Projected formulations do seem to produce Grim Reaper profiles for the boundaries, the Full formulation does not. The Full case actually takes an opposite trajectory to the two other cases and to the analytical solution for this heterogeneous ratio $r = 10$.

A method for calculating the angles at the triple junction as well as the trajectory of the triple point has been developed and used here to measure ξ_3 and v_{TJ}, the y component of the velocity of the triple point. The Appendix A details the algorithm where here the ϵ parameter is taken equal to 0.05. Also, the total interfacial energy of the system E_Γ is calculated using

$$E_\Gamma = \sum_i \sum_{e \in \mathcal{E}} \frac{1}{2}\gamma l_e(\phi_i),$$

where $\mathcal{E}$ is the set of all elements of the mesh and l_e measures the quantity of iso-zero set interface in the element e. The $\frac{1}{2}$ is necessary in order to account for the duplication of the interfaces by the level set framework. Relative errors in the ξ_3 angle e_{ξ_3} and in velocity $e_{v_{TJ}}$ are computed using

$$e_{\xi_3} = \frac{\xi_3^{ana} - \bar{\xi}_3}{\xi_3^{ana}},$$

$$e_{v_{TJ}} = \frac{c - v_{TJ}}{c},$$

113
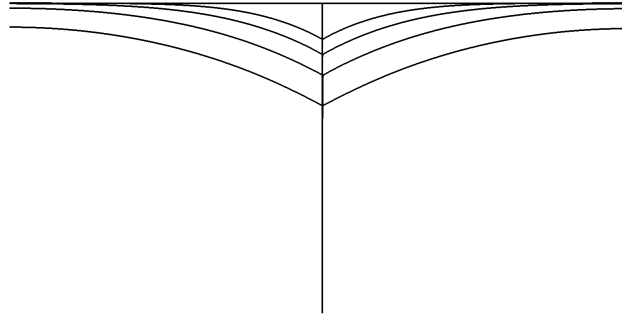
(a) Classic
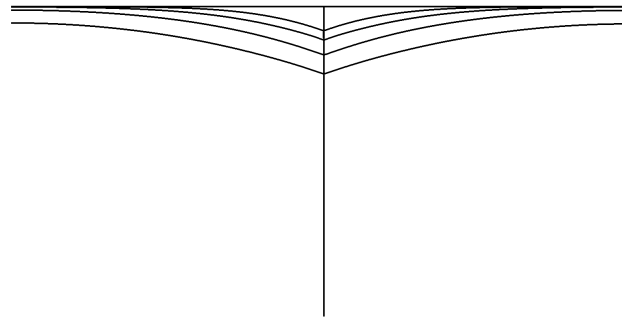
(b) Projected
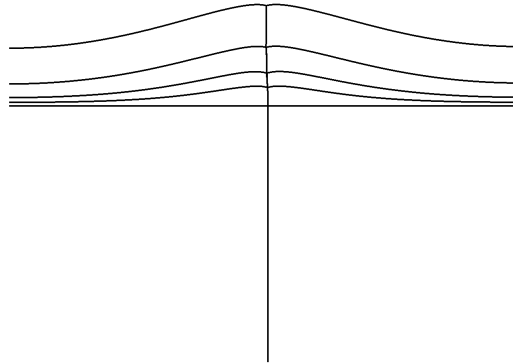
(c) Full

Figure 4.6: Time lapse images of the iso-zero values of the level sets obtained for the different formulations for an initial T junction and $(r = 10, L = 1)$ with the mesh size $h = 1e-3$ and time step $\Delta t = 1e-5$. Plotted level sets correspond to $t = \{0, 0.01, 0.02, 0.04, 0.08\}$ respectfully from top to bottom for the "Classic" and "Projected" formulations and bottom to top for the "Full" case.

where $\bar{\xi}_3$ is the value measured for the ξ_3 angle and ξ_3^{ana} is the analytical value. Figures 4.7, 4.8 and 4.9 show the time evolution of the e_{ξ_3}, $e_{v_{TJ}}$ and E_Γ quantities for all three formulations and for different mesh sizes h. The results, being particularly noisy, are shown smoothed by a Savitzky-Golay [108] algorithm with quintic polynomials and 301 point patches. The same format is adopted for the convergence analysis with respect to the time step in Figures 4.10, 4.11 and 4.12.

In order to better analyze the convergence results, the smoothed data of the most precise simulation ($h = 1e-3, \Delta t = 1e-5$) was interpolated using splines and then used as the reference evolution (X^{ref}) for calculating $e_{L^2}(X)$ values

$$e_{L^2}(X) = \sqrt{\int_0^{t_{end}} (X^{ref} - X)^2 dt}$$

where X can be the value of the measured $\bar{\xi}_3$ angle, the trajectory of the triple point y_{TJ} or the total energy E_Γ. Figures 4.13 and 4.14 show the evolution of e_{L^2} result as a function of h and Δt respectively in logarithmic plots. These two final figures demonstrate the numerical convergence of all three formulations. However, the explicit time evolution show that for this range of $(h, \Delta t)$ numerical parameters the systems are more sensitive to the mesh size than the time step. Also, the strong oscillations in the results reveal that the measurement of the angles, velocities and energies have noise attached to them (which is to be expected given the discrete nature of the mesh). However, the classification of the instability from least to most oscillatory being the Classic, Projected and Full formulations in that order clearly point at the scheme becoming less stable with stronger convective terms. Thus, although the finite elements are stabilized, the localized nature of the convective term is introducing some instability.

Even though the numerical schemes are convergent, the results obtained show significant errors with regards to the analytical values. Figure 4.15 reports on the time evolution of e_{ξ_3}, $e_{v_{TJ}}$ and E_Γ for all three formulations in the most precise case. Looking at the total energy evolution, all formulations generate increases in the total energy of the system. This result, while disappointing, can possibly be related to a numerical error for the Projected case which continues to lower its energy evolution with finer space discretizations in Figure 4.8. Interpreting the results obtained here directly, the E_Γ evolution are not physically coherent with the Projected formulation being the least wrong.

The Full formulation obtains the best fit for the ξ_3 angle but it fails to obtain the correct sign for the velocity, explaining the bizarre forms of triple junction obtained, as well as ultimately increasing the total energy of the system more than the other two. The timeseries data for the Classic and Projected formulations are more similar with generally the Projected cases performing better than the classic case in every measured quantity. Indeed, the Projected scheme reduced the error obtained for the ξ_3 angle by 10% as compared with the Classic case. Considering the analytical form, velocity and
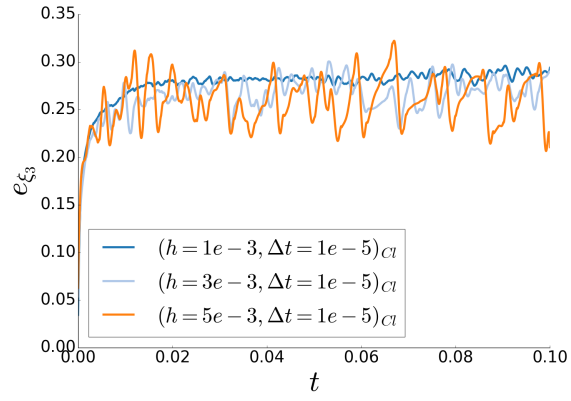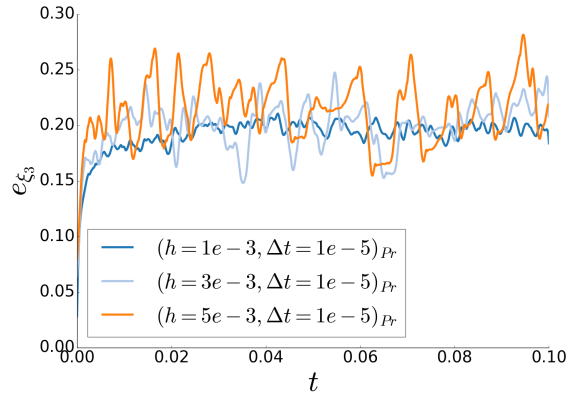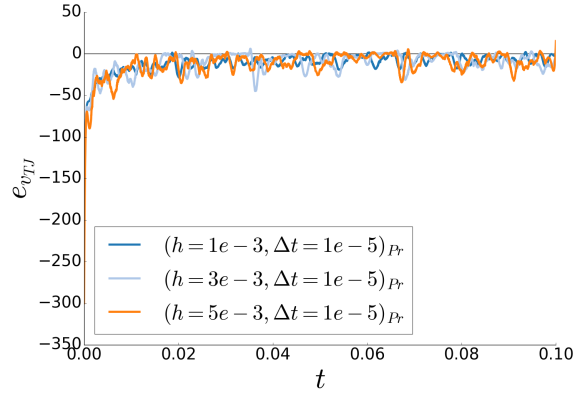
(a) $e_{\xi_3} = f(t, h)$
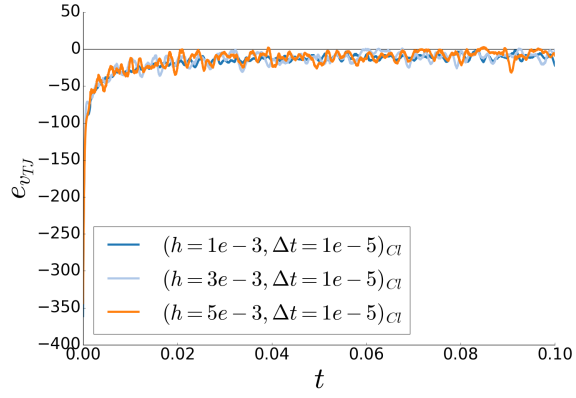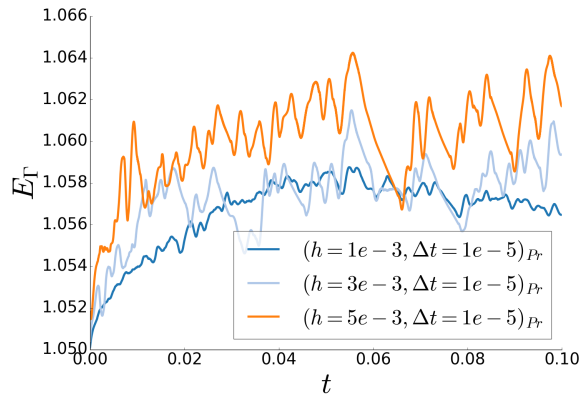

(b) $e_{v_{TJ}} = f(t, h)$
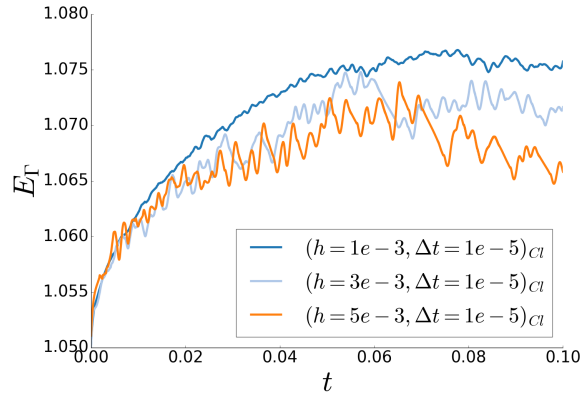
(c) $E_\Gamma = f(t, h)$

Figure 4.7: Time series plots of e_{ξ_3}, $e_{v_{TJ}}$ and E_Γ for the Classic formulation run with $\Delta t = 1e-5$ and $h = \{1e-3, 3e-3, 5e-3\}$. Smoothed by a Savitzky-Golay filter.
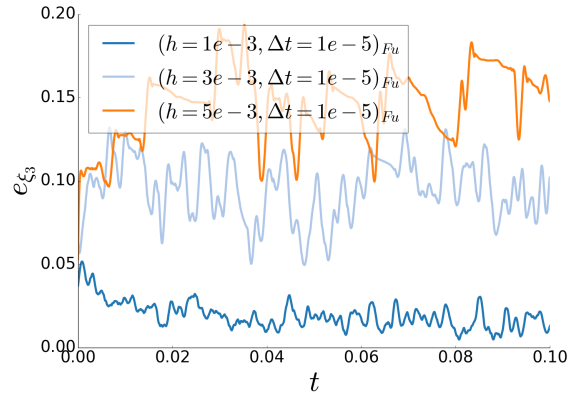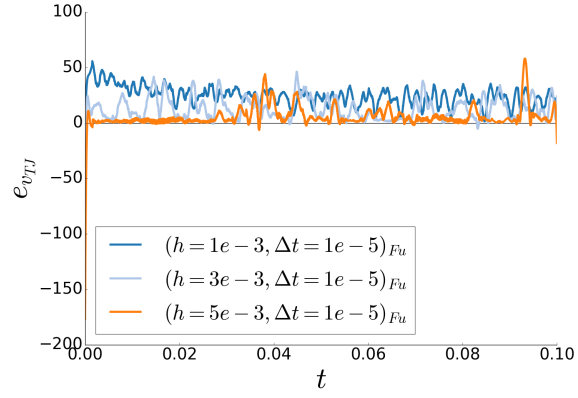
(a) $e_{\xi_3} = f(t, h)$
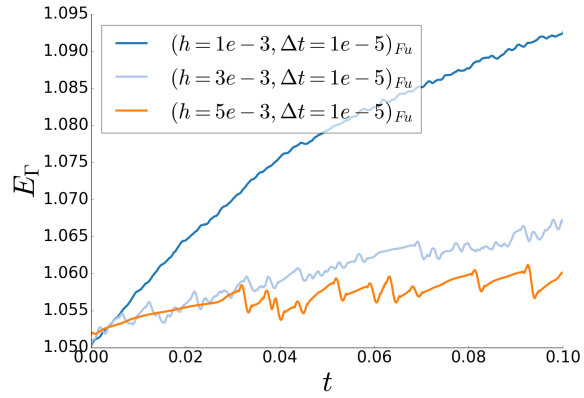

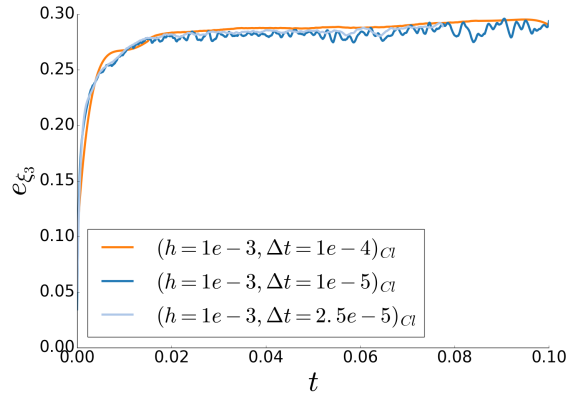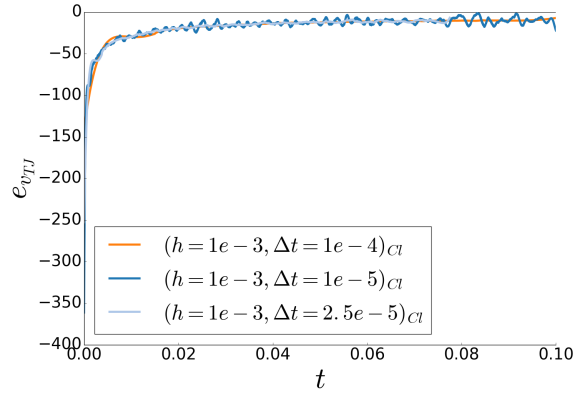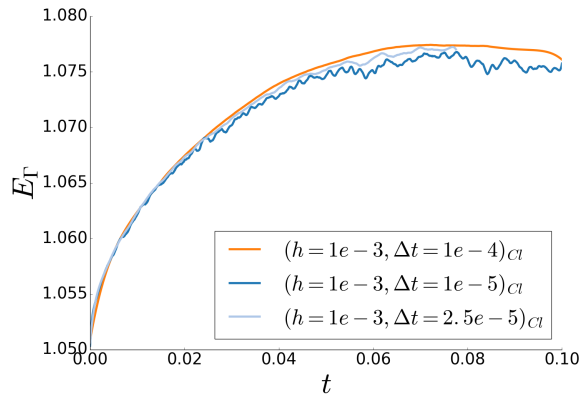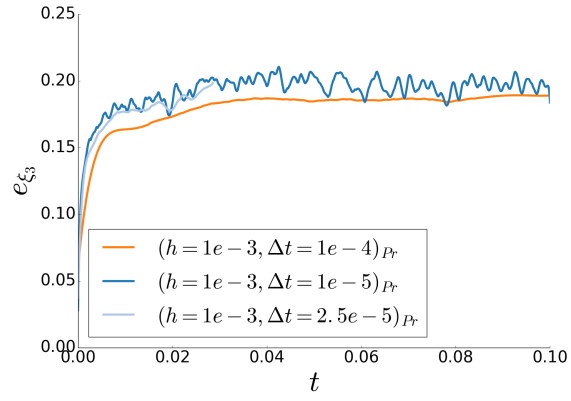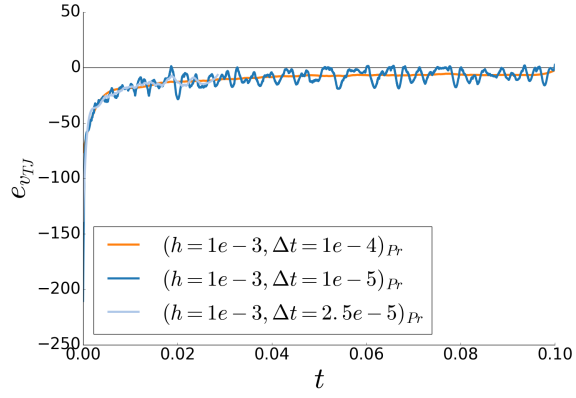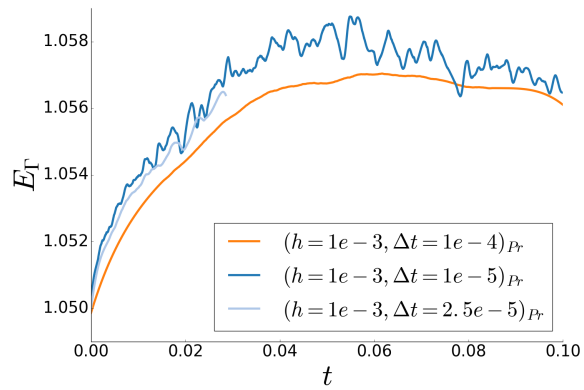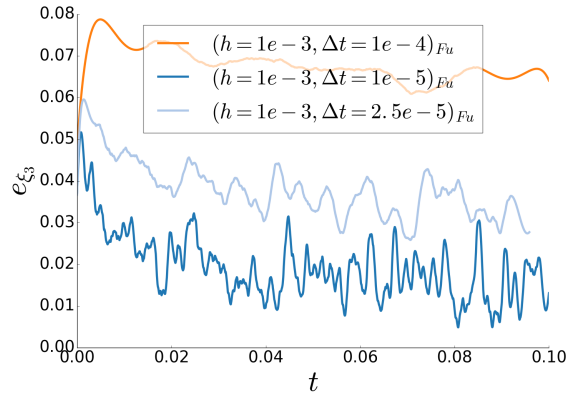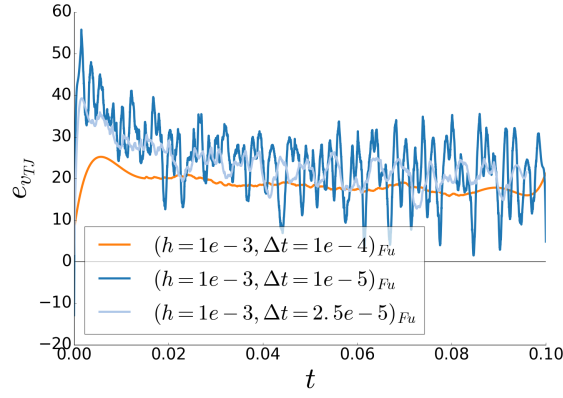(b) $e_{v_{TJ}} = f(t, h)$

(c) $E_\Gamma = f(t, h)$

Figure 4.8: Time series plots of e_{ξ_3}, $e_{v_{TJ}}$ and E_Γ for the Projected formulation run with $\Delta t = 1e-5$ and $h = \{1e-3, 3e-3, 5e-3\}$. Smoothed by a Savitzky-Golay filter.

(a) $e_{\xi_3} = f(t, h)$

(b) $e_{v_{TJ}} = f(t, h)$

(c) $E_\Gamma = f(t, h)$

Figure 4.9: Time series plots of e_{ξ_3}, $e_{v_{TJ}}$ and E_Γ for the "Full" formulation run with $\Delta t = 1e-5$ and $h = \{1e-3, 3e-3, 5e-3\}$. Smoothed by a Savitzky-Golay filter.

(a) $e_{\xi_3} = f(t, \Delta t)$

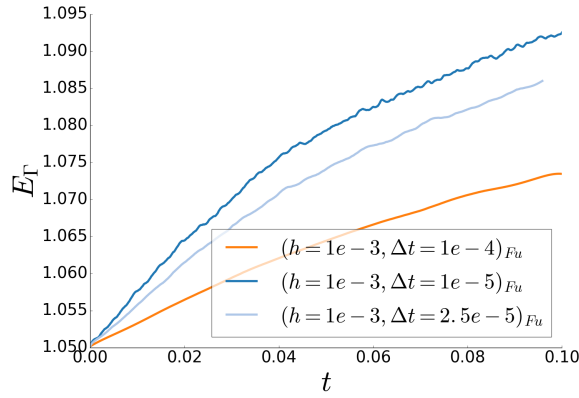(b) $e_{v_{TJ}} = f(t, \Delta t)$

(c) $E_{\Gamma} = f(t, \Delta t)$

Figure 4.10: Time series plots of e_{ξ_3}, $e_{v_{TJ}}$ and E_{Γ} for the Classic formulation run with $\Delta t = \{1e-5, 2.5e-5, 1e-4\}$ and $h = 1e-3$. Smoothed by a Savitzky-Golay filter.

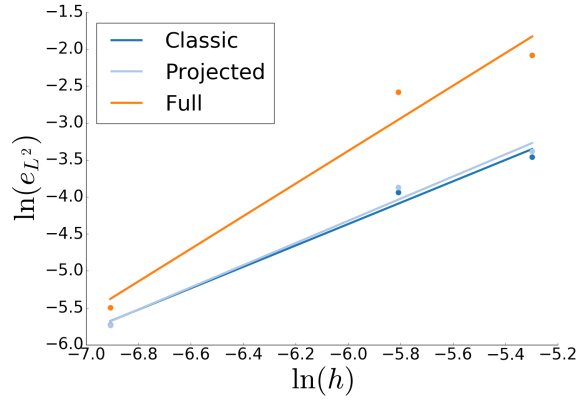(a) $e_{\xi_3} = f(t, \Delta t)$

(b) $e_{v_{TJ}} = f(t, \Delta t)$

(c) $E_\Gamma = f(t, \Delta t)$

Figure 4.11: Time series plots of e_{ξ_3}, $e_{v_{TJ}}$ and E_Γ for the Projected formulation run with $\Delta t = \{1e-5, 2.5e-5, 1e-4\}$ and $h = 1e-3$. Smoothed by a Savitzky-Golay filter.

(a) $e_{\xi_3} = f(t, \Delta t)$

(b) $e_{v_{TJ}} = f(t, \Delta t)$

(c) $E_\Gamma = f(t, \Delta t)$
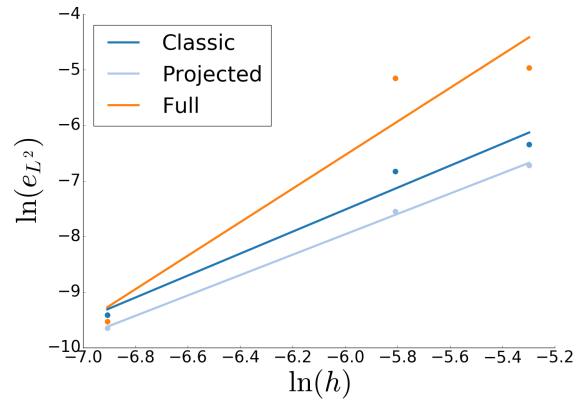
Figure 4.12: Time series plots of e_{ξ_3}, $e_{v_{TJ}}$ and E_Γ for the "Full" formulation run with $\Delta t = \{1e-5, 2.5e-5, 1e-4\}$ and $h = 1e-3$. Smoothed by a Savitzky-Golay filter.
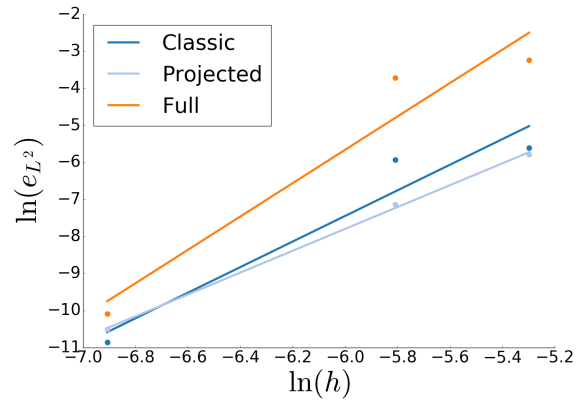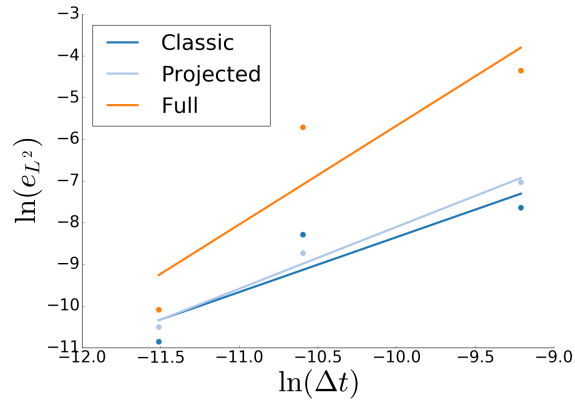
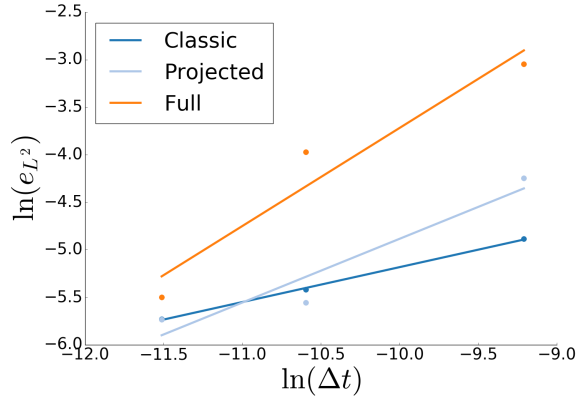(a) e_{L^2} for the y_{TJ}

(b) e_{L^2} for $\bar{\xi}_3$

(c) e_{L^2} for E_Γ

Figure 4.13: $\ln(e_{L^2})$ as a function of $\ln(h)$ for a variety of characteristic degrees of freedom of the triple junction for $\Delta t = 1e - 5$.
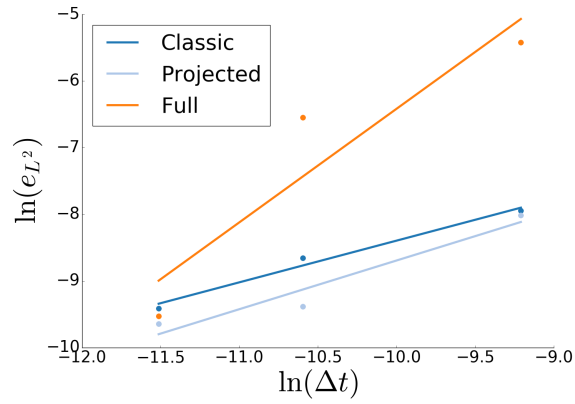
(a) e_{L^2} for the y_{TJ}

(b) e_{L^2} for $\bar{\xi}_3$

(c) e_{L^2} for E_Γ

Figure 4.14: $\ln(e_{L^2})$ as a function of $\ln(h)$ for a variety of characteristic degrees of freedom of the triple junction for $h = 1e - 3$.

energy evolution, the Projected case is the best candidate. With regards to the ξ_3 angle, the Full formulation obtains the best results for this level of heterogeneity but does so by eschewing other constraints.

However, seeing that these results were obtained for a given heterogeneity ($r = 10$) one would be justified in questioning their validity for other heterogeneous ratios. Figure 4.16 summarize the results obtained using $r = \{0.8, 1, 2, 5, 10\}$ with $(h, \Delta t) = (1e-3, 1e-4)$. These data globally support the conclusions made in the ($r = 10$) case.

As such, the results presented in this section seem to point towards the Projected formulation as the one that produces interface flows that are the closest to the analytical case. These new equations provide a definite improvement on the results of the Classical case where no supplemental convection is added at the triple junction. This is, therefore, the form for the equations used here on out. However, the algorithm is far from perfect and cannot account for exactly analytical results at the triple point. Perhaps some adequate mixing of the Full and Projected formulations might do so or maybe a different extension of the γ field might provide a more suitable $\tilde{\nabla}\gamma$ field. Also, it is very possible that the surface terms neglected in Chapter 2, leading from equation (2.25) to (2.26), play a non trivial role. Regardless, seeing as the three formulations are theoretically equivalent and differ in practice due to the singular topology of the triple junction it is remarkable that one observes such striking differences between the results. The case is more than likely exacerbated in 3D where triple points become lines and more exotic junctions (quadruple, etc.) become commonplace. These results show the beginning of the limits of models which attempt to simulate the grain boundary network as a sum of interfaces. In reality, the junctions between interfaces correlate the entire network so that it becomes more than just the sum of its parts.

## 4.4 Torque effects on a triple junction

The heterogeneous cases studied above are very important in regards to polycrystal evolution. However, they do not cover more general anisotropic cases where the boundary energy density might depend on the inclination of the boundary as well. As such, this section is devoted to investigating the dynamics of a triple junction subject to an inclination dependent energy density function. Considering a separable grain boundary energy density

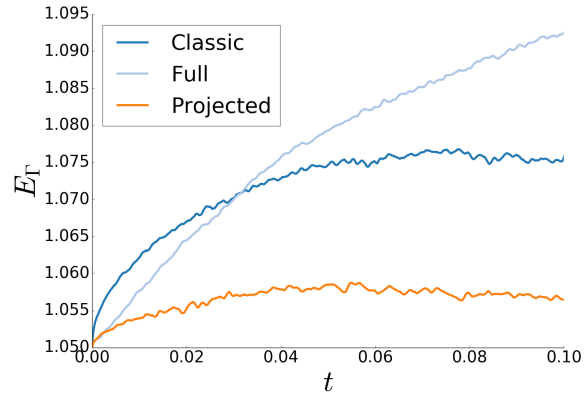$$\gamma(M, n) = \Xi(M)\nu(n)$$

such that Ξ may be calculated as in the previous section and ν is constrained by the conditions expressed in equations (3.20), (3.21) and (3.22). Proposing the following function, with $\lambda = \arccos(n^x)$
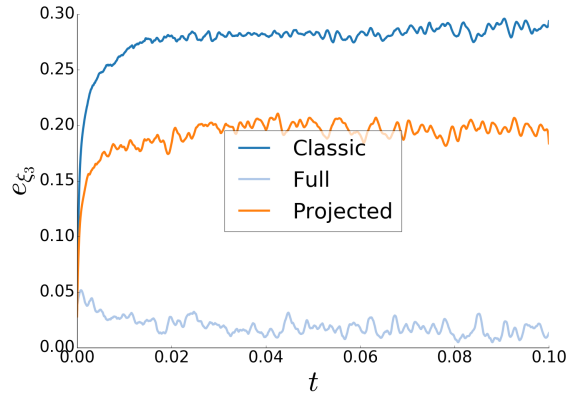
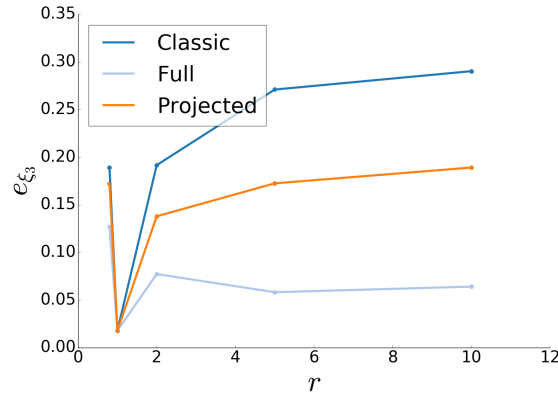(a) $e_{\xi_3} = f(t)$
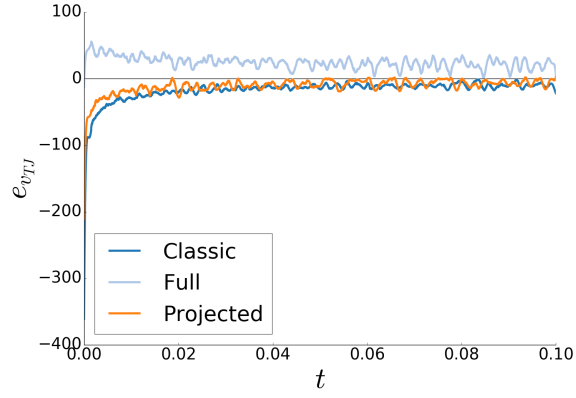
(b) $e_{v_{TJ}} = f(t)$

(c) $E_\Gamma = f(t)$

Figure 4.15: Time series plots of e_{ξ_3}, $e_{v_{TJ}}$ and E_Γ for the three formulations with $h = 1e-3$ and $\Delta t = 1e-5$. Smoothed by a Savitzky-Golay filter.

(a) $e_{\xi_3} = f(r)$
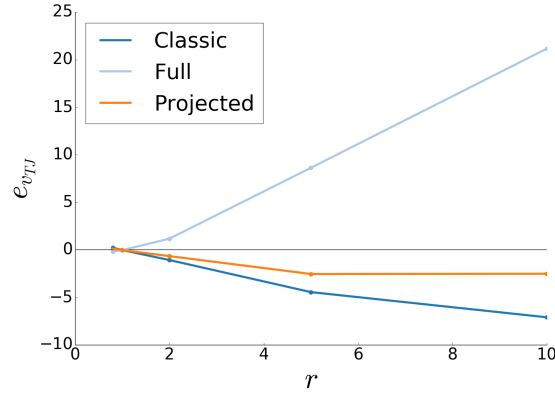
(b) $e_{v_{TJ}} = f(r)$
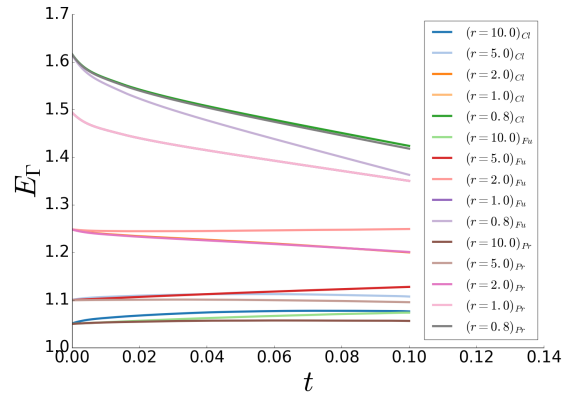
(c) $E_\Gamma = f(t, r)$

Figure 4.16: Plots of the final values of e_{ξ_3}, $e_{v_{TJ}}$ as a function of r and E_Γ as a function of t for the three formulations with $h = 1e-3$ and $\Delta t = 1e-5$ and different heterogeneous ratios. The E_Γ timeseries data is smoothed by a Savitzky-Golay filter.

Figure 4.17: Polar plot of $\nu(\lambda)$ and $N(\lambda)$ components.

$$\nu(\lambda) = 1 + \frac{1}{20}\left(\frac{3}{32}\cos(4\lambda) - \frac{3}{64}\cos(8\lambda) + \frac{1}{96}\cos(12\lambda)\right) \tag{4.18}$$
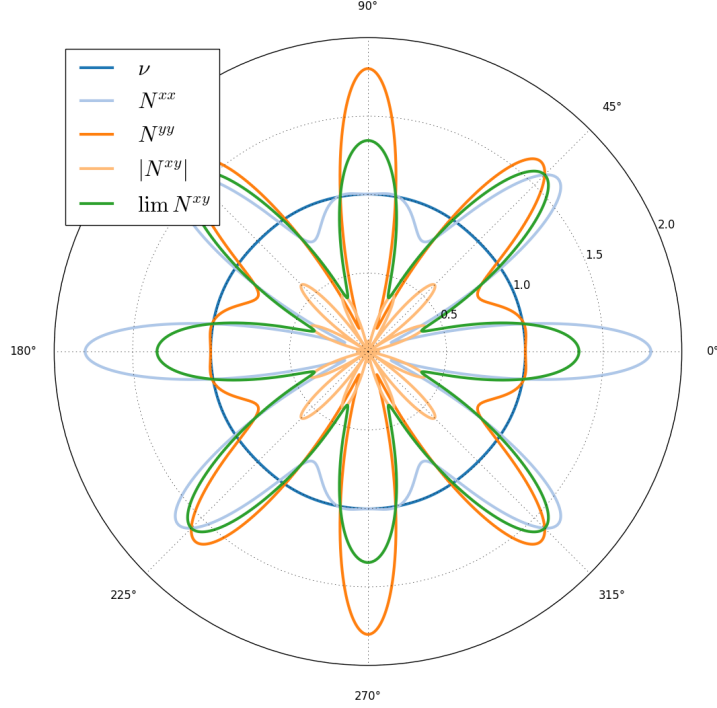
one can compute the various elements of the symmeterized $N^{\alpha\beta} = \nu m^{\alpha\beta} + \frac{\partial^2 \nu}{\partial\tilde{\nabla}_\alpha\phi\tilde{\nabla}_\beta\phi}$ which are reported in Figure 4.17. However, ν should be rotated with respect to each grain so as to weigh the crystallographically equivalent directions in the same way. Using the n^x parameter here instead of the inclination represented in the crystallographic frame of each grain is a simplifying choice which is completely non-physical. Nevertheless, in order to make more sense of the results, this sort of artifact is useful.

With $\Xi(M)$ being characterized here by a heterogeneous ratio of $r = \frac{\Xi_{max}}{\Xi_{min}} = 10$ as in the energy density of the previous section and $D^{\alpha\beta} = \Xi(M)N^{\alpha\beta}(\lambda)$, the initial state of the triple junction is illustrated in Figure 4.18 for a mesh with $h = 1e - 3$. The energetic state is relatively similar to the triple junctions investigated in the previous section.

In order to explore the implications of including the inclination dependence of the energy density and its effect on the migration velocity of the boundaries, two projected formulations for the dynamics are compared
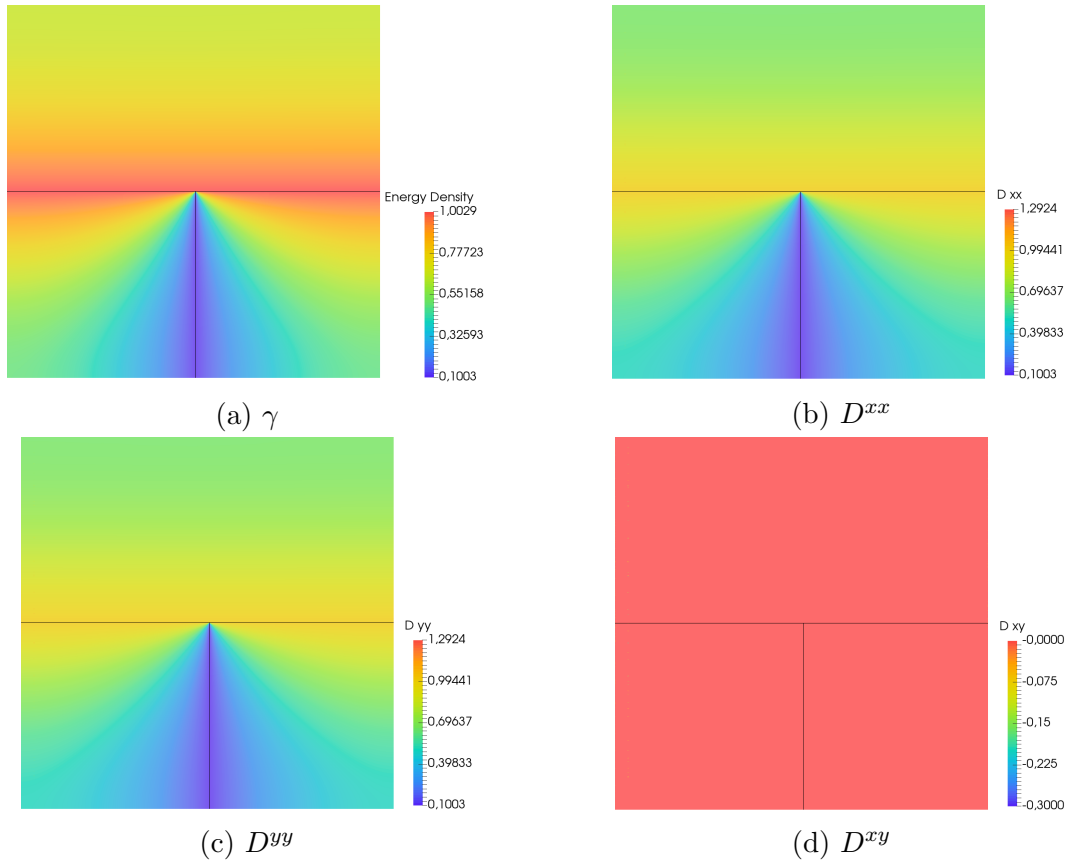
(a) γ

(b) D^{xx}

(c) D^{yy}

(d) D^{xy}

Figure 4.18: Initial γ and D fields of the triple junction. The interfaces are pictured in black.

Heterogeneous

$$\frac{\partial \phi_i}{\partial t} + \mu \left(-\gamma m^{\alpha\beta} \tilde{\nabla}_\alpha \tilde{\nabla}_\beta \phi_i + P^{\alpha\beta} \tilde{\nabla}_\beta \gamma \tilde{\nabla}_\alpha \phi_i \right) = 0$$

Anisotropic

$$\frac{\partial \phi_i}{\partial t} + \mu \left(- \left(\gamma m^{\alpha\beta} + \frac{\partial^2 \gamma}{\partial \tilde{\nabla}_\beta \phi \partial \tilde{\nabla}_\alpha \phi} \right) \tilde{\nabla}_\alpha \tilde{\nabla}_\beta \phi_i + P^{\alpha\beta} \tilde{\nabla}_\beta \gamma \tilde{\nabla}_\alpha \phi_i \right) = 0$$

> **Simplification**   *Flat metric, Cartesian chart*
>
> **Heterogeneous**
>
> $$\frac{\partial \phi_i}{\partial t} - \mu\gamma\Delta\phi_i + \mu(\delta^{a\beta} - n^\alpha n^\beta)\tilde{\nabla}_\beta \gamma \tilde{\nabla}_\alpha \phi_i = 0$$
>
> **Anisotropic**
>
> $$\frac{\partial \phi_i}{\partial t} - \mu\gamma\Delta\phi_i - \mu\frac{\partial^2 \gamma}{\partial \tilde{\nabla}_\beta \phi \partial \tilde{\nabla}_\alpha \phi}\tilde{\nabla}_\alpha \tilde{\nabla}_\beta \phi_i + \mu(\delta^{a\beta} - n^\alpha n^\beta)\tilde{\nabla}_\beta \gamma \tilde{\nabla}_\alpha \phi_i = 0$$

where the goal is once again to evaluate the role of the second derivative. The simulations are performed using $(h, \Delta t) = (1e-3, 1e-4)$ and the junction evolution are presented in Figures 4.19 for the Heterogeneous and Anisotropic cases. The final state of the γ and D fields are presented in Figure 4.20. From these figures the ability of the second derivative term to generate a torque on the junction is remarkable. Given the very low anisotropy induced by the chosen ν, the effect on the triple junction is substantial following along the same lines as the previous chapter.

Using the definition given in equation (3.27), the energy efficiency of both simulations are compared at each time step in Figure 4.21. Unfortunately, the results in Figure 4.21 are inconclusive as to which formulation generates the most energy efficient configurations. However, it is remarkable that the Anisotropic formulation manages to deviate from the classical "Grim Reaper" symmetric solution without losing any general energy efficiency. Supplemental simulations as well as analytical benchmarks are needed to better inform the results using these formulations and move towards more realistic junctions.

In this chapter, the numerical implementation for considering the pure grain growth of polycrystals in a level set formalism was developed. Also, the effect of the term in the equation (2.45) was evaluated in the context of the triple junction. While the formulation exhibits some inconsistencies, it has proven to be better than its non-heterogeneous counterpart. Also, the second derivative in equation (2.44) is shown to generate torque in an anisotropic context, a necessary component of annealing twin modeling. The applications to polycrystals is treated in the next chapter.

(a) t = 0

(b) t = 0.02

(c) t = 0.04

(d) t = 0.06

(e) t = 0.08

(f) t = 0.1
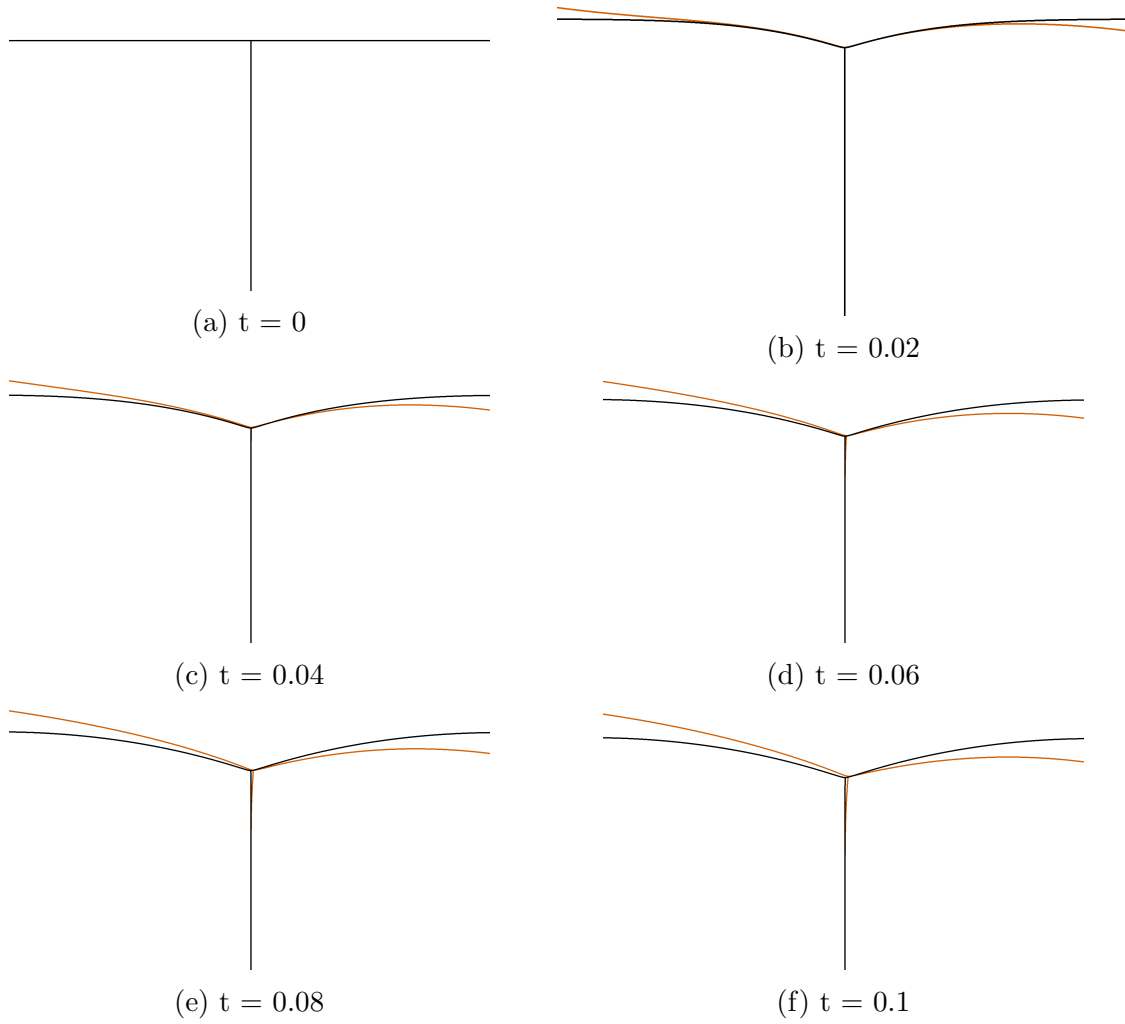
Figure 4.19: Time evolution of the triple junction for the Heterogeneous formulation (in black) and Anisotropic formulation (in orange). Simulations run with $(h, \Delta t) = (1e - 3, 1e - 4)$

(a) γ (b) D^{xx}

(c) D^{yy} (d) D^{xy}

Figure 4.20: Final γ and D fields of the triple junction for the Anisotropic formulation. The interfaces are pictured in black.

Figure 4.21: The energy efficiency Λ of the configuration as a function of time t for the Heterogeneous and Anisotropic formulations.

Résumé en Français du Chapitre 4

Ce chapitre concerne l'élargissement des capacités du formalisme level set, développé dans ce manuscrit, de modélisation des polycristaux. D'abord, les ajouts et modifications du modèle, pour la plupart issus d'autres travaux sur le sujet, 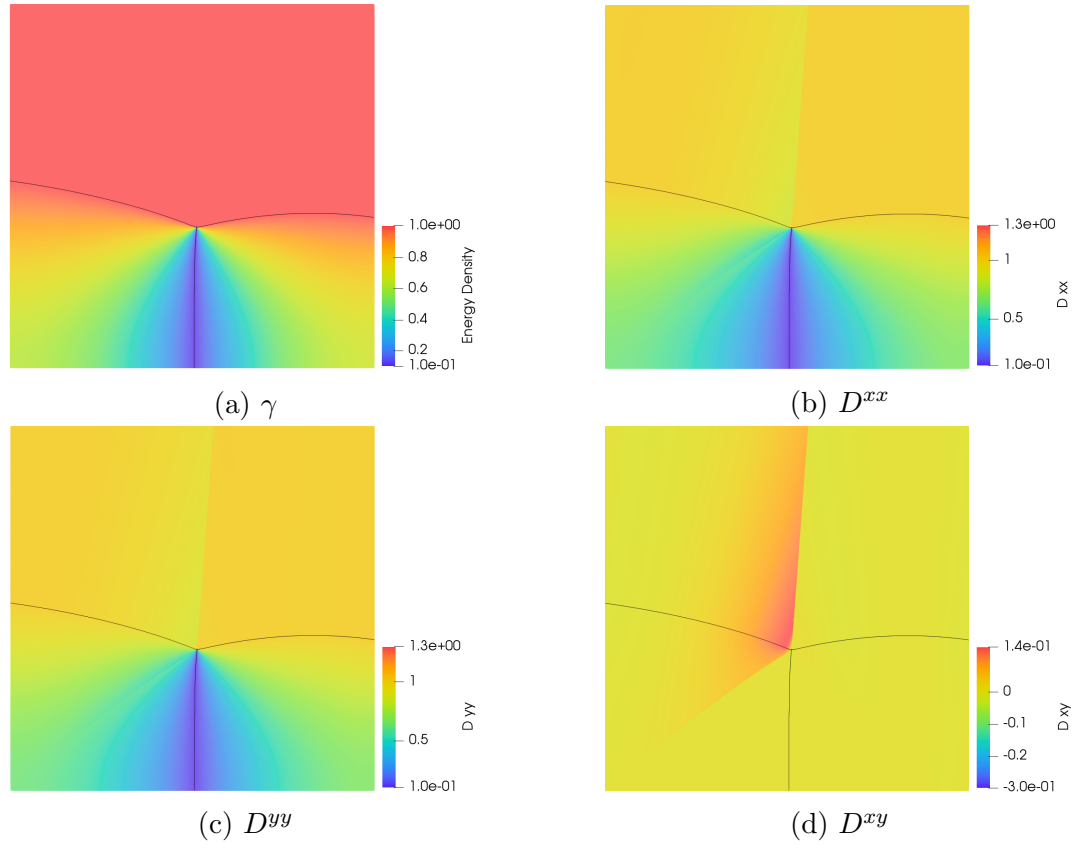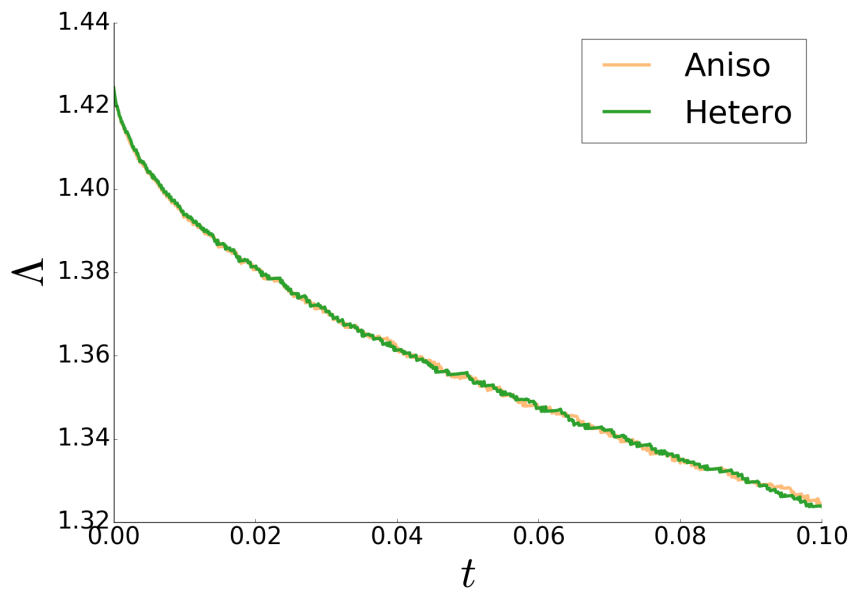sont décrits afin de pouvoir simuler des jonctions multiples, éléments omniprésents dans les microstructures. Une fois que ces modifications sont prises en compte, l'approche numérique est testée sur un cas analytique bien connu, le "Grim Reaper" [101]. La simulation numérique de cette configuration est réalisée pour trois formalismes proches mais toutefois différents. La comparaison des résultats permet de trancher parmi les trois solutions. Cependant, même la plus performante des trois méthodes donne des résultats qui semblent déviés des attentes analytiques pour les cas les plus hétérogènes. Un dernier cas est proposé où une anisotropie complète de l'énergie du joint est prise en compte dans une jonction triple et l'effet du terme de "torque" du joint est évalué.

Chapter 5

Applications

Now that a full field level set formulation for grain growth has been developed and tested on analytical test cases, one may start to look at configurations that are closer to real microstructures. This is the goal of this chapter. The first section is dedicated to investigating "twinned" grains in a controlled environment. Through this study one may start to observe the singular behavior of very low energy grain boundaries. The second section reports on the simulation of virtual microstructures using grain boundary energy densities that depend only on the misorientation. Multiple such test functions are used in order to evaluate the links between the grain boundary energy density function and microstructural evolution during grain growth. The third section is devoted to studying the evolution of virtual microstructures that exhibit an inclination dependence of the grain boundary energy density but no misorientation dependence. As such, the effects of each term of the formulation on polycrystals may be decorrelated from each other.

5.1   Applied test configurations for "twins"

In order to correctly model the twin boundary, one would need to use a 3D model. To differentiate between the coherent and incoherent twin boundaries one would need to know the full inclination parameters of the interface. Even so, a "pseudo-twin" boundary can be thought of in 2D by considering the coherency of the interface at the (11) lines instead of the (111) planes. This is a gross simplification of reality. However, this 2D model of the twin boundary enables one to start thinking about the configurations illustrated in Figure 1.10.

When thinking of benchmark calculations on twinned grain configurations, the ideal case would be to use a grain structure that is fully stable without the twin boundary. As such, the evolution of the configuration is fully controlled by the presence of the singular interface. Isotropic grain boundaries have stable multiple junctions which are isogonic. Thus, tessellations of regular hexagons are metastable for isotropic grain boundary energies under grain growth. Given these considerations, the grain structure illustrated in Figure
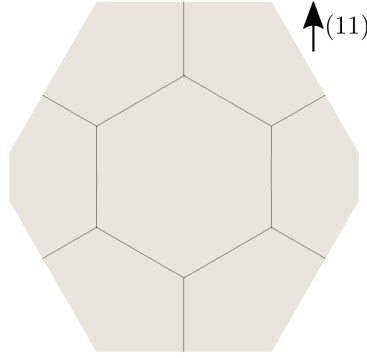
Figure 5.1: Stationary isotropic hexagonal configuration

5.1 is stationary using isotropic grain boundary energies. The meshed domain is an octagon in order to comply with the orthogonality of the interfaces at the boundaries of the domain.

One may then insert a coherent "twin" boundary in the middle of the center hexagonal grain using a separable grain boundary energy

$$\gamma(M, \lambda) = \Xi(M)\nu(\lambda - \frac{\pi}{4}) \tag{5.1}$$

where ν is defined in equation (4.18). The phase shift $\frac{\pi}{4}$ is integrated in order to displace the minima of the grain boundary energy to the $(10, 01, \bar{1}0, 0\bar{1})$ planes and thus make a horizontal boundary a local minimum of the energy function. The logic is that the two middle grains share a (11) plane that happens to be the (01) plane in the reference frame of the domain. In order to keep the stability of the isotropic junctions, the anisotropy of the boundaries is only "activated" at the inserted twin boundary. The Ξ function is devised such that the ratio between the reference isotropic boundaries and the twin boundary r can be calibrated. This initial configuration is represented in Figure 5.2.

The mesh is remeshed at every iteration of the grain growth algorithm for numerical efficiency. The same type of anisotropic remeshing algorithm used in [91, 109] is used here. The idea is to have a zone close to the interface and in the normal direction very concentrated in mesh nodes and to coarsen the mesh elsewhere. As such, maximal precision can be concentrated in the greatest zones of interest. Outside the refined zone the mesh is isotropically defined with a mesh size of $h_{coarse} = 7e - 3$ and inside the refined zone the mesh is anisotropically defined with a mesh size in the normal direction of $h_n = 1e - 3$.

Knowing that the coherent twin boundary is a very low energy boundary one may study multiple iterations of the same configuration by increasing the heterogeneous ratio r (thus steadily decreasing the energy of the twin boundary). Observations in real twinned microstructures promote the idea that this configuration is relatively stable. Even though there is no way for this structure to be completely stationary, increasing the heterogeneous ratio should make it decay less rapidly at least. Figure 5.3 reports on the total energy
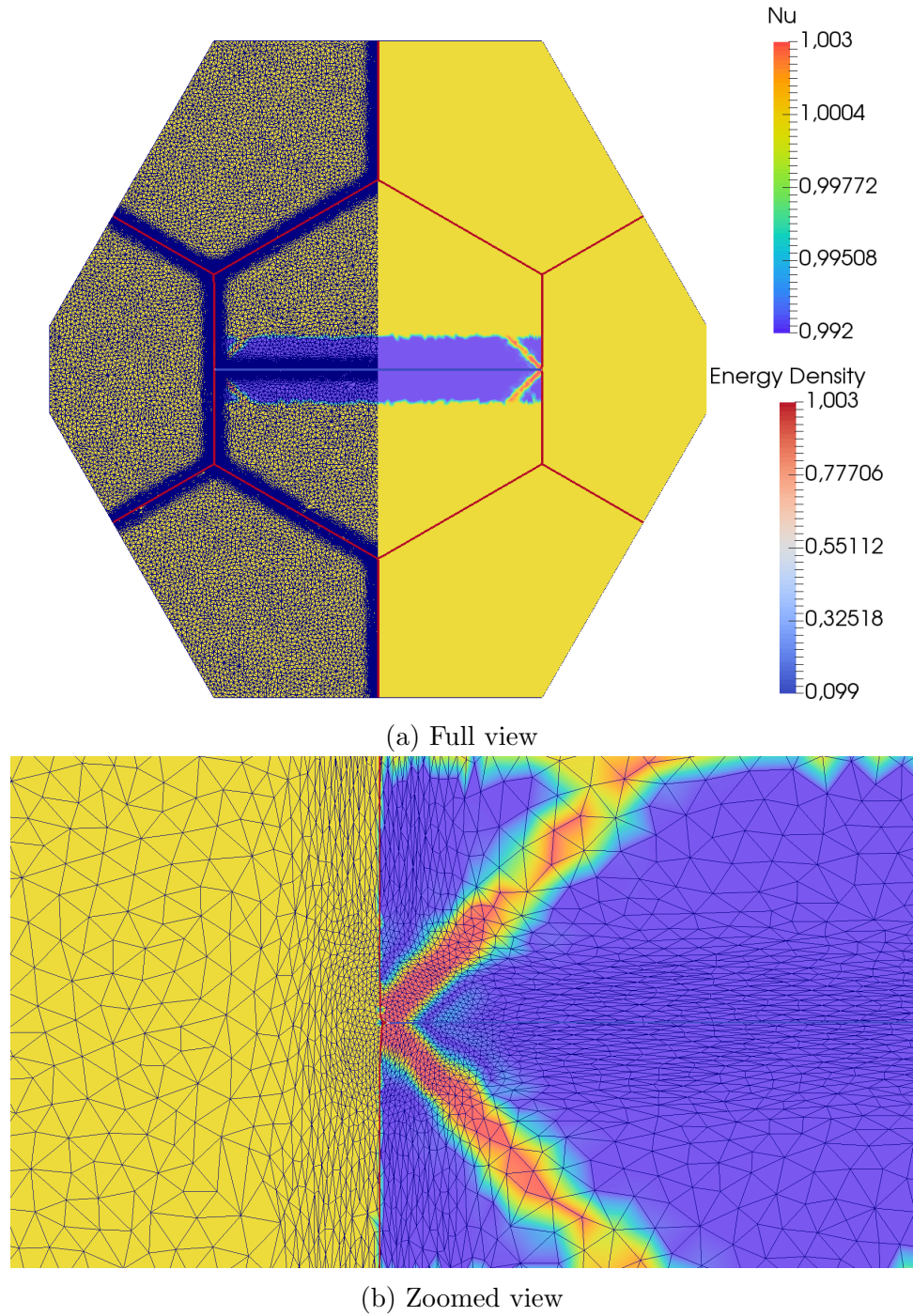
(a) Full view

(b) Zoomed view

Figure 5.2: Initial configuration of the twinned grain benchmark for $r = 10$. The boundaries are colored by their energy density and the ν field values are represented. The mesh is shown on half the figure and a zoomed view is portrayed at the left triple junction of the low energy boundary.
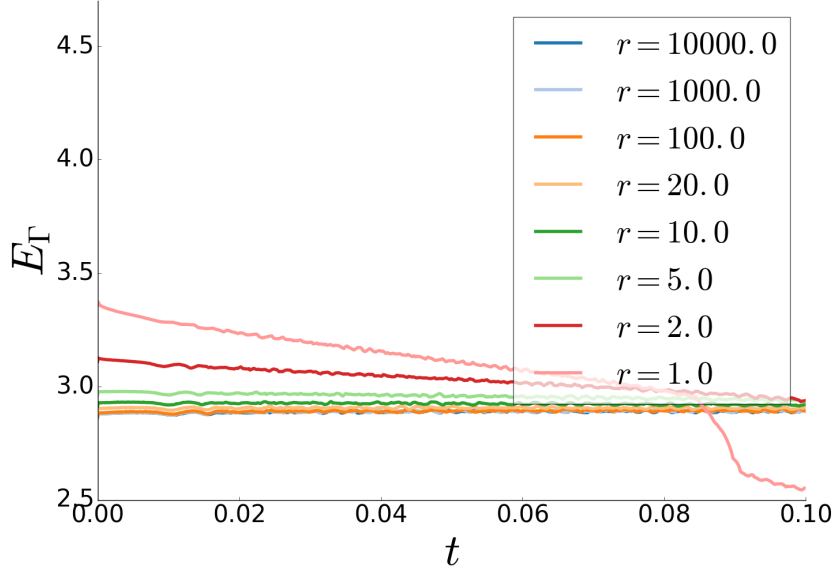
Figure 5.3: Total energy E_Γ as a function of t for various heterogeneous ratios.

evolution of the system as a function of time for different heterogeneous ratios. This figure demonstrates that as the ratio increases, the evolution in total energy of the systems tends to converge. This means that there seems to be a sort of upper limit in the stability of the system which is obtained around $r = 100$.

Figure 5.4 shows different snapshots of the configurations of the boundaries for the $r = \{1, 10, 100\}$ systems. The first observation is that increasing the heterogeneous ratio does stabilize the grain. It takes much longer for the lower energy boundaries to disappear than the boundary in the $r = 1$ case. This is thanks to the more obtuse angles created at the triple junctions in the higher ratio cases. However, what is perhaps surprising is the role of the torque terms in the simulations. There seems to be a competition between the torque generated by the twin boundary, which will tend to keep the boundary horizontal, and the torque generated by the multiple junctions, which tend to lightly incline the twin boundary. Indeed, the twin boundary in both the $r = 1$ and $r = 10$ cases has a tendency to rotate from the influence of both the right and left junctions. The $r = 100$ case seems to be relatively unaffected by the torque terms as compared to the two other simulations. Whether this is because the torque terms at the junctions are relatively less intense or because the torque of the boundary is more dominant is unknown as of now. This sort of interaction is of importance in boundary migration in polycrystals and merits more profound investigation.

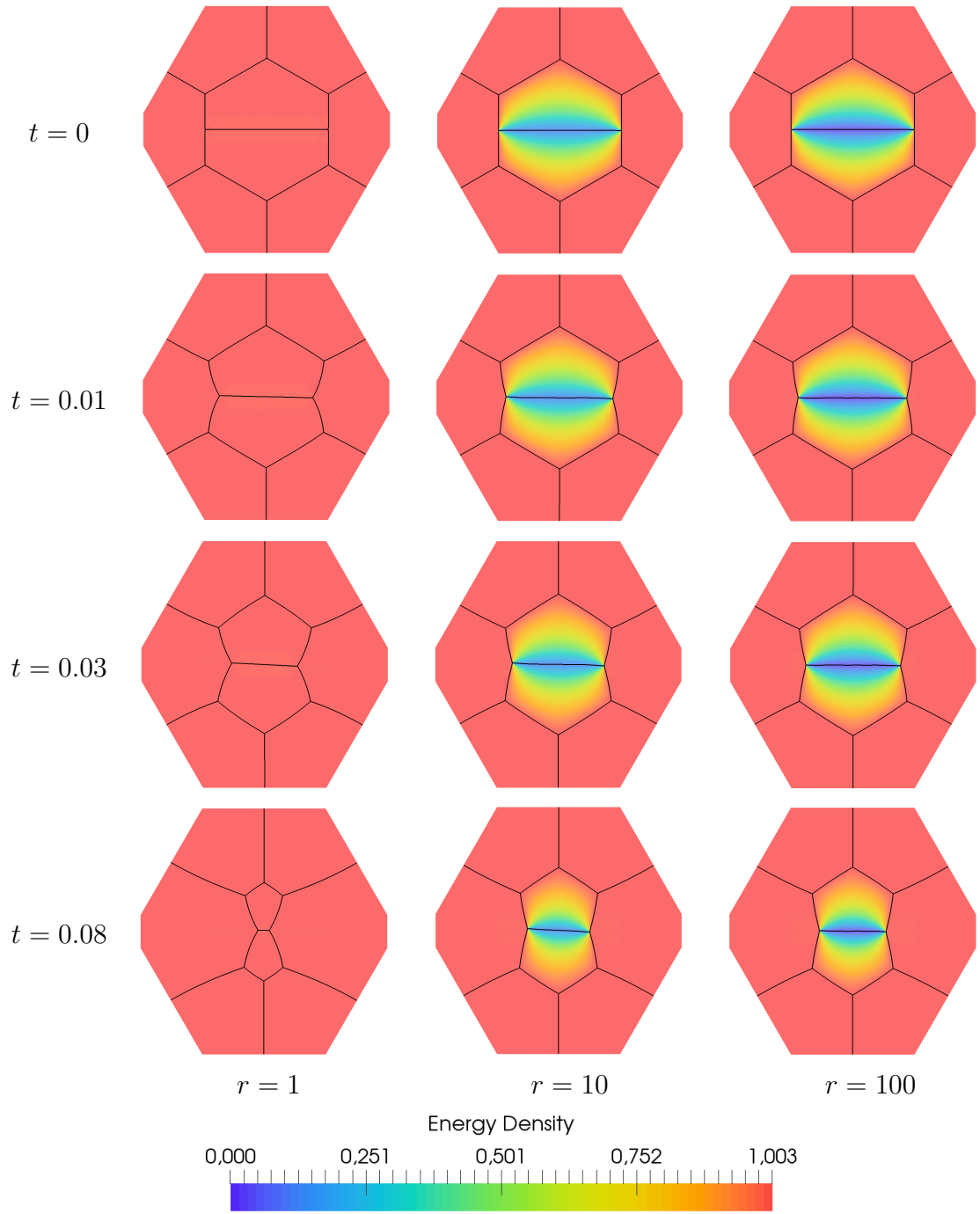Using these insights and setting $r = 100$, other interesting twin boundary configura-

Figure 5.4: Comparison of twinned grain configurations at different simulation times for different heterogeneous ratios r.

tions can be simulated using the same template. Figure 5.5 shows the time evolution of some other grain structures including twin boundaries. Ultimately the "Double" configuration contains much of the same information as the single twin boundary case presented above. Including these results here serves to highlight the flexibility of the formulation to describe complex grain structures. The "Step" configuration appears very often in highly twinned monophase materials. The step itself is often very stable due to the fact that the system prefers to keep as much coherent boundary length as possible. The results of the simulations tend to diffuse this kink along the twin boundary until arriving at a stationary state where the equilibrium at the triple junctions and smoothed profile is obtained. The reason for this discrepancy is most likely due to the very low anisotropy of the ν function used in these tests. Indeed, the differences in between the highest and lowest energy boundaries at a fixed misorientation is only about 6%.

If this is true, the one may question the choice of this anisotropic modifier for testing twin boundary dynamics. Even so, one would be reminded of the constraints on the γ function and its dependence on the inclination of the boundary in equations (3.20), (3.21) and (3.22) for the well-posedness of the problem. Indeed, this ν is, in some sense, already a maximally anisotropic function that satisfies these constraints and keeps all the components of the D tensor bounded. Given these somewhat disappointing results in the "Step" configuration the only answer this model can provide is that the true anisotropy related to the twin boundaries is much stronger than the ν function used here. As such, the only conclusion that one might make is that the components of the D tensor must be *unbounded* for certain values of the inclination of the interface. Letting certain values of the tensor go to ∞ for given inclinations would effectively remove this anisotropy limit and keep the problem essentially well-posed. However, this would also render these special inclinations dynamically impossible to obtain in simulations. As soon as an interface would start to rotate towards these inclination values they would diffuse faster and faster. The unboundedness of the D tensor would effectively render certain boundary inclinations impossible to obtain dynamically and therefore would annihilate their existence in virtual microstructures. This idea of excluded inclination values for crystalline boundaries has been studied since seminal papers by Cahn and Hoffman [98, 99] but in a surface equilibrium sense and not a dynamical setting. To this author's knowledge no work exists on these kinds of dynamical effects arising in polycrystals. From a numerical point of view, unbounded D tensors pose the challenge of computing dynamics with potentially infinite values which is not to be taken lightly.

In any case, what is clear from the results of these simulations is that, although the setting is greatly improved from the classical modeling of isotropic curvature flow, it is currently insufficient to reproduce the exact observed behaviors of the twin boundary.
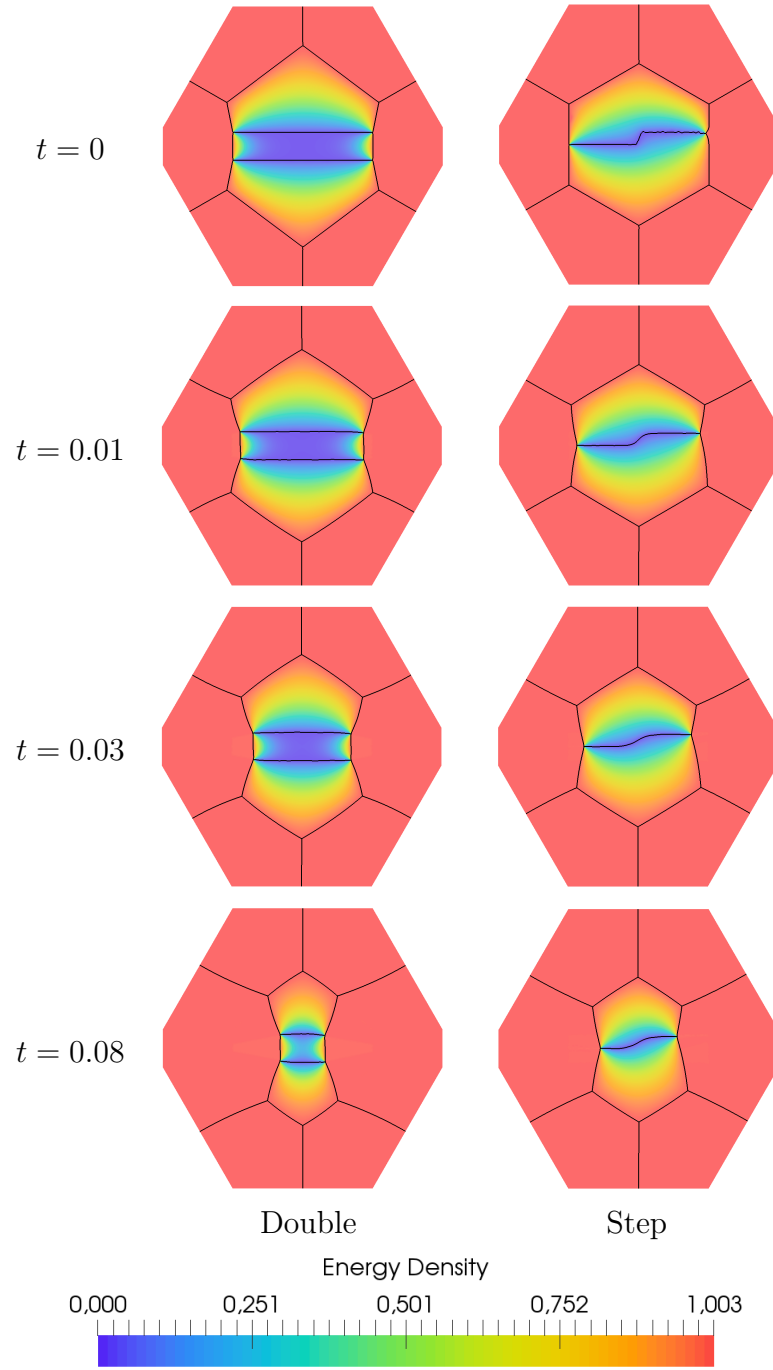
140

Figure 5.5: Time evolution of "Double" and "Step" twinned grain configurations with $r = 100$.
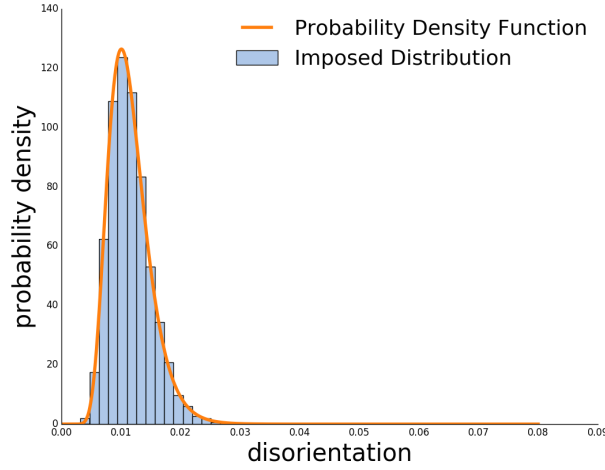
Figure 5.6: Normalized numerical microstructure initial grain radius distribution in both analytical form as well as discretized.

5.2 Purely heterogeneous 2D microstructures

Once a numerical framework capable of simulating heterogeneous microstructures is developed, it can be interesting to see the effects that simple disorientation angle dependent grain boundary energies can have on the evolution of a polycrystal. As such, this section is devoted to simulating grain growth on virtually generated statistical microstructures using a variety of grain boundary energy functions. The results of these simulations are evaluated using both the time evolution of mean values and distributions of characteristic fields (grain size, disorientation angle, coordinance, ...). As a disclaimer, the simulations performed in this section were run before the development of the "Projected" formulation presented in Chapter 4. As such, the "Full" formulation, defined in the same Chapter, for grain growth was utilized. Towards the end of the section the effect of this choice is explored.

A reference numerical microstructure will be studied in what follows. This polycrystal is representative of a monophase material with a log-normal distribution of grain sizes as shown in Figure 5.6.

Crystallographic orientations are attributed to the grains by generating Euler angles randomly, for example Figure 5.7a where the color scheme is developed using the vector magnitude $e = \sqrt{\varphi_1^2 + \Phi^2 + \varphi_2^2}$ where $(\varphi_1, \Phi, \varphi_2)$ are Euler angles, leading to a Mackenzie type disorientation distribution [110] as demonstrated in Figure 5.7b. Also, all the disorientation distributions measured here are weighted by boundary length and not by number.

The polycrystal is generated using a Laguerre-Voronoi tessellation with a dense sphere
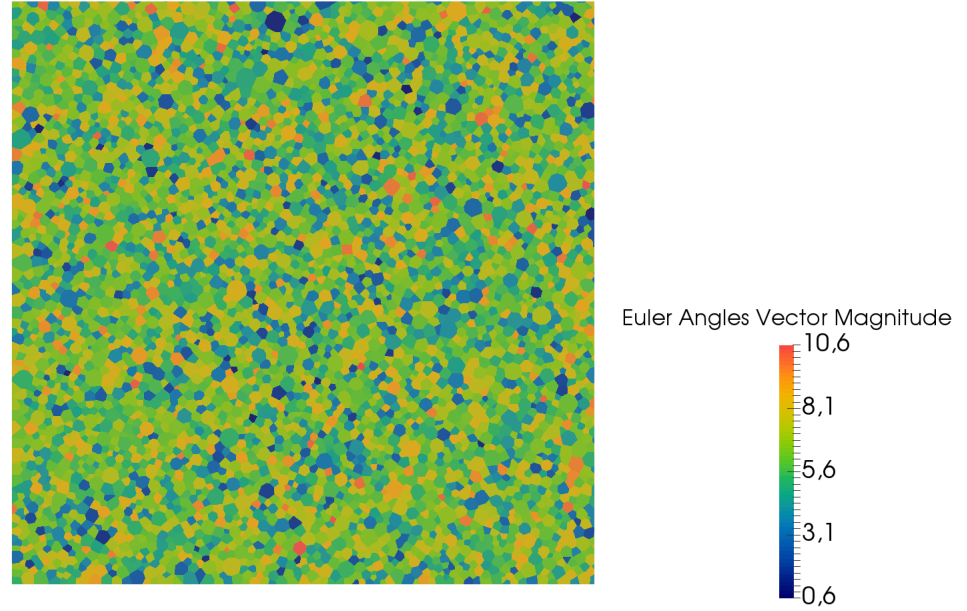
(a) Example of a generated microstructure containing approximately 5000 grains and colored by the magnitude of a vector whose components are the Euler angles of the crystallographic orientations.
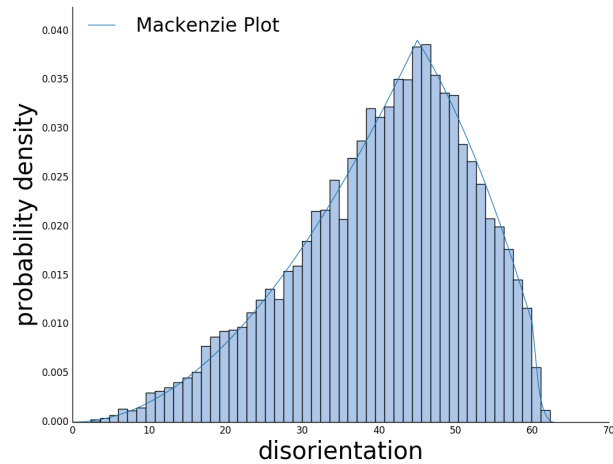
(b) Initial disorientation distribution with the analytical solution for the Mackenzie plot [110]

Figure 5.7: Crystallographic characterization of the microstructure: (a) an image of the numerical microstructure and (b) its disorientation distribution.

Figure 5.8: Illustration of the anisotropic mesh refinement operating at the interfaces between grains as in [91, 109], using the same color map as Figure 5.7a.
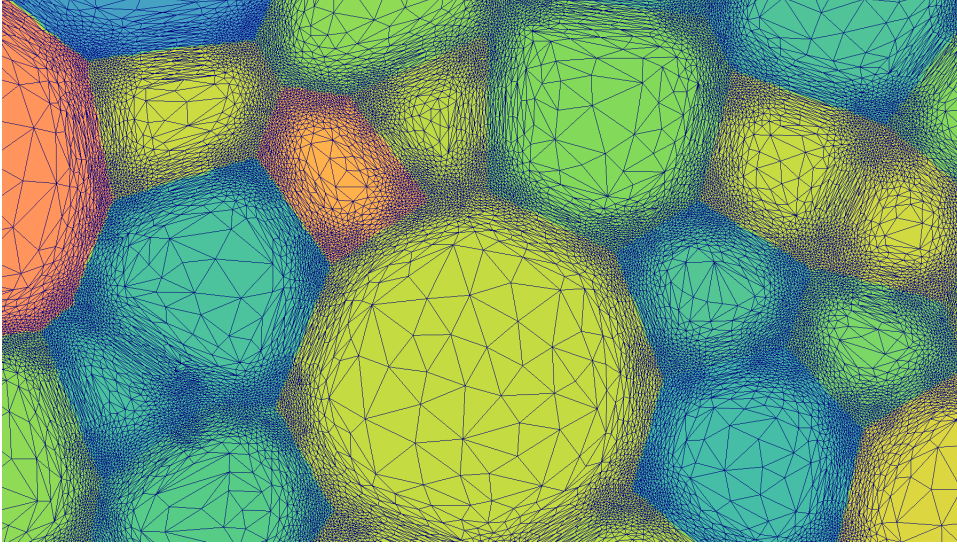
packing algorithm described in [111]. The size of the domain determines the number of grains. Anisotropic re-meshing is used [91, 109] and the mesh is refined close to the interfaces as exhibited in Figure 5.8. With this algorithm, the sizes of the grains at the border of the domain respect the imposed distribution and thus can and are considered in the statistical analysis.

The mesh size in the normal direction is studied in what follows. The mesh size in the tangential direction as well as far away from the interface (at a distance $\eta = 6.2 \mu m$) is fixed at $5 \, \mu m$. The initial average grain radius is $\bar{R} \simeq 12 \, \mu m$. The average grain boundary energy is aimed at $\bar{\gamma} \simeq 1 \, J \cdot m^{-2}$ and the mobility used is $\mu = 0.1 \, mm^4 \cdot J^{-1} \cdot s^{-1}$ which are of the order of pure Nickel at $1400 \, K$ [40, 41].

In order to study the sensitivity to numerical parameters in a heterogeneous setting, a form for the misorientation dependent grain boundary energy must be chosen. Below, due to its prevalence in the literature, a Read-Shockley type function (RS) [36] is chosen

$$
\gamma(\theta) = \begin{cases} \gamma_{max} \left(\dfrac{\theta}{\theta_{max}} \right) \left(1 - \ln \left(\dfrac{\theta}{\theta_{max}} \right) \right), & \theta < \theta_{max} \\ \gamma_{max}, & \theta \geq \theta_{max} \end{cases}
\tag{5.2}
$$

where θ is the disorientation, γ_{max} is the maximal grain boundary energy here equal to $1.012 J \cdot m^{-2}$ and θ_{max} is a threshold angle taken here, to be $30°$. Commonly, when using the Read-Shockley function, the low angle grain boundary cut-off is considered to be in the $10 - 15°$ range. Here, a value of $30°$ was chosen in order to exaggerate the heterogeneity and produce measurable heterogeneous effects. The function is plotted in Figure 5.9.
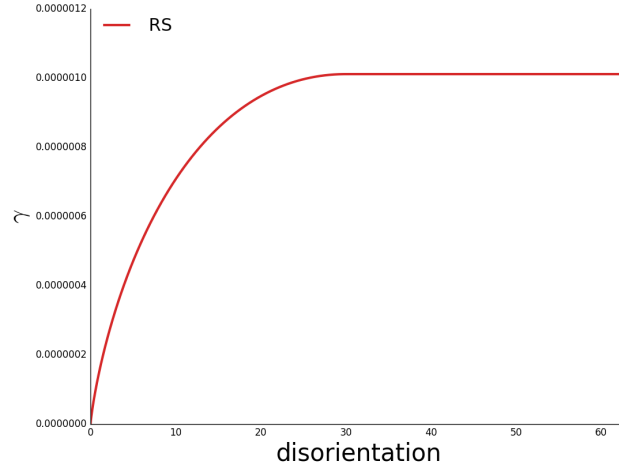
Figure 5.9: The Read-Shockley (RS) function for grain boundary energy.

The sensitivity of the evolution of the mean grain size $\bar{R}$, the number of grains N_{gr} as well as the total interface energy

$$E_\Gamma = \int_\Gamma \gamma d\Gamma, \tag{5.3}$$

will be studied. Convergence with regard to a numerical variable x (where x can be the mesh size or the time step) will be determined using an averaged L^2 error e_{L^2} relative to the energy evolution of the microstructure

$$e_{L^2}(x) = \sqrt{\frac{1}{t_{end}} \int_0^{t_{end}} (E_\Gamma^{ref} - E_\Gamma(x))^2 dt}, \tag{5.4}$$

where E_Γ^{ref} is determined from a linear fit with respect to time of the most precise simulation (i.e. the smallest time step and mesh size). Supposing the evolution of e_{L^2} follows a polynomial type law,

$$e_{L^2}(x) = Ax^n, \tag{5.5}$$

one may extract the convergence parameters A and n using a logarithmic scale plot.

In order to study the sensitivity of the simulation to the discretization of both space and time a microstructure of physical side length $l = 0.5mm$ was generated (containing about 600 grains) and virtually annealed for a physical time of $t_{end} = 30\,min$ with different mesh sizes h_n in mm and time steps Δt in s. The mean value results of these simulations are exposed in Figures 5.10 and 5.11 for the mesh size and time step convergence respectively.
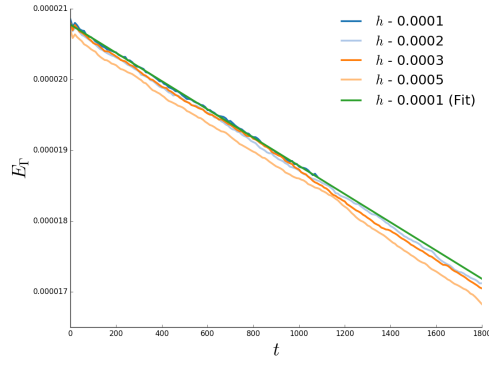
(a) $E_\Gamma = f_{h_n}(t)$ (linear fit)
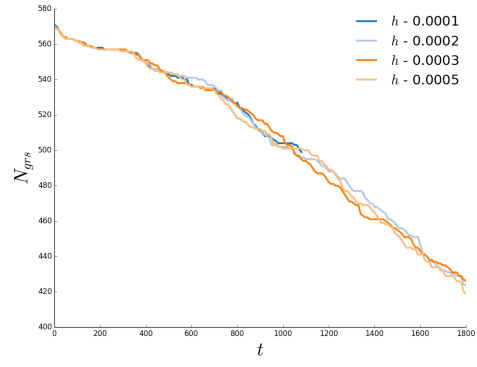
(b) $N_{gr} = f_{h_n}(t)$
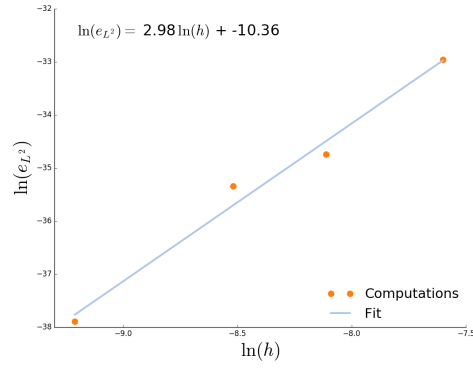
(c) $f(h_n) = e_{L^2}$
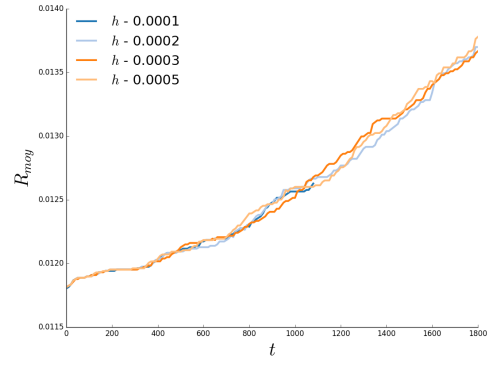
(d) $\bar{R} = f_{h_n}(t)$

Figure 5.10: Evolution of mean field values with the mesh size h_n at a fixed time step $\Delta t = 10s$
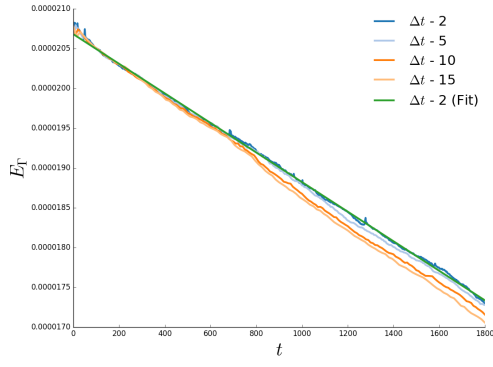
(a) $E_\Gamma = f_{\Delta t}(t)$ (linear fit)
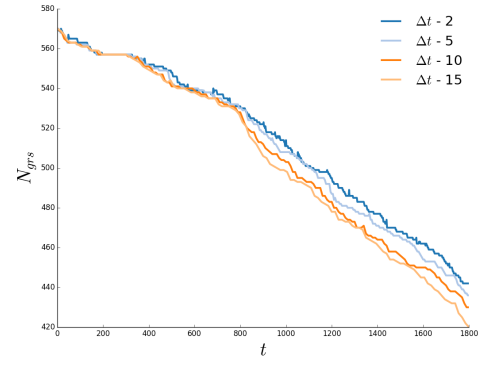
(b) $N_{gr} = f_{\Delta t}(t)$
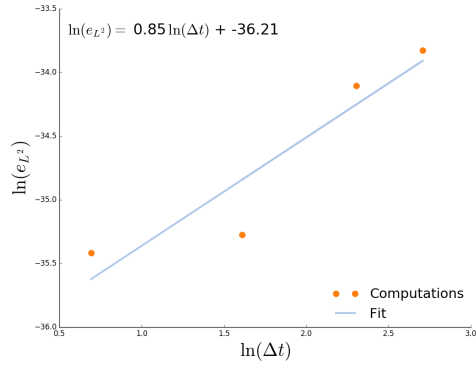
(c) $f(\Delta t) = e_{L^2}$
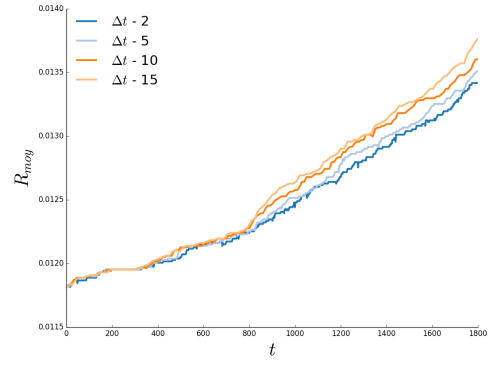
(d) $\bar{R} = f_{\Delta t}(t)$

Figure 5.11: Evolution of mean field values with the time step Δt at a fixed mesh size $h_n = 0.3\mu m$

Convergence is clearly established both as a function of mesh size and time step for the polycrystal simulations in the range of values presented here. This means that the precision of the solutions obtained can be improved by refining both time and mesh discretizations arbitrarily and independently.

With the introduction of spatial heterogeneities comes the question of the representativity of a microstructure [112]. If a given volume of matter is representative of the behavior of the whole when the models do not contain heterogeneities, is this volume as representative when one starts to include local variations in properties? The answer is surely dependent upon the nature of the inserted heterogeneity.

As such, one can study the effect that the size of the polycrystal has on the results of the simulation, but also, the effects that variations in the spatial distributions of grains might generate. Therefore, in order to study the variability of the calculations as a function of size, with l the side length of the square domain, and spatial distribution of heterogeneities 9 simulations were performed in order to test 3 domain sizes and 3 different polycrystal generations. As such, the statistical parameters of the polycrystals described above remain the same, yet the local parameters and the influence of the boundary conditions vary. A supplemental reference simulation with an even larger volume element, $l = 2\,mm$ and approximately 8000 grains, was performed in order to use as a reference point. Figure 5.12 illustrates the numerical plan.

The results of the simulations are presented in Figure 5.13. While the results do vary as a function of the size of the domain, which is expected, sensible distinctions are to be made when comparing the differently generated microstructures. Perhaps most surprisingly, the differences between different randomly generated microstructures are of the same order as the differences between the different sizes of volume elements. In any case, a convergence, in the same sense as for the time step or the mesh size, is observed for the three generated microstructures in that they get closer to the behavior of the most precise simulation as their size increases. Even so, one should probably not trust the representativity of these microstructures for modeling real-life materials. Even if convergence in the size of the domain is observed, there is no reason that bigger more representative microstructures might not deviate from the results shown here.

Indeed, to the present author's knowledge, no such study has been conducted in virtual statistical polycrystal generation such that there is a clear answer as to the number of grain boundaries one might need to simulate in order to obtain trustworthy results in the case of heterogeneous grain boundary energies. As such, in order to circumvent this understandable objection to the results that follow, here we propose to only compare microstructural evolutions that originate from exactly the same microstructure. By fixing not only the geometry of the initial grain boundary network but also the orientations of all the grains, the deviations of simulated microstructural evolutions from one another can only be attributed to the differences in their grain boundary energy functions. By proceeding in this relative sense the representativity of the microstructure is no longer an issue. In the following, a microstructure with a side length of **1.5mm** and approximately
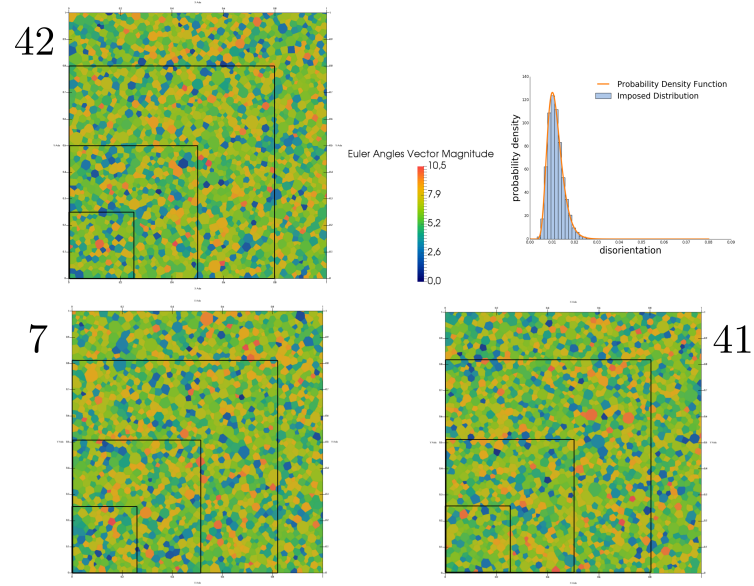
Figure 5.12: Visual explanation of the volume element sensitivity study. The three microstructures were generated using three different random seed generators for the packing algorithm and three sizes were obtained from each of the generations, $l = \{0.5\,mm, 1.0\,mm, 1.5\,mm\}$ (in the images smaller microstructures are used to make the information more visible).The color map is the same as in Figure 5.7a
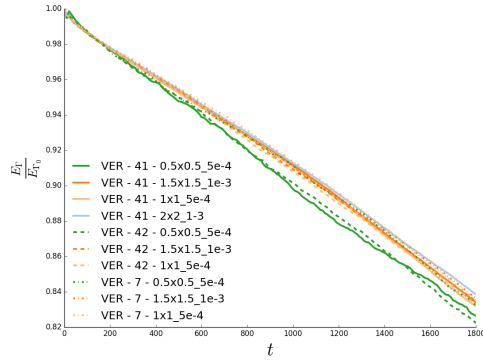
(a) $E_\Gamma = f_l(t)$
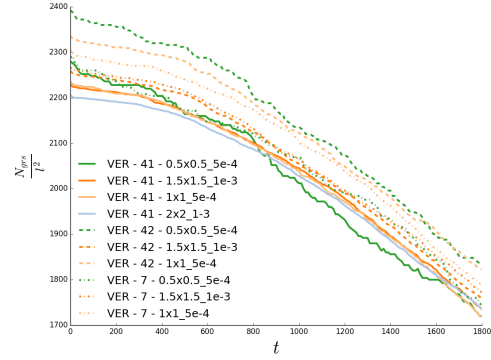
(b) $\frac{N_{gr}}{l^2} = f_l(t)$
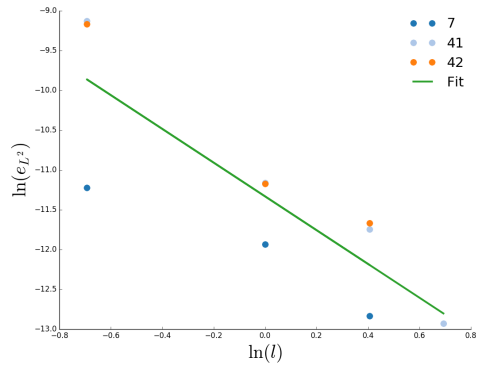
(c) $f(l) = e_{L^2}$
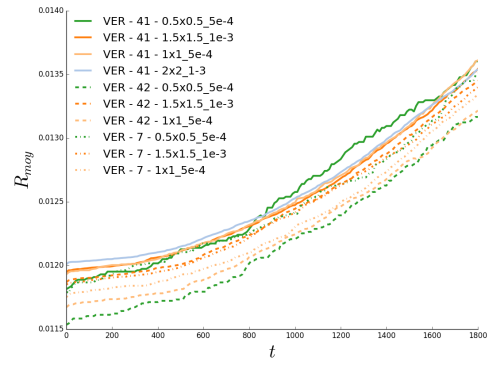
(d) $\bar{R} = f_l(t)$

Figure 5.13: Evolution of the normalized energy, grain number density, L^2 error relative to the normalized energy and mean grain size as a function of the different RVE generations and sizes. The referencing of the microstructures can be found in Figure 5.12.

5000 initial grains is studied.

Now, even though the RS function for the grain boundary energy is widespread, it does not allow for testing large heterogeneities in untextured microstructures. As such, in order to study the response of a polycrystal to different levels of heterogeneity, grain boundary energy test functions must be generated and compared with respect to the homogeneous case. However, in order to compare the effects of different grain boundary energy functions fairly, there must be a common scaling imposed upon the functions such that they become comparable. In this study, an average initial grain boundary energy of the microstructure was imposed constant for all mappings $\gamma(\theta)$:

$$\bar{\gamma} = \frac{\int_{\Gamma} \gamma d\Gamma}{\int_{\Gamma} d\Gamma}, \tag{5.6}$$

which can also be seen as the same initial total energy for all cases given that the initial polycrystal is also unvarying. In order to solve this problem analytically, one can integrate the grain boundary energy function over the disorientation distribution of the microstructure, which is the Mackenzie plot in this case,

$$\bar{\gamma} = \frac{1}{\theta_{lim}} \int_{0}^{\theta_{lim}} \gamma p_{Mac} d\theta, \tag{5.7}$$

where p_{Mac} is the probability density related to the Mackenzie distribution [110] and $\theta_{lim} = 62.8°$ is the limit of the fundamental region of the disorientation for cubic structures.

Even so, when attempting to choose a misorientation dependent grain boundary energy function there are multiple things one might want to look for. The constant grain boundary energy function, i.e. the homogeneous case, is by default the reference case. The Read-Shockley [36] type grain boundary energy is the most popular function in the current literature for modeling low angle grain boundaries. However, if one wishes to introduce a more diverse set of grain boundaries, one may modify the RS function, for example, in a very discontinuous manner such that the disorientation region where twin boundaries are found can be much lower energy than the rest. Also, in both numerical and experimental approaches to determining the grain boundary energy function, cusps are present and one might wish to study the effect these minima might have on the evolution of the grain boundary network, hence one may use a "bumpy" energy function in order to study these cusps as shown below. In a mathematical approach, one may use a more classical function, such as a Gaussian distribution function, in order to probe the effects of a more "naturally" distributed energy. Given this reasoning, five test functions, which do not aim to be physical representations of the grain boundary energy function, are considered in this work:

Homogeneous

$$\gamma = \bar{\gamma} \tag{5.8}$$

(a) $\gamma(\theta)$　　　　　　　(b) $\gamma p_{Mac}(\theta)$
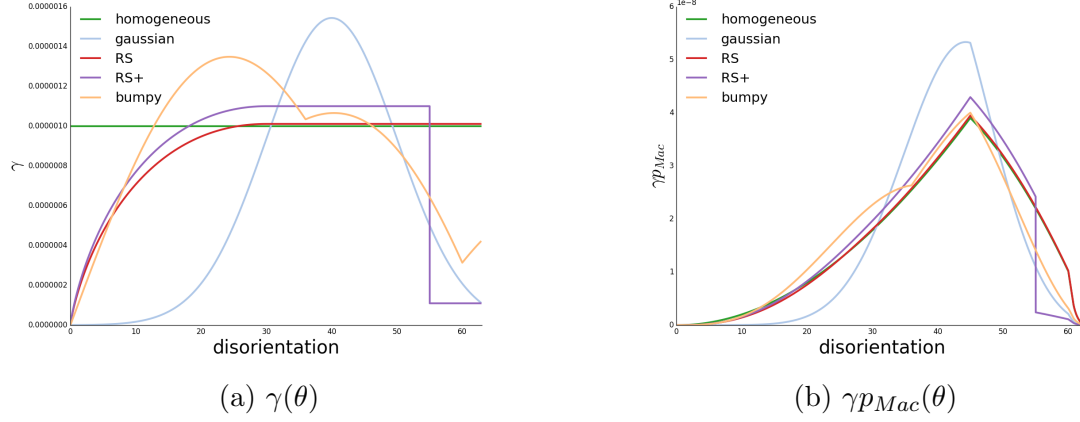
Figure 5.14: Considered test grain boundary energy functions.

RS the same as in equation (5.2).

RS+

$$
\gamma = \begin{cases}
\gamma_{max}\prime \left(\dfrac{\theta}{\theta_{max}}\right)\left(1 - \ln\left(\dfrac{\theta}{\theta_{max}}\right)\right), & \theta < \theta_{max} \\
\gamma_{max}\prime, \quad \theta_{thresh} > \theta > \theta_{max} \\
0.1\gamma_{max}\prime, \quad \theta > \theta_{thresh}
\end{cases}
, \tag{5.9}
$$

where $\gamma_{\mathrm{max}}\prime \simeq 1.1\,J/m^2$ and $\theta_{thresh} = 55°$.

Bumpy

$$
\gamma = \gamma_b(\alpha_3|\sin(3\theta)| + \alpha_5|\sin(5\theta)|) \tag{5.10}
$$

where $\gamma_b \simeq 1.2\,J/m^2$, $\alpha_3 = 0.9$ and $\alpha_5 = 0.3$.

Gaussian

$$
\gamma = \gamma_g e^{\frac{-(\theta-\theta_\mu)^2}{2\theta_\sigma^2}} \tag{5.11}
$$

with $\gamma_g \simeq 1.54 J/m^2$, $\theta_\mu = 40°$ and $\theta_\sigma = 10°$.

Figure 5.14 shows both the plot of the grain boundary energy functions as well as a graph of the analytical grain boundary energy distribution densities γp_{Mac}.

What is most striking in Figure 5.14 is that seemingly large differences in the base grain boundary energy functions can actually have little to no impact on the actual heterogeneity present in the microstructure. For example, Figure 5.14b shows that the RS function is actually extremely close to the homogeneous function when the disorientation distribution is taken into account. Even so, the panel of functions chosen here gives access to a relatively diverse spectrum of heterogeneities in the actual microstructure. This can be

Energy Function	d_{L^2}
RS	2.89e-3
RS+	3.70e-2
Bumpy	2.90e-2
Gaussian	6.44e-2

Table 5.1: The L^2 distances of the heterogeneous γp_{Mac} functions from the homogeneous one.

quantified by the values present in Table 5.1 which represent the L^2 distance of each of the heterogeneous γp_{Mac} functions with respect to the homogeneous γp_{Mac} function calculated using a simple trapezoidal rule for the numerical integration. This table gives a gauge of the heterogeneities present in each of the functions which can be observed to vary from least to most heterogeneous in the following order: RS, Bumpy, RS+ and Gaussian.

The first observation concerning the time evolution of both the mean grain radius and the number of grains is that the more heterogeneous a grain boundary energy function is, the slower its kinetics, a result easily corroborated in most heterogeneous grain growth simulations in the literature [60, 67, 69, 74–78]. Looking at the evolution of the energy however, the cases with the most heterogeneity are also those which dissipate the interface energy the most efficiently. As such, the most heterogeneous case should have the smallest grains and thus the largest amount of interface length and yet it has the smallest total energy. A direct explanation for this phenomenon could be that the most heterogeneous cases have the most diverse grain boundary energy distributions and thus the most degrees of freedom for minimizing the energy of the system.

Also, the slowing of the kinetics of grain growth could be related to the phenomenon discussed in certain experimental studies known as orientation pinning [115, 116]. This mechanism is related to the fact that as grains grow and compete for space, the probability that a grain encounters a particularly unfavorable orientation for its continued expansion increases. As the grain meets this disadvantageous orientation (creating a low energy grain boundary) its kinetics slow and therefore the orientation cohabitation tends to persist during the rest of the grain coarsening process. Typically, this is a process that is not observable in simulations unless using a heterogeneous description of the grain boundary energy and becomes even more evident as the heterogeneity is increased.

More generally, the results presented in Figure 5.15 show that even with the same average grain boundary energy, the kinetics of grain growth can vary significantly. As such, using time evolution of grain size, for example, in order to calibrate average grain boundary energies experimentally is clearly limited. More in depth characterizations of the microstructure are needed in order to probe the nature of the grain boundary energy distribution. In [117] is proposed an interesting idea in which the grain boundary character distribution should be inversely correlated to the grain boundary energy function. In other terms, the most energetic grain boundaries should tend to disappear leaving only the least
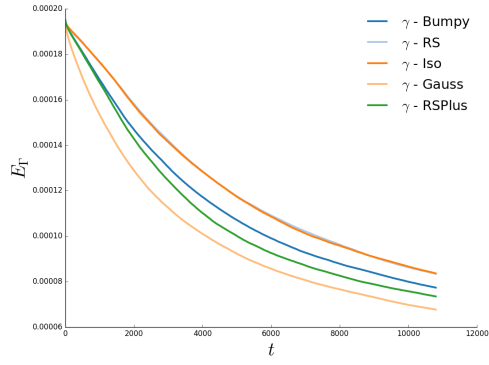
(a) $E_\Gamma = f(t)$
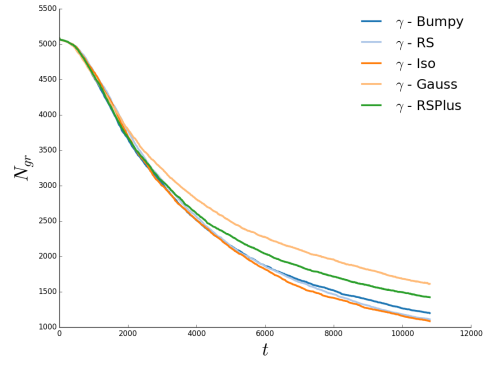
(b) $N_{gr} = f(t)$
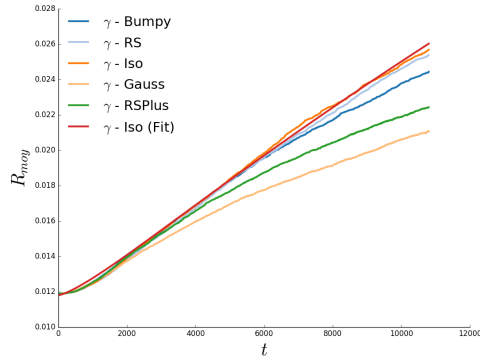
(c) $\bar{R} = f(t)$

Figure 5.15: Time evolution of mean values for the different grain boundary energy functions. The mean grain size evolution of the homogeneous case is fitted with a generalized Burke and Turnbull type law [113, 114].

energetic boundaries during grain growth.

In a three dimensional experimental polycrystal, the grain boundary character distribution would have to be set in the five dimensional grain boundary space [49] in order to be complete. However, this is impractical due to the high dimensionality and small datasets available. Here, given the way in which the grain boundary energy functions are defined, only one variable of the grain boundary character is considered, the disorientation. As such, the disorientation distributions at $10000\,s$ are plotted for the different grain boundary energy functions as well as the grain boundary energy distributions in Figure 5.16. The grain size distributions are also compared in the same figure.

The differences in between the disorientation distributions obtained from the different grain boundary energy functions are striking. While the homogeneous case emulates the Mackenzie plot throughout the simulation, the RS function, even given its proximity to the homogeneous case, favors low angle grain boundaries, a result also found in [77,86,88]. The RS+ case also encourages low angle grain boundaries, as in the RS case, but tilts towards the high angle boundaries as well (the transition is around $55°$). The bumpy case also tends toward keeping its least energetic boundaries, a behavior replicated in the Gaussian case which tilts towards a bimodal distribution. Globally, using this formulation for grain growth, the character distribution of the boundaries are clearly inversely correlated with the grain boundary energy functions, a statement also supported by the grain boundary energy distributions, which would corroborate [117].

The grain size distributions are relatively diverse as well. However, upon closer inspection, they all respect a lognormal type distribution law and their differences can be clearly explained by the different growth kinetics of the different cases shown in Figure 5.15.

The virtual micrographs of the various cases after 3 hours of annealing are presented in Figure 5.17. The quantitative results present in Figure 5.16 are clearly represented in the virtual microstructures qualitatively given the diversity of grain boundary energies. Perhaps more interestingly however, the grain boundary energy landscape is not the only observable difference in between the grain boundary networks developed using different grain boundary energy functions. The morphology of the grains in different cases are also relatively varied. While the least heterogeneous cases tend to favor relatively regular polyhedra, the most heterogeneous cases seem to develop more rectangular and disparate grains. This observation can be made more quantitative with the introduction of Figure 5.18. The distributions of the number of neighboring grains for each grain boundary energy functions remain centered around 5 and 6. However, the more heterogeneous cases tend to flatten their distributions acquiring a greater zoology of grains than in the more homogeneous cases, a result corroborated by [75] but contested by [76]. This polycrystal behavior is most likely a product of the diversity of triple junctions in the most heterogeneous cases compared to the more homogeneous ones. Indeed, as more and more triple junctions stray from the homogeneous $120°$ angle equilibrium, the forms of the grains become more irregular and the polycrystal manages to obtain a more diverse set.

To summarize, the simulations show that more heterogeneous microstructures exhibit
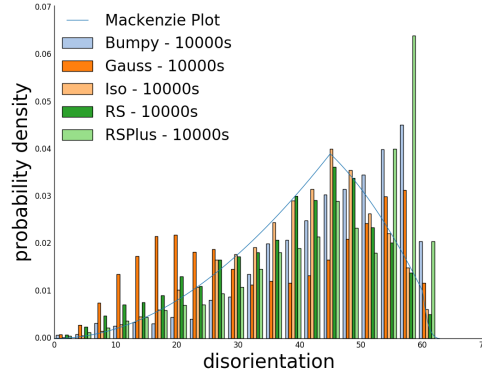
(a) Normalized grain boundary disorientation distribution
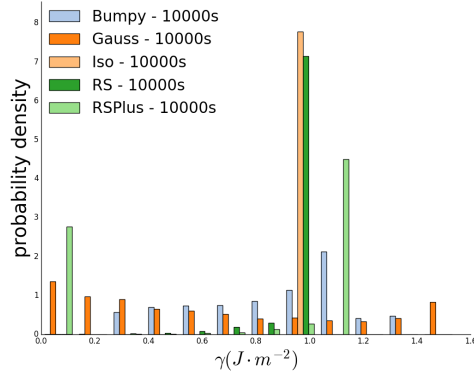
(b) Normalized grain boundary energy distribution
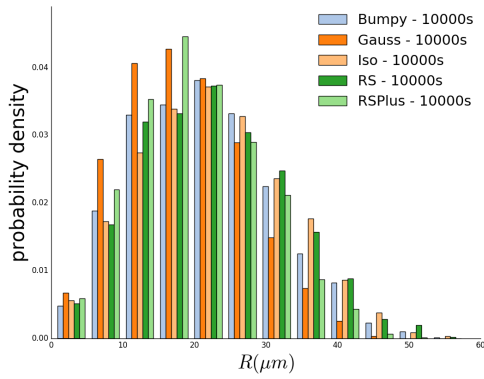
(c) Normalized grain size distribution (in number)

Figure 5.16: Comparisons of the different grain boundary energy functions using various distributions after $10000\,s$ of numerical annealing.

(a) Homogeneous

(b) RS

(c) RS+

(d) Bumpy

(e) Gaussian
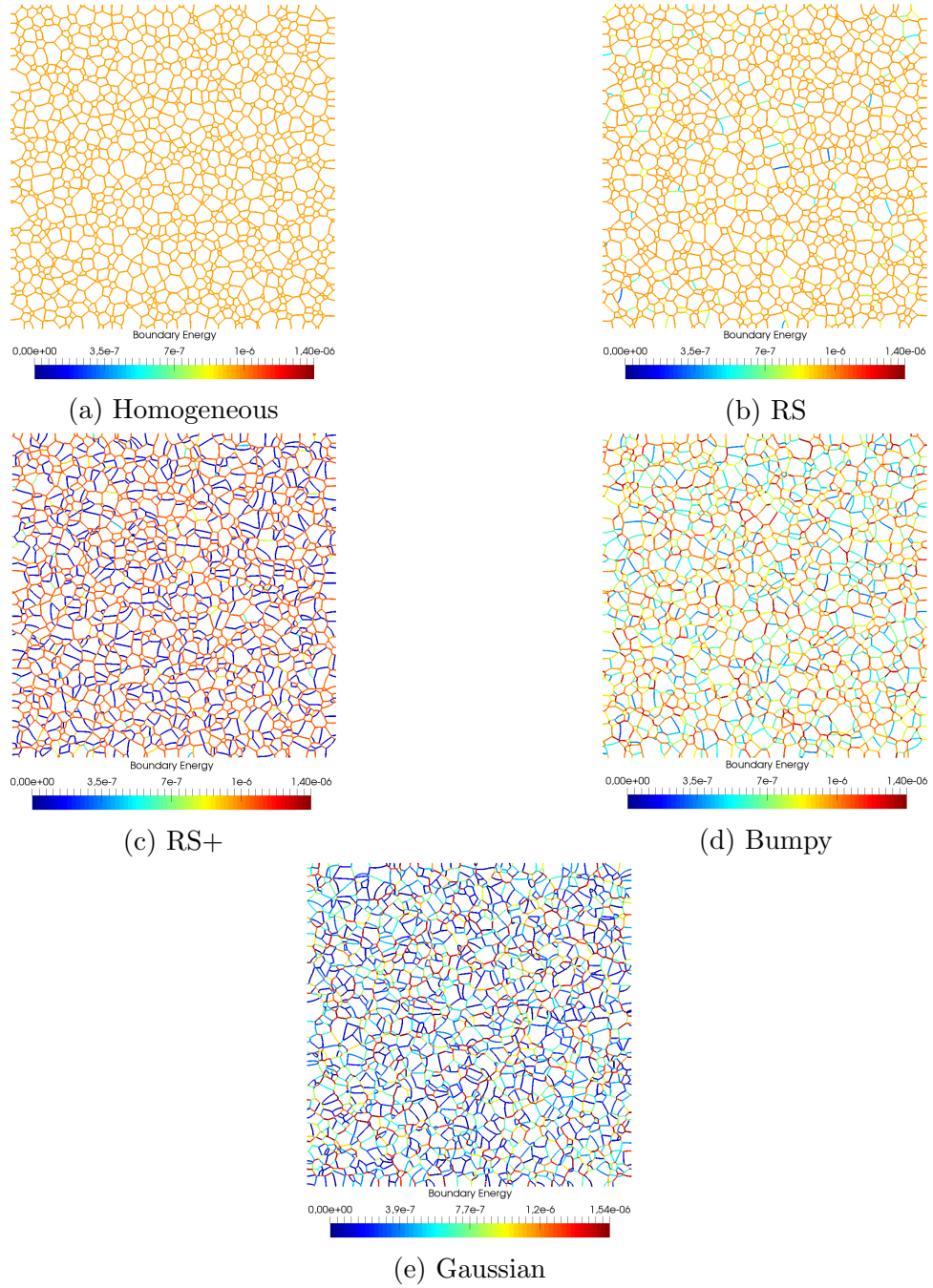
Figure 5.17: States of grain boundary networks obtained for all grain boundary energy functions after 3 hours of numerical heat treatment.
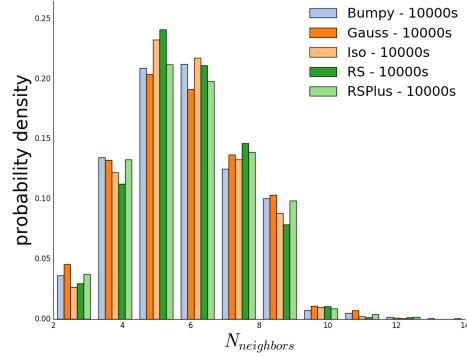
Figure 5.18: Normalized number of neighboring grains distributions for all of the studied grain boundary energy functions at 10000 s.

slower grain growth kinetics. In light of this discovery, common methods for determining mean grain boundary energy values as a function of grain growth kinetics in real microstructures can be flawed. Also, the distribution of disorientation angles is shown to evolve to be inversely correlated to the grain boundary energy function. This observation lends weight to the idea that aspects of the grain boundary energy dependence on the disorientation angle θ can be inferred from the disorientation distributions of real microstructures that have been annealed for long times. As such, if one adopts the hypotheses and simplifications that are made in the elaboration of this framework, then one could possibly use an inverse analysis approach on the misorientation distribution evolution of real materials to generate plausible candidates for misorientation dependent grain boundary energy functions. Finally, the annealed geometry of the grain boundary network depends heavily on the heterogeneity of the microstructure. This is to be expected given that the equilibria at the multiple junctions are completely determined by the grain boundary energies of the polycrystal.

As a sanity check, a further investigation into the effect of using the "Classic", "Projected" and "Full" formulations, presented in Chapter 4, for heterogeneous grain growth in polycrystals has been conducted. Using the same statistical volume element as above, with approximately 2300 initial grains, the Gaussian energy function was imposed on the microstructure so as to exacerbate the heterogeneity. The three formulations were used to simulate a three hour anneal on exactly the same initial microstructure. The mean value results are presented in Figure 5.19 and the disorientation and energy density distributions are reported in Figure 5.20.

Commenting on Figure 5.19, one could propose two different regimes. Initially, as would be expected from the results in Chapter 4, the "Projected" formulation exhibits behavior in between the "Classic" and "Full" cases remaining quantitatively closer to the "Full" results. However, at approximately $4000s$ this trend changes rather brutally.
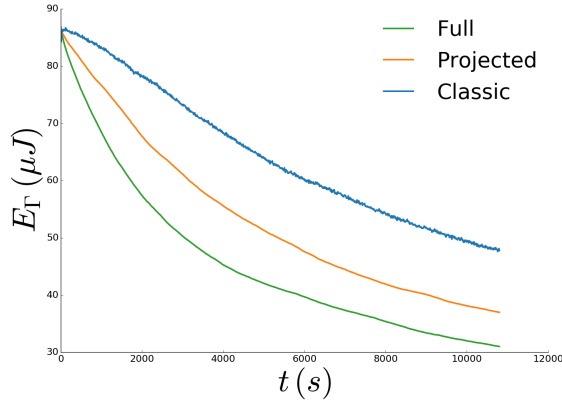
(a) $E_\Gamma = f(t)$
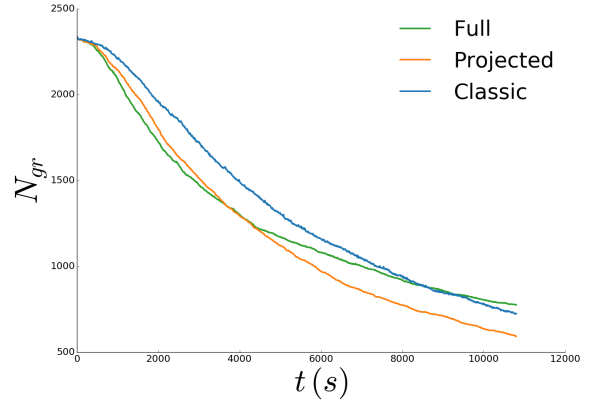
(b) $N_{gr} = f(t)$
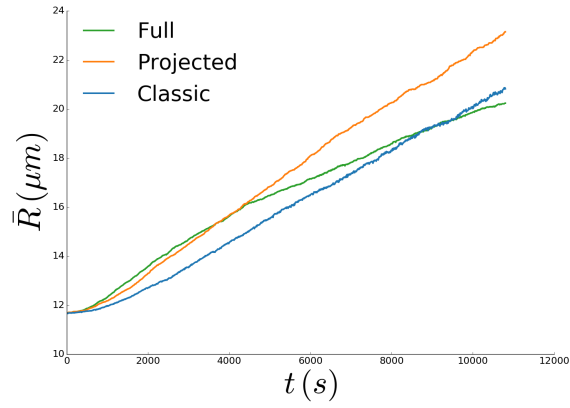
(c) $\bar{R} = f(t)$

Figure 5.19: Time evolution of mean values for the different proposed formulations for grain growth.
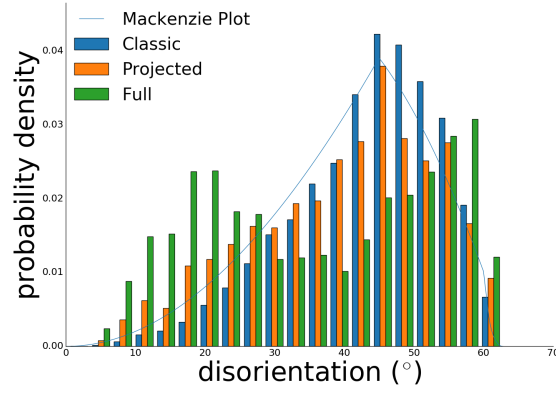
(a) Normalized grain boundary disorientation distribution
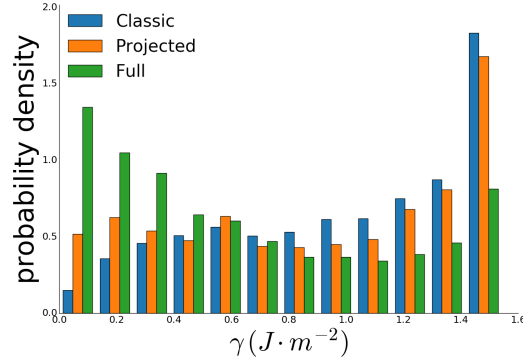
(b) Normalized grain boundary energy distribution

Figure 5.20: Comparisons of the different proposed grain growth formulations using various distributions after $10000\,s$ of numerical annealing.

While the energy E_Γ evolution respects this first regime, the changes in number of grains and average grain size (which are related of course) stop following this simple bounding. Indeed, it would seem that the "Full" formulation suffers from some supplemental pinning phenomena while continuing to minimize its interface energy efficiently. This emergent behavior remains unexplained in terms of possible mechanics of the polycrystal. The results shown in Figure 5.20 respect the fact that the "Projected" formulation exhibits behavior in between the two others even at $10000s$. However, it would seem that the "Projected" case is more similar to the "Classical" evolution of boundary character than to the "Full" case.

While it is indeed possible that the effects observed here are purely kinetics related, from this initial study, it does seem that something deeper is at play. Seeing as the "Projected" formulation was identified as the better candidate in Chapter 4, it is likely that results produced by the "Full" formulation exaggerate the kinetics of heterogeneous microstructures. In any case, these three results, when used in conjunction with each other, might be able to give good estimates concerning some of the limiting behaviors of heterogeneous polycrystals.

5.3 Homogeneously anisotropic 2D microstructures

The dependence of the grain boundary energy density on the inclination of a grain boundary can possibly have singular impacts on the dynamics of a polycrystal. In order to start elucidating these effects one may use numerical annealing experiments on grain boundary networks that exhibit only this inclination dependence. As such, this section is devoted to taking the virtual microstructure developed in the previous section and applying an inclination dependent grain boundary function modeled by

$$\gamma(M, n) = \Xi(M)\nu(n)$$

where ν is once again the function defined in (4.18) and $\Xi(M) = \Xi$ forces a constant misorientation dependence such that $\Xi = 1e - 7 J \cdot mm^{-2}$ and $\mu = 1mm^4 \cdot J^{-1} \cdot s^{-1}$. Besides these grain boundary energy properties, all other aspects of the microstructure are identical to the volume (area) element used in the previous section.

Two different formulations will be studied and compared: one with all the correct terms developed in (2.43) and the other one which is missing the "torque" term $\frac{\partial^2 \gamma}{\partial \tilde{\nabla}\phi^2}$. They will be denoted respectively as the "Torque" and "No Torque" cases. The physical relevance of the cases simulated here is very limited since the grain boundary energy is dependent on the expression of the inclination in the global reference frame and not the local crystallographic frames. However, from a modeling standpoint, this comparison allows one to measure some of the effects that the torque term might generate in a polycrystal setting. The initial state of the generated microstructure is represented in Figure 5.21 and is the same
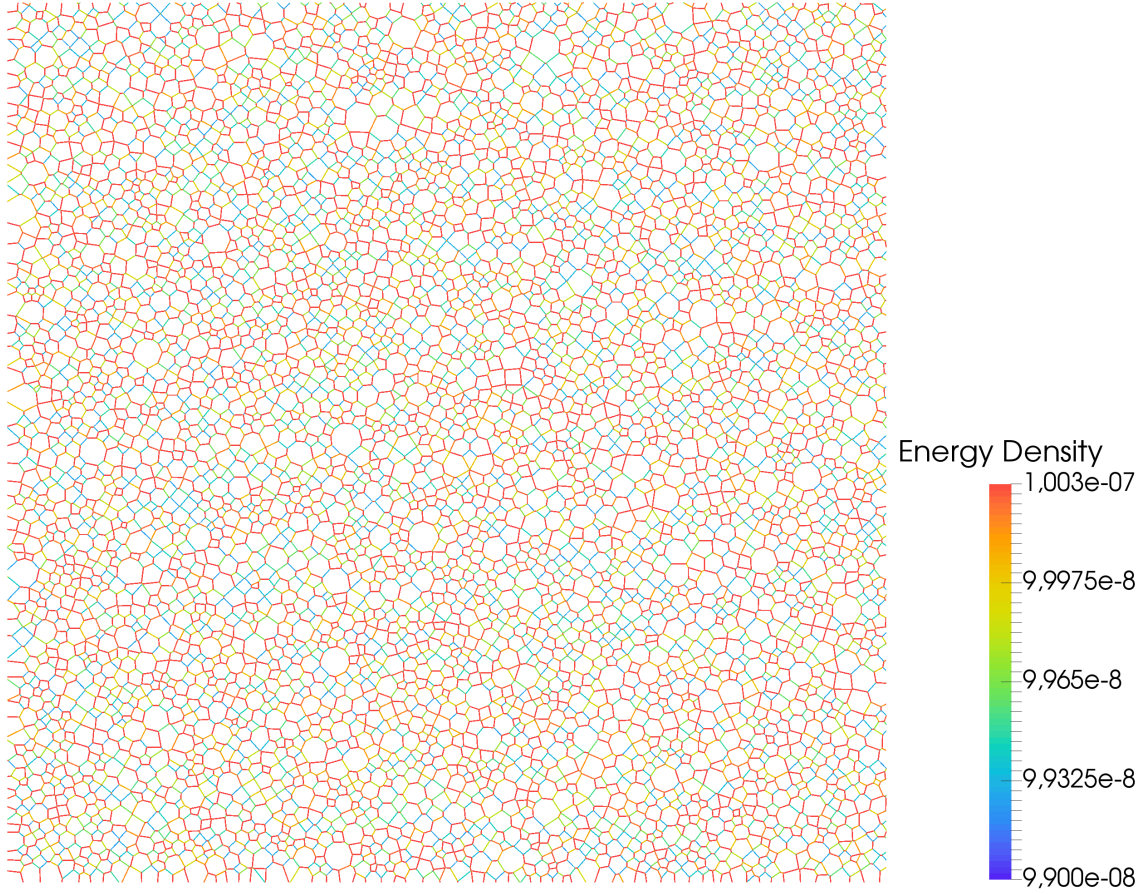
Figure 5.21: Initial state of the purely inclination dependent grain boundary energy microstructure.

for both formulations. The side length of the domain is once again $l = 1.5mm$ and there are approximately 5000 initial grains.

Figure 5.22 plots the time evolution of some of the mean characteristics of the grain boundary network for a simulated anneal of approximately $3000s$. Globally, the cases are relatively close since the torque terms are really very local phenomena and the simulated annealing was performed for less than an hour in physical time. Figure 5.23, which indeed shows that the final states of the microstructures are not very far apart, supports this hypothesis. However, it seems that the kinetics of the case with the torque terms are slower than the case without them. This effect can possibly be attributed to the increased constraints at both the multiple junctions and on the boundaries leading to globally a slower system.

Figure 5.24 reports on the distributions of the inclination ($\lambda = \arctan(\frac{n^y}{n^x})$) for the initial as well as final states of of the grain boundary network for the two formulations. The values of the inclinations are weighted by the number of mesh points and thus can be
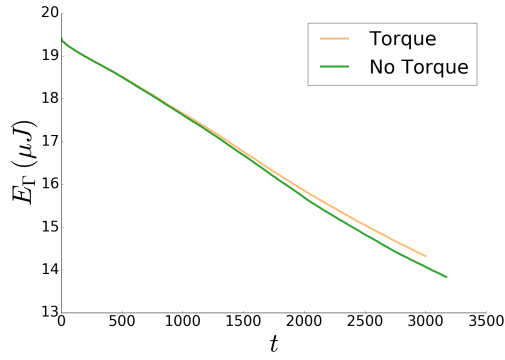
(a) $E_\Gamma = f(t)$
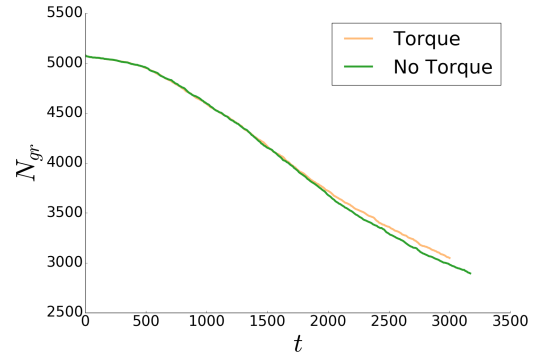
(b) $N_{gr} = f(t)$
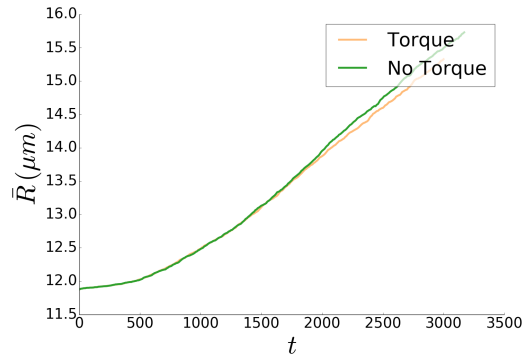
(c) $\bar{R} = f(t)$

Figure 5.22: Time evolution of mean values for the "Torque" and "No Torque" formulations.
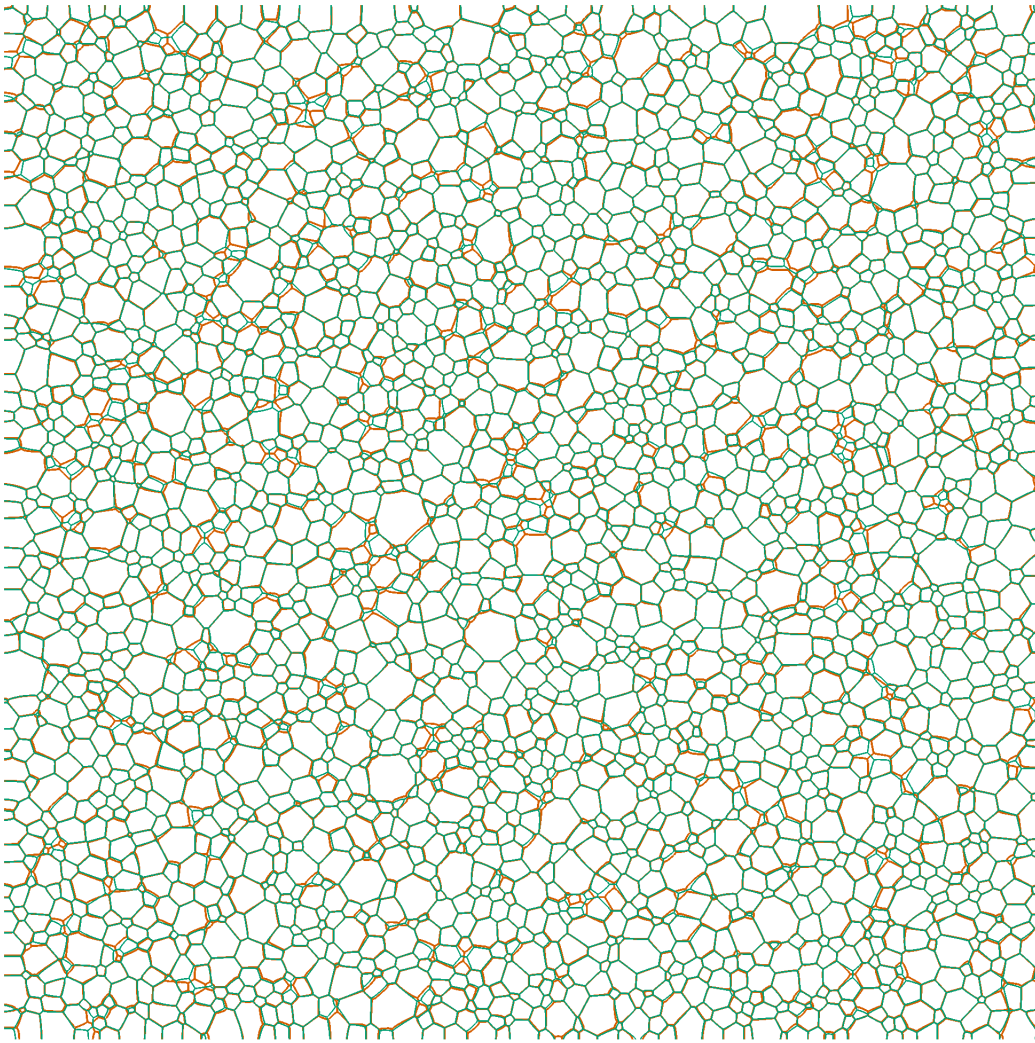
Figure 5.23: Comparison of the final states of the microstructure for the "Torque" (in orange) and "No Torque" (in green) formulations.

considered to be roughly weighted by length of the boundaries. The first observation one may make is that the initial distribution is far from random. Indeed, the Laguerre-Vornoi tessellation algorithm used to generate the polycrystal seems to favor inclinations that satisfy $\lambda = \frac{\pi}{4} + \mod \left(\frac{\pi}{2}\right)$. Secondly, the "No Torque" formulation tends to homogenize the distribution such that most inclinations are around equi-probable without regard for their energy. In the sense of a minimal energy requirement, this type of configuration of the polycrystal seems far from optimal. The "Torque" formulation, on the other hand, does extremize the inclination distribution around the extrema of the $\gamma(\lambda)$ function. However, while some minima of the γ function correspond to maxima of the inclination distribution, which is to be expected, the case of minima of the grain boundary energy coinciding with minima of the inclination distribution is also present. The same can be said for the maxima of the inclination distribution and grain boundary energy density. This is a conundrum. How does the polycrystal decide which inclinations to minimize and which to maximize if it is not a purely energetic consideration? Two main conjectures can be presented:

- A $3000s$ anneal is most likely not sufficient for the polycrystal to stabilize its inclination distribution and that, given more physical time, the microstructure will present a majority of low energy boundaries.

- The dynamical equilibria at the triple junctions admit configurations where a high energy boundary is present and these configurations are relatively common throughout the microstructure.

The two hypotheses are not mutually exclusive and it may be that the grain boundary network is in a metastable state. More data is needed in order to pinpoint the exact chains of causality in the virtual microstructure that lead to this phenomenon.

This section has successively shown the capability of the formulation developed in the previous chapters to simulate some initial polycrystal test cases. These preliminary results do improve the results with respect to the classical formalism for grain growth. This introductory application to polycrystals shows the robustness and flexibility of the approach while underlining new avenues of investigation. Ultimately, the virtual polycrystal exhibits a global behavior that cannot be reduced to a sum of its parts whether it be in the case of a heterogeneous grain boundary energy density, a purely inclination dependent energy or a fully anisotropic one. Finally, implicit throughout this entire chapter, the effects of the multiple junction on the kinematics and dynamics of the polycrystal are shown to be crucial aspects of microstructural evolution.
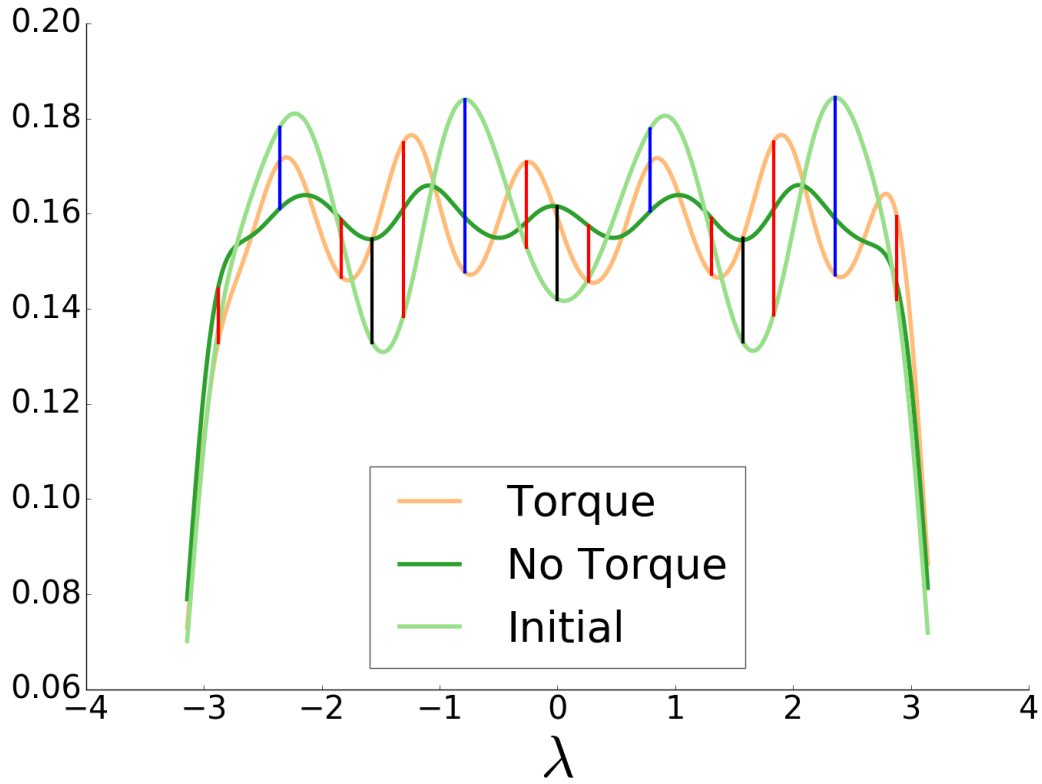
Figure 5.24: Kernel density estimation of the inclination distribution $(\lambda = \arctan(\frac{n^y}{n^x}))$ for the initial case as well as the final states for the "Torque" and "No Torque" formulations. The vertical blue lines represent local minima in the grain boundary energy functions while the red and black lines position the maxima and saddle points respectively.

Résumé en Français du Chapitre 5

Ce chapitre est dédié à l'application du modèle développé aux premiers cas polycristallins. Étant donné la complexité du système réellement anisotrope, ces applications aux polycristaux initiaux sont restreintes à des cas plutôt idéalisés. Le premiers cas concerne la modélisation d'un "joint de macle" 2D avec pour but d'étudier l'effet d'un changement d'énergie de joints de grains sur une configuration censée être stable. En effet, dans ce cas bien précis, la diminution de l'énergie du joint de macle ralentit l'évolution du système et donc le stabilise. Une deuxième application concerne les polycristaux hétérogènes soumis à différentes fonctions de densité d'énergie de joints de grains. Il est montré que l'hétérogénéité de la fonction d'énergie de joints de grains peut ralentir la cinétique de croissance de grains, ayant un effet d'épinglage d'orientation. Aussi, l'évolution de la distribution du caractère de joints de grains tend à être inverse à la fonction de densité énergétique de départ. La dernière application étudiée est une microstructure où la densité énergétique ne dépend que de l'inclinaison du joint dans le repère macroscopique. Les conclusions préliminaires montrent que les extrema de la fonction de densité énergétique jouent un rôle non negligeable dans l'évolution du polycristal.

Conclusion

The goal of this work was to develop the necessary mathematical and numerical frameworks to include annealing twin boundaries in the Level Set Finite Element method for recrystallization and grain growth. As such, the first step consolidated the current information on the behavior of microstructures during annealing, the mechanisms behind the structuring of the microscale and the particularities of the twin boundary. This bibliography led to the conclusion that most of the special behavior of the annealing twin could possibly be attributed to the low energy density of its boundary. Thus, the problem of including the twin boundary into simulation morphed into the issue of integrating the effect of the intrinsic crystallographic structure of an interface on its energy density into microstructural models. In order to accomplish this objective, the internal structure of the crystalline interface was divided into two distinct parts: the misorientation and the inclination. The dependence of the grain boundary energy density on the inclination could thus be treated separately from the effect of a varying misorientation.

The mathematical description of the grain boundary dynamics was developed using concepts from differential geometry. The thermodynamics of a closed system was used to develop a action principle related to the maximal dissipation of energy. This Lagragian has helped elucidate the hypotheses and equations for minimizing energy flows of general energy density boundaries. As a byproduct, a clear definition for a macroscale isotropic mobility parameter arose in relation to the energy dissipation rate during grain growth. This embedded description of the flow was condensed into a Level-Set depiction so as to simplify the degrees of freedom and their use in Finite Element software. As a direct result, the well-posedness of the problem was found to be dependent on a number of very specific characteristics of the grain boundary energy density function.

This newly developed mathematical formulation was then discretized using a classic Galerkin approach. The Finite Element model for simulating the minimizing anisotropic boundary energy flow was generated from this discretization. As such, approximate solutions to the problem could be sought on discrete domains. A completely novel benchmark configuration for the problem, a stationary ellipse, was established. This numerical framework was validated on this benchmark. The numerical model was also tested on a circular case with a more arbitrary inclination dependent boundary energy. Comparisons between the new and classical formulation show superior energetic efficiency associated with the

dynamics of anisotropically valued energy densities using the newer method.

In the effort to extend the formalism toward polycrystals, the numerical framework was expanded to be able to handle multiple junctions of boundaries. This widening of the capabilities of the framework demanded the development of new tools for computing crystallographic quantities on the finite element mesh. When put to the test on the "Grim Reaper" benchmark, the new formulation performed better than the other tested solutions to the problem. However, the particular topology of the multiple junction remains an issue. When strong variations in the energy density are put into play, the framework displays a considerable error. Whether this error is numerical in nature (i.e. a convergence issue) or foundational (i.e. a modelling insufficiency) is as yet unknown. A fully anisotropic triple junction simulation was also run where the torque acting on the junction was manifest.

The final chapter of this manuscript demonstrates the flexibility and robustness of the method. Some 2D "twin" configurations were tested and shown to exhibit certain "twin-like" properties. Heterogeneous statistical volume elements were generated and a virtual annealing treatment was performed. The microstructures exhibit behaviors such as orientation pinning, which has been observed experimentally, and an inverse correlation of the grain boundary character to the boundary energy density, which has been thought to exist in real microstructures. Finally, an initial foray into the effect of the inclination dependence on the grain boundary energy was performed in which certain behaviors of the microstructure are elucidated but remain unexplained.

As such, this work has contributed a certain number of elements towards the full field modeling of annealing twin boundaries. While marked caveats still exist, the numerical model developed here has been demonstrated to be objectively better than the classical Level Set model for grain growth. The complexities related to integrating arbitrary grain boundary energies into simulation of recrystallization and grain growth have been established and many of them have been better understood. Moving forward, some supplemental issues must still be addressed, and yet, the model has proven predictive power concerning polycrystals and can perhaps be used, as is, to understand particular emergent behavior of the microstructure.

Perspectives

As in any research subject, new answers lead to new questions and new applications. As such, there are a number of follow-up investigations that may push the results presented here even further. Also, given the exploratory nature of this work, choices were made during the investigation so as to produce tangible results. Therefore, there are quite a few tangents that remain uncharted and that merit mention as perspectives as well. Taking even a larger step back, there are particular limitations to the models that currently exist in the literature and the one developed here. One may propose some completely alternative ideas to extend the limits of the numerical models even more. These perspectives are meant to serve as short, medium and long term research propositions for investigators who might which to push the bounds of current knowledge on annealing phenomena and their modeling.

Direct Applications

The numerical model developed in this work is directly applicable to a host of potential studies. The first that comes to mind is to use more realistic grain boundary energies in polycrystal simulations. There are a number of investigations [40,42,50,51,118] which have been devoted to proposing grain boundary energy density functions for metallic materials. The implementation of any grain boundary energy density function in the numerical model presented in this work should proceed in two steps:

1. The candidate interface energy density $\gamma(M, n)$ must fulfill the equivalent 3D 3.20, 3.21 and 3.22 conditions for all misorientations. If a candidate density function does not satisfy this positive definiteness of the D tensor then, technically, it cannot be used in the numerical model. Furthermore, this deficiency is a serious issue in terms of the physics of the said candidate function because the interface energy minimization problem becomes ill-posed (i.e. the solution is no longer unique or possibly even exists). Obviously, if the candidate energy density is a product of incontestable experimental data, then the whole modeling approach must be revisited and the minimizing interfacial energy flow in the sharp limit can no longer be used as the explanation for the physics of the problem.

2. In the case where the proposed function does satisfy the positive definiteness constraints, the second step would be to apply it to a virtual polycrystal in the same vein as the second section of Chapter 5. In order to compare the results to experimental data, the simulated microstructure must be "representative". However, this representativity is relatively difficult to define in the fully anisotropic setting given the richness of the crystallographic data. Indeed, this testing of a boundary energy function would most likely be preceded or accompanied by a thorough analysis and definition of what is the smallest microstructure that can be considered representative in an anisotropic setting. Once this representativity is established, the most adequate distributions of properties to compare between the simulated and real microstructures would be the grain boundary character evolution (i.e. the distribution of boundaries in five parameter grain boundary space).

In perhaps a more pragmatic approach, instead of modifying the grain boundary energy density function, one could also take a Read-Shockley [36] type disorientation angle dependent function and apply it to highly textured virtual materials. Textured materials, given their preferential crystal orientation, should exhibit a large proportion of small angle grain boundaries. This means that the Read-Shockley type density function might be more relevant than in the "randomly" orientated case. Also, the equivalent experimental data of grain growth in textured materials should be either readily available in the literature or relatively simple to procure given the correct technological platform (a source of textured materials devoid of dislocations, ovens for heat treatments, scanning electron microscopy equipped with electron back scattered diffraction mapping, etc.).

In the case where no known grain boundary energy functions seem to reproduce sensible microstructural evolutions, an inverse analysis approach can be developed. Assuming that in-situ experimental annealing data is available for a monophase material during grain growth, one could use the numerical model presented in this work to calibrate a grain boundary energy function. Consider

$$\gamma(M, n) = f(X_1, \ldots, X_n)(M, n)$$

where f is a map from $\mathbb{R}^n$ to the adequate function space on the grain boundary space. In this setting, one could attempt to optimize the grain boundary energy by acting on the degrees of freedom $\{X_i, i = 1, \ldots, n\}$. As such, the problem of finding a relevant grain boundary energy function is reduced to finding the X_i parameters that generate an optimal fit between the simulation and the in-situ microstructural data. In the extreme case one would immerse an initial experimental microstructure into the finite element mesh and modify the function's degrees of freedom until the annealing simulation reproduces the subsequent annealed states. This might prove very delicate in terms of the conditioning of the problem and very costly in terms of computational resources. However, the same approach could be used on derived microstructural data such as grain boundary character distributions or mean values which might provide forgiving fits.

Of course, the biggest caveat of this investigation is the absence of three dimensional simulations. While both the mathematical and numerical formalism developed are perfectly dimension independent, only 2D polycrystal simulations have been performed thus far. The reason for remaining in lower dimensional simulation is simple. No anisotropic analytical benchmarks exist for 3D grain boundary configurations. Thus, while one may be able to produce numerical results, it would remain relatively difficult to study the precision of these results. Even something relatively elementary, such as the equilibrium of a quadruple junction, remains analytically elusive in a three dimensional setting. Of course, if one presents numerical results in excellent agreement with experimental data then this can be construed as evidence of a precise numerical model.

As such, the ideal next step in validating the numerical results of the model would be to develop a 3D analogy of the ellipse benchmark presented in Chapter 3. Once this benchmark is validated using numerical simulations, the particularities of the multiple junctions in 3D should be studied. Even if no analytical results exist for these multiple junctions, simulations of quadruple junctions could possibly serve the community as a base to come up with more exact cases. Of course, once these tests are performed and one is convinced of the validity of the model in 3D one may move onto 3D polycrystals with anisotropic grain boundary energies.

Numerical Improvements

Even though the previous section described some cases where the model could possibly be applied immediately, one could also first improve the numerical formalism. The first thing that might need to be enhanced in the numerical algorithm is the remeshing operation. Indeed, the results presented in the second section of Chapter 4 are accompanied by numerical costs. These costs are manifest in the amount of CPU time spent on each computation and can be studied and compared for the different grain boundary energy functions. Indeed, more heterogeneity in the physical system should lead to a numerical problem that is less well conditioned than the homogeneous case, meaning a problem that is generally harder to solve. This means that, using the same algorithms for solving the grain growth problem, when employing a more heterogeneous grain boundary energy the computational time should, technically, be higher.

A small caveat might exist for the well informed reader who would like to compare the calculation times given here to previous works [90–92, 114]. Due to the relatively small mesh sizes as well as the fixed time step used for obtaining these results the costs presented here are higher. Indeed, the goal of this work being to compare cases in which the convergence and precision of the simulation are ensured for all heterogeneities, no numerical parameter optimization (beyond the sensitivity analyses presented in Chapter 4) has been performed. This means that the calculation times presented here for the homogeneous case are relatively large compared with optimized calculations in previous studies. How-

ever, the different heterogeneous systems are on an equal footing regarding the numerical parameters of the simulation. Therefore, the times given in the following paragraphs are not to be taken as absolute performance optimums but as comparable quantities used to evaluate the impact of the heterogeneities on the computational efficiency.

All of the computations were performed on $3 \times 24 = 72$ Bullx R424 Intel Xeon E5-2680 (v3 - 2.5GHz or v4 - 2.4GHz) cores using an in-house computing cluster and a remeshing/re-partitionning algorithm in the same vein as [119]. The CPU times ΔT are compared in Figure 5.25 with regard to both the type of grain boundary energy function as well as the type of numerical operations.

Firstly, all the computations take approximately the same amount of time meaning $\simeq 5 - 6$ days in total. They all start with meshes containing around 13 million elements and end around 5 million elements. Relatively small differences can be observed in between the different heterogeneous simulations which do tend towards an increase in the computational time as the grain boundary energy functions distances itself from the homogeneous case. The most computationally intensive operation performed during the computation is the remeshing which takes around 76% of the total time. This operation has little to do with the nature of the heterogeneity of the grain boundary energy function directly and more to do with the morphology and length of the grain boundaries. Therefore, the small discrepancies between the different heterogeneous simulations can be explained by the fact that the grain boundary energies do not sensibly affect the most time consuming activity. However, Figure 5.25b shows that the operation with the highest relative standard deviation is by far the FE resolution. This fact proves that the operation the most affected in a relative sense by the change in heterogeneity of the grain boundary energy is the search for solutions to the physical problem. This would tend to corroborate the fact that as the grain boundary energy function distances itself from the homogeneous case, the system becomes more ill conditioned and therefore harder to solve.

Seeing the large proportion of simulation time spent in remeshing operations, looking to optimize the numerical in this direction would probably be the most efficient way to proceed. Indeed, the remeshing parameters have been kept constant regardless of the nature of the anisotropy of the grain boundaries in this work. There are rather straightforward studies to perform to answer some optimization questions, such as: Should the lower energy grain boundaries accept more coarsely meshed neighborhood given that their velocities should generally be slower? How does one remesh a heterogeneously valued multiple junction? Then there are more difficult questions: How does one incorporate the calculated D tensor into the remeshing operation so as to have an optimal remshing algorithm? How can the conditioning of an anisotropic grain growth finite element linear algebra problem be improved with better remeshing? All these interrogations related to the spatial discretization must now be re-evaluated in a anisotropic grain boundary energy setting.

Putting the remeshing aspect aside, one could also improve the numerical description of the multiple junction. As a topological space, the triple junction is not a manifold. As
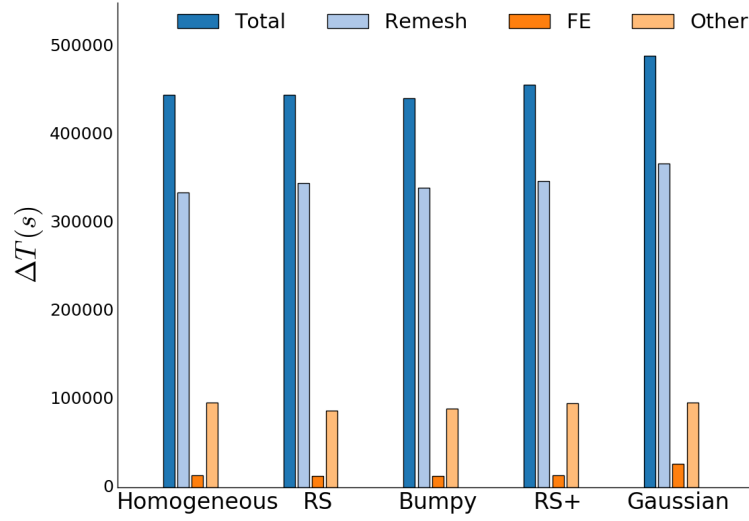
(a) Bar graph of the CPU times spent in total, during remeshing, during the FE resolution and in the rest of the operations (defining the γ field, calculating disorientations, reinitializing level-set functions, ...) for each of the simulations.
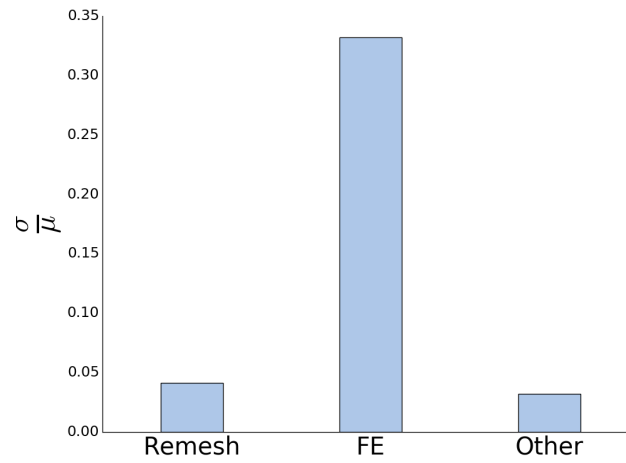
(b) Bar chart representing the standard deviation σ of the CPU time spent in each operation divided by the average μ time spent in the same calculation for all the simulations.

Figure 5.25: Evolution of CPU usage as a function of both the grain boundary energy function and the category of operation performed during the calculation.

such, Level Set method has a hard time describing these singular points of the polycrystal. The method proposed in [82] was used in this work to ensure the continuity of the junction itself. However, another possibility described in [107] could be very promising if rather costly. Indeed, by penalizing the creation of voids and overlaps in a variational sense, the continuity constraints at the triple junctions can be included into the finite element resolution. This would effectively eliminate one step in the complete numerical algorithm and could modify the angle results that one obtains at heterogeneous multiple junctions. Whether these new results would be an improvement, or not, on the current results remains to be seen. Of course, the finite element assembly would need to be drastically revisited given the coupling between level set fields in the variational approach which is not an issue in the post-treatment used here. In any case, a rigorous and holistic comparison in a full anisotropic setting between the results obtained with the two methods would be useful for the community to decide which is best fitted to which application.

Disregarding the treatment of the multiple junctions, with the inclusion of a grain boundary energy density function dependent upon the configuration of the grain boundary network, the grain growth problem becomes highly non-linear. This aspect of the equations was conveniently brushed aside in this manuscript in an explicit/zero order initial approach to the problem. However, it is very possible that the model would benefit greatly from a fully non-linear solver where the γ field and its associated derivatives would become dynamic during the resolution of the level set field. Obviously there is a plethora of non-linear numerical methods that already exist in the literature [120] that could be readily applied to improving the formulation here. Of course, this could greatly increase the numerical cost of each time step. However, this kind of approach could possibly allow for the coarsening of both the spatial and temporal discretizations leading to perhaps a more efficient tool.

Finally, as per the discussion at the end of the first section of Chapter 5, an unbounded D tensor could possibly be necessary to model the particularities of the twin boundary. However, numerical methods generally abhor infinities. As such, one could imagine attempting to model boundaries using an unbounded D tensor and numerically using some sort of cut-off value for its components. As such, one could ensure that the kinetics of the boundary migration would be generally bounded. This would be necessary in order to evaluate a convergent time step parameter. Of course, the non-linear solver aspect described in the previous paragraph could generally improve the performances in exactly these types of cases. Even so, the method would be inherently flawed by this cut-off parameter which would have to be calibrated completely empirically. However, if this cut-off was set high enough, the errors would be completely localized in very fast transient states of microstructural evolution. These types of errors would need to be quantified and there should be a convergence of the method with increasing cut-off values.

Modeling Outlook

While certain "real-world" applications might be exciting and numerical improvements would generally increase the efficiency of the approach, perhaps the most interesting perspectives of this work are in enhancing the modeling approach.

Indeed, there are a number of limits of the model developed in this manuscript when it comes to modeling multiple junctions. Neither the "Full" nor the "Projected" approaches developed in Chapter 4 are completely satisfying. However, they could possibly be combined by using a modified projection tensor

$$P_\epsilon = m^{-1} - \epsilon(n \otimes n)$$

where $\epsilon \in [0;1]$, m is the Riemannian metric of the physical space and n is the normal to the grain boundary. As a matter of fact, the "Full" and "Projected" formulations are respectively the $\epsilon = 0$ and $\epsilon = 1$ limit cases of the above projection tensor formulation. In a completely numerical approach, the ϵ parameter could be optimized for all values of the anisotropic ratio at the multiple junction. While remaining a completely numerical parameter, the formulation would guarantee the correct behavior of triple junctions in 2D simulations. Even performing the optimization study of this parameter might give more insight into the reasons for which the model fails to obtain the exact analytical solution. This type of insight could lead to a much more robust formulation of the velocity at the multiple junction in general.

Multiple junctions aside, in an effort to make the simulated microstructures more realistic one could add terms to the velocity of the boundaries v in order to model more of the physics of hot forging at the microstructural level. In this way, this work could possibly be used in conjunction with a number of past and undergoing developments in level set simulations of metallurgical phenomena [7–9, 63, 92, 106, 114, 121, 122]. For example, the strain tensor ε induced by the deformation of the material could be simply added to the grain growth velocity v_{GG}

$$v = v_{GG}(\mu, \gamma(M, n), \tilde{\nabla}\phi, \tilde{\nabla}\tilde{\nabla}\phi) + v_{Def}(\varepsilon)$$

in a very modular manner much like in [63]. Recrystallization phenomena in the presence of a stored defect energy field ρ is superimposed in the same way

$$v = v_{GG}(\gamma(M, n), \tilde{\nabla}\phi, \tilde{\nabla}\tilde{\nabla}\phi) + v_{Def}(\varepsilon) + v_{RX}(\tilde{\nabla}\rho)$$

such that one could attempt to model dynamic recrystallization in a monophase material as in [106]. Of course, even more complex metallurgical mechanisms may be simulated

$$v = v_{GG}(\gamma(M,n), \tilde{\nabla}\phi, \tilde{\nabla}\tilde{\nabla}\phi) + v_{Def}(\varepsilon) + v_{RX}(\tilde{\nabla}\rho) + v_{SSPT}(C_i, \tilde{\nabla}\phi, \tilde{\nabla}\tilde{\nabla}\phi)$$
$$+ v_{GBS}(M, \tilde{\nabla}\phi)$$

such as solid state phase transformations (SSPT) [122], where the C_i are the concentration fields of the species, or grain boundary sliding (GBS), where the misorientation might become an unknown of the problem as well. However, the inclusion of these supplemental mechanisms is rendered more complicated by the couplings that different terms might generate. Indeed, grain boundary sliding might change the misorientation of a grain boundary. This in turn will affect the grain boundary energy density of the boundary and thus its grain growth velocity. Phase boundary migration due to interface energy minimizing effects will induce a matter flux that acts on the concentration fields. As such, certain aspects of the microstructure that were considered constant in this work might become degrees of freedom in a more realistic modeling approach. Numerically, these couplings must be dealt with in a coherent manner possibly leading to very large systems of non-linear equations.

Of course, when modeling both discontinuous recrystallization and solid state phase transformations, nucleation events are rampant throughout the microstructure. Modeling these nucleation mechanisms go beyond just modifying the velocity formulation since these phenomena occur discontinuously and thus modify the topology of the grain boundary network. Recrystallization simulations containing spontaneous insertions of grains have already been performed in the works [63, 106] and the associated publications. As such, the numerical formalism for including specific nuclei during microstructural evolution already exists and has been tested in the level set framework. However, the exact localization in space and time of these nucleation incidents is the challenging aspect in this type of full field model. Furthermore, with the framework developed here, the grains that appear in the microstructure have supplemental crystallographic degrees of freedom. What kind of orientation does one give a grain nucleus? This question is specifically important when attempting to model thermal twinning where most mechanisms [27, 30] suppose the nucleation of a twin oriented grain. Moreover, looking at the highly twinned microstructures obtained in forged nickel based superalloys, it is most likely that the twin oriented nucleus appears or subsists more often than other, less favorably oriented, nuclei. A numerical model, such as the one developed here, capable of taking into account some of the particularities of the twin boundary allows one to start modeling these nucleation phenomena and the subsequent microstructural evolution. As such, this numerical method can become a tool to explore different hypotheses related to the nucleation of annealing twins during recrystallization and grain growth.

Now, unrelated to these nucleation considerations, the mobility μ of the grain boundary has been taken to be a constant in this work. However, given that it is supposed to be a property of the grain boundary, there is no reason that it should not depend on the five dimensional grain boundary character (M, n). As such, an anisotropic mobility $\mu(M, n)$ is

a physical possibility that should not be brushed aside as easily as it has been. Even so, the definition of μ given in equation (2.28) is a global one and leaves no room for the mobility to vary in the microstructure. How may one reconcile these ideas? From a modeling point of view, the Riemannian metric m of the underlying space has been defined but has not been given very much thought in this work. The simulations conducted here have largely considered a "flat" base space as the natural space containing the microstructure. However, one could induce an intrinsic curvature of the space to deviate from the idealistic flat case. The curvature of the space could act on the passage of time heterogeneously throughout the microstructure. This would generally have the effect of a mobility varying from boundary to boundary depending of the orientation field. Moreover, the metric is a tensorial value which would adhere to the general vision that a boundary might be able to migrate in certain directions more efficiently than in others. However, these considerations would turn the metric m into another unknown of the problem much like the grain boundary energy γ. Moving towards these kinds of models would most likely cement the need for non-linear solvers in order to remain relatively precise. Most exciting perhaps, if this kind of curved space model was to perform well in realistic situations then it would open up new ways to model these types of microstructural evolutions and new interpretations of the physics as well. Perhaps more sophisticated Lorentzian time-space metrics could be developed to fully encapsulate the modeling of microstructural evolution.

Additionally, there is a rather large implicit hypothesis throughout this and almost all studies that model microstructural evolution in metals. That is: the order one defect determining the kinetics of the grain boundary network is the grain boundary. One may call this the "grain boundary hypothesis". However, the three dimensional grain boundary network is also comprised of triple (or multiple) lines and multiple junctions. When modeling the entire network the emphasis is always placed on the grain boundaries. However, it is very likely that the triple line, for example, has its own energy density that cannot be defined as some combination of adjacent boundary energy densities. As the meeting of three grains, the orientation mismatch at the triple line can be much higher than any grain boundary on its own. The modeling approach described in the first sections of Chapter 2 is purposefully dimension independent. As such, it is singularly adapted to a hierarchical description of the microstructure as grains with boundaries comprised of grain boundaries. These grain boundaries have their own boundaries which are lines. These lines also have boundaries which are the junctions. In this sense, considering a hierarchical embedded description of the microstructure, a global velocity field could be constructed so as to produce a minimizing energy flow. This means that the equation for the velocity, in the embedded description model, is the same for each element of the hierarchy and the total velocity is simply a superposition of the velocities at every level with adequate continuity conditions. More pragmatically, one could develop a "vertex model" where the resolution of the velocity proceeds hierarchically from the junctions to the lines to the boundaries where the results at one level are used as boundary conditions for the next level [65, 121]. The interest of this type of model would be to test the effect of affecting an energy density

to triple line or even to multiple junctions that could depend on the orientation field. It is very possible, in the same way that including terms at the triple junction in 2D simulations can greatly modify the kinetics, that including supplemental terms related to the minimization of multiple line energies could lead to kinetics closer to real microstructures. Also, given the lower dimensionality of the hiearchal mesh, the numerical cost of these types of models might be much less prohibitive than the current state of the art.

In a more "back to basics" approach, in order to hopefully do away with the topological considerations of the multiple lines and junctions, one could attempt to model the kinetics of a orientation field. Indeed, polycrystal matter and its associated defects and phases could quite simply be modeled by the correct orientation fields and species concentration fields. More formally, consider a microstructure comprised of n phases with their own crystallographic symmetry groups S_i and compositions $\varphi_i = (C_\alpha, \alpha = H, He, Li, \ldots, C, \ldots)$ occupying a physical space Ω (a smooth manifold). The static description of the entire microstructure is encapsulated in following field

$$\chi : \Omega \longrightarrow \{1, \ldots, n\} \times \mathcal{SO}(3) \times \mathbb{R}^p$$
$$\chi(X) = (i, O, (C_\alpha))$$

where p is the number of different species present in the material. As such, the i parameter labels the phase at the point X, the O element in $\mathcal{SO}(3)$ characterizes the crystal orientation and the (C_α) tuple describes the local composition. The microstructure being completely characterized by this field, the dynamics of the microstructure are thus ultimately defined by

$$\frac{d}{dt}\chi = f(T, \varepsilon, \dot{\varepsilon}, \chi, \nabla\chi, \nabla\nabla\chi, \ldots)$$

with T the temperature, ε the strain and $\dot{\varepsilon}$ the strain rate. The f function would be constrained by first principles in terms of the relevant energy densities present in the microstructure. However, the ∇ operator is slightly more difficult to define. While a covariant derivative in Ω of both the phase parameter ∇i and the composition tuple $\nabla(C_\alpha) = (\nabla C_\alpha)$ are relatively straightforward, the differential quotient in $\mathcal{SO}(3)$ is more difficult. This difficulty is obviously compounded by the fact that each phase φ_i has its own symmetry space S_i and thus its own orientation space $\mathcal{O}_i = \mathcal{SO}(3)/S_i$. However, $\mathcal{SO}(3)$ is a Lie group and thus also a special type of smooth manifold. As such, every element of $\mathcal{SO}(3)$ admits a tangent space isomorphic to the tangent space at the identity. Thus, directional derivatives of the orientation field can be described by elements of the associated tangent space and a ∇O can be defined in this sense using the linearity of this tangent space. Thus, with $u \in T_X\Omega$

$$\nabla_u O \in T_{O(X)}\mathcal{SO}(3)$$

180

can possibly give a somewhat coherent description of a covariant derivative of an orientation field. This covariant derivative might give a more natural and continuous definition of misorientation in the case of a grain boundary. To link this model with the previous developments in this manuscript one could very well define an crystalline defect energy density as depending upon this spatial derivative so that

$$E_{\text{crystal defects}} = \int_{\Omega} g(\nabla_u O)^2 d\Omega$$

where

$$g : \Gamma(T^*\Omega \otimes T\mathcal{SO}(3)) \longrightarrow L^2(\Omega).$$

While using more complex mathematics, and demanding very good knowledge of Lie Groups and differential geometry this kind of so-called "nonlinear sigma model" can perhaps generate a more fundamental approach with which to predict microstructural evolution.

Conclusion en Français

Le but global de ce travail était d'introduire les spécificités du joint de macle dans les simulations en champ complet d'évolutions de microstructures. Pour y parvenir, cette étude s'est concentrée sur l'enrichissement des modèles de migration de joints de grains afin de prendre en compte des densités d'énergie de joint anisotrope. Ce choix a été fait après une bibliographie menée sur les mécanismes de maclage et le comportement des macles thermiques conjointement à l'étude des modèles numériques utiles dans l'état de l'art pour simuler la dynamique des polycristaux. La conclusion majeure de cette revue de la littérature est que l'énergie faible de la macle cohérente semble être une justification adéquate pour expliquer son comportement particulier dans les superalliages base nickel.

Pour introduire les aspects d'anisotropie dans les modèles de migration de joints de grains, un formalisme mathématique basé sur les éléments de la géométrie différentielle a été développé. Une expression pour la vitesse de migration d'une interface a donc pu être proposée en partant des premiers principes de la thermodynamique. À l'aide de ce dévelopement, une définition explicite pour la mobilité d'un joint a pu être exprimée. Par la suite, ce nouveau modèle a été adapté à une description level-set des interfaces avec pour but de simuler la migration des interfaces anisotropes à l'aide de la méthode level set dans un cadre éléments finis.

Ce modèle mathématique a donc été discrétisé afin de pouvoir le simuler numériquement. Le développement éléments finis a été explicité avant d'introduire un nouveau cas analytique anisotrope basé sur une ellipse qui rétrécie. La convergence de la méthode à été démontrée avec ce cas analytique. Ensuite, un certain nombre de conditions sur la fonction de densité énergétique de joints ont pu être exprimées pour préserver l'existence et l'unicité de la solution. À partir de ce développement, un cas utilisant une densité d'énergie plus arbitraire a été proposé. Cette configuration a permis de montrer la supériorité du nouveau formalisme par rapport à l'existant.

Afin de pouvoir simuler les polycristaux, un ensemble de modifications a été apporté au modèle numérique. Ces modifications ont permis au modèle d'intégrer la cristallographie du matériau dans les simulations aussi bien que de simuler les joints multiples. Dans cette optique, le formalisme modifié a été testé sur un cas analytique bien connu : le "Grim Reaper". Les nouveaux développements ont permis de se rapprocher des résultats théoriques. Néanmoins, il reste une marge de progression possible dans l'approche pour améliorer davantage les résultats.

En dernier lieu, quelques cas applicatifs sur des polycristaux idéalisés ont été étudiés afin de montrer l'utilité de la méthodologie. Un premier cas montre une configuration "maclée" qui est mieux décrite lorsque l'énergie du joint de macle est diminuée. Ensuite, un polycristal virtuel est généré et différentes énergies de joints de grains, dépendantes uniquement de la désorientation, sont imposées sur cette microstructure artificielle. Les résultats des simulations mettent en évidence des phénomènes d'épinglage d'orientation aussi bien qu'une correlation inverse entre la fonction d'énergie de joints de grains et la

distribution des angles de désorientation. Un dernier cas réutilise la même microstructure virtuelle afin d'étudier une énergie uniquement dépendante de l'inclinaison du joint dans le repère macroscopique. Cette étude préliminaire lie les extrema de la fonction de densité énergétique de joints à l'évolution des inclinaisons des interfaces présentes dans la microstructure.

Suite à ce travail, les perspectives sont nombreuses. Pour en citer certaines, les simulations 3D des microstructures découlent naturellement du formalisme et peuvent d'ores et déjà être envisagées. Des fonctions de densité énergétique de joints de grains plus réalistes peuvent également être utilisées dans les simulations dans le but d'une comparaison avec des résultats expérimentaux. Le traitement numérique des jonctions multiples peut aussi être modifié et potentiellement amélioré avec une approche variationnelle. De plus, le formalisme bénificierait sûrement de l'utilisation de solveurs non-linéaires pour résoudre le problème éléments finis.

Appendices

Appendix A

A method for measuring angles at a multiple junction

In order to automatically measure the evolution of the angles at multiple junctions during a microstructural evolution simulation one must have two things:

1. A way to accurately track the position of a multiple junction.

2. A method for measuring the angles of a multiple junction given its position.

In a LS-FE setting, both requirements are rather simply met. In order to track the multiple junction points in a domain Ω of dimension 2, one may define a neighborhood parameter ε such the the set of points:

$$\mathcal{N}_J = \{X \in \Omega \,|\, \#\{i \,|\, \phi_i(X) < \varepsilon\} > 2\} \tag{A.1}$$

is the neighborhood of one multiple junction.

If one takes the barycenter of this neighborhood set $\mathcal{N}_J$ than one obtains the multiple junction point:

$$X_J = \frac{\int_{\mathcal{N}_J} X \, d\Omega}{\int_{\mathcal{N}_J} d\Omega}. \tag{A.2}$$

As such, one may track the multiple junction point throughout its evolution. In order to calculate the angles created by the boundaries meeting at the junction, one may define the circle:

$$C_\varepsilon = \{X \in \Omega \,|\, d(X, X_J) = \varepsilon\}, \tag{A.3}$$

where $d(\cdot, \cdot)$ is the euclidean distance function, and the arc of the circle passing through grain G_i as:

$$C_\varepsilon^i = C_\varepsilon \cap G_i. \tag{A.4}$$

Remarking that:

$$\frac{\int_{C_\varepsilon^i} dl}{\int_{C_\varepsilon} dl} = \frac{\varepsilon \xi_i}{2\pi\varepsilon} = \frac{\xi_i}{2\pi}, \tag{A.5}$$

where dl is the infinitesimal length along the circle. There is a simple expression for ξ_i:

$$\xi_i = 2\pi \frac{L_\varepsilon^i}{P_\varepsilon} \tag{A.6}$$

where L_ε^i is the length of the arc of C_ε^i and P is the perimeter of C_ε.

One may calculate these values on a FE mesh for a given ε and junction configuration by defining a radial distance function from the triple junction point X_J and integrating the iso-ε arcs by parts in each element. However, choosing the correct value for ε is relatively important. One would like to use a ε that is as small as possible in order to be as close as possible to the junction and large enough so that the angle calculations are precise. Conducting a sensitivity analysis of the precision of the method with respect to the mesh size h, as shown in Figure A.1, one observes that $\varepsilon \approx 10h$ is sufficient for obtaining good results concerning the calculation of the angles.

One may also develop a comparable procedure for both multiple junctions in 3D using spheres as well as triple lines using cylinders.
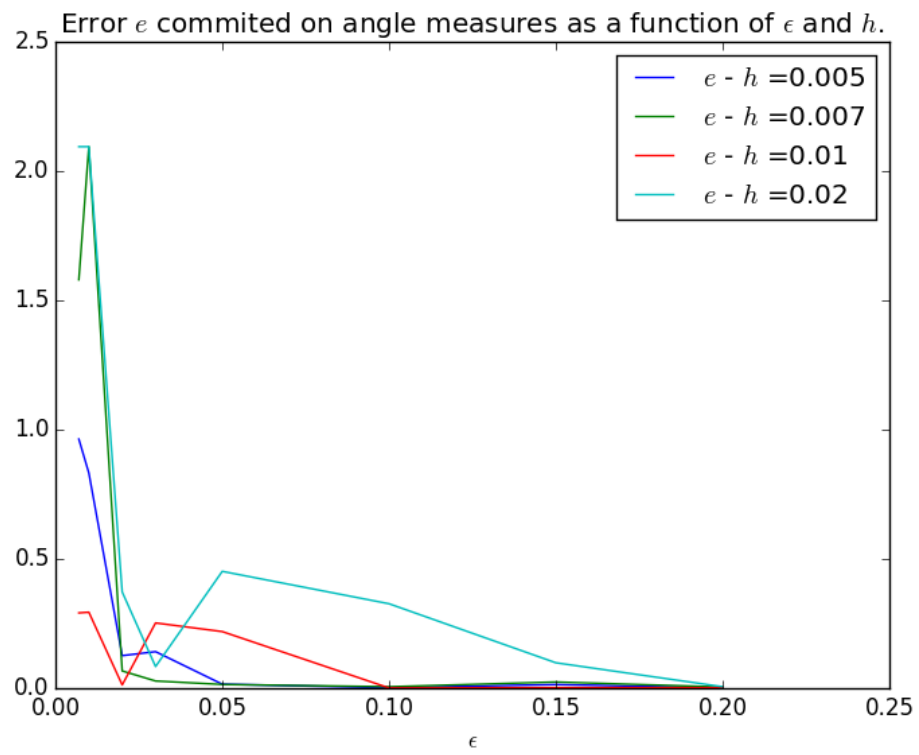
Figure A.1: Sensitivity study of the precision of angle calculations with respect to h and ε

Bibliography

[1] E. Joseph and S. Conway, "Major trends in the worldwide HPC market," (HPC User Forum at HLRS), 2017.

[2] M. D. Sangid, "The physics of fatigue crack initiation," *International Journal of Fatigue*, vol. 57, pp. 58–72, 2013.

[3] M. Sakaguchi, R. Komamura, X. Chen, M. Higaki, and H. Inoue, "Crystal plasticity assessment of crystallographic stage I crack propagation in a Ni-based single crystal superalloy," *International Journal of Fatigue*, vol. 123, pp. 10 – 21, 2019.

[4] M. Dakshinamurthy and A. Ma, "Crack propagation in trip assisted steels modeled by crystal plasticity and cohesive zone method," *Theoretical and Applied Fracture Mechanics*, vol. 96, pp. 545 – 555, 2018.

[5] J. Li, H. Proudhon, A. Roos, V. Chiaruttini, and S. Forest, "Crystal plasticity finite element simulation of crack growth in single crystals," *Computational Materials Science*, vol. 94, pp. 191 – 197, 2014. IWCMM23 Special Issue.

[6] P. Zhao, T. S. E. Low, Y. Wang, and S. R. Niezgoda, "An integrated full-field model of concurrent plastic deformation and microstructure evolution: Application to 3D simulation of dynamic recrystallization in polycrystalline copper," *International Journal of Plasticity*, vol. 80, pp. 38 – 55, 2016.

[7] B. Scholtes, R. Boulais-Sinou, A. Settefrati, D. P. Muñoz, I. Poitrault, A. Montouchet, N. Bozzolo, and M. Bernacki, "3D level set modeling of static recrystallization considering stored energy fields," *Computational Materials Science*, vol. 122, pp. 57 – 71, 2016.

[8] D. Ilin, N. Bozzolo, T. Toulorge, and M. Bernacki, "Full field modeling of recrystallization: Effect of intragranular strain gradients on grain boundary shape and kinetics," *Computational Materials Science*, vol. 150, pp. 149 – 161, 2018.

[9] L. Maire, B. Scholtes, C. Moussa, N. Bozzolo, D. P. Muñoz, A. Settefrati, and M. Bernacki, "Modeling of dynamic and post-dynamic recrystallization by coupling

a full field approach to phenomenological laws," *Materials Design*, vol. 133, pp. 498 – 519, 2017.

[10] W. Wang, A. Helbert, F. Brisset, M. Mathon, and T. Baudin, "Monte carlo simulation of primary recrystallization and annealing twinning," *Acta Materialia*, vol. 81, pp. 457 – 468, 2014.

[11] A. J. Detor, A. D. Deal, and T. Hanlon, "Grain boundary engineering alloy 706 for improved high temperature performance," in *Superalloys 2012: 12th International Symposium on Superalloys* (TMS, ed.), 2012.

[12] A. Ma, F. Roters, and D. Raabe, "On the consideration of interactions between dislocations and grain boundaries in crystal plasticity finite element modeling - theory, experiments, and simulations," *Acta Materialia*, vol. 54, pp. 2181–2194, 2006.

[13] U. Krupp, "Improving the resistance to intergranular cracking and corrosion at elevated temperatures by grain-boundary-engineering-type processing," *Mater. Sci.*, vol. 43, pp. 3908–3916, 2008.

[14] T. Watanabe, "Grain boundary design for desirable mechanical properties.," *Journal de Physique Colloques*, vol. 49, 1988.

[15] J. Stinville, N. Vanderesse, F. Bridier, P. Bocher, and T. Pollock, "High resolution mapping of strain localization near twin boundaries in a nickel-based superalloy," *Acta Materialia*, vol. 98, pp. 29 – 42, 2015.

[16] D. Texier, J. Cormier, and P. Villechaise, "Crack initiation sensitivity of wrought direct aged alloy 718 in the very high cycle fatigue regime: the role of non-metallic inclusions," *Material Science and Engineering*, vol. 678, pp. 122–136, 2016.

[17] J. Genée, L. Signor, and P. Villechaise, "Slip transfer across grain/twin boundaries in polycrystalline ni-based superalloys," *Materials Science and Engineering A*, vol. 701, pp. 24–33, 2017.

[18] Q. He, T. Huang, L. Shuai, Y. Zhang, G. Wu, X. Huang, and D. J. Jensen, "In-situ investigation of the evolution of annealing twins in high purity aluminium," *Scripta Materialia*, vol. 153, pp. 68 – 72, 2018.

[19] S. Liu, J. Zhang, G. Xi, X. Wan, D. Zhang, M. Zhong, C. Yang, and F. Pan, "Effects of intermediate annealing on twin evolution in twin-structured Mg-Nd alloys," *Journal of Alloys and Compounds*, vol. 763, pp. 11 – 17, 2018.

[20] X.-M. Chen, Y. Lin, and F. Wu, "EBSD study of grain growth behavior and annealing twin evolution after full recrystallization in a nickel-based superalloy," *Journal of Alloys and Compounds*, vol. 724, pp. 198 – 207, 2017.

192

[21] B. Lin, Y. Jin, C. Hefferan, S. Li, J. Lind, R. Suter, M. Bernacki, N. Bozzolo, A. D. Rolett, and G. S. Rohrer, "Observation of annealing twin nucleation at triple lines in nickel during grain growth," *Acta Materialia*, vol. 99, pp. 63–68, 2015.

[22] K. Song, Y. Chun, and S. Hwang, "Direct observation of annealing twin formation in a Pb-base alloy," *Materials Science and Engineering: A*, vol. 454-455, pp. 629 – 636, 2007.

[23] W. Wang, S. Lartigue-Korinek, F. Brisset, A. L. Helbert, J. Bourgon, and T. Baudin, "Formation of annealing twins during primary recrystallization of two low stacking fault energy Ni-based alloys," *Journal of Material Science*, vol. 50, pp. 2167–2177, 2015.

[24] Y. Jin, B. Lin, A. D. Rolett, G. S. Rohrer, M. Bernacki, and N. Bozzolo, "Thermo-mechanical factors influencing annealing twin development in nickel during recrystallization," *Journal of Material Science*, vol. 50, pp. 5191–5203, 2015.

[25] A. Leff and M. L. Taheri, "Quantitative assessment of the driving force for twin formation utilizing Nye tensor dislocation density mapping.," *Scripta Meterialia*, vol. 121, pp. 14–17, 2016.

[26] W. G. Burgers, "'stimulation crystals' and twin-formation in recrystallized aluminium," *Nature*, vol. 157, pp. 76–77, 1946.

[27] M. A. Meyers and L. E. Murr, "A model for the formation of annealing twins in f.c.c. metals and alloys," *Acta Metallurgica*, vol. 26, pp. 951–962, 1978.

[28] S. Dash and N. Brown, "An investigation of the origin and growth of annealing twins," *Acta Metallurgica*, vol. 11, pp. 1067–1075, 1963.

[29] J. P. Nielsen, "The origin of annealing twins," *Acta Metallurgica*, vol. 15, pp. 1083–1085, 1967.

[30] S. Mahajan, C. S. Pande, M. A. Imam, and B. B. Rath, "Formation of annealing twins in f.c.c. crystals," *Acta Metallurgica*, vol. 45, no. 6, pp. 2633–2638, 1997.

[31] V. Randle, "Twinning-related grain boundary engineering.," *Acta Materialia*, vol. 52, pp. 4067–4081, 2004.

[32] F. Humphreys and M. Hatherly, *Recrystallization and Related Annealing Phenomena.* Elsevier Science, 2012.

[33] J. Lee, *Introduction to Smooth Manifolds.* Graduate Texts in Mathematics, Springer, 2003.

[34] M. Spivak, *A Comprehensive Introduction to Differential Geometry.* Publish or Perish Inc., 2005.

[35] G. S. Rohrer, E. A. Holm, A. D. Rollett, S. M. Foiles, J. Li, and D. L. Olmsted, "Comparing calculated and measured grain boundary energies in nickel," *Acta Materialia*, vol. 58, pp. 5063–5069, 2010.

[36] W. T. Read and W. Shockley, "Dislocation models of crystal grain boundaries," *Physical Review*, vol. 78, pp. 275–289, 1950.

[37] B. Adams, D. Kinderlehrer, W. Mullins, A. Rollett, and S. Ta'asan, "Extracting the relative grain boundary free energy and mobility functions from the geometry of microstructures," *Scripta. Materialia*, vol. 38, pp. 531–536, 1997.

[38] A. Morawiec, "Method to calculate the grain boundary energy distribution over the space of macroscopic boundary parameters from the geometry of triple junctions," *Acta Materialia*, vol. 48, pp. 3525–3532, 2000.

[39] D. M. Saylor, A. Morawiec, and G. S. Rohrer, "The relative free energies of grain boundaries in magnesia as a function of five macroscopic parameters," *Acta Materialia*, vol. 51, pp. 3675–3686, 2003.

[40] D. L. Olmsted, S. M. Foiles, and E. A. Holm, "Survey of computed grain boundary properties in face-centered cubic metals: I. Grain boundary energy," *Acta Materialia*, vol. 57, pp. 3694–3703, 2009.

[41] D. L. Olmsted, S. M. Foiles, and E. A. Holm, "Survey of computed grain boundary properties in face-centered cubic metals: II. Grain boundary mobility," *Acta Materialia*, vol. 57, pp. 3704–3713, 2009.

[42] V. V. Bulatov, B. W. Reed, and M. Kumar, "Grain boundary energy function for fcc metals," *Acta Materialia*, vol. 65, pp. 161–175, 2013.

[43] E. A. Holm, G. N. Hassold, and M. A. Miodownik, "On misorientation distribution evolution during anisotropic grain growth," *Acta Materialia*, vol. 49, pp. 2981–2991, 2001.

[44] D. Schwarzenbach, "The success story of crystallography," *Acta Crystallographica Section A*, vol. 68, no. 1, pp. 57–67, 2012.

[45] D. Sands, *Introduction to Crystallography.* Dover Books on Chemistry Series, Dover Publications, 1993.

[46] R. Abbaschian and R. Reed-Hill, *Physical Metallurgy Principles.* Cengage Learning, 2008.

[47] A. Nicolay, *Supersolvus forging of Inconel 718 using screw press technologies*. PhD thesis, MINES Paristech, 2019.

[48] Z. C. Cordero, B. E. Knight, and C. A. Schuh, "Six decades of the Hall-Petch effect a survey of grain-size strengthening studies on pure metals," *International Materials Reviews*, vol. 61, no. 8, pp. 495–512, 2016.

[49] A. Sutton and R. Balluffi, *Interfaces in crystalline materials*. Monographs on the physics and chemistry of materials, Clarendon Press, 1995.

[50] B. Runnels, I. J. Beyerlein, S. Conti, and M. Ortiz, "An analytical model of interfacial energy based on a lattice-matching interatomic energy," *Journal of the Mechanics and Physics of Solids*, vol. 89, pp. 174 – 193, 2016.

[51] B. Runnels, I. J. Beyerlein, S. Conti, and M. Ortiz, "A relaxation method for the energy and morphology of grain boundaries and interfaces," *Journal of the Mechanics and Physics of Solids*, vol. 94, pp. 388 – 408, 2016.

[52] B. B. Straumal, O. A. Kogtenkova, A. S. Gornakova, V. G. Sursaeva, and B. Baretzky, "Review: grain boundary faceting–roughening phenomena," *Journal of Materials Science*, vol. 51, pp. 382–404, Jan 2016.

[53] C. Kittel, *Introduction to solid state physics*. Wiley, 1986.

[54] X. Chen, L. Li, H. Sun, L. Wang, and Q. Liu, "Studies on the evolution of annealing twins during recrystallization and grain growth in highly rolled pure nickel," *Materials Science and Engineering: A*, vol. 622, pp. 108 – 113, 2015.

[55] J. Cahoon, Q. Li, and N. Richards, "Microstructural and processing factors influencing the formation of annealing twins," *Materials Science and Engineering: A*, vol. 526, no. 1, pp. 56 – 61, 2009.

[56] J. Bair, S. Hatch, and D. Field, "Formation of annealing twin boundaries in nickel," *Scripta Materialia*, vol. 81, pp. 52 – 55, 2014.

[57] Y. Jin, *Annealing twin formation mechanism*. Theses, Ecole Nationale Supérieure des Mines de Paris, Dec. 2014.

[58] H. C. H. Carpenter and S. Tamura, "The formation of twinned metallic crystals," *Proceedings of the Royal Society of London. Series A, Containing Papers of a Mathematical and Physical Character*, vol. 113, no. 763, pp. 161–182, 1926.

[59] B. Lin, *Investigating annealing twin formation mechanisms in face-centered cubic nickel*. Phd thesis, Carnegie Mellon University, 2015.

[60] Y. Jin, B. Lin, M. Bernacki, G. Rohrer, A. Rollett, and N. Bozzolo, "Annealing twin development during recrystallization and grain growth in pure nickel," *Materials Science and Engineering: A*, vol. 597, pp. 295 – 303, 2014.

[61] J. Lind, S. F. Li, and M. Kumar, "Twin related domains in 3D microstructures of conventionally processed and grain boundary engineered materials," *Acta Materialia*, vol. 114, pp. 43 – 53, 2016.

[62] D. B. Bober, J. Lind, R. P. Mulay, T. J. Rupert, and M. Kumar, "The formation and characterization of large twin related domains," *Acta Materialia*, vol. 129, pp. 500 – 509, 2017.

[63] L. Maire, *Full field and mean field modeling of dynamic and post-dynamic recrystallization in 3D - Application to 304L steel.* PhD thesis, MINES Paristech, 2018.

[64] J. Lépinoux, D. Weygand, and M. Verdier, "Modeling grain growth and related phenomena with vertex dynamics," *Comptes Rendus Physique*, vol. 11, no. 3, pp. 265 – 273, 2010.

[65] K. A. Brakke, "The surface evolver," *Experimental Mathematics*, vol. 1, no. 2, pp. 141–165, 1992.

[66] J. Allen, C. Cornwell, B. Devine, and C. Welch, "Simulations of anisotropic grain growth in single phase materials using Q-state Monte Carlo," *Computational Materials Science*, vol. 71, pp. 25 – 32, 2013.

[67] Q. Yu, M. Nosonovsky, and S. K. Esche, "Monte Carlo simulation of grain growth of single-phase systems with anisotropic boundary energies," *International Journal of Mechanical Sciences*, vol. 51, pp. 434–442, 2009.

[68] A. Rollett, D. Srolovitz, and M. Anderson, "Simulation and theory of abnormal grain growth - anisotropic grain boundary energies and mobilities," *Acta Metallurgica*, vol. 37, no. 4, pp. 1227 – 1240, 1989.

[69] G. S. Grest, D. J. Srolovitz, and M. P. Anderson, "Computer simulation of grain growth - IV. Anisotropic grain boundary energies," *Acta Metallurgica*, vol. 33, pp. 509–520, 1985.

[70] L. Rauch, L. Madej, P. Spytkowski, and R. Golab, "Development of the cellular automata framework dedicated for metallic materials microstructure evolution models," *Archives of Civil and Mechanical Engineering*, vol. 15, no. 1, pp. 48 – 61, 2015.

[71] L. Sieradzki and L. Madej, "A perceptive comparison of the cellular automata and Monte Carlo techniques in application to static recrystallization modeling in polycrystalline materials," *Computational Materials Science*, vol. 67, pp. 156 – 173, 2013.

196

[72] A. Rollett and D. Raabe, "A hybrid model for mesoscopic simulation of recrystallization," *Computational Materials Science*, vol. 21, no. 1, pp. 69 – 78, 2001.

[73] Y. Liu, T. Baudin, and R. Penelle, "Simulation of normal grain growth by cellular automata," *Scripta Materialia*, vol. 34, no. 11, pp. 1679 – 1683, 1996.

[74] K. Chang, L.-Q. Chen, C. E. Krill, and N. Moelans, "Effect of strong nonuniformity in grain boundary energy on 3-D grain growth behavior: A phase-field simulation study," *Computational Materials Science*, vol. 127, pp. 67–77, 2017.

[75] K. Chang and N. Moelans, "Effect of grain boundary energy anisotropy on highly textured grain structures studied by phase-field simulations," *Acta Materialia*, vol. 64, pp. 443–454, 2014.

[76] A. Mallick and S. Vedantam, "Phase field study of the effect of grain boundary energy anisotropy on grain growth," *Computational Materials Science*, vol. 46, pp. 21–25, 2009.

[77] E. Miyoshi and T. Takaki, "Multi-phase-field study of the effects of anisotropic grain-boundary properties on polycrystalline grain growth," *Journal of Crystal Growth*, vol. 474, pp. 160–165, 2017.

[78] M. A. Zaeem, H. E. Kadiri, P. Wang, and M. Horstemeyer, "Investigating the effects of grain boundary energy anisotropy and second-phase particles on grain growth using a phase-field model," *Computational Materials Science*, vol. 50, pp. 2488–2492, 2011.

[79] I. Steinbach, "Phase-field models in materials science," *Modelling and Simulation in Materials Science and Engineering*, vol. 17, jul 2009.

[80] L.-Q. Chen, "Phase-field models for microstructure evolution," *Annual Review of Materials Research*, vol. 32, no. 1, pp. 113–140, 2002.

[81] J. A. Sethian, "Theory, algorithms, and applications of level set methods for propagating interfaces," *Acta Numerica*, vol. 5, pp. 309 – 395, 1996.

[82] B. Merriman, J. K. Bence, and S. J. Osher, "Motion of multiple junctions: A level set approach," *Journal of Computational Physics*, vol. 112, pp. 334–363, 1994.

[83] M. Bernacki, Y. Chastel, T. Coupez, and R. Logé, "Level set framework for the numerical modelling of primary recrystallization in polycrystalline materials," *Scripta Materialia*, vol. 58, no. 12, pp. 1129 – 1132, 2008.

[84] M. Bernacki, H. Resk, T. Coupez, and R. E. Logé, "Finite element model of primary recrystallization in polycrystalline aggregates using a level set framework," *Modelling and Simulation in Materials Science and Engineering*, vol. 17, no. 6, 2009.

[85] R. Logé, M. Bernacki, H. Resk, L. Delannay, H. Digonnet, Y. Chastel, and T. Coupez, "Linking plastic deformation to recrystallization in metals using digital microstructures," *Philosophical Magazine*, vol. 88, no. 30-32, pp. 3691–3712, 2008.

[86] M. Elsey, S. Esedoglu, and P. Smereka, "Simulations of anisotropic grain growth: Efficient algorithms and misorientation distributions," *Acta Materialia*, vol. 61, pp. 2033–2043, 2013.

[87] Y. Jin, N. Bozzolo, A. D. Rollett, and M. Bernacki, "2D finite element modeling of misorientation dependent anisotropic grain growth in polycrystalline materials: Level set versus multi-phase-field method," *Computational Materials Science*, vol. 104, pp. 108–123, 2015.

[88] H. Hallberg, "Influence of anisotropic grain boundary properties on the evolution of grain boundary character distribution during grain growth - a 2D level set study," *Modelling and Simulation in Materials Science and Engineering*, vol. 22, no. 8, 2014.

[89] H. Hallberg, "Approaches to modeling of recrystallization," *Metals*, vol. 1, no. 1, pp. 16–48, 2011.

[90] M. Bernacki, R. Logé, and T. Coupez, "Level set framework for the finite-element modelling of recrystallization and grain growth in polycrystalline materials," *Scripta Materialia*, vol. 64, pp. 525–528, 2011.

[91] B. Scholtes, M. Shakoor, A. Settefrati, P.-O. Bouchard, N. Bozzolo, and M. Bernacki, "New finite element developments for the full field modeling of microstructural evolutions using the level-set method," *Computational Materials Science*, vol. 109, pp. 388–398, 2015.

[92] L. Maire, B. Scholtes, C. Moussa, N. Bozzolo, D. Pino Muñoz, and M. Bernacki, "Improvement of 3D mean field models for capillarity-driven grain growth based on full field simulations," *Journal of Materials Science*, vol. 51, no. 24, pp. 10970–10981, 2016.

[93] M. Elsey, S. Esedolu, and P. Smereka, "Large-scale simulation of normal grain growth via diffusion-generated motion," *Proceedings of the Royal Society A: Mathematical, Physical and Engineering Sciences*, vol. 467, no. 2126, pp. 381–401, 2011.

[94] J. Fausty, D. Pino Muñoz, N. Bozzolo, and M. Bernacki, "A novel level-set finite element formultion for grain growth with heterogeneous grain boundary energies," *Materials and Design*, vol. 160, pp. 578–590, 2018.

[95] H. Hallberg and V. V. Bulatov, "Modeling of grain growth under fully anisotropic grain boundary energy," *Modelling and Simulation in Materials Science and Engineering*, vol. 27, no. 4, 2019.

[96] P. Halmos, *Naive Set Theory*. Undergraduate Texts in Mathematics, Springer New York, 1998.

[97] J. Lee, *Introduction to Topological Manifolds*. Graduate Texts in Mathematics, Springer New York, 2010.

[98] D. W. Hoffman and J. W. Cahn, "A vector thermodynamics for anisotropic surfaces : I. Fundamentals and applications to plane surface junctions," *Surface Science*, vol. 31, pp. 368–388, 1972.

[99] D. W. Hoffman and J. W. Cahn, "A vector thermodynamics for anisotropic surfaces : II. Curved and Faceted Surfaces," *Acta Metallurgica*, vol. 22, pp. 1205–1214, 1974.

[100] C. Herring, *Surface Tension as a Motivation for Sintering*. Springer Berlin Heidelberg, 1999.

[101] H. Garcke, B. Nestler, and B. Stoth, "A multiphase field concept: Numerical simulation of moving phase boundaries and multiple junctions," *SIAM Journal on Applied Mathematics*, vol. 60, pp. 295–315, 1999.

[102] M. Shakoor, B. Scholtes, P.-O. Bouchard, and M. Bernacki, "An efficient and parallel level set reinitialization method - Application to micromechanics and microstructural evolutions," *Applied Mathematical Modelling*, vol. 39, no. 23-24, pp. 7291–7302, 2015.

[103] Y. Belhamadia, A. Fortin, and É. Chamberland, "Anisotropic mesh adaptation for the solution of the stefan problem," *Journal of Computational Physics*, vol. 194, no. 1, pp. 233 – 255, 2004.

[104] A. N. Brooks and T. J. Hughes, "Streamline upwind/Petrov-Galerkin formulations for convection dominated flows with particular emphasis on the incompressible Navier-Stokes equations," *Computer Methods in Applied Mechanics and Engineering*, vol. 32, no. 1, pp. 199 – 259, 1982.

[105] C. Geuzaine and J.-F. Remacle, "Gmsh: A 3-D finite element mesh generator with built-in pre- and post-processing facilities," *International Journal for Numerical Methods in Engineering*, vol. 79, no. 11, pp. 1309–1331, 2009.

[106] B. Scholtes, *Development of an efficient level set framework for the full field modeling recrystallization in 3D*. Theses, PSL Research University, Dec. 2016.

[107] H.-K. Zhao, T. Chan, B. Merriman, and S. Osher, "A variational level set approach to multiphase motion," *Journal of Computational Physics*, vol. 127, no. 1, pp. 179 – 195, 1996.

[108] A. Savitzky and M. J. E. Golay, "Smoothing and differentiation of data by simplified least squares procedures.," *Analytical Chemistry*, vol. 36, no. 8, pp. 1627–1639, 1964.

[109] E. Roux, M. Bernacki, and P. Bouchard, "A level-set and anisotropic adaptive remeshing strategy for the modeling of void growth under large plastic strain," *Computational Materials Science*, vol. 68, pp. 32–46, 2013.

[110] J. K. Mackenzie, "Second paper on statistics associated with the random disorientation of cubes," *Biometrika*, vol. 45, pp. 229–240, 1958.

[111] K. Hitti, P. Laure, T. Coupez, L. Silva, and M. Bernacki, "Precise generation of complex statistical Representative Volume Elements (RVEs) in a finite element context," *Computational Materials Science*, vol. 61, pp. 224–238, 2012.

[112] L. Madej, "Digital/virtual microstructures in application to metals engineering - a review," *Archives of Civil and Mechanical Engineering*, vol. 17, no. 4, pp. 839 – 854, 2017.

[113] J. Burke and D. Turnbull, "Recrystallization and grain growth," *Progress in Metal Physics*, vol. 3, pp. 220 – 292, 1952.

[114] A. L. Cruz-Fabiano, R. E. Logé, and M. Bernacki, "Assessement of simplified 2D grain growth models from numerical experiments based on a level set framework," *Computational Materials Science*, vol. 92, pp. 305–312, 2014.

[115] S. Takajo, C. Merriman, S. Vogel, and D. Field, "In-situ EBSD study on the cube texture evolution in 3wt% Si steel complemented by ex-situ EBSD experiment - From nucleation to grain growth," *Acta Materialia*, 2018.

[116] O. Engler, "On the influence of orientation pinning on growth selection of recrystallisation," *Acta Materialia*, vol. 46, no. 5, pp. 1555 – 1568, 1998.

[117] E. A. Holm, G. S. Rohrer, S. M. Foiles, A. D. Rollett, H. M. Miller, and D. L. Olmsted, "Validating computed grain boundary energies in fcc metals using the grain boundary character distribution," *Acta Materialia*, vol. 59, pp. 5250–5256, 2011.

[118] D. Wolf, "A read-shockley model for high-angle grain boundaries," *Scripta Metallurgica*, vol. 23, no. 10, pp. 1713 – 1718, 1989.

200

[119] T. Coupez, H. Digonnet, and R. Ducloux, "Parallel meshing and remeshing," *Applied Mathematical Modelling*, vol. 25, no. 2, pp. 153 – 175, 2000.

[120] A. Najah, B. Cochelin, N. Damil, and M. Potier-Ferry, "A critical review of asymptotic numerical methods," *Archives of Computational Methods in Engineering*, vol. 5, pp. 31–50, Mar 1998.

[121] S. Florez, M. Shakoor, T. Toulorge, and M. Bernacki, "A new finite element strategy to simulate microstructural evolutions," *Computational Materials Science*, vol. 172, 2020.

[122] J. Furstoss, M. Bernacki, C. Petit, J. Fausty, D. P. Muñoz, and C. Ganino, "Full field and mean field modeling of grain growth in a multiphase material under dry conditions : application to peridotites," *Submitted to Journal of Geophysical Research: Solid Earth*.

RÉSUMÉ

Le dimensionnement des disques de superalliage base nickel dans les moteurs d'avion est un processus complexe et critique pour le bon fonctionnement du transport aérien. L'amélioration continue des performances de ces composants doit assurer la bonne tenue du moteur dans des conditions mecaniques et thermiques extrêmes. Un des aspects les plus importants dans la genèse de ces produits est l'état microstructural de la matière. Les ingénieurs qui développent ces turbines ont donc un besoin spécifique pour des modèles capables de prédire les évolutions microstructurales pendant le forgeage. Ce travail a pour but d'améliorer les approches numériques de type Élément Finis - Level Set appliquées à l'évolution des microstructures métalliques en enrichissant la description des joints de grains. L'enrichissement de la représentation des joints de grains est nécessaire afin de prendre en compte des joints particuliers - comme les joints de macles - qui sont observés en très grand nombre dans les superalliages forgés. Cette activité vise particulièrement à incorporer l'effet des énergies arbitraires des interfaces cristallines dans les modèles de migration de joints de grains. Les modifications apportées à la méthode sont à la fois numériques et mathématiques. En incluant des termes supplémentaires dans l'expression de la vitesse de migration de l'interface, cette étude montre, par la simulation de cas analytiques et non-analytiques, que l'approche est capable de simuler un éventail de phénomènes. À la fois l'effet de l'ancrage dû à l'orientation et le moment sur les joints multiples sont mis en évidence. La méthode donne aussi des résultats plus fiables sur la simulation des joints avec des propriétés particulières comme les joints de macles.

MOTS CLÉS

Métallurgie, Éléments Finis, Modélisation, Joints de Macles, Anisotropie

ABSTRACT

The design of nickel based superalloy disks in an industrial setting is a stringent process which must produce critical components of the aircraft engine. Improving these components is no small feat given the extreme mechanical and thermal constraints endured by these types of parts. One of the most important aspects of the design is the microstructure of the unerlying material. As such, the engineers who design these machines have a specific need for models capable of predicting microstructural evolution in metallic materials during the forging process. This work aims to improve on the existing Level Set Finite Element framework for microstructural evolution by including enriched descriptions of grain boundaries. These enriched characterizations are needed in order to take into account special boundaries - such as the twin boundary - which can be observed in great number in forged superalloys. This effort is concentrated on integrating arbitrary values for the grain boundary energy density into the numerical models. This enhancement of the model lies not only in the numerical aspects but also in the underlying mathematical formulation. By including supplemental terms in the expression of the velocity of a migrating grain boundary, this investigation has found, using analytical and non-analytical benchmarks, that the new approach is able to take into account a host of phenomena. Evidence of both orientation pinning and torque applied to triple junctions has been found in virtually annealed polycrystals. Also, the model has proven to be more capable of taking into account the singular behavior of the twin boundary then previous iterations of the method.

KEYWORDS

Metallurgy, Finite Elements, Modeling, Twin Boundaries, Anisotropy